Transplanting Assembly of Individual Carbon Nanotubes

by

Soohyung Kim

B.S. Mechanical Design and Production Engineering
Seoul National University, 1995

M.S. Mechanical Design and Production Engineering
Seoul National University, 1997

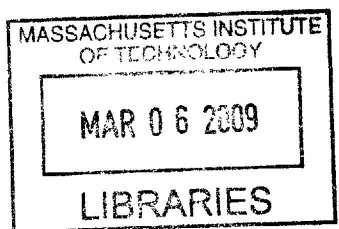
MASSACHUSETTS INSTITUTE
OF TECHNOLOGY
MAR 0 6 2009
LIBRARIES

SUBMITTED TO THE DEPARTMENT OF MECHANICAL ENGINEERING
IN PARTIAL FULFILLMENT OF THE REQUIREMENTS FOR THE DEGREE OF

DOCTOR OF PHILOSOPHY IN MECHANICAL ENGINEERING
AT THE
MASSACHUSETTS INSTITUTE OF TECHNOLOGY

FEBRUARY 2009

© 2009 Massachusetts Institute of Technology
All right reserved

Signature of Author:

Department of Mechanical Engineering
October 2, 2008

Certified by:

Sang-Gook Kim
Associate Professor of Mechanical Engineering
Thesis Supervisor

Accepted by:

David E. Hardt
Chairman, Department Committee on Graduate Students

ARCHIVES

Transplanting Assembly of Individual Carbon Nanotubes

by

Soohyung Kim

Submitted to the Department of Mechanical Engineering
on October 2, 2008 in Partial Fulfillment of the
requirements for the Degree of Doctor of Philosophy in
Mechanical Engineering

ABSTRACT

Handling and assembling individual nanostructures to bigger scale systems such as MEMS have been the biggest challenge. A deterministic assembly of individual carbon nanotubes by transplanting them to MEMS structures is demonstrated with a new assembly method, "transplanting assembly." This thesis describes development of a novel assembly technique by transforming individual CNTs assemblable, which enables manual, parallel or automated assembly of individual CNTs in a deterministic way.

The key idea of transplanting assembly is to grow individual CNT strands on a substrate at optimal growth conditions, to encapsulate individual CNTs into micro-scale carrier blocks and to transplant them to the target locations. This new assembly method enables products such as CNT-tipped AFM probes in a predictable and repeatable manner. The major research topics discussed in this thesis are: (1) the methods to grow vertically aligned single strand CNTs at predefined locations, (2) the encapsulation method to preserve/control the orientation/exposed length of an individual CNT during transplanting, and (3) the assembly scheme to locate/release an individual CNT at the target location.

An array of CNTs was grown from the nickel nano-dots, which were defined on Si substrates using electron-beam lithography followed by metal deposition and lift-off processes. Each CNT strand was embedded into a MEMS scale polymer block which serves as a CNT carrier. A double polymeric layer encapsulation was designed and implemented: the top SU-8 forms the body of the carrier while the bottom PMGI layer holds the body until the release of the carrier from the substrate and then is going to be removed to expose the CNT tip with a predefined length. A model was developed to predict mechanical behavior of individual CNTs under the flow of liquid polymers. Manual assembly of a polymer block to the end of a tipless AFM cantilever forms a CNT-tipped AFM probe, which can be accomplished in minutes without laborious weeding, trimming and welding process. The AFM scanning results confirmed the CNT-tipped AFM probe's much improved imaging performance and potential for scanning soft biological samples at nanometer resolutions.

Thesis Supervisor: Sang-Gook Kim
Title: Associate Professor of Mechanical Engineering

Acknowledgements

First, I would like to thank my advisor, Prof. Sang-Gook Kim, his support, guidance, and continuous encouragement. I would also like to thank Prof. Kamal Youcef-Toumi and Prof. Carol Livermore for being my thesis committee members and giving me their comments and support throughout my thesis work.

I was fortunate to work with our group members, Dr. Hyung Woo Lee, Stephen Bathurst, Arman Hajati, Heonju Lee, Nathan Reticker-Flynn, Jordan Peck, Zachary J. Traina, Sunil D. Gouda, Robert Xia, and Clemens Mueller-Falcke.

I would like to express my appreciation to the entire MTL and CMSE staff for their help.

I have enjoyed the time with many friends, especially members of Korean graduate student association of Mechanical engineering. Especially I would like to thank Kyungyoon Noh, my best friend who introduced me to MIT and helped my family settle down in Boston.

Lastly, my great gratitude and appreciation goes to my family. Special thanks to my wife, Jae Kyung Jung, and my children, Dohyun Kim and Ashley Jiyoon Kim, for their support and patience during my study at MIT.

Table of Contents

1 Introduction 15
1.1 Objective 15
1.2 Assembly of carbon nanotubes (CNTs): review 17
1.2.1 Langmuir-Blodgett films for nanostructure assembly 19
1.2.2 Nano assembly with templates 24
1.2.3 External force field assisted assembly 27
1.3 The CNT-tipped AFM probes: review 32
1.3.1 The CNT-tipped AFM probes by direct attachment approaches 33
1.3.2 The CNT-tipped AFM probes by the field assisted assembly 37
1.3.3 The CNT AFM probes by catalytic growth 42
1.3.4 The post-processes to improve the qualities of the CNT tips 47
1.4 The scope and organization of the thesis 53
2 Introduction 54
2.1 Introduction: Transplanting assembly towards deterministic assembly of CNTs 54
2.2 Design for an array of the individual CNTs 59
2.3 Design and material selections for the encapsulation procedures with dual layers 61
2.3.1 The material selection for the MEMS carrier layer 61
2.3.2 The double (or multiple) layer design for MEMS carriers 62
2.3.3 Selection of the thickness and material of the bottom layer 64
2.3.4 Discussion on the double layer design 68
2.4 The change of the orientation of the individual CNTs during spin-coating step.. 69
2.5 Design for transferring the individual CNT with carriers 74
2.6 Summary 76
3 The controlled growth of an array of vertically aligned CNTs 77
3.1 Introduction 77
3.2 An array of nickel (Ni) catalytic nano dots 82
- Step 1: Deposition of a titanium (Ti) layer on a silicon (Si) substrate 82
- Step 2: Spin-coating of a PMMA layer 83
- Step 3: Exposure and development of the PMMA layer 84
- Step 4: Deposition catalytic material (Ni) 84
- Step 5: Lift-off step 85

3.3 CNT growth by PECVD 87
3.3.1 Plasma enhanced chemical vapor deposition (PECVD) 87
3.3.2 The PECVD machine of MIT 88
3.3.3 PECVD machine modification for stable plasma and uniform heating.... 94
3.4 Summary 103
4 Integration of the individual CNTs into micro-scale carriers 104
4.1 Introduction: encapsulation procedure 104

4.2 Experimental results of encapsulation procedure 105
- Step 1: Growth of an array of vertically aligned CNTs 106
- Step 2: Coating of the bottom (PMGI SF 11) layer over the array of CNTs 108
- Step 3: Coating of the top (SU8-2015) layer 108
- Step 4: Patterning of the top (SU8-2015) layer 109
- Etching of the bottom (PMGI SF 11) layer 112

4.2.1 Release of the CNTs from the substrate 114
4.3 Characterization of the structural integrity of CNTs 115
4.3.1 High resolution transmission electron microscopy 115
4.3.2 Raman spectroscopy 120
4.4 Summary 122
5 Fabrication of CNT probes and their application for scanning probe microscopy (SPM) 123
5.1 Introduction 123
5.2 Transfer of the individual CNTs 123
- Step 1: Partial etching of the bottom layer 128
- Step 2: Approach a cantilever to a target CNT 129
- Step 3: Cure the adhesive 131
- Step 4: Shear the block with a single CNT 131
- Step 5: Release the block 132
- Step 6: Etch the bottom layer 132

5.3 Discussion about the assembly results 137
5.3.1 CNT tips on various cantilevers 137
5.3.2 Effective CNT tip shape and radius 141
5.4 AFM scanning results with CNT probes over various samples 144
5.4.1 Standard grating for AFM calibrations 144
5.4.2 Critical-angle transmission grating 146
5.4.3 Biological samples 149
5.5 Summary 151
6 CNT probes for tip enhanced Raman spectroscopy (TERS) 152
6.1 Introduction 152
6.2 The CNT probe for tip enhance Raman spectroscopy (TERS) 153
6.2.1 Surface enhanced Raman spectroscopy as a tool for single molecule detection 153
6.2.2 Tip-enhanced Raman spectroscopy (TERS) 160
6.3 A conical plasmonic resonator 163
6.3.1 Design of a novel plasmonic resonator 164
6.3.2 Finite element analysis and the simulation results 167
6.3.3 Discussion on fabrication and assembly of the plasmonic resonator 174
6.4 Summary 176
7 Conclusion 177
7.1 Summary and major contributions 177

7.2 Discussions and future work 181
7.2.1 CNT growth 181
7.2.2 Encapsulation of the individual CNTs 182
7.2.3 Transfer of the individual CNTs 183

List of figures

Figure 1.1 An electrical interconnection by a CNT through the catalytic growth [5]: (A) An array of devices. (B) A suspended CNT device. 18
Figure 1.2 An electrical interconnection by a CNT through direct assembly by dielectrophoresis [6]: (A) Comb-shaped electrodes. (B) One MWNT spanning a gap.... 18
Figure 1.3 LB Films of SWNTs [8]: (A~C) Schematic illustration of the mechanism for the in-plane orientation of s-SWNT. Compression-induced orientation in the LB film by barrier compression (A), in-plane tube orientation for films prepared by horizontal lifting (B), and flow orientation of tubes induced by the vertical motion of the substrate (C). (D) AFM images of an s-SWNT single layer on mica prepared by vertical dipping. The arrow indicates the dipping direction. 20
Figure 1.4 Parallel assembly of NW arrays [9]: (A~B) Schematic of fluidic channel structures for flow assembly. Parallel arrays (A) and multiple crossed NW arrays (B). (C~D) SEM images of parallel arrays of InP NWs aligned by channel flow. Periodic NW arrays (C: scale bar = 2 μm) and crossed NW arrays (D: scale bar = 500 nm). 21
Figure 1.5 Parallel and scalable interconnection of NW devices without registration [10]: (A) Central electrode region of a single array. (B) Schematic illustrating key steps of the interconnection approach. (C) Optical micrograph of integrated metal electrode arrays (scale bar = 1 mm). (D) SEM image of the central active region (scale bar = 40 μm). (E) SEM image of three NW devices connected between the common and finger electrodes (scale bar = 3 μm). (F, G) SEM images of higher-density NW devices defined by electron beam lithography (scale bars = 300 nm). 22
Figure 1.6 AFM images of (A) cross-aligned SWNTs/PVP composite fibers and (B) cross-aligned SWNT array after polymer component removal. [11] 23
Figure 1.7 TASR [12]. Schematic of templated assembly by selective removal. (A) Assembly setup and enlarged cross-sectional view of ultrasonic forces acting on substrate. (B) Cross-sectional schematic of a sphere in a hole and a sphere on a flat surface, along with forces and torques acting on the sphere. (C) Optical microcraph of assembly results for the array with largest exposure dose. 25
Figure 1.8 (A) Process steps of DNA templated self-assembly of CNTs. (B~D) Localization of a SWNT at a specific address on the scaffold dsDNA molecule using RecA. (E~F) A DNA-templated carbon nanotube FET and metallic wires contacting it. (scale bar = 100 nm) (E) An individual SWNT. (F) A rope of SWNT. [14] 26
Figure 1.9 Top- and cross-sectional views of the electrode structures used in the field assisted assembly experiments and optical microscope images of 5 μm-long, 200 nm-diameter Au NWs (A) without and (B) with upper field electrodes [15]. 28
Figure 1.10 Schematic of deposition with ac only, dc only, and composite electric fields [6]: (A) Before applying an electric field. (B) AC electric field of 5 MHz. (C) DC electric field. (D) The composite electric field. 30
Figure 1.11 Perfectly aligned arrays of long, linear SWNTs and their implementation in thin-film-type transistors [20]: (A) SEM image of a pattern of perfectly aligned, perfectly linear SWNTs formed by CVD growth on a quartz substrate. (B) Schematic illustration of

the layout of a type of transistor that incorporates these aligned SWNTs as the semiconductor. (C) SEM image of the channel region of a device. 31
Figure 1.12 A CNT-tipped AFM probe. 32
Figure 1.13 (A~C) Single nanotube attached to the pyramidal tip of a silicon cantilever for AFM. (A, B) SEM images showing the MWNT bundle attached to the steeper slope of the back side of the Si pyramid. (C) Transmission electron microscopy (TEM) image. (E~F) Tapping-mode AFM image of a 400-nm-wide, 800-nm-deep trench. (E) Image taken with a bare pyramidal Si tip. (F) Image taken with a nanotube attached to the pyramid of the same cantilever. [23]. 34
Figure 1.14 The CNT-tipped AFM probes by picking up SWNTs directly [29]: (A) Schematic depicting the process by which a microfabricated pyramidal tip picks up a vertically aligned carbon nanotube. TEM images of (B) a 0.9 nm diameter nanotube tip and (C) a 2.8 nm diameter nanotube tip.(scale bars = 10 nm). 35
Figure 1.15 Procedures to fabricate a CNT-tipped AFM probe by manipulating a single carbon nanotube/nanofiber (CN) using an electrothermal gripper [30]: (A, B) Aligning of gripper to CN. (C) Gripping. (D) Detachment. (E) Aligning of CN to AFM probe. (F) Attachement. (G, H) Mechanical test. 36
Figure 1.16 Single CNT AFM tips using an arc discharge method [31]: (A) Schematics of attachment apparatus. (B) An SEM micrograph of a nanotube tip. 38
Figure 1.17 The CNT AFM probes by magnetic field assisted assembly [33]: (A) Schematic of the experimental apparatus atop a solenoid. The inset shows the area through which the changing flux goes. (B, C) Examples of nanotube functionalized probes prepared with the method. 39
Figure 1.18 Optical microscope images of a Si AFM probe (A) before, (B) during, and (C) after the dielectrophoresis process of assembling the CNT tip. An ac field was applied between the AFM probe and the counter electrode during the deposition. A CNT tip assembled on the apex of the Si AFM probe is visible in image (C) [34]. 40
Figure 1.19 TEM images of an SWNT bundle attached to a commercial Si AFM probe by the dielectrophoresis process. The SWNT bundle has a diameter of ~20 nm near the tip and has conical geometry [34]. 41
Figure 1.20 An FE-SEM (A) and a TEM (B) images of a CVD nanotube tip that has been shortened for imaging (scale bar: 1 μm in (A) and 100 nm in (B)) [35]. 42
Figure 1.21 SWNT-tipped AFM probes [36]: (A) Overview of the approach used to prepare SWNT tips. (B, C) FE-SEM images of a CVD nanotube tip grown from a Si cantilever/tip assembly (B) before and (C) after shortening (scale bar: 500nm). 43
Figure 1.22 (A) 4 in. wafer containing 375 AFM cantilevers with integrated Si tips. (B) Schematic process flow for placing catalyst onto Si tips on a wafer. (C) CVD setup for growth on a wafer. (D) Long nanotubes extending out of the Si tips are shortened [37]. 44
Figure 1.23 (A), (B) SEM images of as-grown nanotube tips. (C) TEM image of a SWNT extending from a Si tip [37]. 45
Figure 1.24 Large-scale fabrication of CNT-tipped AFM probe tips by PECVD [38]: (A) Wafer-scale fabrication process flow for making CNT-tipped AFM probes. (B) Photograph of a 4-in. wafer containing 244 CNT-tipped AFM probes. (C) SEM images of

CNT-tipped AFM probes with an individual CNT grown from a 200 nm catalyst site on a cantilever beam. 46
Figure 1.25 (A) A schematic diagram showing the CNT orientation angle with respect to each trench wall. (B) Two-dimensional profile scan of the right and left edges of a silicon grating overlaid to allow comparison and [43]. 49
Figure 1.26 (A) SEM image of an AFM cantilever with a metal-coated nanotube on the pyramid. The arrow shows the direction of the FIB and the metal coating. Inset: Image of the metal-coated nanotube at the apex of the pyramid. (B) and (C) A metal-coated nanotube tip before (B) and after (C) alignment with FIB. It is 1.2 μm long and has a diameter of 45 nm, as determined from the SEM image, which gives it an aspect ratio of 27 [50]. 51
Figure 1.27 The CNT-tipped AFM probe of Nanoscience Instruments, Inc. [51]. 51
Figure 2.1 The concept of transplanting assembly of CNTs. (A) growth of vertically aligned single strand CNTs. (B) Encapsulation of CNTs into polymer blocks. (C) Transplanting the CNTs to the target location. 54
Figure 2.2 An overview of nanopelleting processes for bundles of CNTs. The pellets are fabricated by etching trenches, growing CNTs with vertical alignment in the trenches, then spin-casting an epoxy polymer, and planarizing the substrate to create isolated pellets with uniform-length CNTs. The pellets can then be released, harvested, and transplanted in large scale [3]. 55
Figure 2.3 Results of transplanting assembly of CNT bundles: (A) A bundle of CNTs on a Si substrate. (B) A double row of circular pellets in trenches. [2]. 56
Figure 2.4 Transplanting assembly procedure in fabricating a CNT AFM probe. (A) CNT growth: An array of vertically aligned CNT is grown at the predefined locations. (B) Encapsulation: Two layers of polymers are spin-coated to encapsulate the array of CNs. (C) Pattern and transfer: Top polymer layer is patterned such that each polymer block contains a single CNT, and the individual polymer block is transferred to MEMS cantilever. (D) CNT tip release: Any remaining bottom-layer polymer is etched way, and the CNT tip, top polymer block, and cantilever form a CNT AFM probe. 57
Figure 2.5 A pattern of an (21 by 21) array of circular dots for electron beam writing. (d: the spacing between the dots, L: the overall range of the array) 60
Figure 2.6 Encapsulation procedures: an array of CNTs (A) is embedded in two polymer layers (B), and the layers are patterned using photolithography (C). 63
Figure 2.7 A schematic of SU patterns (dotted circles) with the individual CNTs (small solid circles). 63
Figure 2.8 A CNT tip (the length = L, the radius = r). 65
Figure 2.9 The thermal vibration of the CNT tip ends at the temperature of 300K for CNTs with length of 1 μm, 3 μm and 5 μm. 66
Figure 2.10 The thermal vibration of the CNT tip ends at the temperature of 300K for a case of a CNT with 1 nm diameter. 67
Figure 2.11 Procedures of spin-coating of a polymer layer. (A) An array of vertically aligned CNTs. (B) Spinning of the sample after dispensing the liquid polymer solution. (C) Formation of the polymer layer with a target thickness. 69

Figure 2.12 Model for interaction of the single CNT with encapsulating polymers: (A) One dimensional fluid mechanics model. (B) An array of CNTs.................................. 72
Figure 2.13 The deflection at the CNT tips under fluidic shearing. 73
Figure 2.14 A schematic showing the procedures in transferring the individual CNTs to the end of cantilever: (A) Approach the cantilever to a target CNT (encapsulated in a MEMS carrier). The cantilever already picked up a small droplet of an adhesive. (B) Wait until the adhesive is cured. (C) Shear the bottom layer with the CNT horizontally by manipulating the cantilever. (D) Lift off the CNT with the carrier. (E) Etch the remaining bottom layer to form a CNT-tipped AFM probe. 75
Figure 3.1 Schematic of arc-discharge (A) and laser ablation (B) methods [54]. 78
Figure 3.2 The CNTs grown by (A) arc-discharge [55] and (B) laser ablation [57]. In general, CNTs grown by arc-discharge and laser ablation have a form of soot, which makes assembly of the individual CNTs impossible. 78
Figure 3.3 Schematic of CVD [54]. 79
Figure 3.4 CNTs grown by thermal CVD [61]. (A) They may look vertically aligned macroscopically. (B) Enlarged view of each CNT. They are not straight....................... 79
Figure 3.5 An array of aligned CNTs [63]: (A) An inclined view of one array pattern. (B) A magnified view along the edge of one pattern. 80
Figure 3.6 Procedures in growing an array of vertically aligned CNTs: (A) A substrate. (B) An array of catalytic dots on the substrate. (C) An array of vertically aligned CNTs from the array of the catalysts... 81
Figure 3.7 Ti layer deposition (25 nm thick) by electron beam evaporation.................. 82
Figure 3.8 PMMA layer deposition. 83
Figure 3.9 Pattern PMMA layer.. 84
Figure 3.10 Ni layer deposition... 85
Figure 3.11 Ni layer lift-off.. 85
Figure 3.12 An array of Ni catalytic dots with 5 μm spacing (scale bar = 10 μm). The inset shows an enlarged view of a single Ni dot (scale bar = 100 nm)........................... 86
Figure 3.13 CNT growth.. 87
Figure 3.14 Schematic of CNT growth by PECVD. A negative DC voltage is applied to the cathode while the anode is grounded. 88
Figure 3.15 The PECVD machine for CNT growth in Microsystems Technology Laboratories (MTL) of MIT.. 89
Figure 3.16 Assembled main parts of the PECVD machine... 90
Figure 3.17 Ceramic posts to support the heater holder. 90
Figure 3.18 Metal heater holder. Holes in four legs match four ceramic posts shown in Figure 3.17. 91
Figure 3.19 A pair of thermocouples that measure the temperature of the bottom of the ceramic heater. 91
Figure 3.20 Cathode made of Ti. This will sit on the ceramic heater. There are traces of amorphous carbon deposition on top of the cathode. 92
Figure 3.21 The results of CNT growth: (a) An array of CNTs with 5μm spacing. (b) An enlarged view of the CNT array (scale bar = 2 μm). 93

Figure 3.22 Improvement 1 – shielded metal holder with ceramic fabric tubes. The fabric tubes require replacement after 4~5 CNT growth experiments. 95
Figure 3.23 An exploded view of a modified design. 95
Figure 3.24 The improved CNT machine and stable plasma: (A) The modified CNT machine for stable plasma and uniform temperature. (B) Stable plasma after modification. 97
Figure 3.25 (A) An array of vertically aligned single strand CNTs. (B) Enlarged view of a part of (A). 98
Figure 3.26 The results of CNT growth with the modified PECVD machine. (Enlarged view of the single CNTs). 99
Figure 3.27 (A) TEM of a tip part of a CNT. (B) An enlarged view of the Ni catalyst. The Ni catalyst is capsulated by multiple graphene layers. 100
Figure 3.28 (A) TEM of a body part of a CNT. (B) An enlarged view of (A). It consists of three parts: the external graphene layers, the (intermediate) stacked cone-shaped layers, and the central layers. 101
Figure 3.29 (A) HRTEM of the graphene layers near the Ni catalyst. (B, C) Each graphene layer is resolved with HRTEM, and the layers are parallel to the surface of the catalyst. 102
Figure 4.1 Encapsulation procedures: an array of CNTs (A) is embedded in two polymer layers (B), and the layers are patterned using photolithography (C). 104
Figure 4.2 An array of CNTs (optical microscopy, top view). An array of small dark dots represents an array of vertical CNTs (scale bar = 40 μm) 106
Figure 4.3 An array of CNTs (scanning electron microscopy, tilted by 30°). The inset shows an enlarged view of one single CNT. 107
Figure 4.4 (A) An optical microscopy image of the sample after the CNT growth step (scale bar = 2 mm). (B) An enlarged view of mask alignment marks (scale bar = 1 mm). 107
Figure 4.5 An array of CNTs after spin-coating of the bottom (PMGI SF 11) layer; (A) Image by optical microscopy (scale bar = 40 μm). (B) Image by SEM (scale bar = 10 μm). 108
Figure 4.6 An array of CNTs after spin-coating of the top (SU8-2015) layer. An array of CNTs can hardly be seen due to thick top and bottom layers (scale bar = 40 μm). 109
Figure 4.7 A schematic of the edge bead removal procedure. (A) Before the edge bead removal step. (B) After the edge bead removal step. 110
Figure 4.8 An optical microscope image of the top (SU8-2015) layer after the exposure and hard-bake procedure (scale bar = 40 μm). 111
Figure 4.9 (A) An array of SU8 pellets (scale bar = 40 μm). (B) A single CNT is located at the center of the pellet (scale bar = 10 μm). 111
Figure 4.10 An array of MEMS carriers (scanning electron microscopy). 112
Figure 4.11 (A) An optical microscope image of the sample after encapsulation and bottom layer etching processes (scale bar = 2 mm). (B) An array of MEMS carriers (scale bar = 100 μm). (C) A CNT located at the center of the carrier (scale = 10 μm). 113
Figure 4.12 A released SU8 block with a single CNT. 114
Figure 4.13 TEM of a CNT after encapsulation steps. 116

Figure 4.14 HRTEM (JEOL 2011) of a CNT (close to the Ni catalyst). (A) and (B) show the graphene layers near the both sides of a Ni catalyst. In the region close to the catalyst, the graphene layers are parallel to the surface of the Ni catalyst. The external graphene layers are parallel to the CNT axis. The spacing between the graphene layers is 0.34 nm. 117
Figure 4.15 HRTEM (JEOL 2011) of a CNT (body). (A) and (B) show the graphene layers on the both sides of a CNT body part. The graphene layers are parallel to the CNT axis with disordered external layers . The spacing between the graphene layers is 0.34 nm. 118
Figure 4.16 Comparison of the graphene layers before and after the encapsulation step using HRTEM (JEOL 2010): Before (A) and after (B) the encapsulation step. It can be seen that there are no noticeable increases of the defects in external graphene layers... 119
Figure 4.17 Comparison of Raman spectroscopy. 121
Figure 5.1 Assembly procedure to fabricate CNT probes. (A) An array of MEMS carriers with single CNTs. (B) Further etching of the bottom layer for easy release. (C) A CNT-tipped AFM probe through transferring one block to the end of an AFM cantilever..... 124
Figure 5.2 A setup for fabricating a CNT-tipped AFM probe. 126
Figure 5.3 An enlarged view of the sample, probes and holders. 127
Figure 5.4 An array of MEMS carriers after partial etching of the bottom layer (scale bar = 20 μm) 128
Figure 5.5 Progress of etching procedures of the bottom (PMGI) layer: (A) 0 min. (B) 25 min. (C) 45 min. (D) 60 min. 129
Figure 5.6 3 tipless cantilevers of NCS12 130
Figure 5.7 A probe approaching to a target CNT encapsulated in MEMS carrier. 131
Figure 5.8 A CNT-tipped AFM probe. (A) A CNT-tipped AFM probe is fabricated by transplanting a single CNT encapsulated in a polymer block to the end of an AFM cantilever. (B) An enlarged view of the CNT tip. The CNT tip is located at the center of the carrier, and its length is 1.5 μm 134
Figure 5.9 Another view of the CNT-tipped AFM probe. (A) A tilted view of the CNT-tipped AFM probe. (B) An enlarged view of the CNT tip 135
Figure 5.10 (A) A side view of a CNT-tipped AFM probe. (B) An enlarged view of the CNT tip. It is parallel to the block axis and normal to the sample surface. 136
Figure 5.11 A CNT probe for tapping mode: (A) A tilted view (30°). (B) A side view (scale bar = 10 μm) 138
Figure 5.12 A CNT probe for contact mode: (A) A tilted view (30°). (B) A side view (scale bar = 10 μm). 139
Figure 5.13 A CNT probe for contact mode: (A, B) A tilted view. (C) A side view. (scale bars = 10 μm) 140
Figure 5.14 The effective radius of the CNT tip, r, vs. the radius of the CNT, R. 141
Figure 5.15 A CNT tip of a CNT AFM probe showing a conical end 142
Figure 5.16 A Sharp CNT tip defined by the root shape of the CNT (the effective radius is about 15 nm). (A) TEM of a CNT. (B) The root of the CNT. (C) The part close to the Ni catalyst. 142

Figure 5.17 HRTEM of a single CNT (the effective radius is about 10 nm): (A) A tip of a CNT. (B) A root of a CNT. 143
Figure 5.18 SEM image of an AFM standard grating (TGZ02). 144
Figure 5.19 AFM scanning results of an calibration grating by a standard Si probe: (A) A standard Si AFM probe. (B) A sectional profile of (A). 145
Figure 5.20 AFM scanning results over a standard AFM calibration grating: (A) A CNT tipped AFM probe by transplanting assembly. (B) A sectional profile of (A). 145
Figure 5.21 A hard mask patterns for critical-angle transmission grating: (A) tilted view. (B) top view. 147
Figure 5.22 Comparison of AFM scanning images of the transmission grating: (A) An AFM image using a Si probe (scanning range: 3 × 3 μm). (B) An AFM image using a CNT probe (scanning range: 3 × 3 μm). 148
Figure 5.23 Fluorescence microscopy images of filament actions in buffer solution (scale bar = 10 μm). 149
Figure 5.24 AFM scanning results of F-actins: (A) 3D image (scanning range: 3 μm). (B) 2D image (height mode). (C) 2D image (deflection mode). 150
Figure 6.1 Conventional Raman spectroscopy (A) and SERS (B). 154
Figure 6.2 Field contours for a single dimer of silver particles and for an array of 150 dimers [73]. (A) Single dimer with 2,800 E.F.. (B) Array of 150 dimers with 36,500 E.F. 156
Figure 6.3 Local fields of the linear center-symmetric self-similar chain of six silver nanospheres in the cross section through the equatorial plane of symmetry [75]. The inset in (A) depicts the configuration of the chain of six silver nanospheres. 158
Figure 6.4 Electric field contour in the single nanolens [77]. 158
Figure 6.5 TNPR [78]. (A) The effect of the number of layers. (B) One single Au layer design. (C) Six Au layer design. 159
Figure 6.6 A schematic of TERS. 161
Figure 6.7 A conical plasmonic resonator. 164
Figure 6.8 Design parameters of a conical plasmonic resonator. 165
Figure 6.9 Frequency dependent relative permittivity of thin film silver. 166
Figure 6.10 FEM mesh modeling of the conical plasmonic resonator. 168
Figure 6.11 The hot-spot of the conical plasmonic resonator. 169
Figure 6.12 The electric field enhancement factor vs. the height of the cone. 170
Figure 6.13 The electric field enhancement factor vs. the number of Ag layers. 172
Figure 6.14 The conical plasmonic resonators: (A) A resonator with 3 Ag layers. (B) A solid single Ag resonator. 172
Figure 6.15 A CNT probe for TERS with gold coating: (A) Before gold deposition. (B) After 10nm gold layer deposition. 175
Figure 7.1 Transplanting assembly of the individual CNTS: (A) The single CNT. (B) A CNT-tipped AFM probe with a single CNT tip. 177
Figure 7.2 SEM images of Ni catalysts with various diameters: (A) diameter = 175 nm. (B) 117 nm. (C) 87 nm. (D) 50 nm. (scale bars = 100 nm). 182
Figure 7.3 Large-scale transplanting assembly of the individual CNTs using patterns defined on the substrate. 184

List of tables

Table 2.1 Properties of SU8-2015 and PMGI SF 11 68
Table 3.1 The CNT growth procedure. 92
Table 4.1 Procedures in fabricating a CNT-tipped AFM probe by transplanting a single CNT.. 105
Table 5.1 Procedures in fabricating a CNT-tipped AFM probe by transplanting a single CNT.. 125
Table 5.2 Characteristics of the CNT-tipped AFM probes 137
Table 6.1 SMD using SERS... 155

1 Introduction

1.1 Objective

Assembly of individual nanostructures is an essential step in their integration into micro or macro-scale devices for many practical applications. However, handling and assembling the individual nanostructures has been a challenge because assembly efforts to locate micro- and nano-scale objects into a functional device or a system accompany enormous complexity with the scales of currently available assembly tools [1].

Most natural materials synthesize at the atomic and molecular scale and assume patterns of structures to reach the most stable configurations with reduced free energy. The information about how the molecular components assemble into the microstructure of natural materials is precisely embedded in the individual nano-components with relatively little control from outside as well as yet very little information known to researchers. Self-assembly has been eagerly studied to understand natural nano-scale assembly processes ranging from organic chemistry, the growth of quantum dots and di-block copolymers to DNA-machines. However, most self-assembly studies at the present time are inherently stochastic and involve large variations in quality.

Transplanting assembly is a new concept of deterministic assembly for nanostructures developed at Micro and Nano Systems Laboratory of Massachusetts Institute of Technology [1-3]. Deterministic assembly is an assembly technique which

controls the number, shape, location, and orientation of individual nanostructures when they are integrated to bigger scale structures, such as MEMS devices. A deterministic assembly method would enable reliable handling and assembling of the individual nanostructures, and designs for large scale parallel assembly of nanostructures. The primary goal of this thesis is to develop a method to implement the transplanting assembly of individual nanostructures and demonstrate a micro-scale device consisting of the nanostructures with their superior functionality preserved during and after the assembly. The scanning probes for atomic force microscopy (AFM) with a single carbon nanotube (CNT) tip is the case in which transplanting assembly of the individual nanostructures will be demonstrated. It is one of the simplest micro-scale devices with a single nanostructure: the probe requires the single tip at the apex of the probe with the predefined length and orientation.

1.2 Assembly of carbon nanotubes (CNTs): review

Carbon nanotubes (CNTs) are one of the important nanostructures because of their excellent chemical, mechanical, and electrical properties, and they have attracted a lot of attention since their first discovery by Dr. Iijima in 1991 [4]. Despite the several attempts for CNT assembly, a deterministic assembly of CNTs, with control over the number, shape, location, and orientation of the individual CNTs, still remains elusive. The major challenges of assembling CNTs as well as nanowires (NWs) lie in the fact that they involve more degrees-of-freedom – the diameter, length, location and orientation – than that of assembling nanoparticles – the location. In this regard, assembling individual CNTs has not been achieved yet in a reproducible and efficient manner.

One example of CNT assemblies is a catalytic growth method in which CNT catalysts are seeded at the desired locations of CNTs, and CNTs are grown as a final step after fabricating other parts as shown in Figure 1.1 [5]. CNTs were grown and suspended between Mo electrodes on top of two elevated SiO_2 terraces. The main problem with these growth approaches is that the materials and processes before the CNT growth process should be compatible with the process conditions during the CNT growth such as high temperature and voltage. The yield of this assembly is determined by that of the CNT growth that is very low compared to the general microfabrication techniques, which requires redundant devices with multiple seeds, and excessive CNTs must be removed manually.

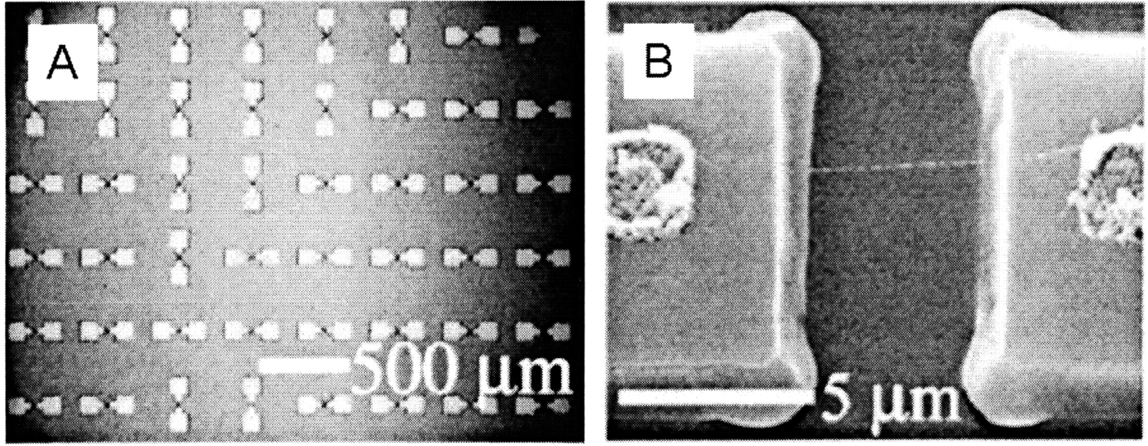

Figure 1.1 An electrical interconnection by a CNT through the catalytic growth [5]: (A) An array of devices. (B) A suspended CNT device.

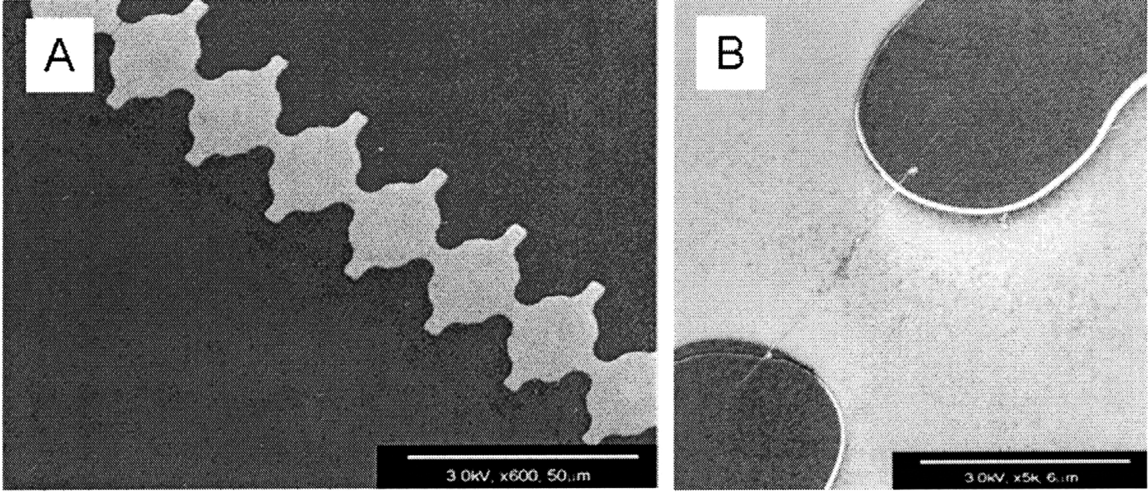

Figure 1.2 An electrical interconnection by a CNT through direct assembly by dielectrophoresis [6]: (A) Comb-shaped electrodes. (B) One MWNT spanning a gap.

Other assembly attempts can be categorized as direct assembly of CNTs in which pre-grown CNTs are handled and assembled using manipulators, electric/magnetic fields, hydrophobic/hydrophilic treatment of patterns, fluid shearing, and electrostatic forces.

Figure 1.2 shows an example of the direct assembly where a pair of electrodes are connected with a multi-walled carbon nanotube (MWNT) using a combination of alternating current (AC) and direct current (DC) dielectrophoretic forces [6]. The main drawback of these direct assembly approaches is that, due to the small sizes of CNTs and the limited control over those driving forces at the small scales, the assembly of CNTs is not deterministic but stochastic, and involves low yield and large variations. The following sections review the approaches of assembling CNTs or NWs directly using various driving forces.

1.2.1 Langmuir-Blodgett films for nanostructure assembly

One of the conventional techniques of creating monolayer or nano-films on substrate surfaces is Langmuir-Blodgett (LB) technique. One or more monolayer can be transferred from the surface of a liquid onto a solid substrate by immersing the solid substrate into the liquid. A mono-layer is absorbed at the gas-liquid interface; thereby films with very accurate thickness can be formed and then transferred to the desired substrate surface [7]. LB technique can be used to form a homogeneous thin layer of chemically stabilized single-walled nanotubes (SWNTs). Kim et al. made a stable monolayer of SWNTs on water surface, which were then oriented in a specific direction by the barrier compression as shown in Figure 1.3 [8].

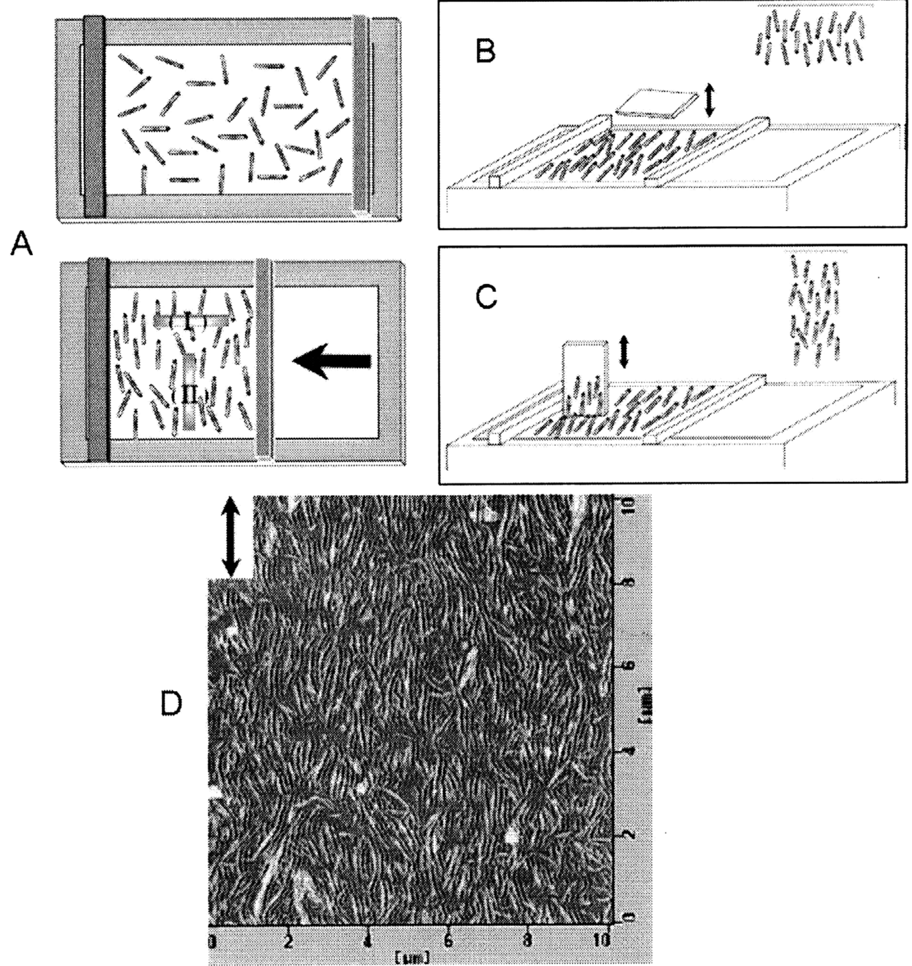

Figure 1.3 LB Films of SWNTs [8]: (A~C) Schematic illustration of the mechanism for the in-plane orientation of s-SWNT. Compression-induced orientation in the LB film by barrier compression (A), in-plane tube orientation for films prepared by horizontal lifting (B), and flow orientation of tubes induced by the vertical motion of the substrate (C). (D) AFM images of an s-SWNT single layer on mica prepared by vertical dipping. The arrow indicates the dipping direction.

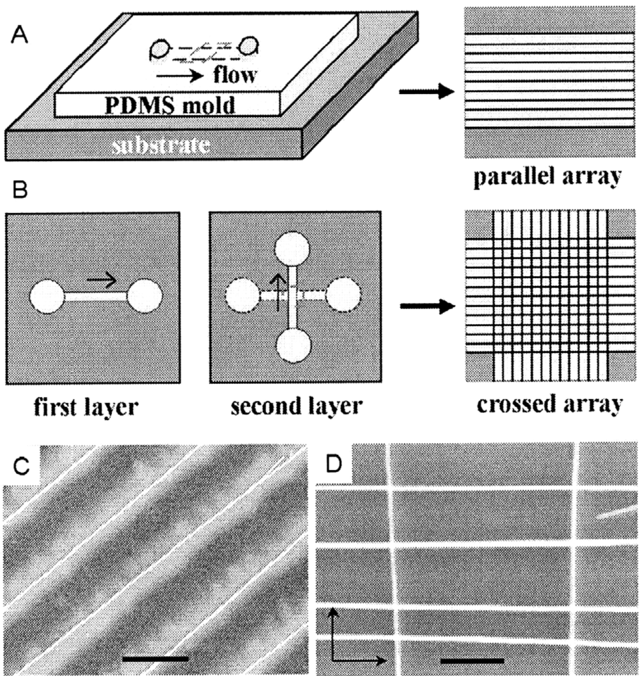

Figure 1.4 Parallel assembly of NW arrays [9]: (A~B) Schematic of fluidic channel structures for flow assembly. Parallel arrays (A) and multiple crossed NW arrays (B). (C~D) SEM images of parallel arrays of InP NWs aligned by channel flow. Periodic NW arrays (C: scale bar = 2 μm) and crossed NW arrays (D: scale bar = 500 nm).

Lieber's group reported directed, one-dimensional alignment of nanostructures (Figure 1.4) [9]. By combining fluid flow of NW suspension through microfluidic channel and selectively functionalized and patterned surface on the target substrate, NWs were assembled into parallel arrays with control of average separation and periodicity. They used NWs made of gallium phosphide (GaP), indium phosphide (InP) and silicon. NW orientation was made by flowing NW suspension inside the polydimethylsiloxane (PDMS) mold flow channel, which was brought in contact with a flat substrate. Flow duration is also a factor to determine the NW density: in their experiments, 30 minute flow produced a density of about 250 NWs per 100 μm. Layer-by-layer assembly with

orthogonal flow direction change for the sequential steps could result crossed array of InP NWs.

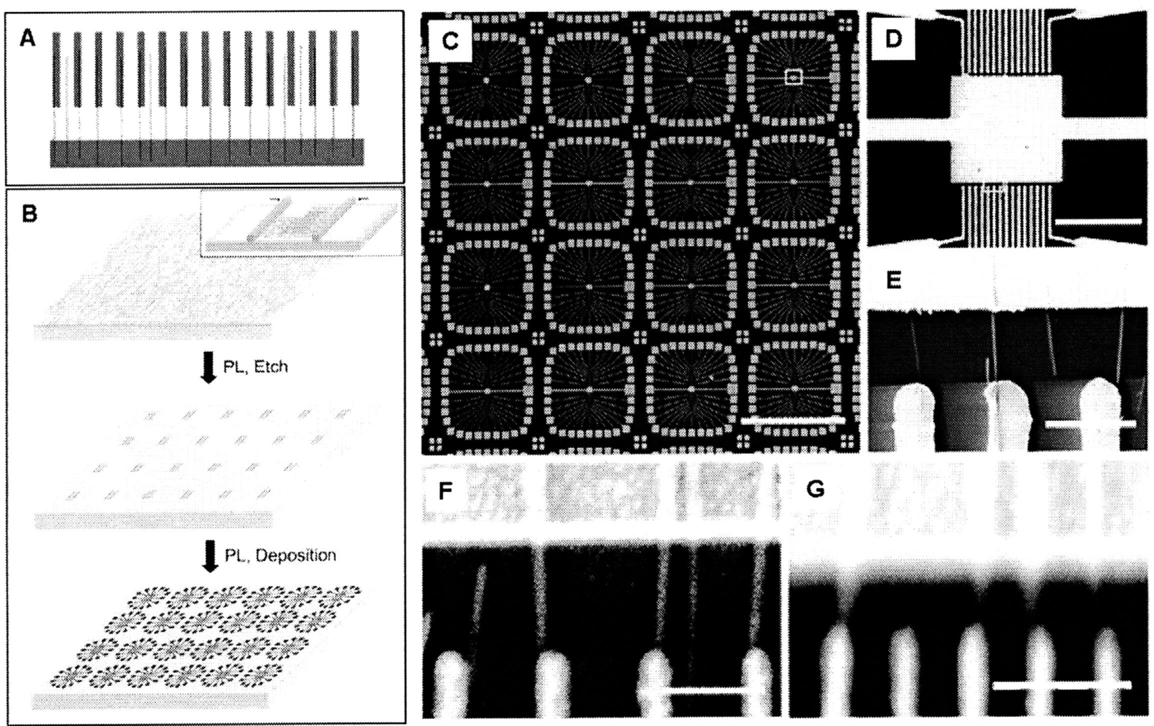

Figure 1.5 Parallel and scalable interconnection of NW devices without registration [10]: (A) Central electrode region of a single array. (B) Schematic illustrating key steps of the interconnection approach. (C) Optical micrograph of integrated metal electrode arrays (scale bar = 1 mm). (D) SEM image of the central active region (scale bar = 40 μm). (E) SEM image of three NW devices connected between the common and finger electrodes (scale bar = 3 μm). (F, G) SEM images of higher-density NW devices defined by electron beam lithography (scale bars = 300 nm).

This method has been extended to assemble centimeter-scale arrays containing thousands of single silicon NW field-effect transistors with reasonably good reproducibility, scalability and at least 100 nm level positioning accuracy as shown in

Figure 1.5 [10]. A general strategy for the parallel and scalable integration of NW devices over large areas without the need to register individual NW-electrode interconnects has been developed. The approach was implemented using a LB method to organize NWs with controlled alignment and spacing over large areas and photolithography to define interconnects. Centimeter-scale arrays containing thousands of single silicon NW field-effect transistors were fabricated in this way and were shown to exhibit both high performance with unprecedented reproducibility and scalability to at least the 100-nm level. Moreover, scalable device characteristics were demonstrated by interconnecting a controlled number of NWs per transistor in "pixel-like" device arrays. The general applicability of this approach to other NW and nanotube building blocks could enable the assembly, interconnection, and integration of a broad range of functional nanosystems.

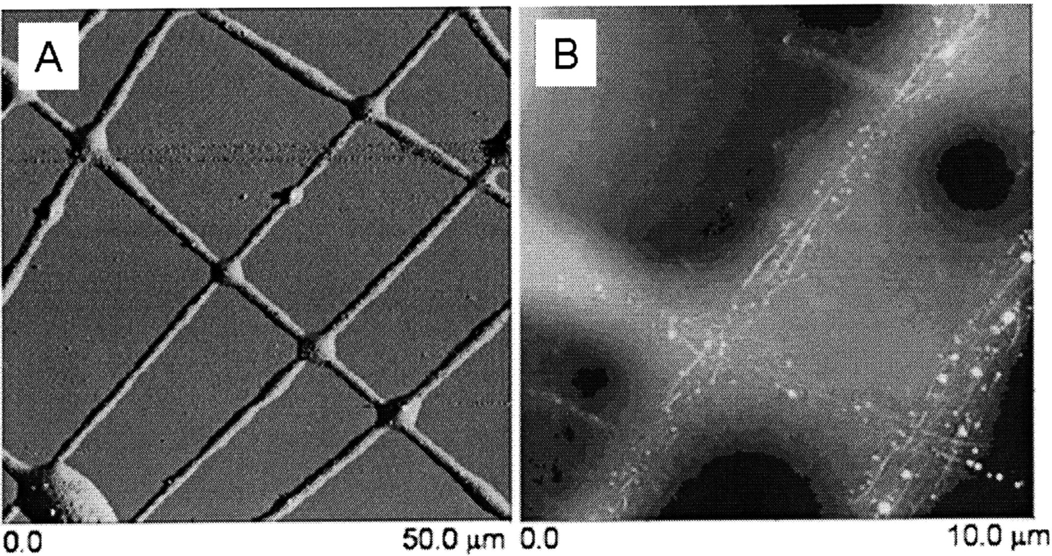

Figure 1.6 AFM images of (A) cross-aligned SWNTs/PVP composite fibers and (B) cross-aligned SWNT array after polymer component removal. [11]

Electrospinning is an electrostatic method for the fabrication of long thin organic fibers, which can be used to align SWNTs along the polymer spinning direction. Gao et al. obtained large-scale aligned SWNT arrays by transferring the local SWNT orientation in the electrospun composite fiber to macroscopically aligned SWNT structure [11]. To demonstrate the directional control of SWNT alignment, they deposited electrospun fibers along perpendicular directions by simply rotating the substrate between depositions. The cross-aligned nanofibers are shown in Figure 1.6 (A). After the exposure to ethanol for 12 hours, the polymer component was removed and the hierarchical SWNT assembly was revealed as shown in Figure 1.6 (B).

1.2.2 Nano assembly with templates

A site-selective self-assembly technique called "template assisted by selective removal" is introduced by Jung et al. [12, 13]. They demonstrated selective assembly of micro/nano spheres of sizes between of 400 nm and 2 μm into shape-matched near-spherical holes (templates) which were e-beam patterned on a silicon substrate (Figure 1.7). The substrate and silica spheres were chemically functionalized (to hydrophobic surface) to promote adhesion of the substrate and spheres, which were then immersed in a fluid bath with ultrasonic excitation. Very high frequency ultrasound selectively removes components from poorly matched holes as shown in Figure 1.7 (B). The spheres stick preferentially in shape and size matching holes with near 100% yield. This technique is

expected to be scalable to the assembly of nano-components in various optical and biological applications.

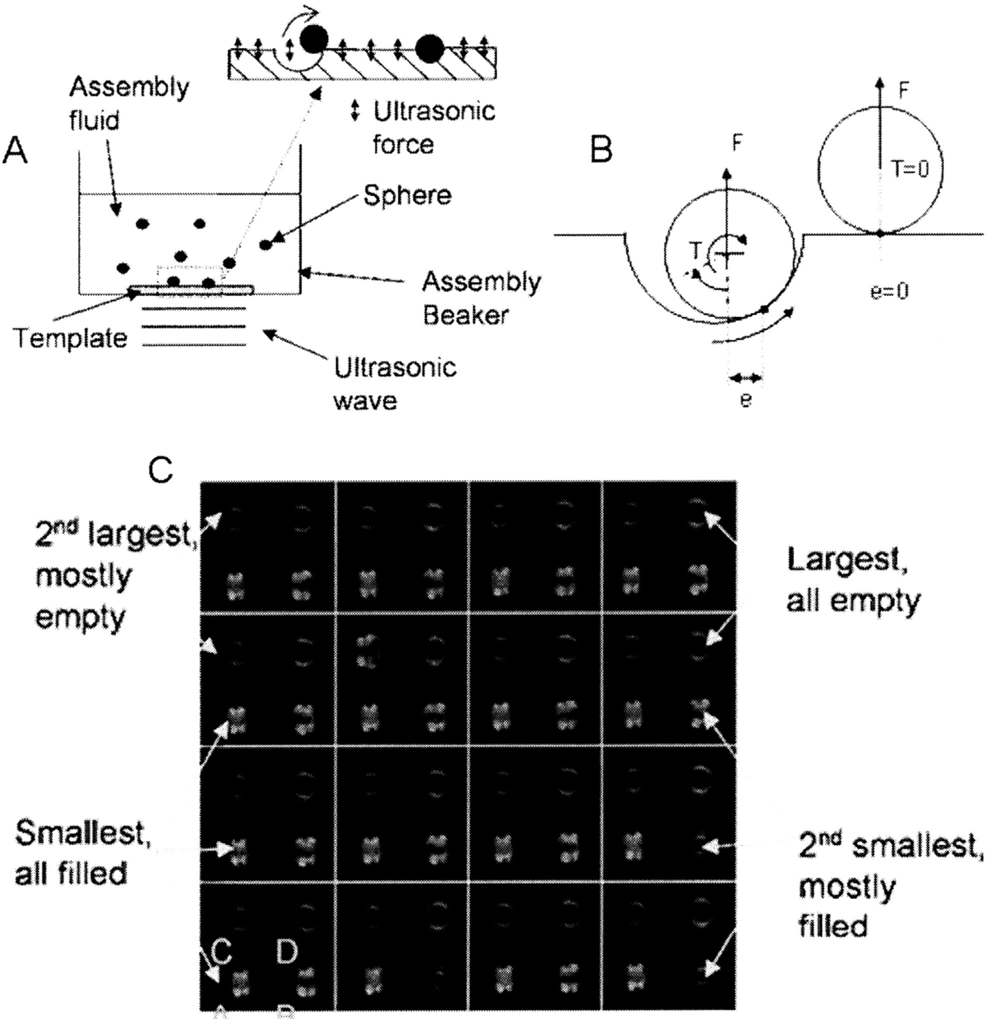

Figure 1.7 TASR [12]. Schematic of templated assembly by selective removal. (A) Assembly setup and enlarged cross-sectional view of ultrasonic forces acting on substrate. (B) Cross-sectional schematic of a sphere in a hole and a sphere on a flat surface, along with forces and torques acting on the sphere. (C) Optical micrograph of assembly results for the array with largest exposure dose.

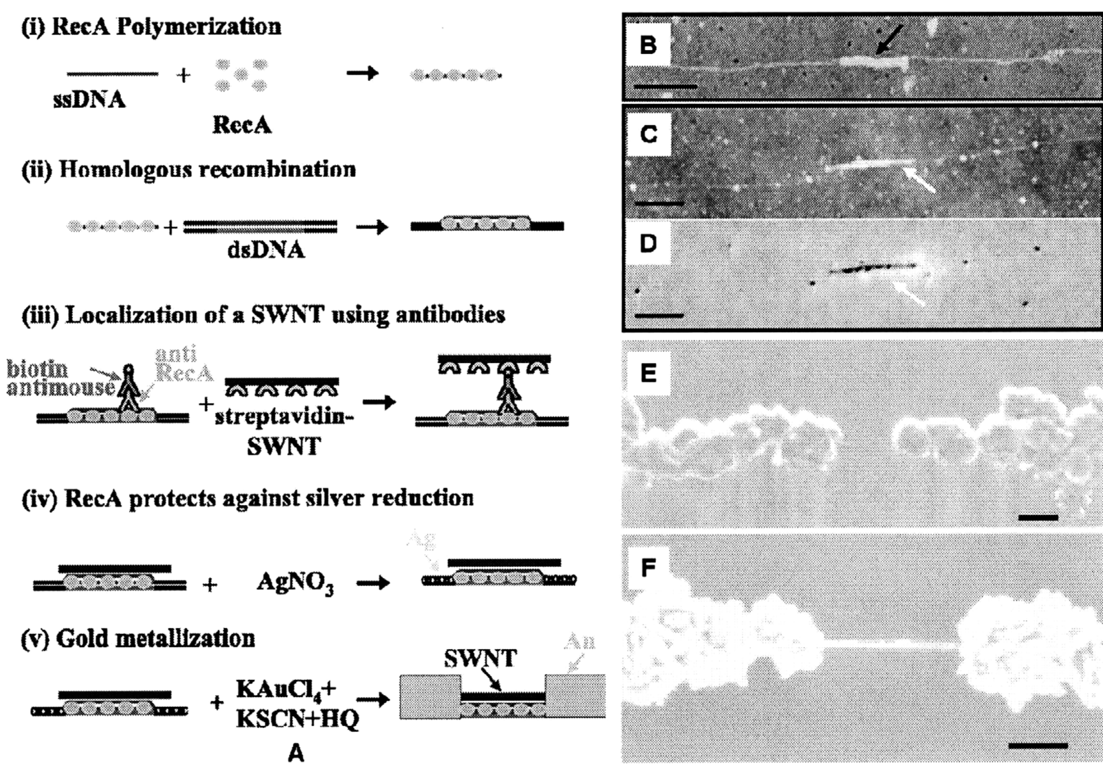

Figure 1.8 (A) Process steps of DNA templated self-assembly of CNTs. (B~D) Localization of a SWNT at a specific address on the scaffold dsDNA molecule using RecA. (E~F) A DNA-templated carbon nanotube FET and metallic wires contacting it. (scale bar = 100 nm) (E) An individual SWNT. (F) A rope of SWNT. [14].

Using a scheme based on recognition between molecular building blocks, Keren et al. reported the DNA templated self-assembly of carbon nanotubes for field-effect transistors (FETs) [14]. A DNA scaffold provides the address for precise location of a semiconducting single-wall carbon nanotube as well as the template for the extended metallic wires contacting it. DNA-templated assembly process steps are shown in Figure 1.8. A semiconducting SWNT was located at a desired address on a DNA scaffold molecule using homologous recombination by the RecA protein from Escherichia coli (E.

coli) bacteria. DNA metallization led to the formation of extended conductive wires that electrically interconnect the SWNTs. Experimental results showed that the current through the SWNTs was controlled by a voltage applied to the substrate supporting the structure, which confirmed the electrical characteristic of an FET.

1.2.3 External force field assisted assembly

Many groups have studied the assembly of nanostructures with the external electric or magnetic field to handle, locate or align nanostructures with the precision needed for functional multi-scale devices such as logic and memory devices.

Dielectrophoresis was used to align and place gold NWs on the predefined electrodes where non-uniform alternating electric fields are applied at the gap [15]. Au metal is electrodeposited into a nanoporous alumina membrane and then is released by dissolving alumina membrane to form Au NWs ranging from 70 to 350 nm in diameter. NWs are suspended in isopropyl alcohol (IPA). The interdigitated metal electrodes are patterned by metal liftoff process of 50 nm Ti and 150 nm Au on a SiO_2 substrate. An interdigitated finger is 3 μm wide and 5 μm in gap separation. The electrodes were coated with 500 nm Si_3N_4, with a trench right on along the electrodes to increase the field strength. A dilute solution of NW suspension was dispensed onto the electrodes with AC voltages ranging from 5V to 7V.

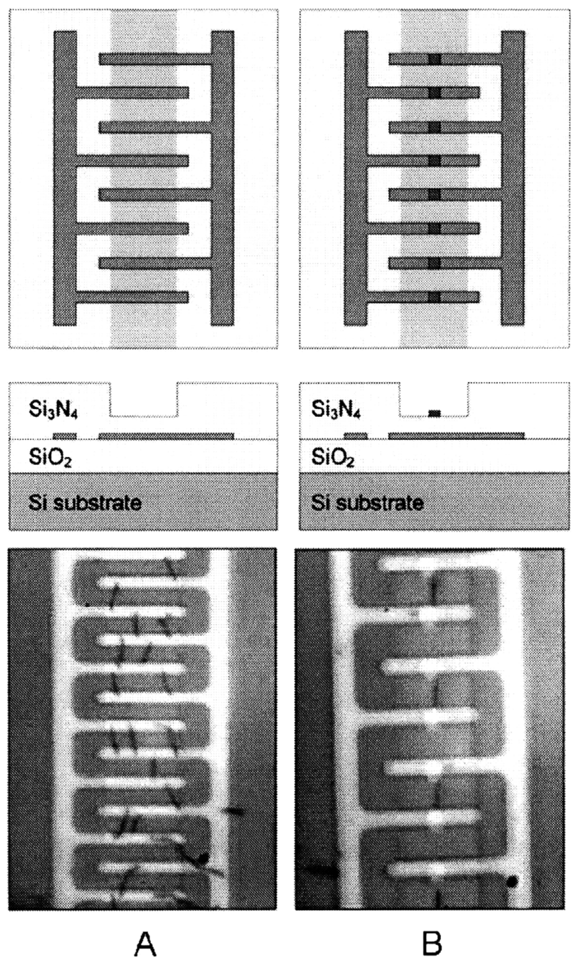

Figure 1.9 Top- and cross-sectional views of the electrode structures used in the field assisted assembly experiments and optical microscope images of 5 μm-long, 200 nm-diameter Au NWs (A) without and (B) with upper field electrodes [15].

Figure 1.9 shows that NWs are aligned perpendicular to the interdigitated electrodes, but are distributed randomly at the bottom of the trenches. They reported NWs as small as 35 nm were aligned under similar conditions. The alignment of NWs is due to the forces that direct the polarized NWs toward regions of high electric field strength. Since metal NWs are more polarizable than the IPA medium, the dielectrophoretic force moves the NWs toward the direction of increasing electric field strength [16]. As one end of the

NW approach the electrode, the other end also touches the opposite electrode since the gap is nearly the length of one NW. After the contacts are made, the local electric field strength reduces significantly within about 2 μm region around the NW which prevents further arrival of other NWs near the aligned NW.

A similar approach has been made for the orientation and spatial positioning of the SWNTs or MWNTs by inducing an AC electric field to the diluted suspension of them [17]. This approach, however, results in large variations and randomness in locating nanostructures, and many research groups still rely of fortuitous alignment of target nanostructures at massive number of electrode pairs when they assemble individual MWNT or SWNT to them. Lieber's group showed that the NWs were aligned parallel to the direction of the strong DC fields [19]. By changing the field direction, the alignment could be achieved in a layer-by-layer fashion to produce crossed NW junctions. However, the control over the number of the NWs is still a difficult task because initially aggregated NWs can be aligned and assembled together between electrodes. The length and purity of NWs should also be controlled for a better assembly.

Both AC and DC electric fields were used to attract and trap individual carbon nanotube between the two electrodes. Chung et al. showed that MWNTs dispersed in a liquid could be aligned to 6 μm electrode gaps by combining an AC and DC electric field in a given ratio [6]. It was shown that the AC field (5 MHz) served to selectively attract MWNTs and the DC field to guide individual MWNT alignment. Repeated trials demonstrated reasonably accurate, discrete, and aligned deposition of MWNTs with

about 90 % yield over an electrode array having 100 gaps. The assembly was made in a unidirectional manner as shown in Figure 1.10.

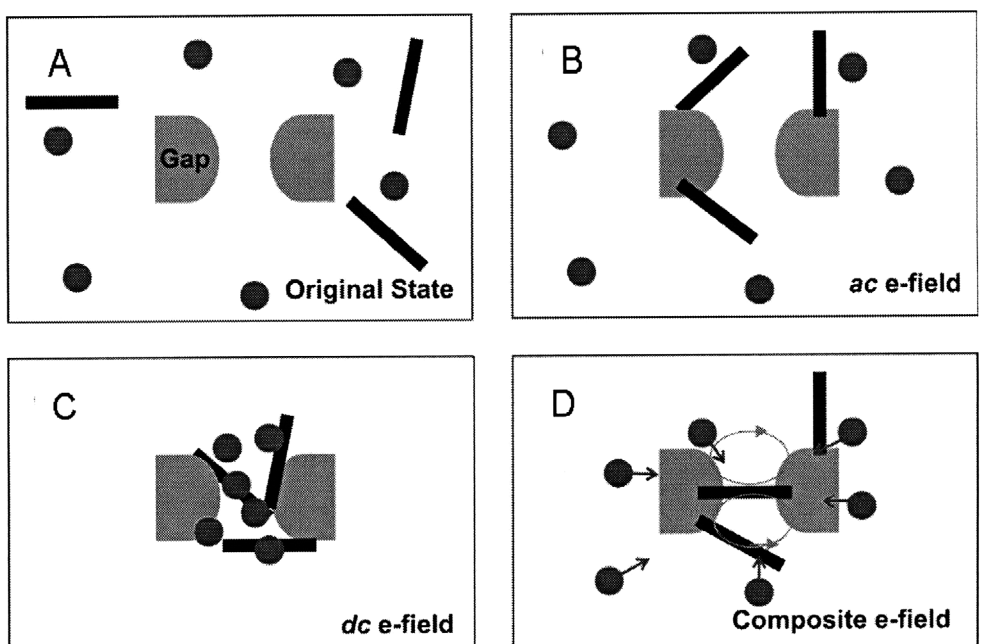

Figure 1.10 Schematic of deposition with ac only, dc only, and composite electric fields [6]: (A) Before applying an electric field. (B) AC electric field of 5 MHz. (C) DC electric field. (D) The composite electric field.

Well aligned arrays of SWNTs grown on a quartz substrate were integrated into transistors, which showed good device level switching properties [20]. Chemical vapor deposition on stable temperature cut quartz wafers using patterned stripes of iron catalyst and methane feed gas forms arrays of individual SWNTs with an average diameter of about 1 nm, length of up to 300 μm, and density ~10 SWNTs μm^{-1}. This study shows a potential toward a large-scale nanotube-based electronics (Figure 1.11).

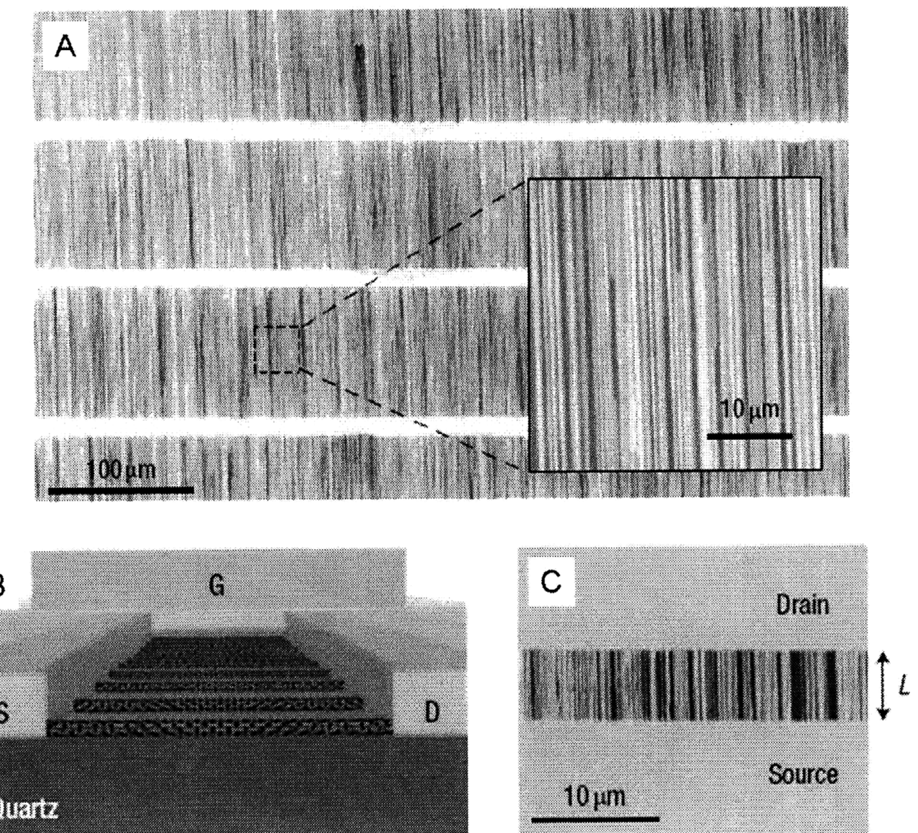

Figure 1.11 Perfectly aligned arrays of long, linear SWNTs and their implementation in thin-film-type transistors [20]: (A) SEM image of a pattern of perfectly aligned, perfectly linear SWNTs formed by CVD growth on a quartz substrate. (B) Schematic illustration of the layout of a type of transistor that incorporates these aligned SWNTs as the semiconductor. (C) SEM image of the channel region of a device.

1.3 The CNT-tipped AFM probes: review

The CNT-tipped AFM probe for the atomic force microscope (AFM) is one of the well-known applications of CNTs. It is almost the same as the standard AFM cantilever except for the CNT tip at the end (Figure 1.12). The advantages of the CNT-tipped AFM probes over the standard sharpened Si tip AFM probes include higher spatial resolution because of the small sizes of CNTs [21, 22], and precise measurement of deep-narrow features because of the high-aspect ratio CNT tips [23, 24]. There are also the AFM probes with high-aspect-ratio Si tips, but CNT tips show higher wear resistance compared to the Si tips [21, 25, 26].

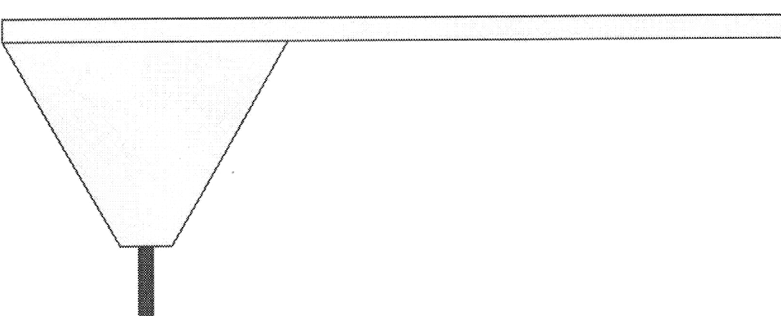

Figure 1.12 A CNT-tipped AFM probe.

However, mechanical instability due to the small diameter and the high-aspect-ratio CNT tips induces artifacts in AFM scanning images [21, 27]. In order to avoid the mechanical instability, it is suggested that the length should be less than 500 nm for MWNTs and 50 nm for SWNTs. Akita et al. also reported that the CNT tips shorter than 500 nm is required for a stable and high-resolution imaging [27].

There have been rigorous studies in improving the fabrication methods of the CNT-tipped AFM probes, and they can be classified into three main categories: the direct manual attachment, the field assisted attachment, and the catalytic growth. From the view point of assembly quality, the CNT-tipped AFM probe requires only one CNT tip (the number) at the end of the AFM cantilever (the location), and the CNT tip should possess the predefined length, aspect ratio (the shape) and the orientation. Each approach will be discussed in terms of the quality of the fabricated CNT-tipped AFM probes, and the effects of CNT tip quality on AFM scanning images.

1.3.1 The CNT-tipped AFM probes by direct attachment approaches

The first CNT-tipped AFM probe was demonstrated by picking and gluing bundles CNTs to an AFM probe [23]. First, a 1~10 nm thick soft acrylic adhesive was coated at the bottom 1~2 μm section of a Si tip. The tip was brought into contact with the side of a bundle of 5-10 MWNTs under direct view of an optical microscope using dark-field illumination. This assembly procedure inherently selects toward thick bundles of nanotubes, and excessive CNTs needed to be removed manually, requiring a relatively long time to in fabricating a CNT-tipped AFM probe.

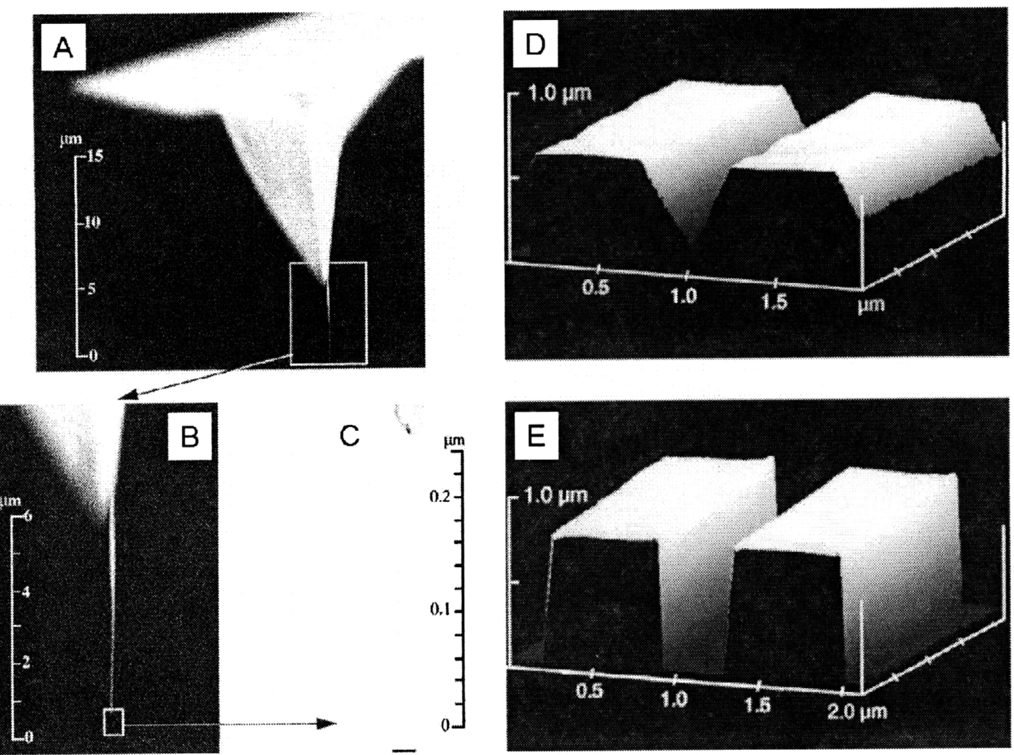

Figure 1.13 (A~C) Single nanotube attached to the pyramidal tip of a silicon cantilever for AFM. (A, B) SEM images showing the MWNT bundle attached to the steeper slope of the back side of the Si pyramid. (C) Transmission electron microscopy (TEM) image. (E~F) Tapping-mode AFM image of a 400-nm-wide, 800-nm-deep trench. (E) Image taken with a bare pyramidal Si tip. (F) Image taken with a nanotube attached to the pyramid of the same cantilever. [23].

In order to provide better alignment in assembly, Nishijima et al. reported three step assembly process [28]: (1) purification and alignment of carbon nanotubes using electrophoresis, (2) transfer of a single aligned nanotube onto a conventional Si tip under the view of a scanning electron microscope, and (3) attachment of the nanotube on the Si tip by carbon deposition.

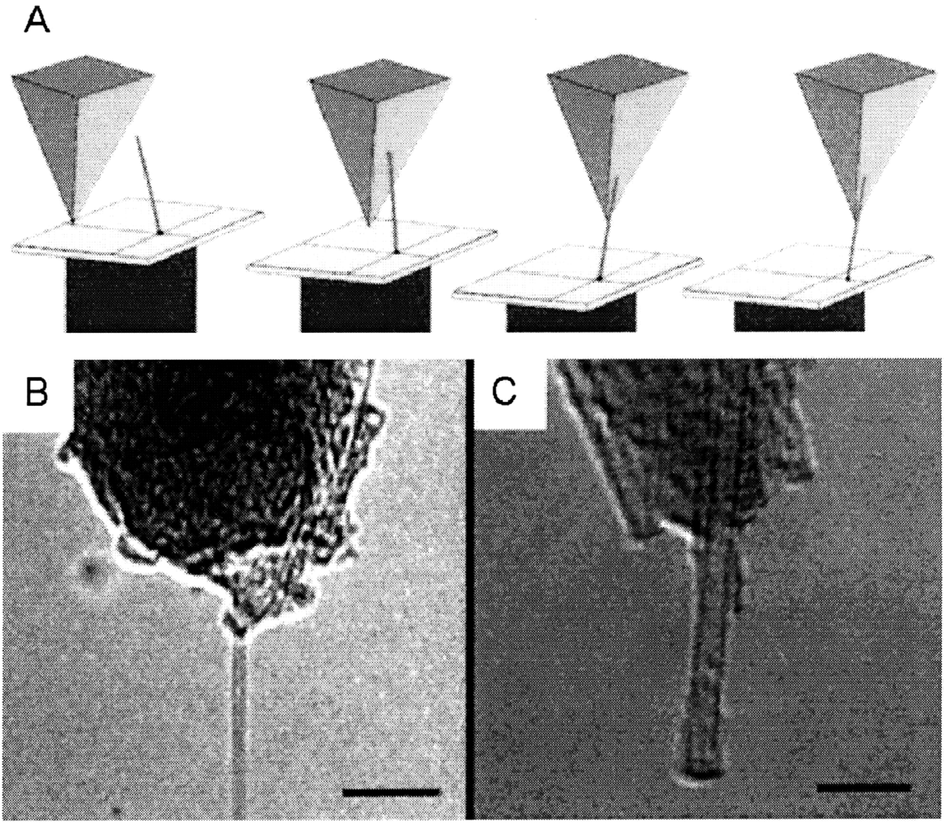

Figure 1.14 The CNT-tipped AFM probes by picking up SWNTs directly [29]: (A) Schematic depicting the process by which a microfabricated pyramidal tip picks up a vertically aligned carbon nanotube. TEM images of (B) a 0.9 nm diameter nanotube tip and (C) a 2.8 nm diameter nanotube tip.(scale bars = 10 nm).

A method of picking a CNT during AFM scanning to fabricate a CNT-tipped AFM probe was demonstrated in order to provide a better control over the number [29]. In this method, nanotubes were grown on oxidized silicon substrates by CVD using iron (Fe) catalysts. The nanotube-covered wafers were directly imaged in AFM tapping mode with silicon tips whose microfabricated pyramids are coated with a thin layer of a UV-curing adhesive. After a nanotube is picked up to the tip, the glue is cured in UV for 30 min.

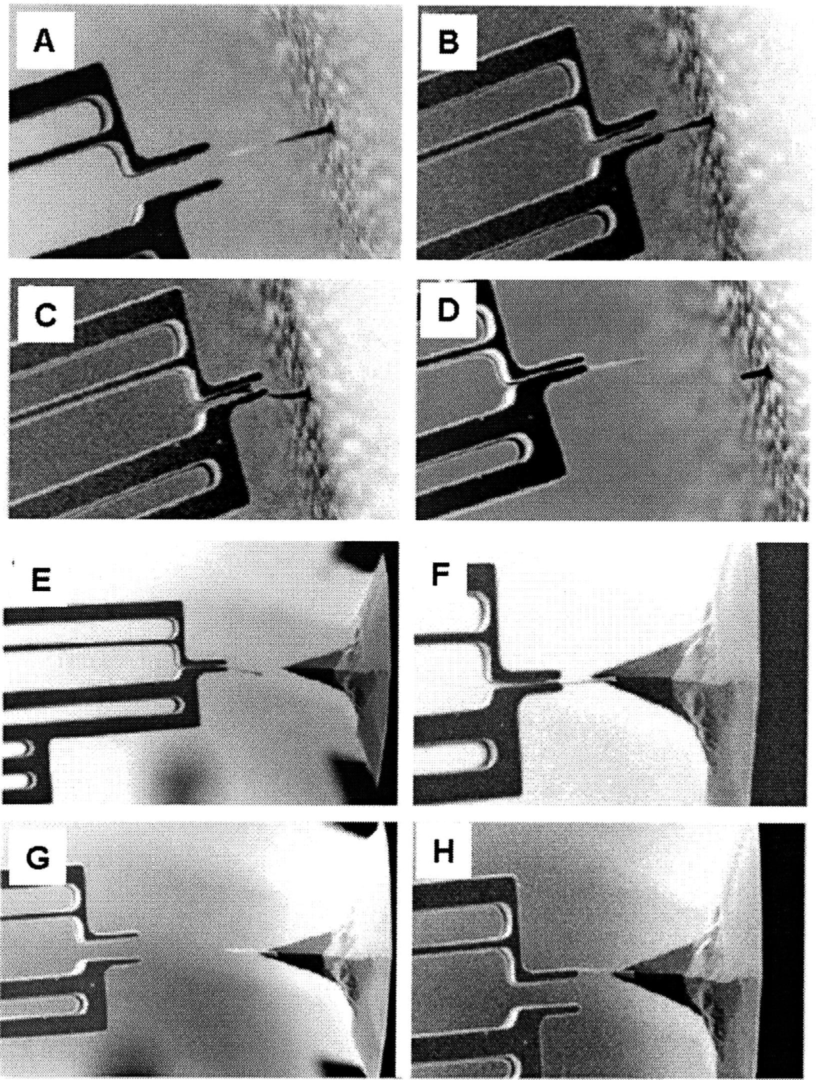

Figure 1.15 Procedures to fabricate a CNT-tipped AFM probe by manipulating a single carbon nanotube/nanofiber (CN) using an electrothermal gripper [30]: (A, B) Aligning of gripper to CN. (C) Gripping. (D) Detachment. (E) Aligning of CN to AFM probe. (F) Attachement. (G, H) Mechanical test.

Recently, direct manipulation of the individual CNTs is used to fabricate a CNT-tipped AFM probe [30]. An electrothermal actuator is used to transfer a catalytically

grown multi-walled carbon nanofiber from a position on a substrate to the tip of an AFM cantilever, inside a scanning electron microscope. Based on manipulation experiments as well as a simple analysis, it is shown that shear pulling (lateral movement of the gripper) is far more effective than tensile pulling (vertical movement of the gripper) for the mechanical removal of carbon nanotubes from a substrate.

The major disadvantages of these direct attachment approaches are the fact that manual consoling effort is needed to remove ill-attached or extra CNTs. This is due to the limited control over those driving forces at the nanometer scale, so the assembly of CNTs is not deterministic which inevitably results in a very low yield and a large performance variation of the assembled product. In addition to that, direct attachment assembly method is time-consuming and requires proficient experimental technique and ultra-precision equipment. Most of the CNT tips realized through direct attachment sit on the sides of the pyramid cantilevers, degrading control over the orientation of CNT tips.

1.3.2 The CNT-tipped AFM probes by the field assisted assembly

Direct attachment method is straightforward but suffers laborious efforts to place and align CNTs with respect to an AFM probe. In order to address these issues, there have been a lot of attempts to use field assisted assembly techniques in fabricating the CNT-tipped AFM probes.

Stevens et al. reported two-step method to make nanotube probes [31, 32]. First, a nanotube cartridge is created using chemical vapor deposition, and the nanotubes are

transferred from the cartridge to a device using an electric field. The attraction is due to the induced electrostatic dipole moment in the nanotubes and the alignment is due to the geometry of the field created by the cantilever tip shape.

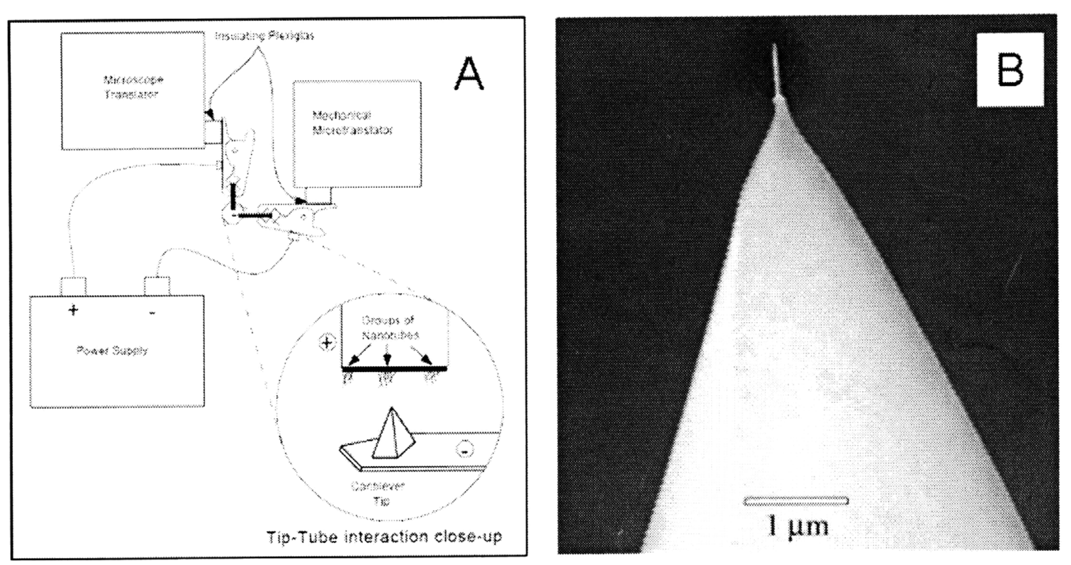

Figure 1.16 Single CNT AFM tips using an arc discharge method [31]: (A) Schematics of attachment apparatus. (B) An SEM micrograph of a nanotube tip.

Hall et al. demonstrated the fabrication of nanotube probes by magnetic fields [33]. This approach is based on the liquid deposition of a CNT onto AFM tips. An apparatus was assembled in order to introduce a magnetic field onto a single AFM probe and a nanotube suspension, as shown in Figure 1.17. Here, a custom-made beaker is positioned above a solenoid (~340 turns) containing a high permeability, type I, low carbon magnetic iron core (Scientific Alloys, Westerly, RI). 5 ml of carbon arc-synthesized MWNTs suspended in dichloromethane was introduced into the beaker. Prior to this introduction, the suspension was sonicated for 10–15 min to ensure maximum

homogeneity. An AFM probe was sputter coated with 60 nm of gold and introduced onto the submerged platform. The probe tip was visually aligned above the pole piece. An alternating current of 7 A at 60 Hz was then applied to the solenoid, resulting in a measured magnetic field amplitude B ~ 0.1 T. With this apparatus, the anisotropic properties of the CNT cause the tubes that come into contact with the probe tip to be preferentially oriented parallel to the tip direction and hence protruding down from the end.

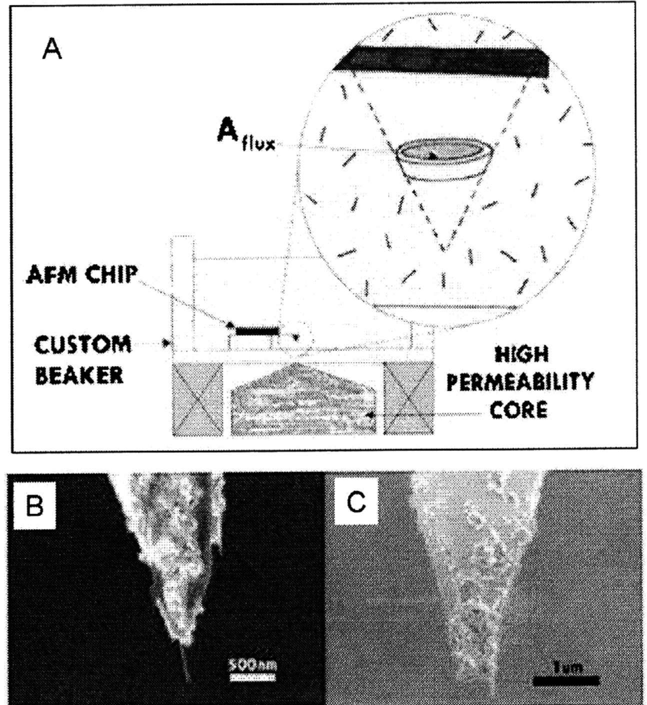

Figure 1.17 The CNT AFM probes by magnetic field assisted assembly [33]: (A) Schematic of the experimental apparatus atop a solenoid. The inset shows the area through which the changing flux goes. (B, C) Examples of nanotube functionalized probes prepared with the method.

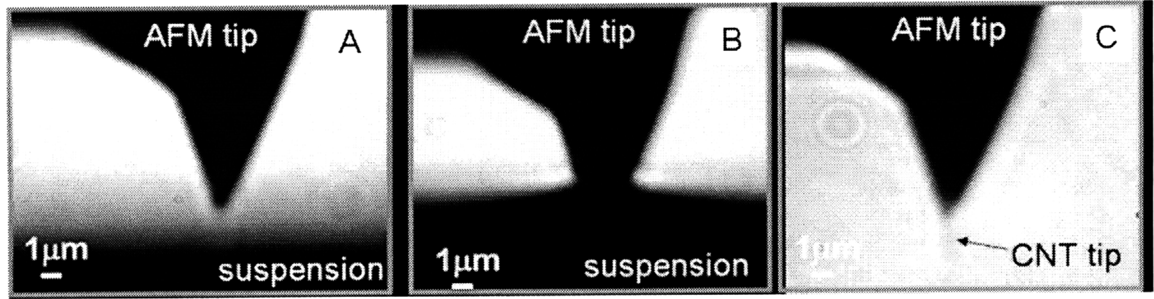

Figure 1.18 Optical microscope images of a Si AFM probe (A) before, (B) during, and (C) after the dielectrophoresis process of assembling the CNT tip. An ac field was applied between the AFM probe and the counter electrode during the deposition. A CNT tip assembled on the apex of the Si AFM probe is visible in image (C) [34].

Tang et al. demonstrated the fabrication of nanotube probes by dielectrophoresis [34]. A commercial Si AFM probe was used as the working electrode, and a small metal ring was used as the counter electrode. The counter electrode was mounted on a translation stage that provides vertical translation with submicrometer resolution. A charge-coupled device (CCD) connected to a computer was used to monitor the process. SWNT bundles produced by the laser ablation method were first purified and etched to 0.5 μm in length and were rendered hydrophilic. The second type of CNTs used was etched small-diameter MWNT bundles that have an average length of ~ 1 μm and a tube diameter of less than 10 nm. The processed CNTs were then dispersed in deionized water, centrifuged, and homogenized in an ultrasonic bath before use. A droplet of the suspension was placed inside the metal ring. A 2-MHz ac field was applied between the two electrodes. Under the guidance of the CCD image, the counter electrode was raised slowly until the suspension surface wetted the apex of the AFM probe, as shown in

Figure 1.18. The electrode was then gradually withdrawn until a CNT tip with the desired length was assembled.

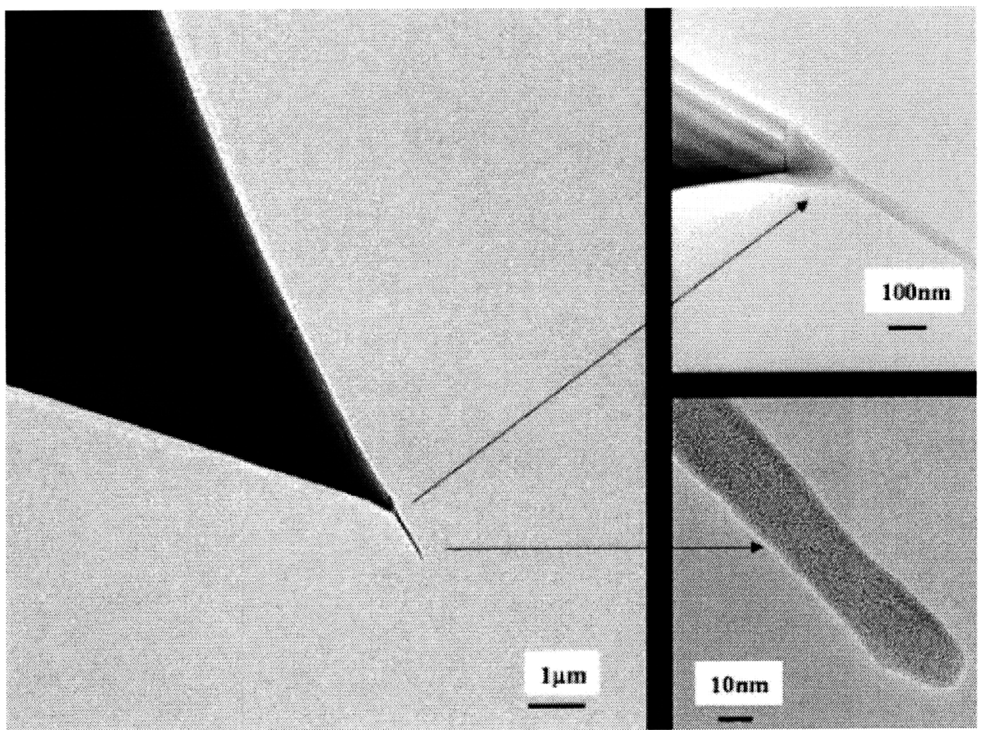

Figure 1.19 TEM images of an SWNT bundle attached to a commercial Si AFM probe by the dielectrophoresis process. The SWNT bundle has a diameter of ~20 nm near the tip and has conical geometry [34].

Although the field assisted assembly methods provide better schemes to position the CNTs close to the apex of the AFM probes and align the CNTs with respect to the directions of the external field, these approaches cannot provide a deterministic way to control the number, length, location, and orientation of the CNT tips. These approaches also involve laborious removing steps followed by shortening and aligning processes. Additionally, these field assisted assembly methods are inherently a serial process and

may not be applicable to large scale assembly because the fields have only one local extreme site which is difficult to achieve at the very small scales.

1.3.3 The CNT AFM probes by catalytic growth

In the catalytic growth method, the CNT catalyst nanoparticles are seeded at the apex of AFM probes, where the single strand CNTs are grown. This approach may be suitable for a large scale fabrication. However, the main problem with this approach is that the materials and processes prior to the CNT growth step should be compatible with the CNT growth conditions such as high temperature with rich carbonaceous gas environment. Due to the possible low yield, multiple catalytic seeds need to be planted, which requires manual weeding and trimming effort after the CNT growth.

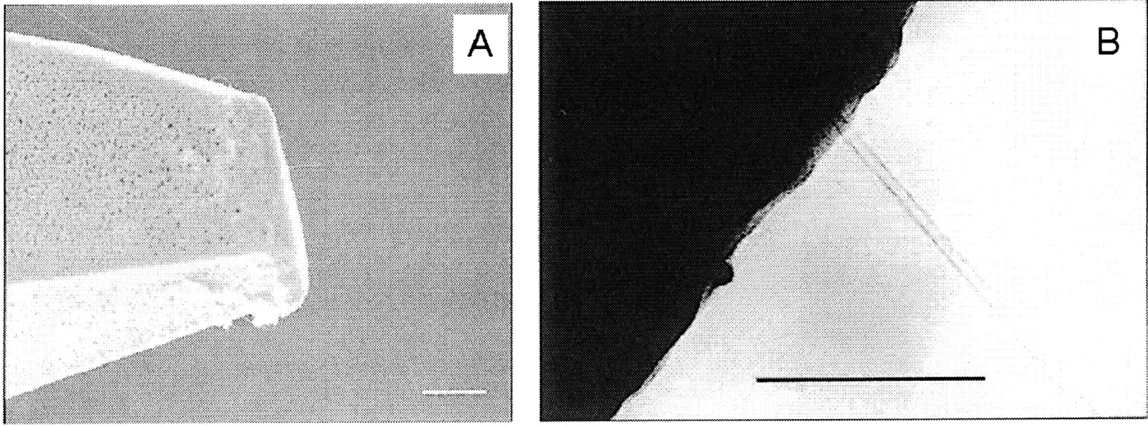

Figure 1.20 An FE-SEM (A) and a TEM (B) images of a CVD nanotube tip that has been shortened for imaging (scale bar: 1 μm in (A) and 100 nm in (B)) [35].

Hafner et al. first demonstrated the growth of CNT tips on AFM probe by CVD [35]. Nanotubes were grown by CVD from pores about 50-100 nm in diameter with 150 pores per μm^2, and the pores were formed by anodizing the Si tip in hydrogen fluoride, Iron catalyst was electrodeposited into the pores from $FeSO_4$ solution.. But, the preparation of a porous layer can be time consuming and cannot place individual CNTs at the optimal location on the flattened apex.

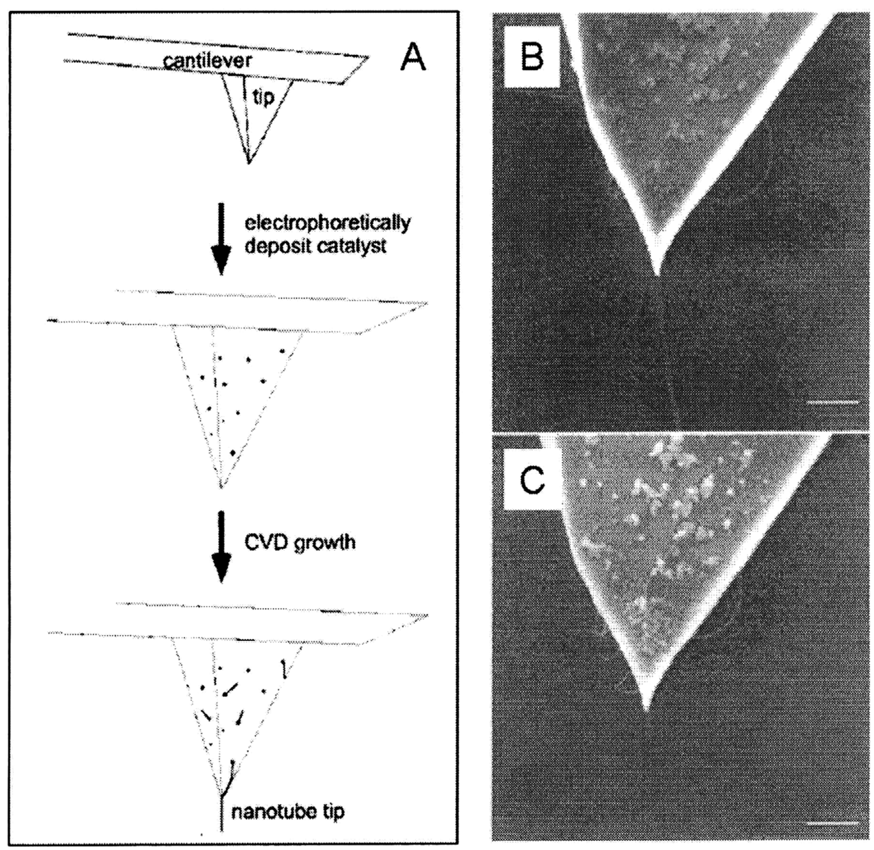

Figure 1.21 SWNT-tipped AFM probes [36]: (A) Overview of the approach used to prepare SWNT tips. (B, C) FE-SEM images of a CVD nanotube tip grown from a Si cantilever/tip assembly (B) before and (C) after shortening (scale bar: 500nm).

Hafner et al. also demonstrated the growth of single-walled CNTs for SPM tips [36]. Fe-Mo and colloidal Fe-oxide catalysts were electrophoretically deposited onto a pyramidal tip of a commercial cantilever, then SWNT were grown using thermal CVD at 800 °C for 3 min. However, the number, location, length, and orientation of CNT tips were not predictable.

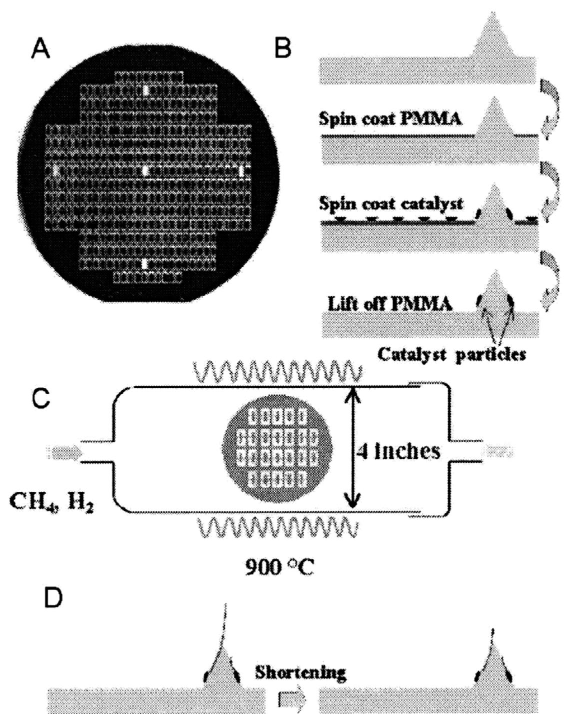

Figure 1.22 (A) 4 in. wafer containing 375 AFM cantilevers with integrated Si tips. (B) Schematic process flow for placing catalyst onto Si tips on a wafer. (C) CVD setup for growth on a wafer. (D) Long nanotubes extending out of the Si tips are shortened [37].

The first large scale fabrication of the CNT-tipped AFM probes was reported by Yenilmez et al [37]. However, this approach also has limitations. CNT location, density, length, and orientation can not be well controlled by the thermal CVD methods. Although

they can get many tips in one thermal CVD process, seldom they could get individually free-standing and vertically oriented CNTs. The yield of usable tips is very low. After the fabrication of CNT tips, a one-at-a-time manual effort is required to shorten the longer-than-needed CNTs for the AFM scanning use. This shortening process makes mass production impossible with this manufacturing process.

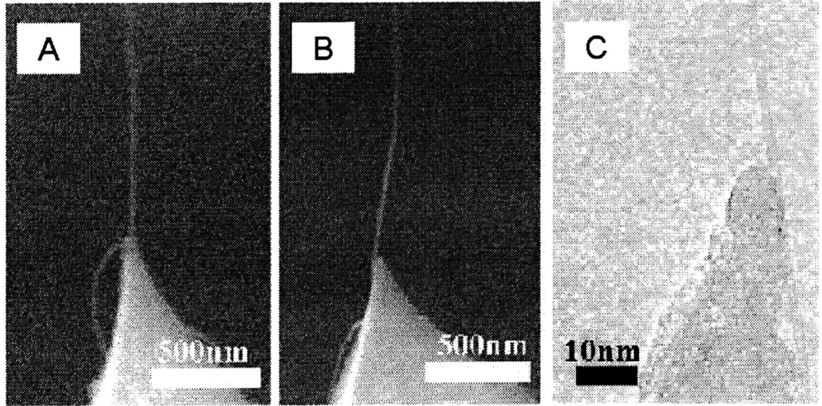

Figure 1.23 (A), (B) SEM images of as-grown nanotube tips. (C) TEM image of a SWNT extending from a Si tip [37].

Another large scale fabrication of CNT-tipped AFM probes by PECVD was also demonstrated by Ye et al [38]. Nanopatterning and nanomaterials synthesis were integrated with traditional silicon cantilever microfabrication technology, which could produce 244 CNT probe tips on a 4-in. wafer with controlled CNT location, diameter, length, and orientation. PECVD was used to provide a better orientation of CNT tips (this will be described in more detail in Chapter 3).

However, the CNT growth step and device fabrication processes are coupled each other in catalytic growth approaches. Therefore, the yield of CNT tips is very low, and

device materials should be compatible with the CNT growth conditions. Additionally, they require post-processing to control the length of CNT tips.

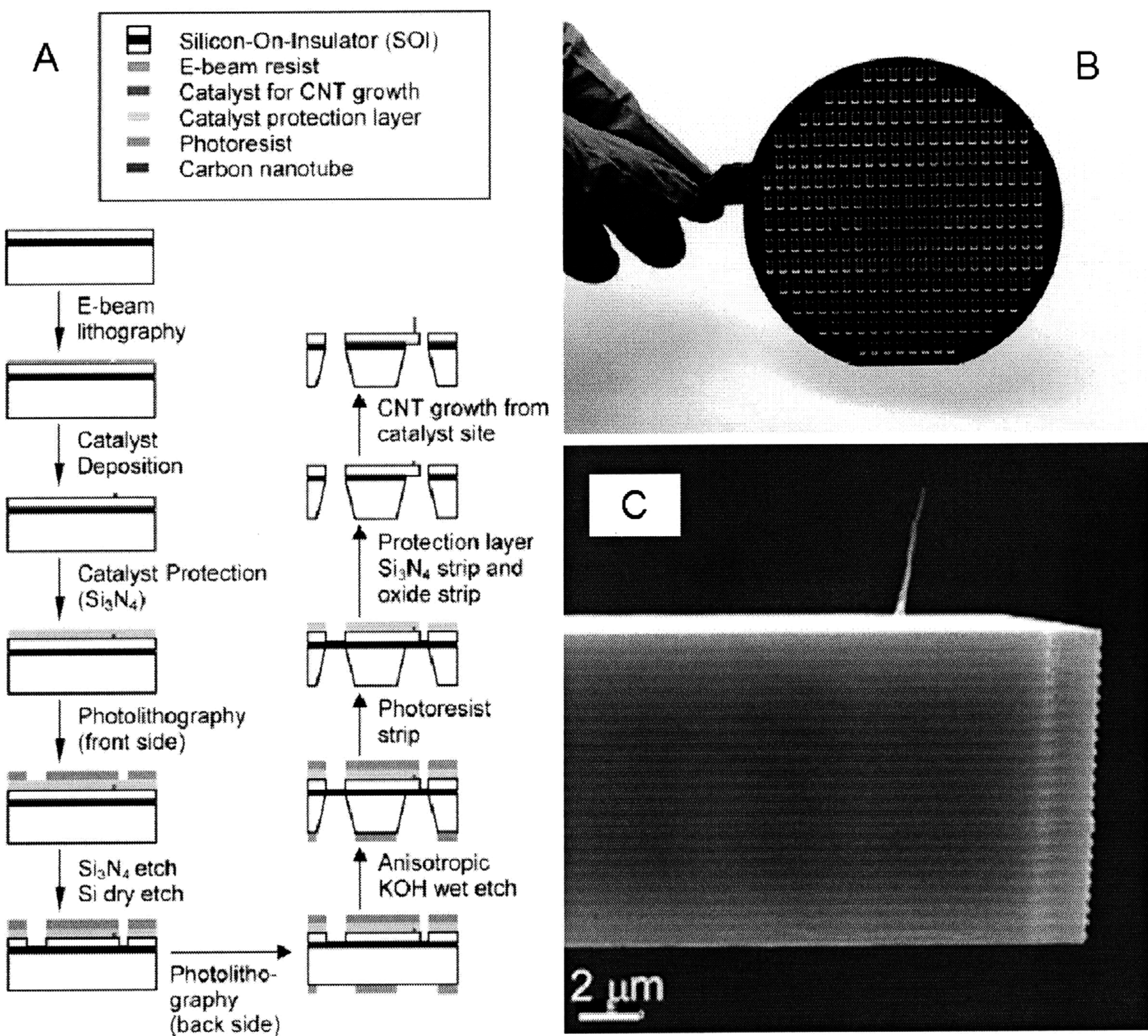

Figure 1.24 Large-scale fabrication of CNT-tipped AFM probe tips by PECVD [38]: (A) Wafer-scale fabrication process flow for making CNT-tipped AFM probes. (B) Photograph of a 4-in. wafer containing 244 CNT-tipped AFM probes. (C) SEM images of CNT-tipped AFM probes with an individual CNT grown from a 200 nm catalyst site on a cantilever beam.

1.3.4 The post-processes to improve the qualities of the CNT tips

Successful operations of AFM require optimized control gains and scan parameters, careful sample preparations and high quality tips. More efforts should be done in expanding the potential of the CNT-tipped AFM probes. Burns et al. reported a method to indirectly measure and shorten CNT tips in applying CNT-tipped AFM probes for AFM-based DNA sequencing [39]. The number, the geometry (the diameter and the length), the orientation, and the bonding strength of CNT tips are the four main factors of CNT tips that determine the quality of AFM scanning images. There have been rigorous both theoretical and experimental studies to correlate these factors with the quality of AFM images.

Wade et al. investigated the correlation of AFM probe morphology to image resolution with single walled CNT tips [40]. It is reported that CNT tips must be attached perpendicular in order to achieve maximum lateral resolution, and they should be shortened to an optimal length by applying electric currents to etch the tip away.

Snow et al. examined the factors that govern the stability of imaging using SWNTs as probes for atomic force microscopy [41, 42]. It was reported that non-vertical alignment of the nanotube causes such probes to bend in response to the surface-nanotube interaction forces during imaging, and for long nanotubes, this elastic response causes the nanotube tip to jump into contact with the surface and renders it unsuitable for imaging. For short nanotubes, stable noncontact-mode imaging can be achieved using a small

amplitude of cantilever vibration. However, the bending response is enhanced on highly textured surfaces, which limits the ability to image non-planar features.

Solares et al. presented a quantitative theoretical investigation of the effect of the tilt angle of SWNT and MWNT probes with respect to vertical axis on tapping mode AFM imaging [43]. They found that CNT probes of diameters 3.4-5.5 nm and aspect ratio 7.5 had been ideal for imaging. The effect of the probe tilt angles on CNT probe stiffness was also investigated using molecular and classical dynamics. It was shown that the stiffness decreases linearly with increasing tilt angles, becoming negligible at around 40°, thus confirming the conclusions of previous studies. It was observed that MWNT probe stiffness is proportional to the number of walls, but that the difference in stiffness between SWNTs and MWNTs also decreases linearly with increasing tilt angles and becomes negligible at around 40°.

Strus et al. investigated the connection of two distinct imaging artifacts, the formation of divots and large ringing artifacts, of CNT-tipped AFM probe operation to CNT bending, adhesion, and stiction by adjusting AFM operation parameters [44]. As the schematic diagram of Figure 1.25 (B) shows, the CNT orientation angle relative to each trench wall causes an added distortion on the right edge (RE). The measured angle of the right edge angle is about 15° larger than the left edge's measured angle, while the CNT orientation angle calculated from the field emission scanning electron microscope (FESEM) image in Figure 1.25 was 20°. When scanning the left edge, the free end of the CNT encounters interaction forces from the wall first. But when scanning the right edge,

portions of the CNT closer to its attachment base actually encounter the trench wall before the tip of the CNT does, thus the resolution of the scanning decreases.

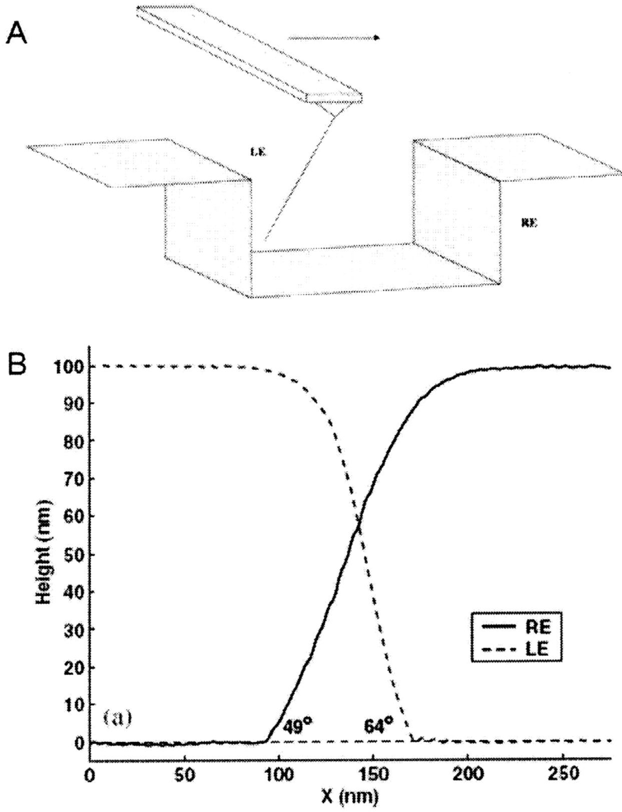

Figure 1.25 (A) A schematic diagram showing the CNT orientation angle with respect to each trench wall. (B) Two-dimensional profile scan of the right and left edges of a silicon grating overlaid to allow comparison and [43].

Most of the CNT-tipped AFM probes fabricated by either direct attachment or catalytic growth require labor intensive post-processing to control the number, length, and the orientation of CNT tips. Several methods were reported to control those properties of the CNT tips based on the experimental and theoretical investigations.

Moloni et al. reported a method for controlling end form of a nanotube bundle that is mounted on a Si tip so that a single nanotube protrudes from it. [45, 46] The method to control the length of CNT tips include cutting the CNT with the SEM electron beam [47], and burning off by applying the voltage [48]. Chang et al. demonstrated that the bundled tubes can be bent gradually and almost continuously, and both the bent position and angle of the attached tube probe can be adjusted by scanning a patterned sample [49]. Deng et al. demonstrated the ability to straighten and align metal-coated carbon nanotubes with a focused ion beam [50].

Although these post-processes have been useful in improving the qualities of CNT tips, the manufacturing of them is still time-consuming and heavily depends on the sophisticated precision equipment. Even commercial CNT-tipped AFM probes (Figure 1.26) are not available anymore since they required too laborious manipulation of individual MWNTs, a DC current-induced welding process, or a tip sharpening process [51]. Those CNT-tipped AFM probes manufactured with the above methods still involve large variations in terms of the length (500~3000 nm) and orientation (± 5°) of CNT tips, which implies that users need to tune and customize the CNT tips for their uses. A deterministic assembly technique should be developed to provide simple but reliable schemes to control the number, length and orientation of CNT tips so that those post-processes can be even eliminated.

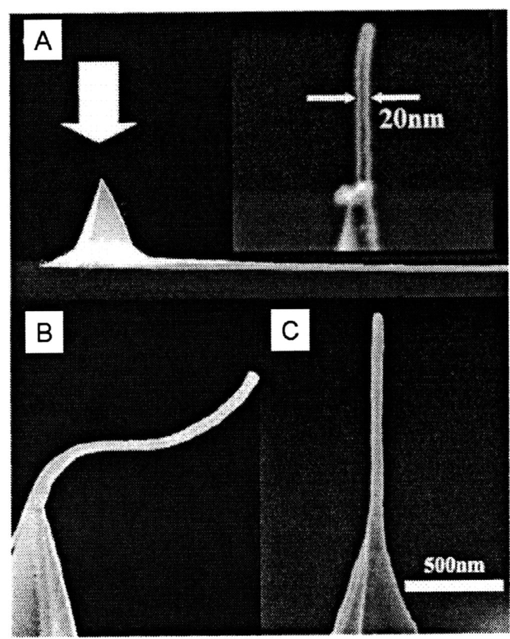

Figure 1.26 (A) SEM image of an AFM cantilever with a metal-coated nanotube on the pyramid. The arrow shows the direction of the FIB and the metal coating. Inset: Image of the metal-coated nanotube at the apex of the pyramid. (B, C) A metal-coated nanotube tip before (B) and after (C) alignment with FIB. It is 1.2 μm long and has a diameter of 45 nm, as determined from the SEM image, which gives it an aspect ratio of 27 [50].

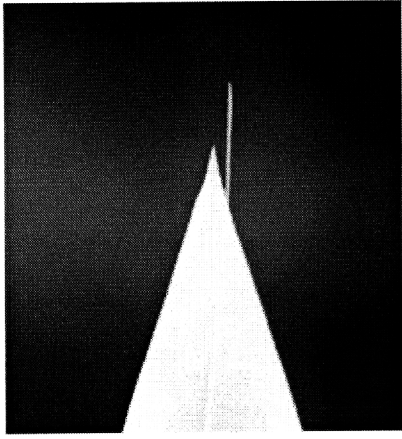

Figure 1.27 The CNT-tipped AFM probe of Nanoscience Instruments, Inc. [51].

In general, direct attachment methods are intuitive and seem straightforward, but they cannot provide deterministic assembly schemes. They are a time-consuming process, and require expensive ultra-precision equipment to monitor and manipulate CNTs. Even with external fields, difficulty in controlling those fields at the nanometer scale prevents a deterministic assembly of CNTs.

Catalytic growth methods are easier to scale-up for parallel fabrication, but they require material compatibility, and a CNT growth process should be optimized at the apex of probe, which is quite different from the sites in the reported CNT growth process optimization.

1.4 The scope and organization of the thesis

In this thesis, the detail methods and steps for implementing the transplanting assembly idea have been investigated and studied: finding the optimum parameters of growing CNTs by controlling the PECVD process variables, the methods to preserve the initial properties and geometry of CNTs during and after the encapsulation and assembly processes, the design of the polymer nanopellets for the encapsulation and assembly with an improved quality and yield, and the physicochemical interactions of CNTs with polymers/etchants during encapsulation and release. The major contributions of this thesis will be: 1) realizing practical products with CNTs by providing a new CNT assembly method in a predictable and reproducible manner, and 2) understanding the CNT growth mechanism and their interactions with surrounding factors.

Chapter 2 presents the overall designs for transplanting assembly of the individual CNTs in fabricating the CNT AFM probes. Chapters 3~5 describe three main steps in transplanting assembly: Chapter 3 presents the controlled growth of an array of vertically aligned CNTs. Chapter 4 describes the integration of the individual CNTs into MEMS carriers. Chapter 5 describes fabrication of CNT probes and their application for SPM. Chapter 6 discusses one application of CNT probes for tip enhanced Raman spectroscopy (TERS) with design for plasmonic resonator and its simulation results. Chapter 7 summaries the results and contributions of this thesis with suggested future work. In this thesis, the general procedures for microfabrication are listed in Appendix while the detailed process parameters are described in the corresponding sections.

2 Introduction

2.1 Introduction: Transplanting assembly towards deterministic assembly of CNTs

As described in chapter 1, the number, diameter, length and orientation of CNT tips have crucial effects on AFM images and require elaborated efforts to tune them after the fabrication of the CNT AFM probes. The main goal of this thesis is to develop a method to implement the transplanting assembly concept. By assembling only one CNT to the target location, and making the process reproducible and scaled-up easily, it will be shown that nanotechnology products can be produced in mass.

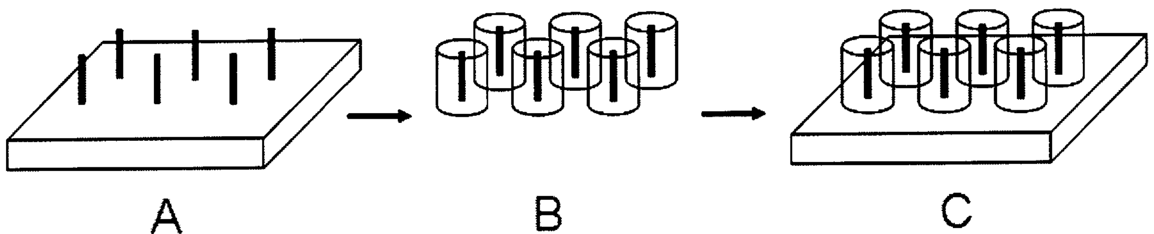

Figure 2.1 The concept of transplanting assembly of CNTs. (A) growth of vertically aligned single strand CNTs. (B) Encapsulation of CNTs into polymer blocks. (C) Transplanting the CNTs to the target location.

A schematic diagram of transplanting assembly of the individual CNTs is shown in Figure 2.1. An array of vertically aligned CNTs is encapsulated into polymer blocks, and they are transplanted to the target location.

The concept of transplanting assembly was first demonstrated for a bundle of CNTs previously [2, 3]. Bundles of vertical CNTs were grown using plasma enhanced chemical vapor deposition (PECVD), and they were encapsulated in polymer pellets. The length of CNTs was controlled by chemical mechanical polishing process of CNTs and the polymer layer before patterning the polymer pellets. Finally, the CNTs in the polymer pellets were released from the silicon (Si) substrate by etching the parts of the substrate, and the pellets were transferred to the target locations.

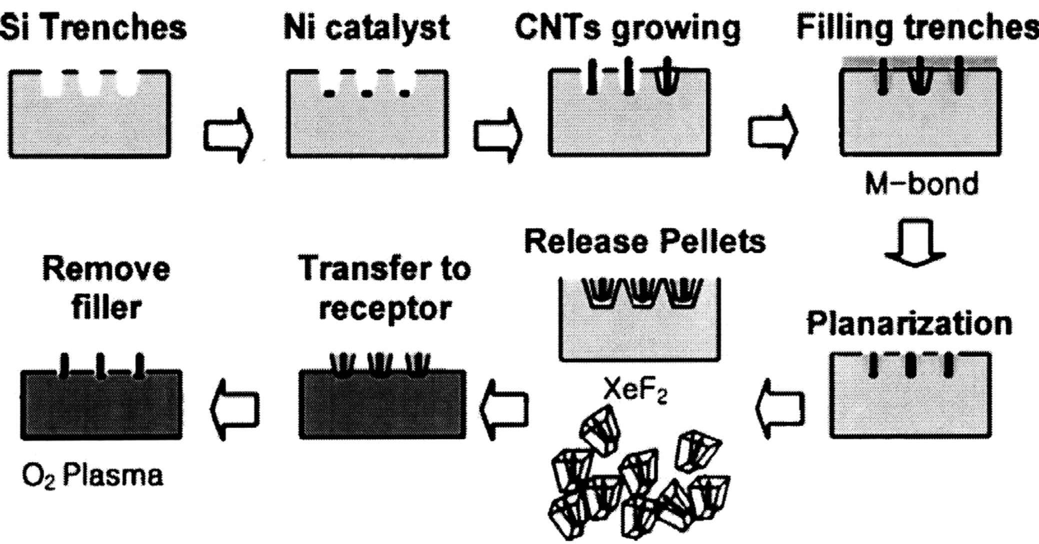

Figure 2.2 An overview of nanopelleting processes for bundles of CNTs. The pellets are fabricated by etching trenches, growing CNTs with vertical alignment in the trenches, then spin-casting an epoxy polymer, and planarizing the substrate to create isolated pellets with uniform-length CNTs. The pellets can then be released, harvested, and transplanted in large scale [3].

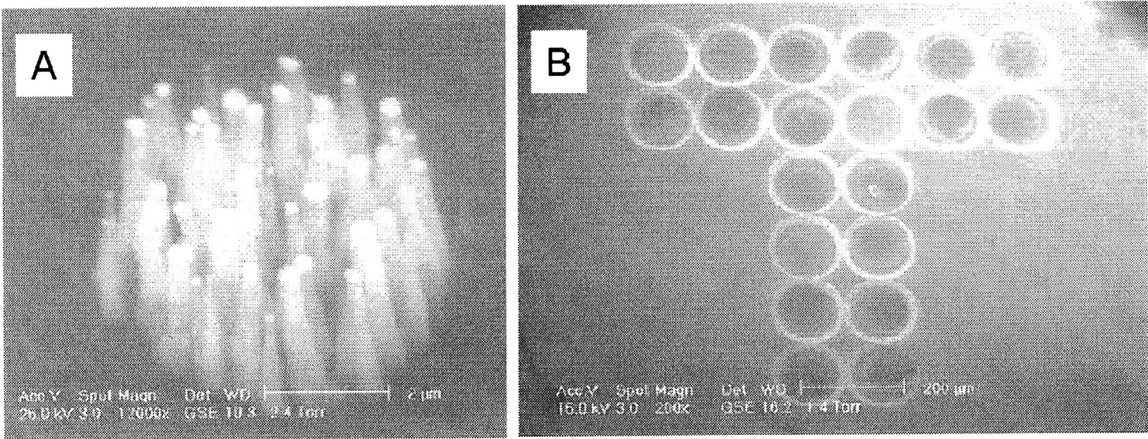

Figure 2.3 Results of transplanting assembly of CNT bundles: (A) A bundle of CNTs on a Si substrate. (B) A double row of circular pellets in trenches. [2].

In transplanting assembly of the individual CNTs, the CNT growth process is decoupled from the CNT assembly process, so each can be done under its optimal process conditions. In addition to that, the scale of assembly is shifted from the nanometers to the micrometers, so various assembly techniques at the micro-scale can be readily implemented in assembling the individual CNTs encapsulated in the single MEMS carriers.

This thesis focuses on transplanting assembly of individual CNTs with a novel scheme to control the length of CNTs, release them from substrate and transplant them to the target location in a repeatable manner. The CNT-tipped probes for atomic force microscopy (AFM) have been chosen as a sample case in which transplanting assembly of the individual CNTs are demonstrated.

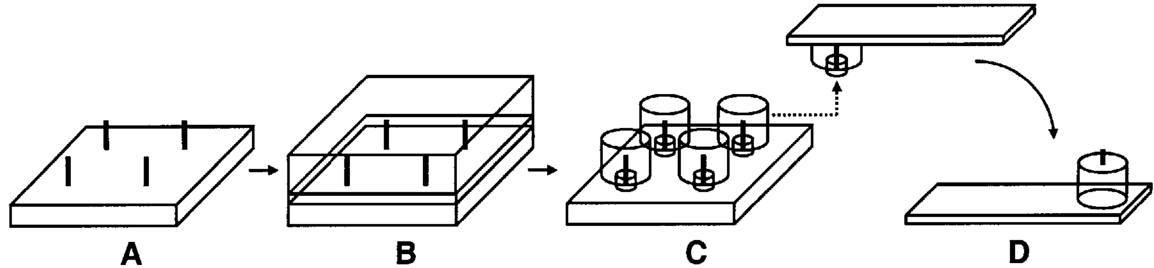

Figure 2.4 Transplanting assembly procedure in fabricating a CNT AFM probe. (A) CNT growth: An array of vertically aligned CNT is grown at the predefined locations. (B) Encapsulation: Two layers of polymers are spin-coated to encapsulate the array of CNs. (C) Pattern and transfer: Top polymer layer is patterned such that each polymer block contains a single CNT, and the individual polymer block is transferred to MEMS cantilever. (D) CNT tip release: Any remaining bottom-layer polymer is etched way, and the CNT tip, top polymer block, and cantilever form a CNT AFM probe.

An array of vertically aligned CNTs is grown by plasma enhanced chemical vapor deposition (PECVD) from Ni catalytic dots arrayed at the predefined locations (Figure 2.4 (A)). The catalytic seeds for nanotube growth are formed on top of a flat silicon wafer surface, so the new method provides a better condition in defining the size of catalytic dots using electron beam lithography.

Each vertically aligned CNT is then embedded into polymer micro-blocks which serve as CNT carriers (Figure 2.4 (B) and (C)). This polymer block (nanopellet) containing a single strand of CNTs can be readily assembled at the end of an AFM cantilever, thus forming a CNT tipped AFM probe. One of the key ideas of transplanting assembly of individual CNTs is to implement two (or multiple) polymer layers to encapsulate the individual CNTs into the separate polymer blocks. Two layers of photoresists with different etch selectivity are used to control the exposed length of a

CNT and to release the polymer nanopellets from the substrate easily. Finally, each polymer nanopellet carrying a single CNT can be assembled at the target position which is the end of AFM probe (Figure 2.4 (D)).

In the following sections, detailed design and fabrication schemes will be presented in fabricating the CNT-tipped AFM probes by transplanting assembly of the individual CNTs. The key issue in growing vertically aligned individual CNTs is how to define the number, the location, the shape (the diameter and the length), and the orientation of CNTs.

- Number: only one CNT should grow from one catalyst.

- Location: the location of each CNT needs to be defined by that of catalytic dots.

- Shape: each CNT needs to be longer than 5 μm for the application to scanning probe microscopy (SPM), and it requires cylindrical shape.

- Orientation: the individual CNTs should be aligned normal to the substrate.

2.2 Design for an array of the individual CNTs

The key issue in the step of growing vertically aligned individual CNTs is how to define the number, the location, the shape (the diameter and the length), and the orientation of CNTs. Among them, the number, shape, and location of each CNT can be controlled by the shape and location of the individual catalytic dots as well as CNT growth parameters.

- Location: the location of each CNT needs to be defined by that of catalytic dots.
- Number: only one CNT at each point of arrays.
- Shape: each CNT needs to be longer than 5 μm for the application to scanning probe microscopy (SPM) with cylindrical shapes.

The diameter and length of the vertically grown individual CNTs are governed by those of the catalytic dots. The geometries (the diameter, thickness, and the location) of the catalytic dots are defined by electron- beam lithography in combination with thin metal deposition. The patterns written by electron beam lithography are an array (21 by 21) of circular dots as in Figure 2.5. The diameter of dots ranges between 100 nm and 200 nm, which can be achieved and controlled repeatedly by the path and exposure dose of electron beams using the electron-beam writing facility available in MIT. The thickness of the catalytic dots is 10-40 nm, which will be optimized through the CNT growth experiments. The spacing between dots, d, ranges from 5-40 μm depending on the size of micro-scale carriers.

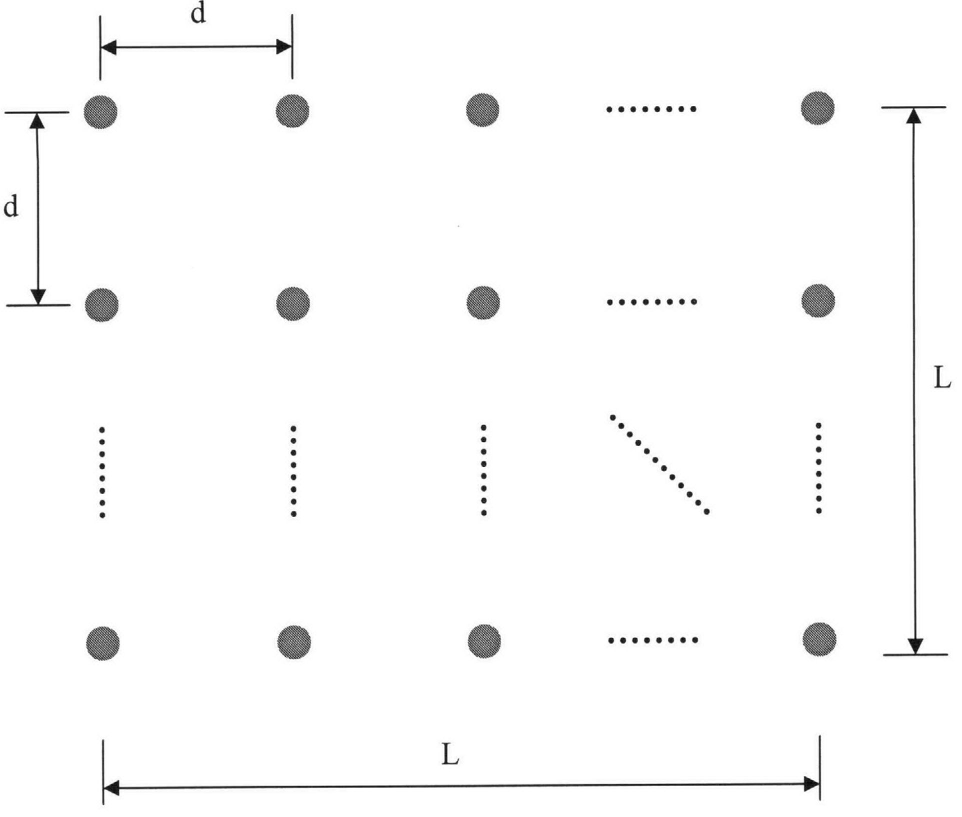

Figure 2.5 A pattern of an (21 by 21) array of circular dots for electron beam writing. (d: the spacing between the dots, L: the overall range of the array)

2.3 Design and material selections for the encapsulation procedures with dual layers

As the second major step in transplanting assembly of the individual CNTs, the individual CNTs are encapsulated into microelectromechanical systems (MEMS) carriers so that each MEMS carrier contains a single CNT. This section presents the main issues involved in the encapsulation step, and the design approaches and fabrication results to address the following issues.

- Easy CNT length control: The length of the exposed CNT parts should be controlled in a deterministic way, so it should not involve any laborious shortening or etching steps.

- Easy release: The CNTs with MEMS carriers should be release from the substrate easily without damaging the CNTs and should not involve any substrate etching process.

- Minimal physicochemical interaction of CNTs: During the encapsulating process, the initial orientation of vertically aligned CNTs, which was defined by the direction of the electric fields during the CNT growth step, should be maintained. Additionally the physicochemical interactions of CNTs with encapsulating polymers and etchants need to be minimized.

2.3.1 The material selection for the MEMS carrier layer

In encapsulating the individual CNTs into MEMS carriers, the design and material of the MEMS carriers should address the issues involved in the encapsulation step. SU8-2015 (MicroChem Corp., Newton, Massachusetts) is selected as a material for the top MEMS carrier layer. It is chemically compatible with CNTs and easy to pattern with the thickness of 10~30 μm. However, SU8-2015 is difficult to remove once it is patterned via photolithography. Therefore, exposing the part of CNTs involves chemical or physical etching processes which may affect CNTs, and the length of CNTs cannot be controlled in a deterministic manner. Additionally, releasing SU8 MEMS polymer from the substrate requires etching the Si substrates or breaking SU8 block mechanically as explained in the section 2.1.

2.3.2 The double (or multiple) layer design for MEMS carriers

The key idea to address the problems with SU8-2015 for MEMS carriers and provide an simple way to control the length of the exposed CNTs is to implement a double polymeric layers with different etch selectivity, and the overall bi-layer encapsulation process steps are illustrated in Figure 2.6. After the CNT growth step, the two layers of the polymers are coated using spin-coating process. The top layer (SU8 2015) works as a MEMS carrier through patterning processes using photolithography. The key roles of the bottom layer are to define the length of the CNT tips, to maintain the orientation of the CNTs with the top MEMS carrier during the assembly step, and to release the CNTs easily from the substrate as soon as the bottom layer is etched.

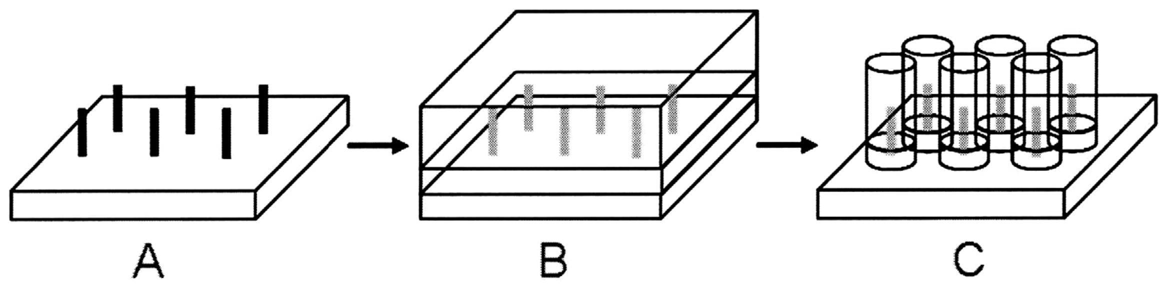

Figure 2.6 Encapsulation procedures: an array of CNTs (A) is embedded in two polymer layers (B), and the layers are patterned using photolithography (C).

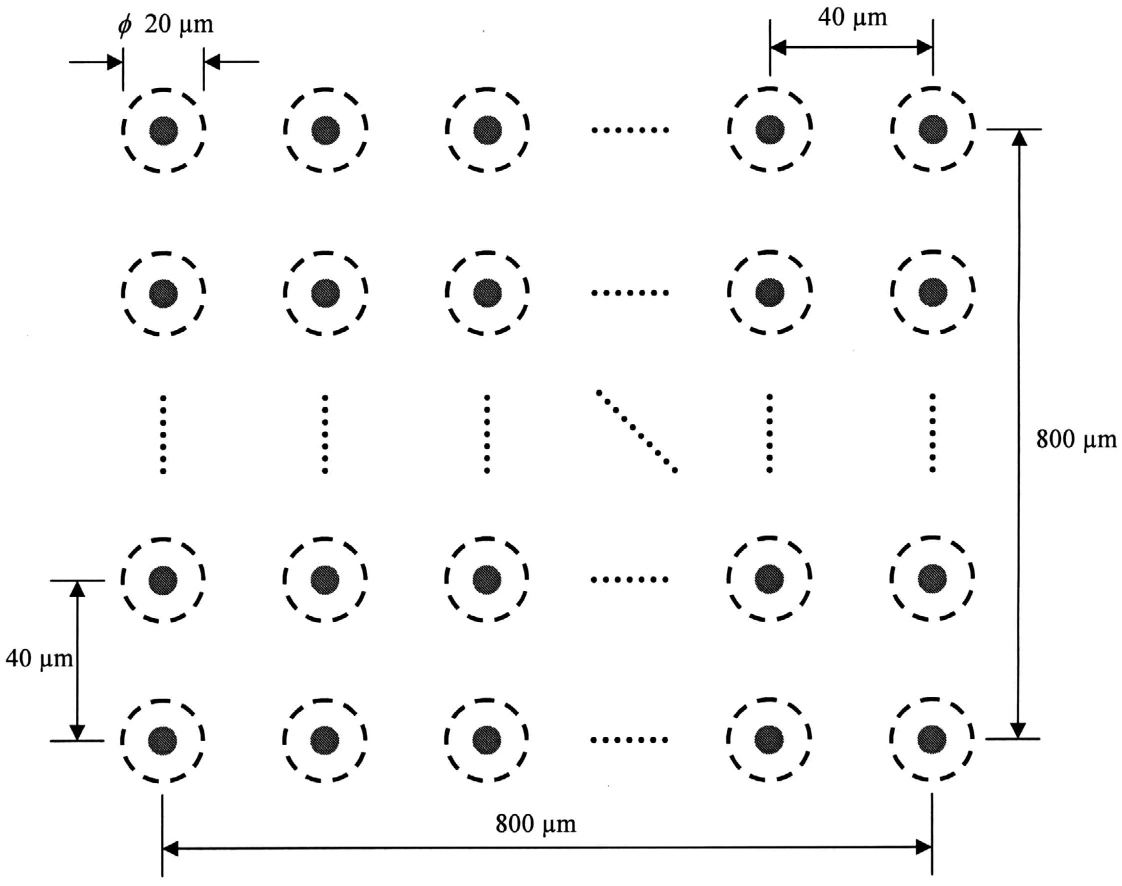

Figure 2.7 A schematic of SU patterns (dotted circles) with the individual CNTs (small solid circles).

Figure 2.7 depicts the design of the array of SU8 blocks along with an array (21 by 21) of single strand CNTs. The dotted circles represent the individual SU8 cylindrical blocks encapsulating the single CNTs represented with dots. The diameter of SU8 blocks is 20 μm with the 40 μm distance between the centers of blocks.

The diameter of the CNT tips is determined by that of catalytic dots as well as CNT growth parameters. In order to achieve the nano-scale catalytic dots, electron beam lithography with thin metal deposition will be used. Considering the process capability of the electron beam writer of MIT, the tentative diameter of the catalytic dots is 100-200 nm, and there needs to be only one CNT from one catalytic dots

2.3.3 Selection of the thickness and material of the bottom layer

The thickness of the bottom layer is set to 1.5-2.0 μm so that the final aspect ratio of CNT tips is about 10. The thickness of the bottom layer determines the final CNT tip length when the bottom layer is etched away. The length of the CNT tips requires a careful consideration because the vibration of the tips due to thermal fluctuation can be a problem with high-aspect ratio probes as it influences the scanning images.

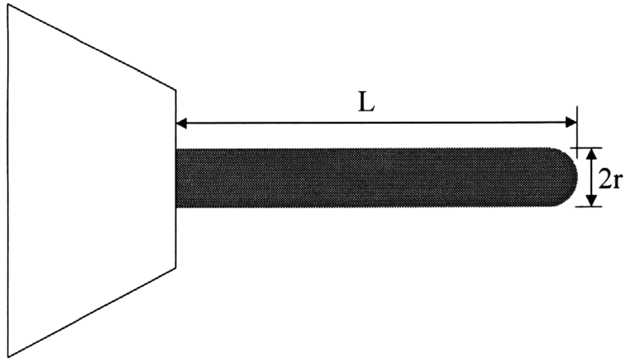

Figure 2.8 A CNT tip (the length = L, the radius = r).

The amplitude of the thermal vibration of a CNT tip is estimated by modeling the CNT tip as a rod with one end clamped.

$$\frac{1}{2}K_B\langle x\rangle^2 = \frac{1}{2}k_B T \Rightarrow \langle x\rangle = \sqrt{\frac{k_B T}{K_B}} << r \quad (2.1)$$

where $\langle x\rangle$, the amplitude of the thermal vibration

k_B, Boltzmann constant = $1.38\times10^{-23}\,JK^{-1}$

T, the temperature = $300K$

K_B, the bending stiffness of the CNT tip: $K_B = \frac{3EI}{L^3} = \frac{3\pi r^4 E}{4L^3}$

E, Young's modulus of the CNT (estimated) = 100 GPa

r, the radius of the CNT tip = 50 nm

L, the length of the CNT tip.

The amount of thermal vibrations at the tip end is plotted for different length of CNTs in Figure 2.9. The CNT tips of which the aspect ratio is 10 (diameter = 150 nm,

length = 1.5 μm) show a change of the orientation less than 1° in the ambient environment (27 °C = 300 K).

For a case of CNTs with very small diameters such as SWNTs, the amount of the tip vibration induced by thermal fluctuation can significant compared to the diameters of CNTs. For example, a 1 μm long CNT whose diameter is 1 nm has a thermal vibration larger than 100 nm. The amount of thermal vibrations at the tip end for a CNT with 1 nm diameter is plotted in Figure 2.10. It can be seen that the CNT should be shorter than 40 nm to have a thermal vibration less than 1 nm. A 10 nm long CNT (aspect ratio of 10) can give a thermal vibration less than 0.1 nm (10 % of the diameter).

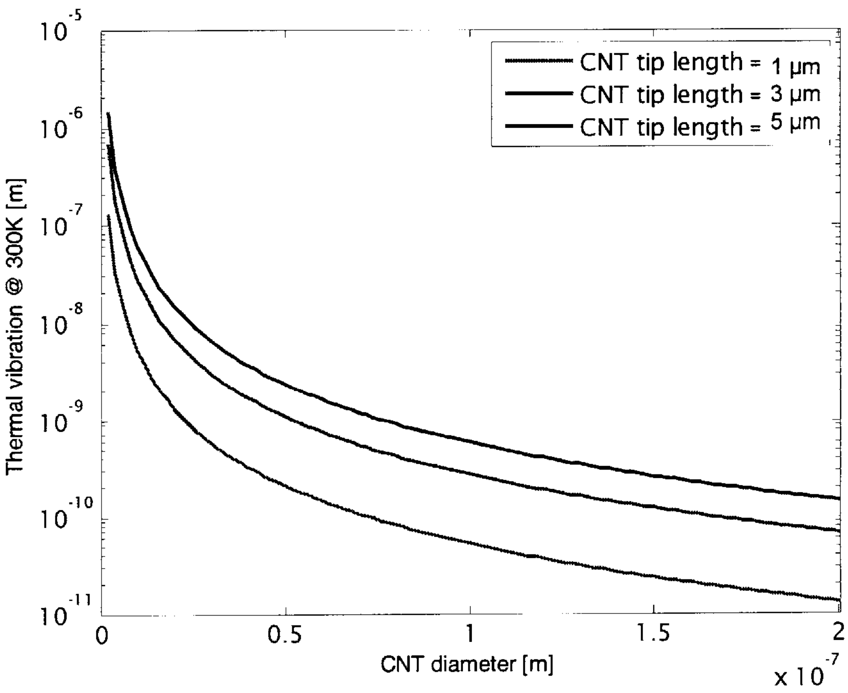

Figure 2.9 The thermal vibration of the CNT tip ends at the temperature of 300K for CNTs with length of 1 μm, 3 μm and 5 μm.

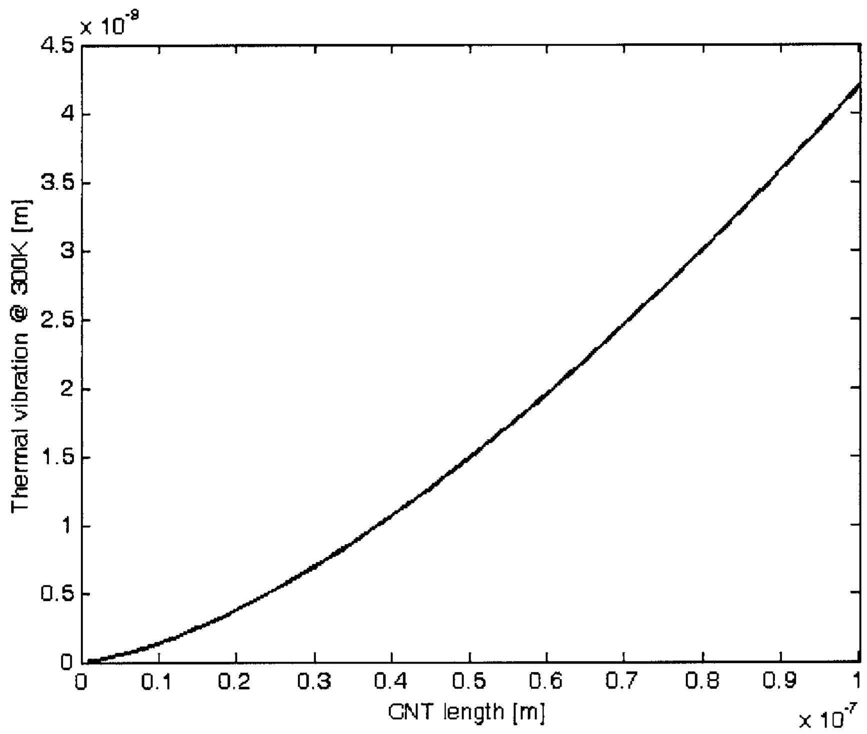

Figure 2.10 The thermal vibration of the CNT tip ends at the temperature of 300K for a case of a CNT with 1 nm diameter.

Among many candidate materials for the bottom layer, polymethylglutarimide (PMGI) resist (MicroChem Corp., Newton, Massachusetts) is used for the bottom layer primarily because of its good selectivity to SU8-2015. PMGI SF series is an organic polymer solution, and its primary application is to promote adhesion of SU8 to a substrate or to lift-off the SU8 layer [64, 65]. PMGI-based resists are positive-toned and can be patterned using deep-UV (DUV) radiation. PMGI has also have been patterned using electron-beam and proton beam exposure. Its insolubility in the casting solvent used by most novolac photoresist formulations enables the application for lift-off

processes. Based on chemical composition, PMGI SF series show a wide range of achievable thicknesses according to the viscosity. Among them, PMGI SF 11 is chosen for its available thickness range (1~3μm) and low viscosity (1/100~1/50 that of SU8-2015).

2.3.4 Discussion on the double layer design

The major material properties of SU8-2015 and PMGI SF 11 are listed in Table 2.1. The surface energy of both polymers is lower than that of water, and this provides easy wetting with the individual single strand CNTs. The low viscosity of PMGI SF 11 can reduce the effect of fluidic shearing during the spin-coating process. The baking temperature of SU8-2015 and PMGI SF 11 make them compatible with each other because PMGI SF 11 is coated firstly in the double layer spin-coating process as the bottom layer.

Table 2.1 Properties of SU8-2015 and PMGI SF 11.

	SU8-2015	PMGI SF 11
Type	Organic resin solution	Organic polymer solution
Specific gravity	1.200	0.992
Viscosity	1250 cSt	~ 200 cSt
Surface energy	~ 30 mJ/m^2	~ 40 mJ/m^2

2.4 The change of the orientation of the individual CNTs during spin-coating step

The change of the orientation of the individual CNTs is one of the major concerns involved in spin-coating process of polymers. Figure 2.11 shows the detailed steps in the spin-coating process. A polymer solution is dispensed statically over an array of vertical CNTs on the substrate. The sample is spinning at faster than 3000rpm for a minute to form a polymer layer with the target thickness. In general, the accuracy of the thickness is about 100nm.

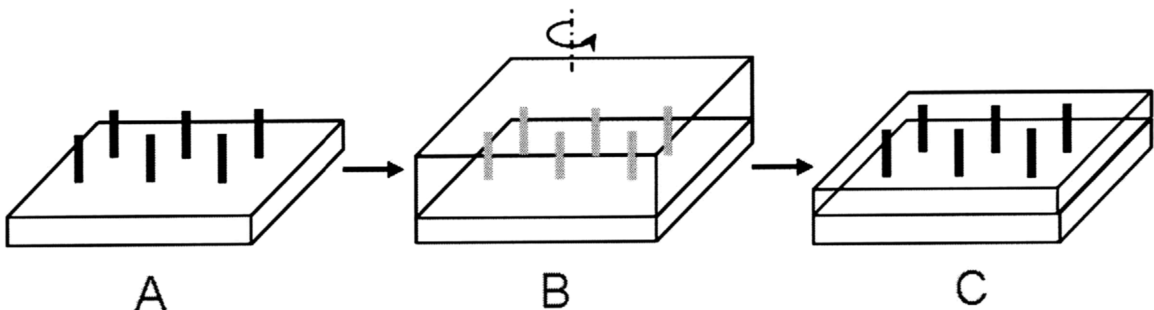

Figure 2.11 Procedures of spin-coating of a polymer layer. (A) An array of vertically aligned CNTs. (B) Spinning of the sample after dispensing the liquid polymer solution. (C) Formation of the polymer layer with a target thickness.

The spin-coating process involves two main requirements in general. A viscous liquid is spread quickly over the substrate, and the thickness of the layer is controlled with uniformity. In the spin-coating process of transplanting assembly, the first requirement can be met by static dispense of polymers over the small sample (15mm by

15 mm). Then, the spin-coating process is fully dedicated to reaching the target thickness of the polymer uniform over the sample. The array of the CNTs is located close to the center of the rotation, so the velocity of the fluid, in turn the centrifugal force of the fluid, can be reduced in order to minimize the shearing effects on the individual CNTs.

The effect of fluidic shearing on the orientation of a single CNT during spin-coating process is quantified using a simplified fluid mechanics including an interaction with structural rigidity of the CNTs. Spin-coating process is modeled as one dimensional laminar flow by the centrifugal force and the frictional force, and the resultant fluidic velocity and shearing force are shown in Figure 2.12. (We consider the outmost cell for analysis.)

The Navier-Stokes equation for an incompressible Newtonian fluid in cylindrical coordinates (r, θ, z) can be used to derive the velocity profile. The r-momentum equation is

$$\frac{\partial \upsilon_r}{\partial t} + \left(\vec{V} \cdot \nabla\right)\upsilon_r - \frac{1}{r}\upsilon_\theta^{\,2} = -\frac{1}{\rho}\frac{\partial p}{\partial r} + g_r + \nu\left(\nabla^2 \upsilon_r - \frac{\upsilon_r}{r^2} - \frac{2}{r^2}\frac{\partial \upsilon_\theta}{\partial \theta}\right). \tag{2.2}$$

The following assumptions are applied to simplify the equation

- Steady state flow

- Axisymmetric and 1-dimensional (r) flow: $\upsilon_r << \upsilon_\theta, \upsilon_\theta \approx r\omega, \upsilon_z \approx 0$

- Constant pressure

The resulting simplified equation is

$$\upsilon_r \frac{\partial \upsilon_r}{\partial r} - \frac{1}{r}\upsilon_\theta^{\,2} = \nu \frac{\partial^2 \upsilon_r}{\partial z^2}. \tag{2.3}$$

The continuity equation with an approximation on the angular velocity gives

$$\nu \frac{\partial^2 \upsilon_r}{\partial z^2} = -\frac{1}{r}(r\omega)^2 = r\omega^2 \tag{2.4}$$

Boundary conditions are applied at z = 0 and z = t, resulting in the velocity profile

$$U(r,z) = \frac{\omega^2 R z}{\nu}\left(t - \frac{z}{2}\right) \quad . \tag{2.5}$$

where ω, the rotational speed

R, the distance from the center of rotation

z, the height from the substrate

ν, the viscosity of a polymer

t, the thickness of a polymer layer.

The corresponding Reynolds number is $\mathrm{Re} = \frac{Ud}{\nu}$, and it is about 5×10^{-4} at the maximum velocity, indicating a laminar flow.

A CNT is modeled as a tube rigidly clamped to the substrate as there is no drag at the root of the CNT based on no-slip boundary condition. Drag coefficients are calculated from the velocity along the length of the CNT [52]

$$C_D = \left(\frac{8\pi}{\mathrm{Re}\ln(7.4/\mathrm{Re})}\right)\left(\frac{3+2\phi^{5/3}}{3-4.5\phi^{1/3}+4.5\phi^{5/3}-3\phi^2}\right), \tag{2.6}$$

where Re, Reynolds number

ϕ, the occupation of a CNT in each cell

and force distributions [53] are obtained

$$F_D = \frac{1}{2} C_D \rho U^2 A. \tag{2.7}$$

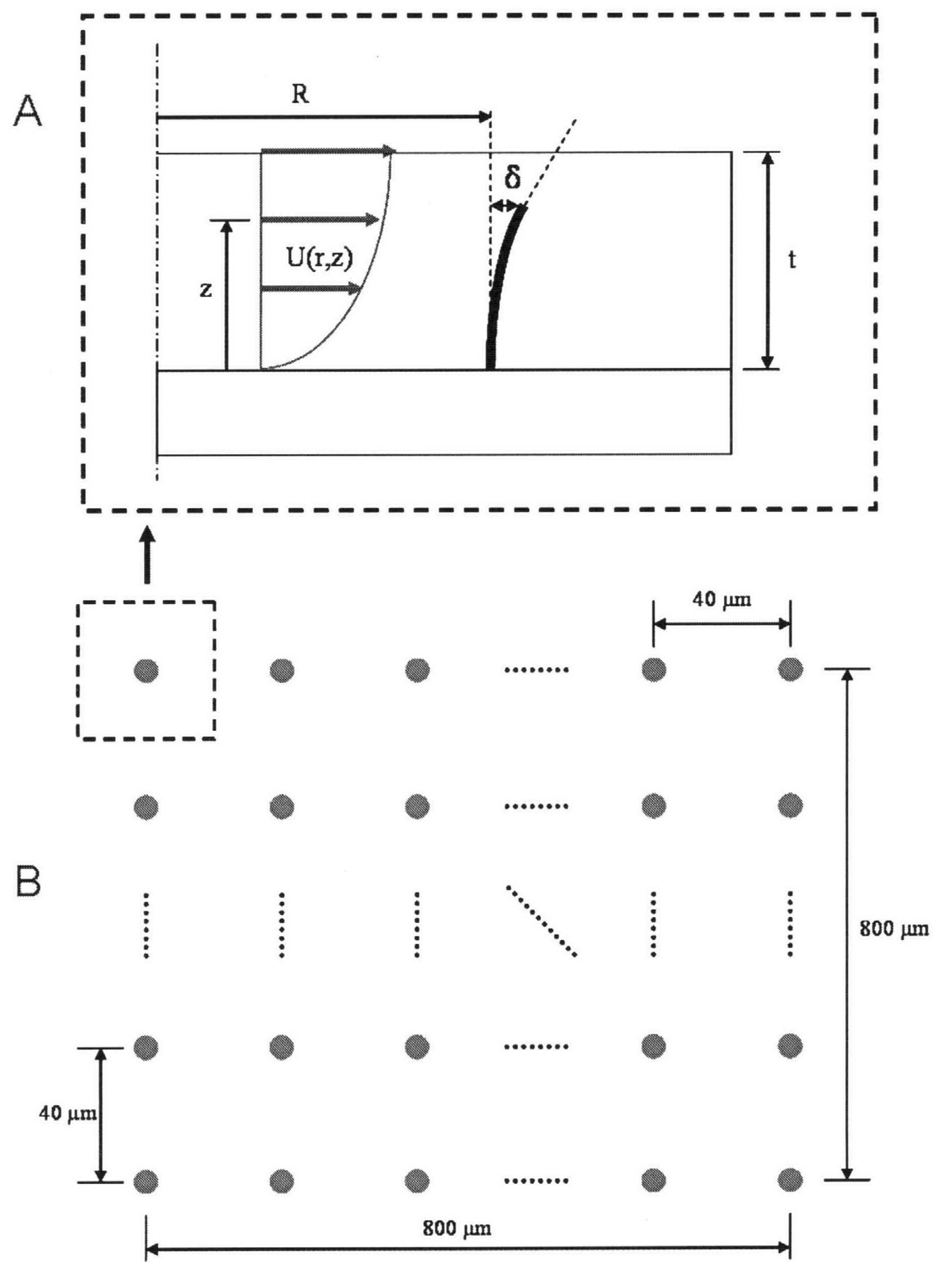

Figure 2.12 Model for interaction of the single CNT with encapsulating polymers: (A) One dimensional fluid mechanics model. (B) An array of CNTs..

Finally, the deflection δ and the orientation change α at the end of the CNT are calculated using a linear beam bending under distributed loads.

$$\delta = \frac{11F_D L^4}{120EI} \quad and \quad \alpha \approx \frac{11F_D L^3}{120EI} \tag{2.8}$$

where I, the moment of inertia: $I = \frac{\pi r^4}{4}$

E, Young's modulus of the CNT (estimated) = 100 GPa

r, the radius of the CNT tip = 50 nm

L, the length of the CNT tip.

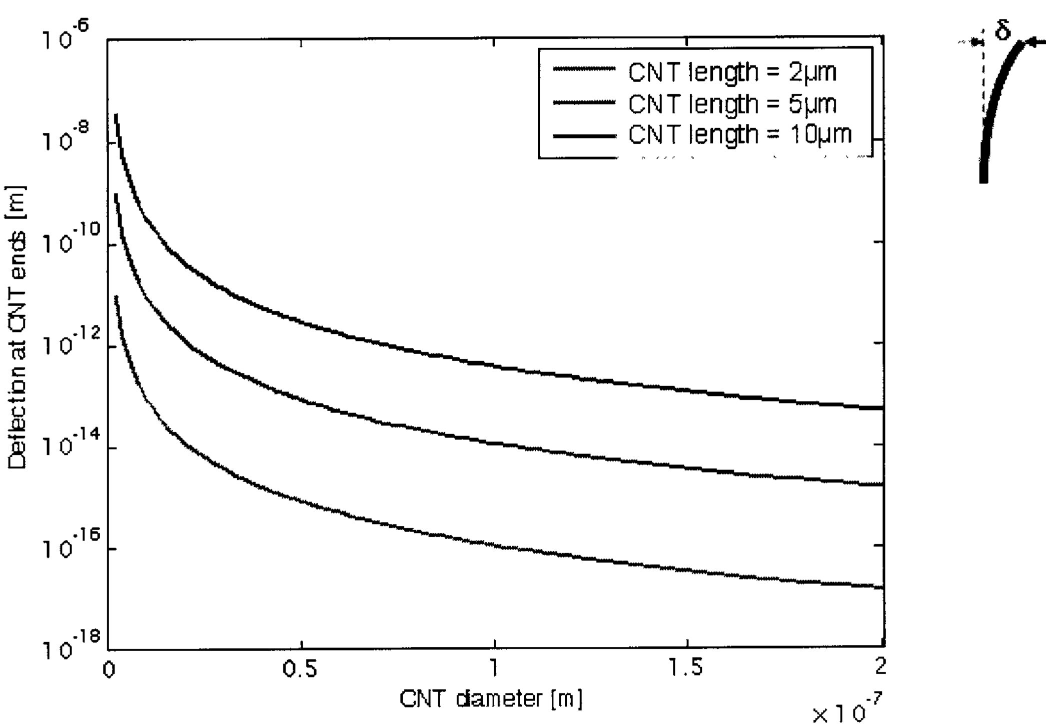

Figure 2.13 The deflection at the CNT tips under fluidic shearing.

The calculated deflection is less than 10^{-16} m, which is much small compared to the diameter of the CNT, and the amount of deflections at CNT tips with various CNT diameters and lengths are summarized in Figure 2.13. It is certain that the deflections at the CNT tips are several orders less than the diameters of CNTs. The small magnitude of fluidic shearing forces results form the reduced velocities of liquid polymers near the individual CNTs close to the center of rotation. The static dispense of liquid polymer covers the whole array of CNTs before spinning, and fluidic drag forces induced by a spinning disk enables the fluid film to reach the target thickness. This indicates that the spinning polymer on the whole wafer (for example, 4-inch wafer) may not work for coating the CNTs located outer region of the wafer or CNTs with small diameters. The feasibility of spin-coating for encapsulating the individual CNTs should be check using the model presented in this section before spin-coating experiments.

2.5 Design for transferring the individual CNT with carriers

In order to demonstrate the concept of transplanting assembly as a deterministic assembly method for the individual CNTs, each CNT encapsulated inside a MEMS carrier needs to be assembled to the end of an AFM cantilever through manual transfer of the individual CNTs. The initial orientation of the individual CNTs should be reserved during assembly step, and a schematic describing the assembly steps is shown in Figure 2.14. The bottom

layer is etched so that its minimal portion can maintain the orientation of the CNTs and preserve the integrity of CNTs.

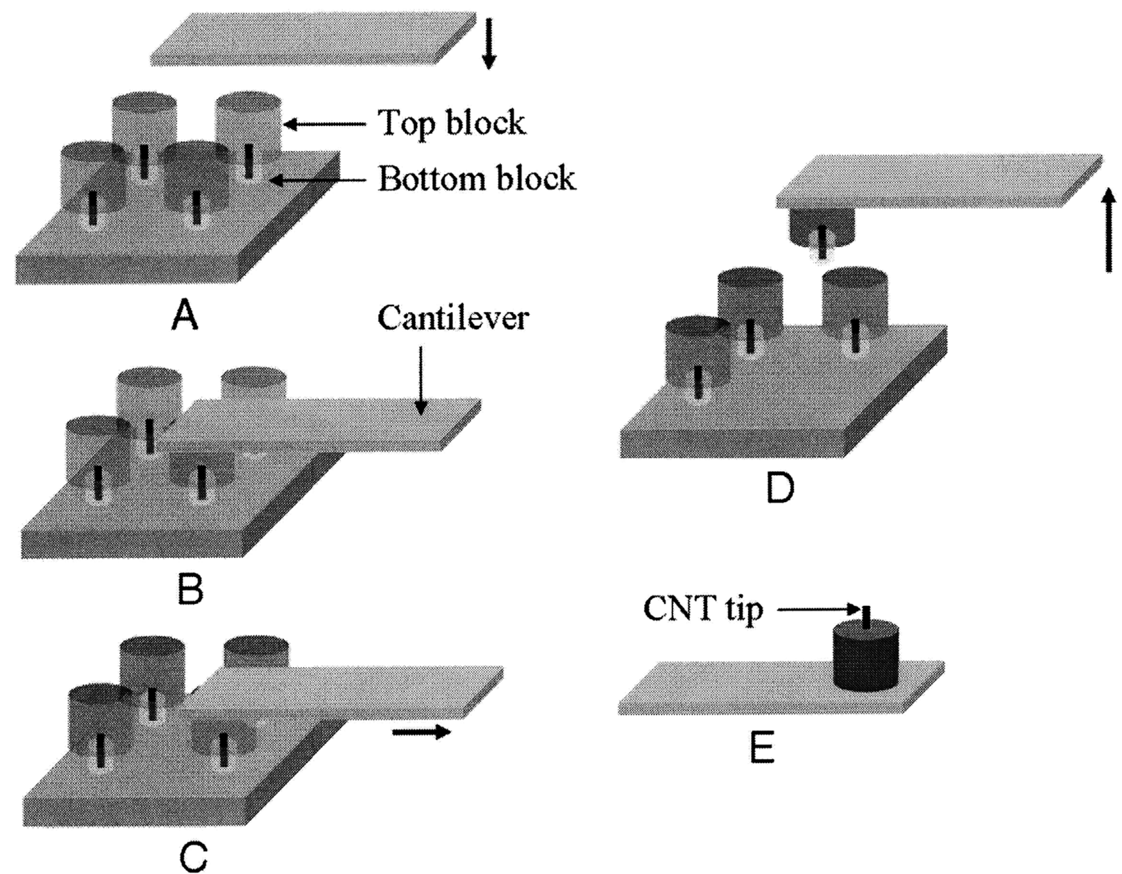

Figure 2.14 A schematic showing the procedures in transferring the individual CNTs to the end of cantilever: (A) Approach the cantilever to a target CNT (encapsulated in a MEMS carrier). The cantilever already picked up a small droplet of an adhesive. (B) Wait until the adhesive is cured. (C) Shear the bottom layer with the CNT horizontally by manipulating the cantilever. (D) Lift off the CNT with the carrier. (E) Etch the remaining bottom layer to form a CNT-tipped AFM probe.

2.6 Summary

Design and fabrication schemes have been proposed in demonstrating transplanting assembly of the individual CNTs. A 21 by 21 array of Ni catalytic dots and grown CNTs with 40 μm spacing can accommodate standard photolithography with circular MEMS carriers with diameter of 20 μm. The location of each CNT is defined precisely using electron-beam lithography, and the length of the exposed CNT tip is designed to be 1.5 μm considering the diameter of CNTs and thermal vibration at their ends. The orientations of CNTs are preserved through spin-coating of liquid polymers, and their change during spin-coating process has been calculated using an analytic model developed with structural and fluidic mechanics. Manual transfer scheme has been presented in order to maintain the initial orientation of the individual CNTs during assembly steps.

3 The controlled growth of an array of vertically aligned CNTs

3.1 Introduction

An array of Ni catalytic dots works as the seeds in growing single strand CNTs. The method to grow or synthesize CNTs need to be selected by considering the requirements for deterministic assembly of the individual CNTs: the vertically aligned individual CNTs at the predefined locations.

Various methods have been reported to synthesize CNTs [54], and they can be categorized into three main approaches: arc discharge [55, 56], laser ablation [57] and chemical vapor deposition [58]. In arc-discharge method, carbon atoms are evaporated by plasma of helium gas ignited by high currents passed through opposing carbon anode and cathode. Arc-discharge has been developed into an excellent method for producing both high quality MWNTs and SWNTs. MWNTs can be obtained by controlling the growth conditions such as the pressure of inert gas in the discharge chamber and the arcing current. For the growth of SWNTs, a metal catalyst is needed in the arc-discharge system. The first success in producing substantial amounts of SWNTs by arc-discharge was achieved by Bethune et al. in 1993 [59]. They used a carbon anode containing a small percentage of cobalt catalyst in the discharge experiment, and found abundant SWNTs generated in the soot material.

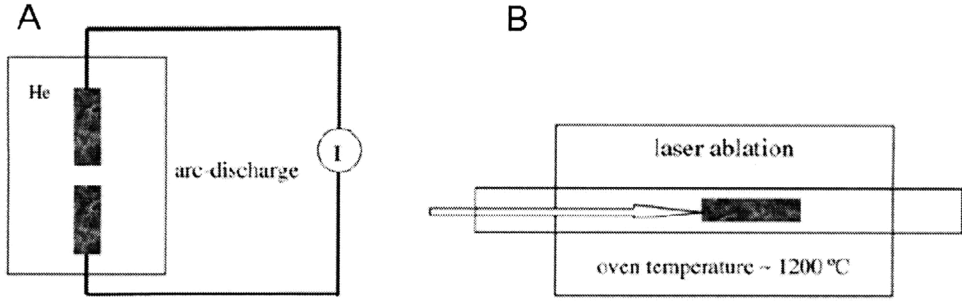

Figure 3.1 Schematic of arc-discharge (A) and laser ablation (B) methods [54].

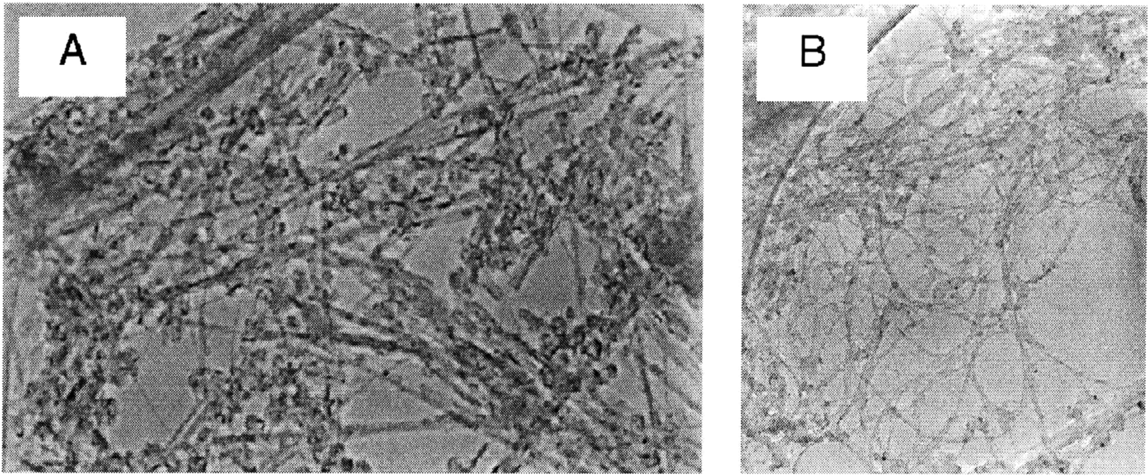

Figure 3.2 The CNTs grown by (A) arc-discharge [55] and (B) laser ablation [57]. In general, CNTs grown by arc-discharge and laser ablation have a form of soot, which makes assembly of the individual CNTs impossible.

The growth of high quality SWNTs at the 1–10 g scale was achieved by Thess et al. using a laser ablation (laser oven) method [60]. The method utilized intense laser pulses to ablate a carbon target containing 0.5 atomic percent of nickel and cobalt. The target was placed in a tube-furnace heated to 1200 °C. During laser ablation, a flow of inert gas was passed through the growth chamber to carry the grown nanotubes downstream to be

collected on a cold finger. The SWNTs are mostly in the form of ropes consisting of tens of individual nanotubes close-packed into hexagonal crystals via van der Waals interactions.

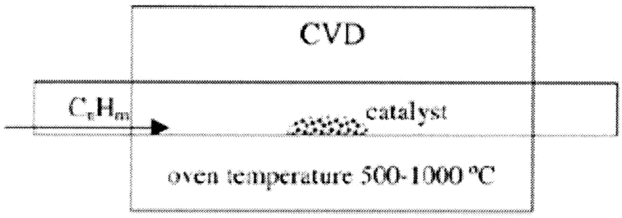

Figure 3.3 Schematic of CVD [54].

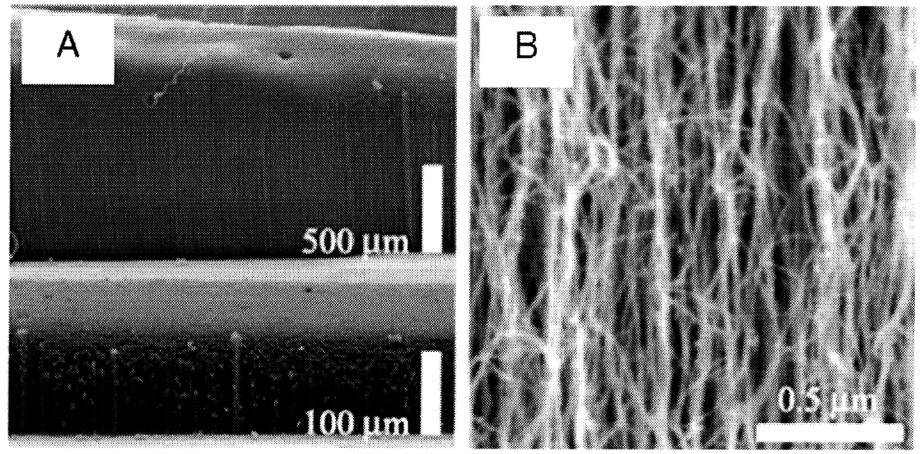

Figure 3.4 CNTs grown by thermal CVD [61]. (A) They may look vertically aligned macroscopically. (B) Enlarged view of each CNT. They are not straight.

Chemical vapor deposition (CVD) methods have been successful in making carbon fiber, filament and nanotube materials, and a schematic experimental setup for CVD growth is depicted in Figure 3.3 [54]. The growth process involves heating a catalyst

material to high temperatures in a tube furnace and flowing a hydrocarbon gas through the tube reactor for a period of time. Materials grown over the catalyst are collected upon cooling the system to room temperature. The key parameters in nanotube CVD growth are the hydrocarbons, catalysts and growth temperature. The active catalytic species are typically transition-metal nanoparticles.

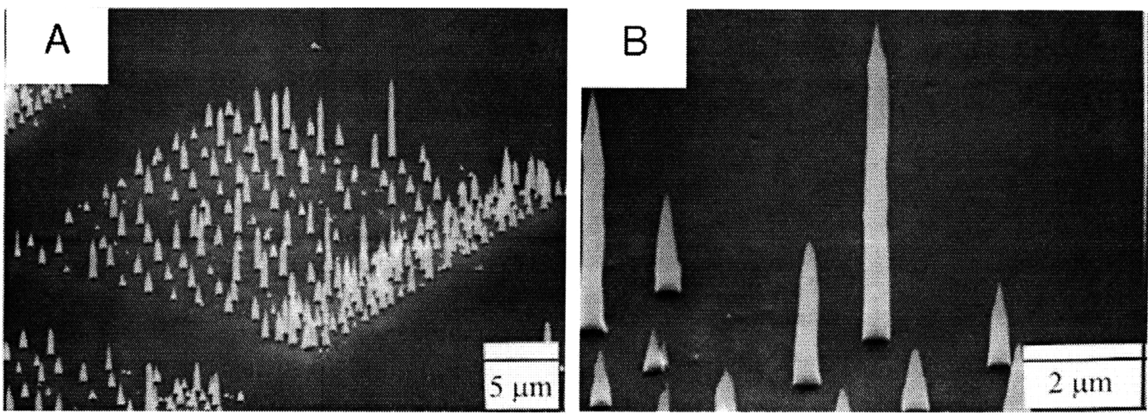

Figure 3.5 An array of aligned CNTs [63]: (A) An inclined view of one array pattern. (B) A magnified view along the edge of one pattern.

All of the methods presented in the above involve high growth temperature and lead to large variations in terms of sizes, locations, and orientations. Moreover, it is almost impossible to separate and handle the individual CNTs for their applications. Plasma enhanced chemical vapor deposition (PECVD) has received considerable attentions because of its capability to produce carpets of well vertically aligned MWNTs at a relatively low temperature with a high yield [62], however, no control of CNT placements was the main limitation of this technique. Recently, Z. F. Ren's group [63] demonstrated the growth of patterned individual CNTs with controlled location and

density. Transplanting assembly of the individual CNTs utilizes the potential of this method in growing the array of vertically aligned single strand CNTs.

The first step in transplanting assembly of the individual CNTs is to grow an array of vertically aligned single strand CNTs at the predefined locations. This chapter presents the experimental results and discussions on forming form an array of catalytic dots and grow an array of CNTs from those dots by plasma enhanced chemical vapor deposition (PECVD). The improvement of the PECVD machine for stable plasma and a uniform temperature on the anode is described, and CNT growth results are summarized.

The step of growing vertically aligned CNTs is summarized in Figure 3.6. An array of catalytic dots is seeded at the predefined locations. Each catalytic dot results in a single strand CNT, so an array of freestanding CNTs is grown.

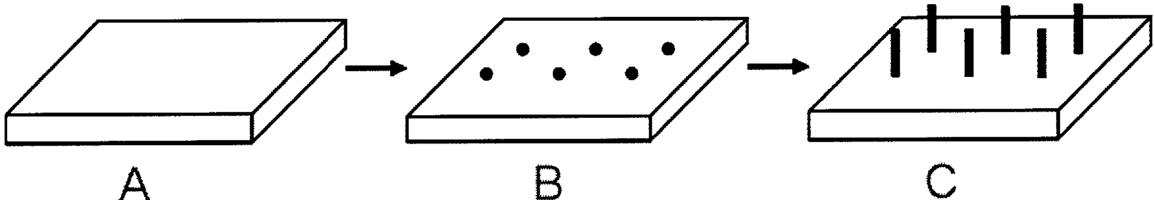

Figure 3.6 Procedures in growing an array of vertically aligned CNTs: (A) A substrate. (B) An array of catalytic dots on the substrate. (C) An array of vertically aligned CNTs from the array of the catalysts.

This chapter presents the experimental results of forming an array of Ni catalytic dots using electron-beam lithography and thin metal deposition, and growing an array of vertically aligned single strand CNTs from those catalytic dots.

3.2 An array of nickel (Ni) catalytic nano dots

An array of Ni catalytic dots works as the seeds in growing single strand CNTs by PECVD, and they determine the diameters and locations of the individual CNTs. This section presents detailed procedure and results of forming an array of Ni catalytic dots at the predefined locations using electron-beam lithography, metal deposition and lift-off process.

- **Step 1: Deposition of a titanium (Ti) layer on a silicon (Si) substrate**

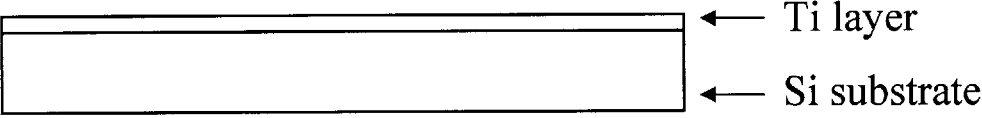

Figure 3.7 Ti layer deposition (25 nm thick) by electron beam evaporation.

A 25 nm thick Ti layer is deposited on a Si wafer using electron beam evaporation. Electron beam evaporation process enables accurate control over the thickness of deposited layers up to Å. This Ti layer promotes adhesion of the catalytic (Ni) layer to the substrate, and prevents the formation of Ni silicide ($NiSi_X$) during the growth step. If Ni catalysts are deposited directly on a Si substrate, Ni diffuses into Si to form $NiSi_X$ at temperatures above 450 C, resulting in poor growth yield. It is also known that the buffer layers help the formation of cylindrical CNTs [], and the reported thickness of the buffer layer (or diffusion barrier) varies from a few Å up to several hundred nm depending on

the process parameters, buffer layer materials and the size of Ni catalytic dots []. In our case, 25 nm thick Ti layer is thick enough to serve as a buffer layer in PECVD for Ni catalysts (150 nm in diameter and 30 nm in thickness).

- **Step 2: Spin-coating of a PMMA layer**

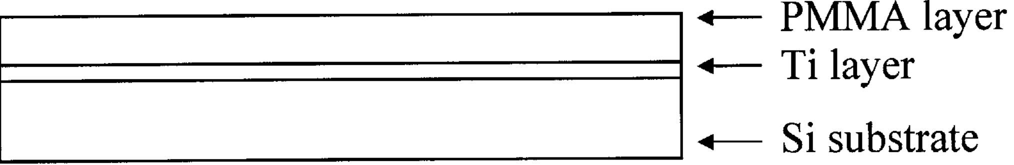

Figure 3.8 PMMA layer deposition.

A 75~100 nm thick polymethyl methacrylate (PMMA) layer is spin-coated on top of the Ti layer. The thickness of PMMA layer was determined by the depth of field of electron beam (~ 500 nm in general) and required layer thickness for lifting-off thin (30 nm for Ni films) metal films. PMMA positive resist is based on a special grade of polymethyl methacrylate designed to provide high contrast, high resolution for e-beam lithographic processes. 5ml of PMMA solution is dispensed statically on the substrate. The substrate is spinning at 500 rpm for 5 sec to spread the PMMA solution followed by spinning at 3000 rpm for 45 sec for a uniform layer of PMMA. Then the sample is prebaked on a hot plate at 180 °C for 5 min.

- **Step 3: Exposure and development of the PMMA layer**

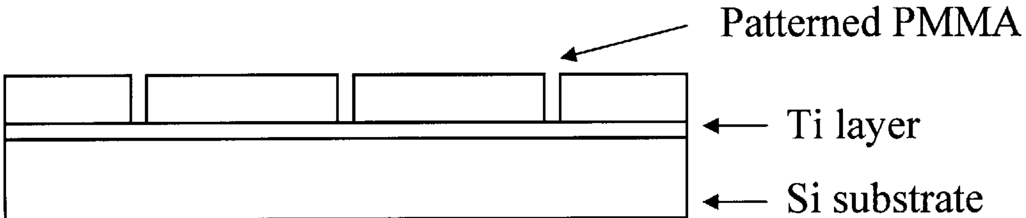

Figure 3.9 Pattern PMMA layer.

Patterns of small holes are formed by using a scanning electron-beam lithography system, Raith-150, followed by PMMA development with MIBK (methyl isobutyl ketone). The Raith 150 is a scanning electron microscope modified for e-beam lithography and has the operating voltage up to 30 keV. It has an acceleration voltage variable from 1-30 keV and an approximate beam diameter (for low currents) of 3 nm. The pattern generator can deflect the beam at the effective speed of about 1 MHz and can write 50~300 μm sized fields. The step size on this tool is fixed at 2 nm. This tool has written isolated lines as fine as 17 nm and gratings with a pitch smaller than 70 nm.

- **Step 4: Deposition catalytic material (Ni)**

After patterning holes on the PMMA layer, a 30 nm thick Ni layer is deposited using electron beam metal evaporator. The target thickness of Ni catalytic dots, 30 nm, in combination with the diameter of 150 nm was determined through the CNT growth

optimization in achieving the straight CNTs longer than 5 μm, and they were achieved through the optimization of process parameters.

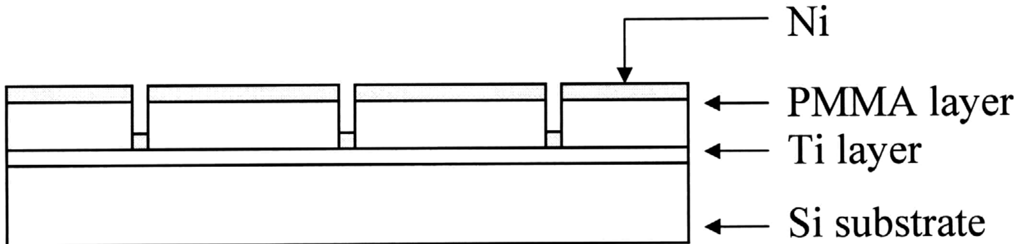

Figure 3.10 Ni layer deposition.

- **Step 5: Lift-off step**

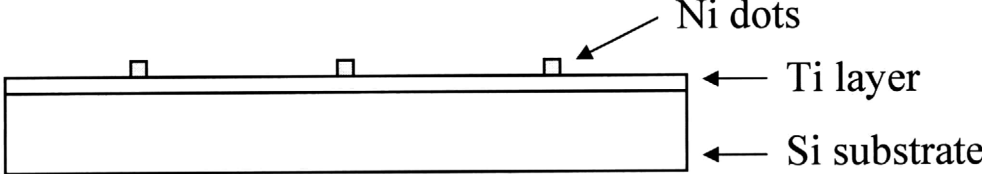

Figure 3.11 Ni layer lift-off.

The Ni layer is lift-off by removing the PMMA layer with NMP (1-methyl-2-pyrrolidinone). The Ni nano-dots fabricated by these process steps are shown in the Figure 3.12 in which all the dots are circular with the diameter of about 150 nm. The process parameters such as the exposure dose and the thickness of PMMA layers were optimized to achieve these experimental results.

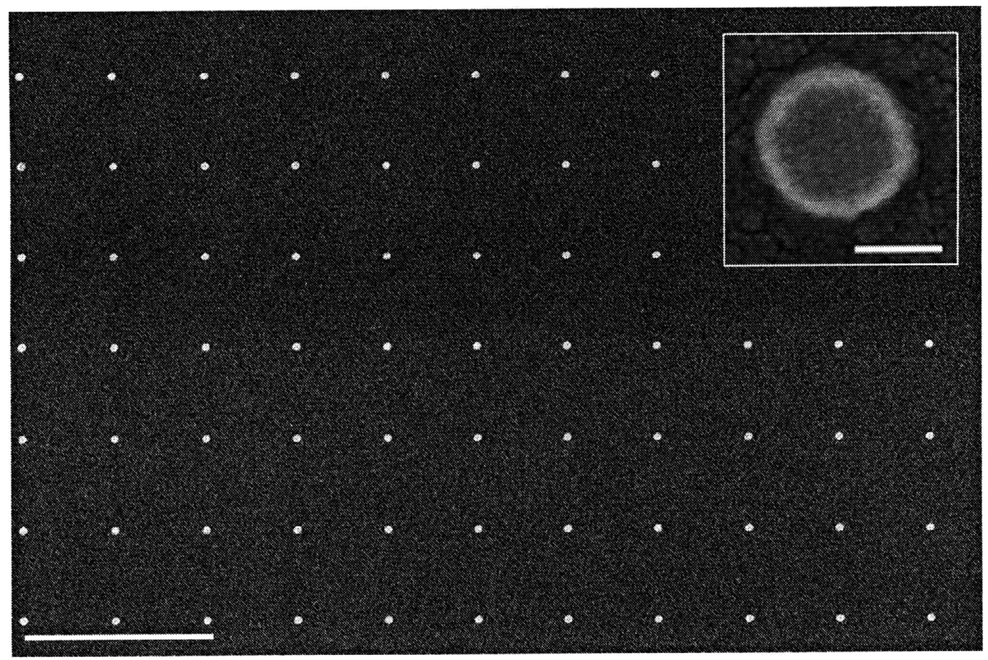

Figure 3.12 An array of Ni catalytic dots with 5 μm spacing (scale bar = 10 μm). The inset shows an enlarged view of a single Ni dot (scale bar = 100 nm).

3.3 CNT growth by PECVD

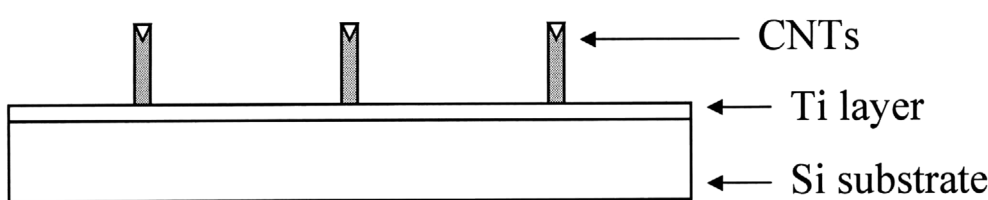

Figure 3.13 CNT growth.

As the final procedure in the CNT growth step, an array of vertically aligned single strand CNTs is grown from the array of Ni catalytic dots. Detailed procedures of the CNT growth by PECVD are described in the following chapters. This section describes the improvement of the PECVD machine for the stable plasma and a uniform temperature in order to grow straight CNTs with uniform diameters.

3.3.1 Plasma enhanced chemical vapor deposition (PECVD)

PECVD is widely used to obtain well-aligned multi-walled CNTs at the temperatures below 700 °C. The individual free standing CNTs are grown by PECVD, and they are key elements of transplanting assembly with defined locations and orientations. The essential component used in a PECVD system is its electric field (plasma). The electric fields across the electrodes induce the dipole moment in catalysts guiding the alignment of each CNT during the growth process.

Among various plasma sources for CNT growth available, we use a DC plasma method. The dc plasma reactor consists of a pair of electrodes in a grounded chamber, and one electrode is grounded while the other is connected to a power supply. The negative dc bias voltage applied to one electrode on the sample side (cathode) dissociates the feedstock gas (C_2H_2) and generates many carbon-bearing radicals for carbon nanotube growth.

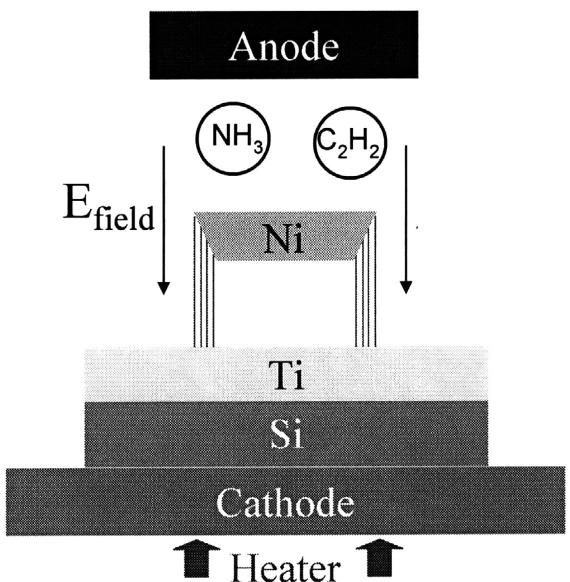

Figure 3.14 Schematic of CNT growth by PECVD. A negative DC voltage is applied to the cathode while the anode is grounded.

3.3.2 The PECVD machine of MIT

A PECVD machine for CNT growth has been developed by Micro & Nano systems laboratory (MNSL) of MIT as shown in Figure 3.15 [2, 3]. The machine consists of 5

main parts: the vacuum chamber, the plasma controller, the vacuum controller, the temperature controller, and the gas flow controller.

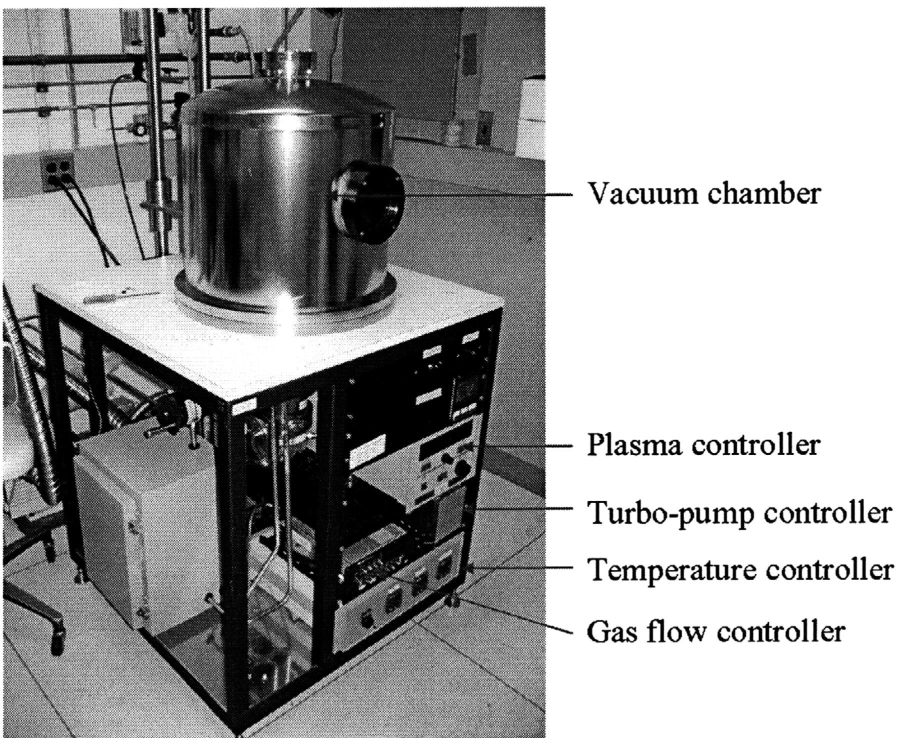

Figure 3.15 The PECVD machine for CNT growth in Microsystems Technology Laboratories (MTL) of MIT.

The roles of NH_3 plasma during the CNT growth are 1) to guide the direction of CNT growth by DC electric fields, 2) to etch the amorphous carbons, and 3) to supply additional heating for the CNT growth. Therefore, the stable plasma with uniform heating is an essential requirement for successful CNT growth by PECVD.

Inside the vacuum chamber, there are a ceramic heater and thermocouples, an anode and a cathode, gas (C_2H_2 and NH_3) suppliers, and holders (Figure 3.16). 4 ceramic posts

(Figure 3.17) support the metal heater holder (Figure 3.18). The ceramic holder sits on the metal heater holder and two thermocouples (Figure 3.19), and the cathode (Figure 3.20) is placed on top of the ceramic holder. The temperature of the heater is controlled by measuring that of the bottom of the heater using two thermocouples.

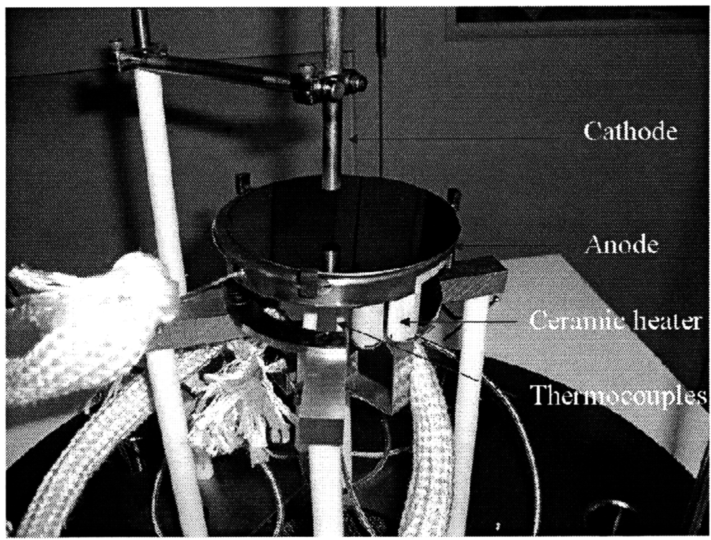

Figure 3.16 Assembled main parts of the PECVD machine.

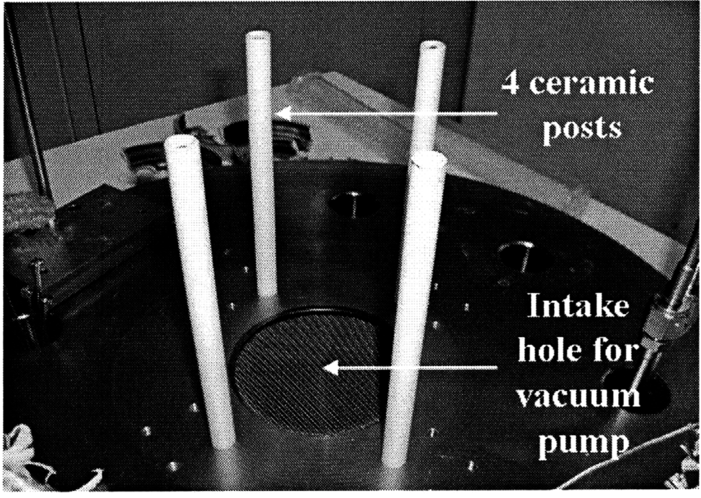

Figure 3.17 Ceramic posts to support the heater holder.

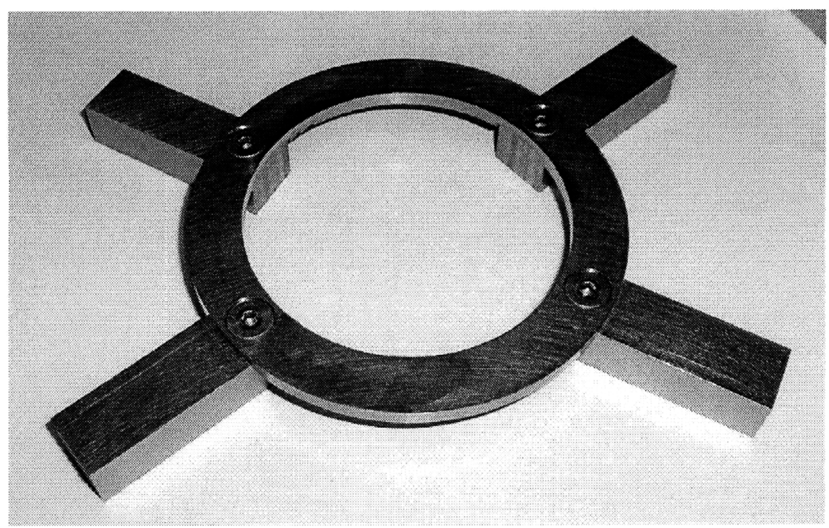

Figure 3.18 Metal heater holder. Holes in four legs match four ceramic posts shown in Figure 3.17.

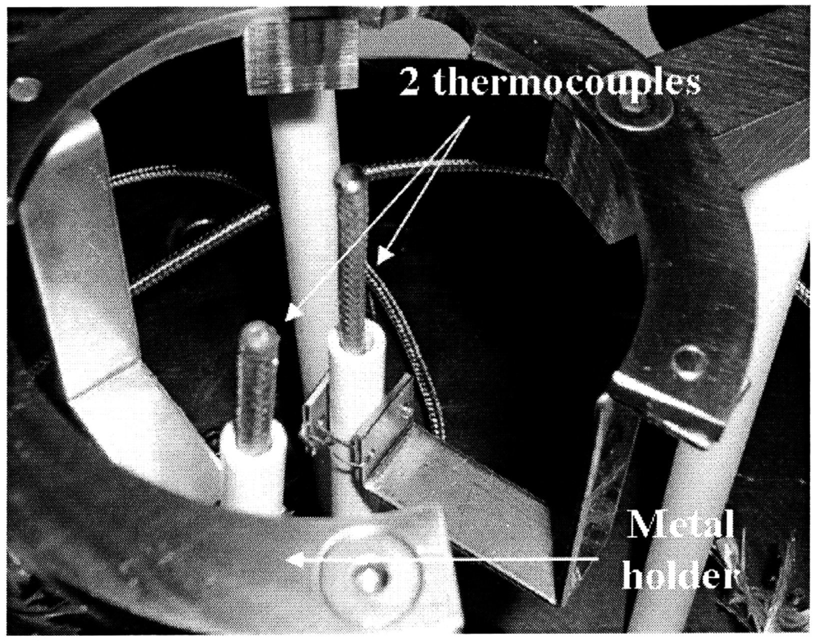

Figure 3.19 A pair of thermocouples that measure the temperature of the bottom of the ceramic heater.

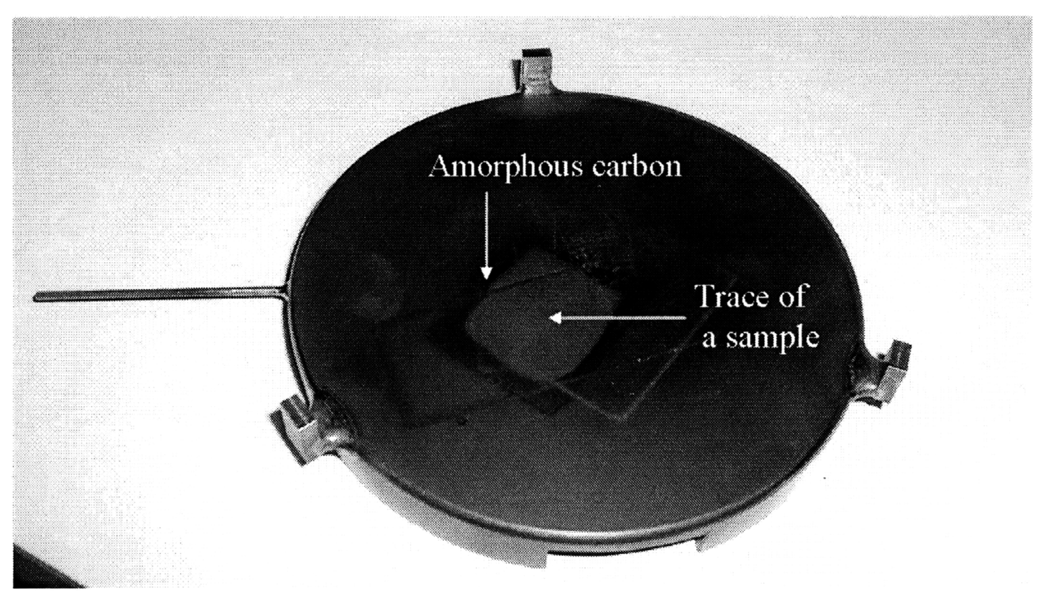

Figure 3.20 Cathode made of Ti. This will sit on the ceramic heater. There are traces of amorphous carbon deposition on top of the cathode.

Table 3.1 The CNT growth procedure.

1	the plasma chamber pressure goes down to 1×10^{-6} Torr using both a rotary pump (down to 3 Torr) and a turbo molecular pump.
2	the cathode is heated by the ceramic heater up to 580°C
3	NH_3 is applied for 7 min at the rate of 160 sccm until the pressure inside the chamber reaches 8 Torr
4	C_2H_2 is applied for 1 min at the rate of 45 sccm
5	plasma is on by applying a negative dc bias voltage (-500V) to the cathode
6	Control the pressure to 8 Torr for 10~20min during the CNT growth

The sample (an array of Ni catalytic dots on Si substrates) is placed on top of the cathode for CNT growths, and the PECVD procedures for CNT growth are listed in Table 3.1.

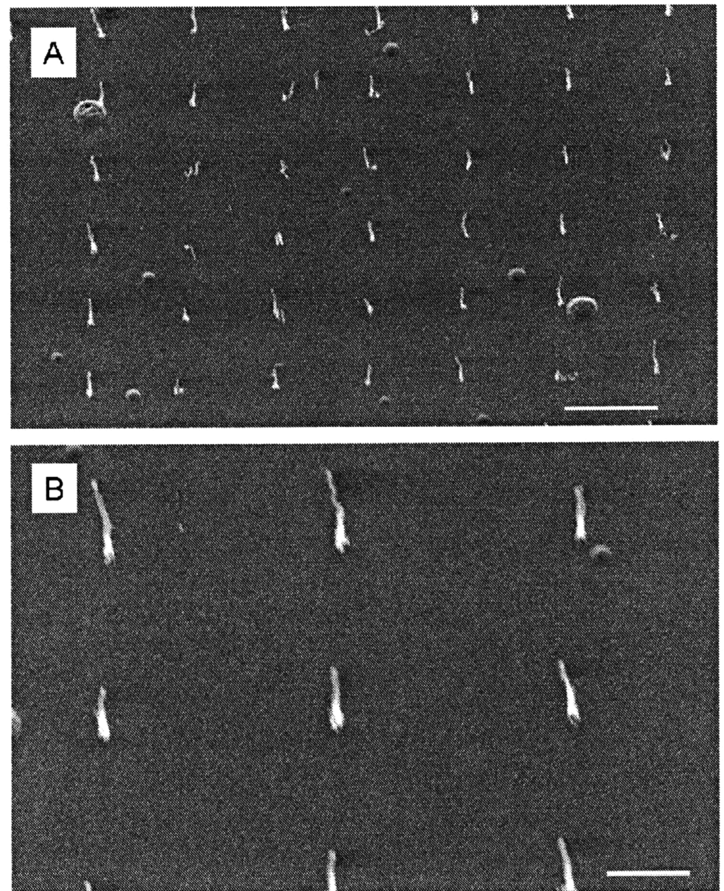

Figure 3.21 The results of CNT growth: (a) An array of CNTs with 5μm spacing. (b) An enlarged view of the CNT array (scale bar = 2 μm).

The previous PECVD machine has a metal holder to support the ceramic heater, and it causes unstable plasma due to repeated carbon deposition resulting in the unstable plasma, and the heater circuits can be electrically short from the electrical contact between the metal holder and the circuits. The previous cathode is vulnerable to thermal

deformations, so it results in a non-uniform heating on top of the cathode. These factors resulted in bad CNT growth results as shown in Figure 3.21. It can be seen that 1) CNT growth results have large variations in terms of the yield and geometries (diameter and length) of CNTs, 2) most of the CNTs have a conical shape, and 3) CNTs are not straight (kinked structures).

3.3.3 PECVD machine modification for stable plasma and uniform heating

The first modification of the PECVD machine is to shield the metal holder with ceramic fabric tubes as shown in Figure 3.22. The main purpose of shielding the metal holder with (electrically) insulating tubes is to prevent the current leakage from the anode to the metal holder. The negative voltage (-500 V) is applied to the cathode, and the electrical potential difference between the cathode and the anode (grounded: 0 V) is the key factor in forming a plasma across them. Any current leakages from the cathode to the places other than the anode cause the drop in the potential across the cathode and anode, resulting in less energy (or lower temperature), uneven etching and less alignment for the CNT growth due to unstable plasma. Although it can prevent the current leakage through the metal holder, repeated PECVD processes deposited carbons on the tubes, and it causes the electrical shortage finally, resulting in unstable plasma as described in the above. Additionally, particles of the ceramic tubes may contaminate the inside of the vacuum chamber, and the ceramic heater is not mechanically fixed still.

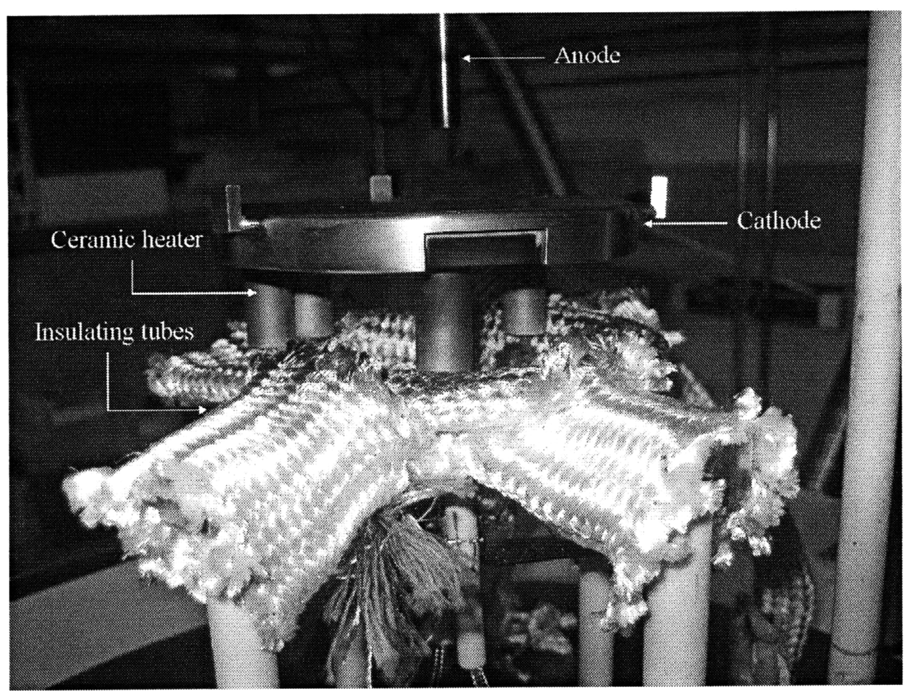

Figure 3.22 Improvement 1 – shielded metal holder with ceramic fabric tubes. The fabric tubes require replacement after 4~5 CNT growth experiments.

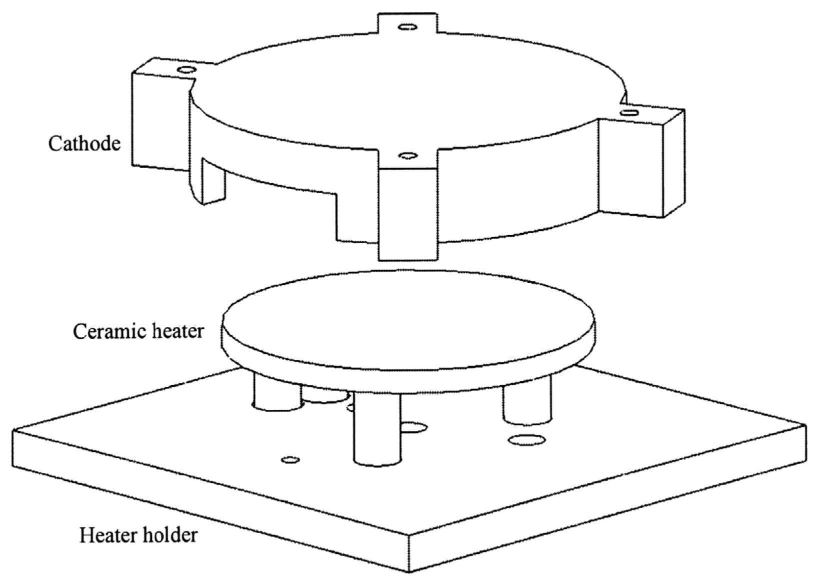

Figure 3.23 An exploded view of a modified design.

A new heater holder is designed to prevent any current leakages and hold the ceramic heater securely. The heater holder is made of alumina silicate ceramics, and the material shows high temperature insulation up to 1000°C. It can be easily machined using carbide tools, and the mechanical strength and hardness are increased after being fully fired. The heater holder is supported by 4 ceramic posts, and the ceramic heater is assembled on top of the heater holder using screws. The cathode is machined from a Ti plate, and its side ribs add mechanical rigidity to minimize thermal distortions. The new design and fabrication of the cathode and the heater holder, and the plasma state are shown in Figure 3.24.

The results of CNT growth with the modified PECVD machine are shown in Figure 3.25 and Figure 3.26. With stable plasma, uniform temperature, and optimized process parameters, the grown CNTs have higher yield, uniform diameter and length up to 5μm, and straight and clean outer surface. The yield and variation in the diameter, length, and orientation of the grown CNTs need to be measured quantitatively to confirm the process capability of the CNT growth process by PECVD, which should be pursued in the future.

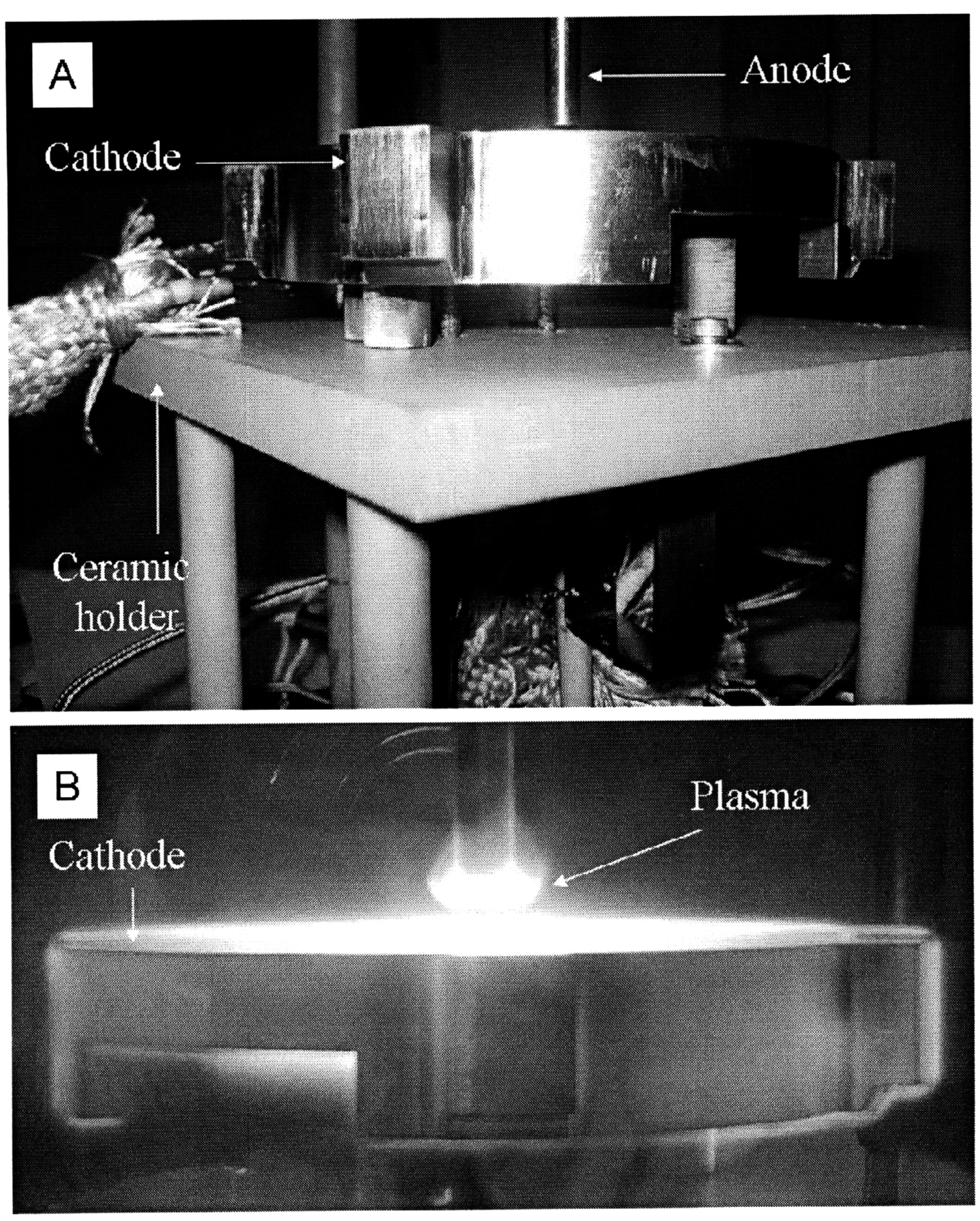

Figure 3.24 The improved CNT machine and stable plasma: (A) The modified CNT machine for stable plasma and uniform temperature. (B) Stable plasma after modification.

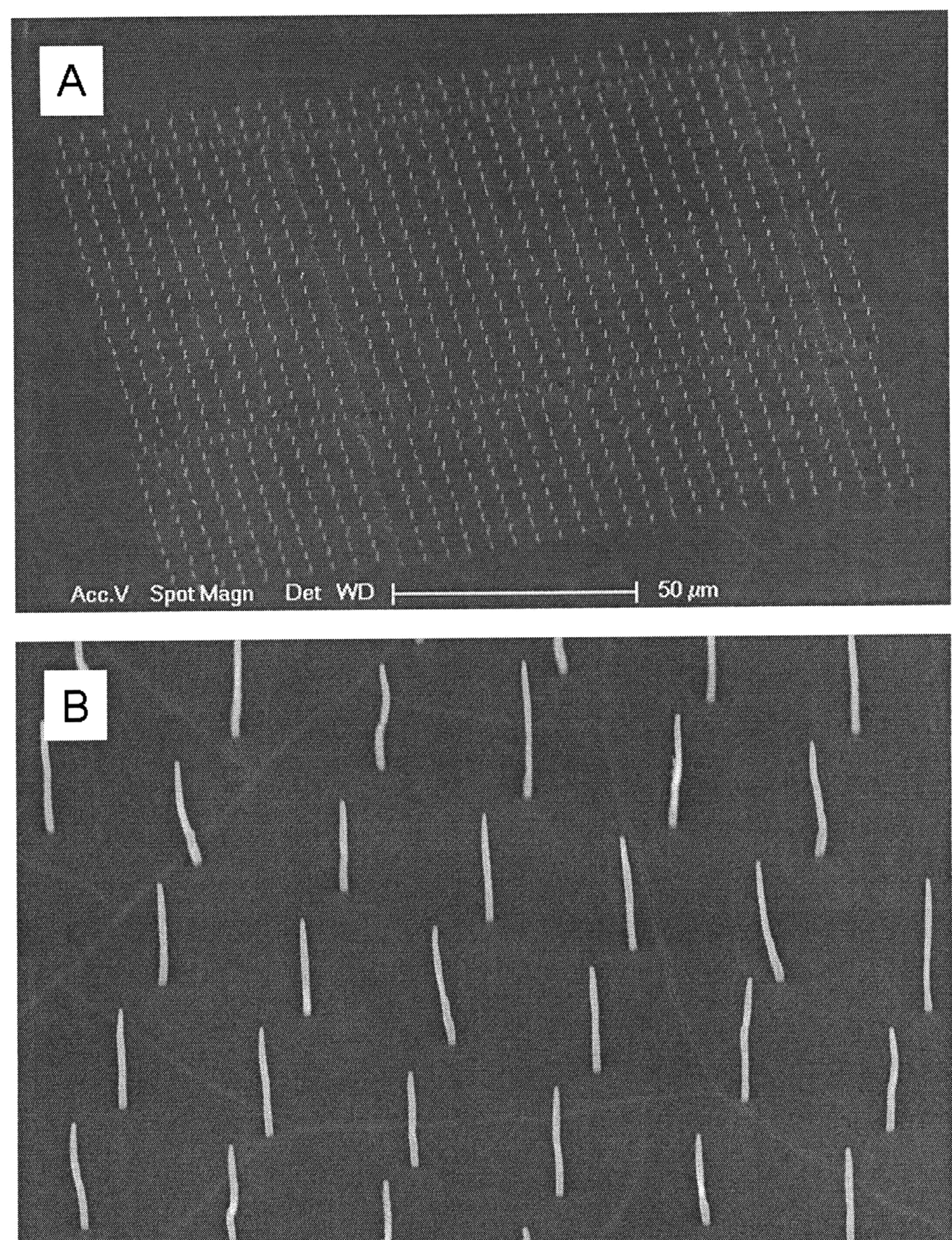

Figure 3.25 (A) An array of vertically aligned single strand CNTs. (B) Enlarged view of a part of (A).

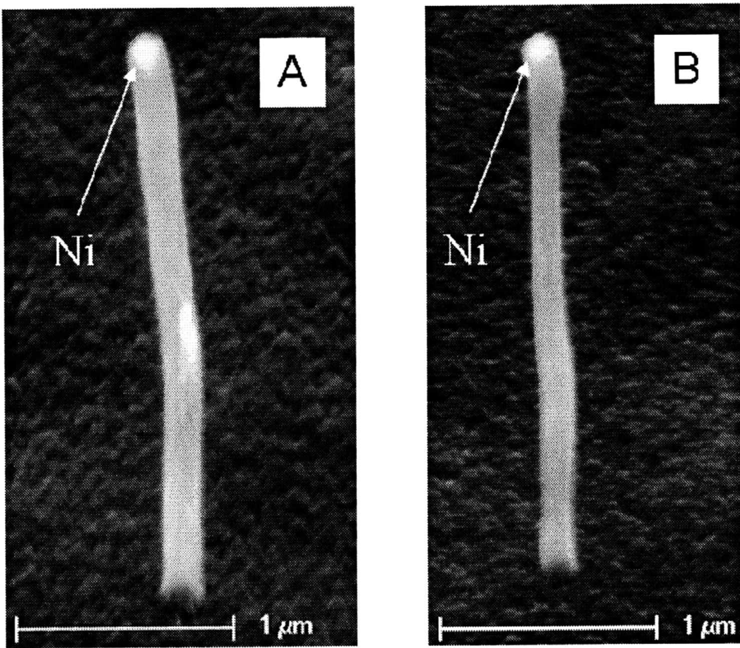

Figure 3.26 The results of CNT growth with the modified PECVD machine. (Enlarged view of the single CNTs).

Internal structures of CNTs are characterized using TEM as shown in Figures 3.27-3.29. It can be seen that Ni catalyst has a shape of cone, it is wrapped with thin graphite layers, and the CNT body consists of 3 layers: central, intermediate, and outer layers, central and intermediate layers represent a bamboo-like structure, and outer layer consists of multiple graphite layers.

High contrast TEM (JEOL 2011: a quality general-purpose microscope with a point-to-point resolution of 0.25 nm, equipped with a 6Mpix digital camera) at 200 kV is used to characterize the overall wall structures of the CNTs (Figure 3.27 and Figure 3.28). Dispersing the CNTs in a solvent and dropping the solvent on a TEM is a general way to prepare the CNT samples for TEM characterization. However, direct transfer of the CNTs from the substrate to a TEM grid was used in this case in order to remove the

interaction of CNTs with the solvent. For high resolution TEM shown in Figure 3.29, JEOL 2110 was used because of its ultimate point-to-point resolution of 0.19 nm in order to resolve the individual graphene layers.

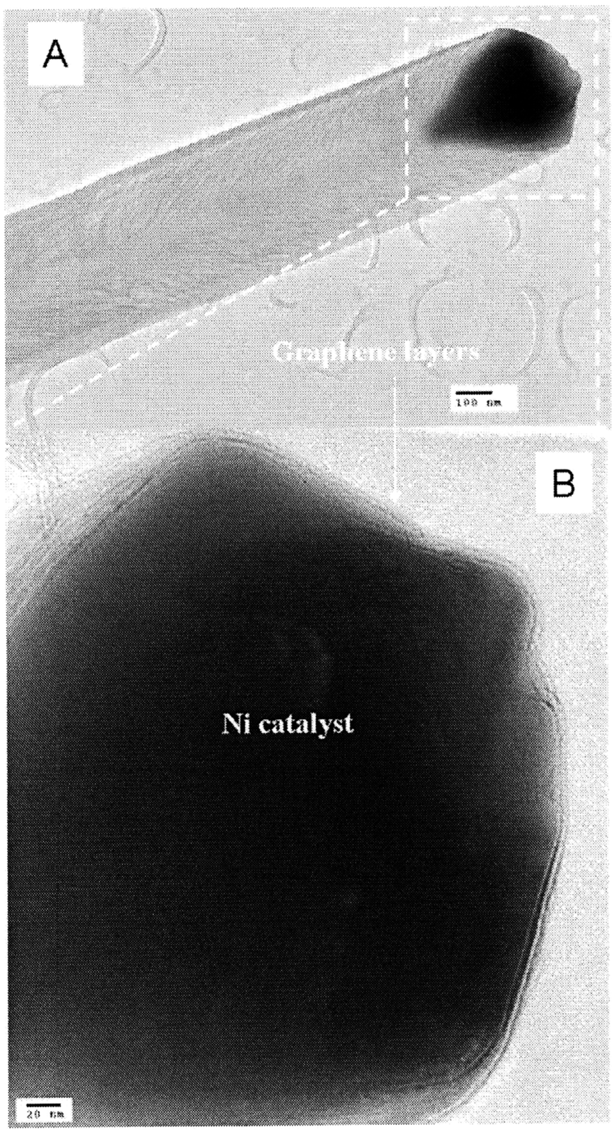

Figure 3.27 (A) TEM of a tip part of a CNT. (B) An enlarged view of the Ni catalyst. The Ni catalyst is capsulated by multiple graphene layers.

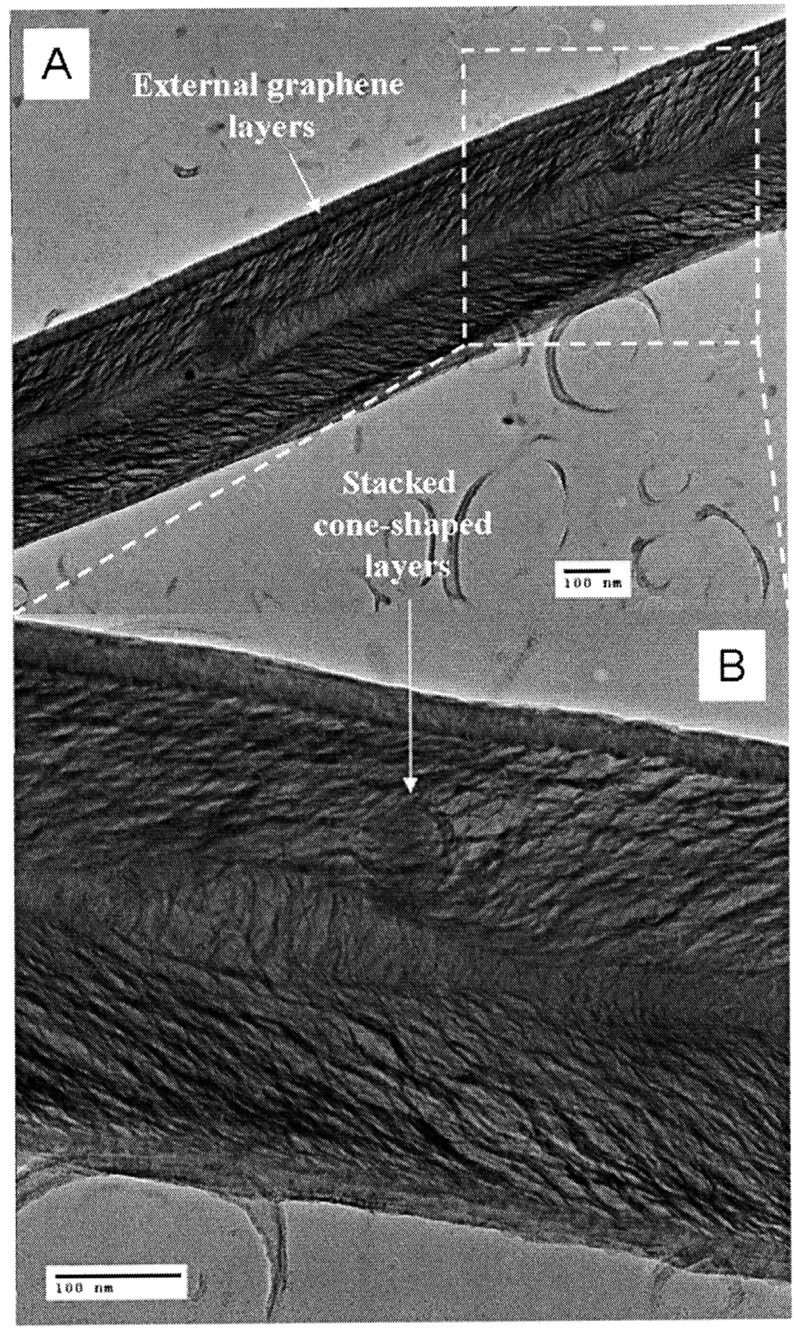

Figure 3.28 (A) TEM of a body part of a CNT. (B) An enlarged view of (A). It consists of three parts: the external graphene layers, the (intermediate) stacked cone-shaped layers, and the central layers.

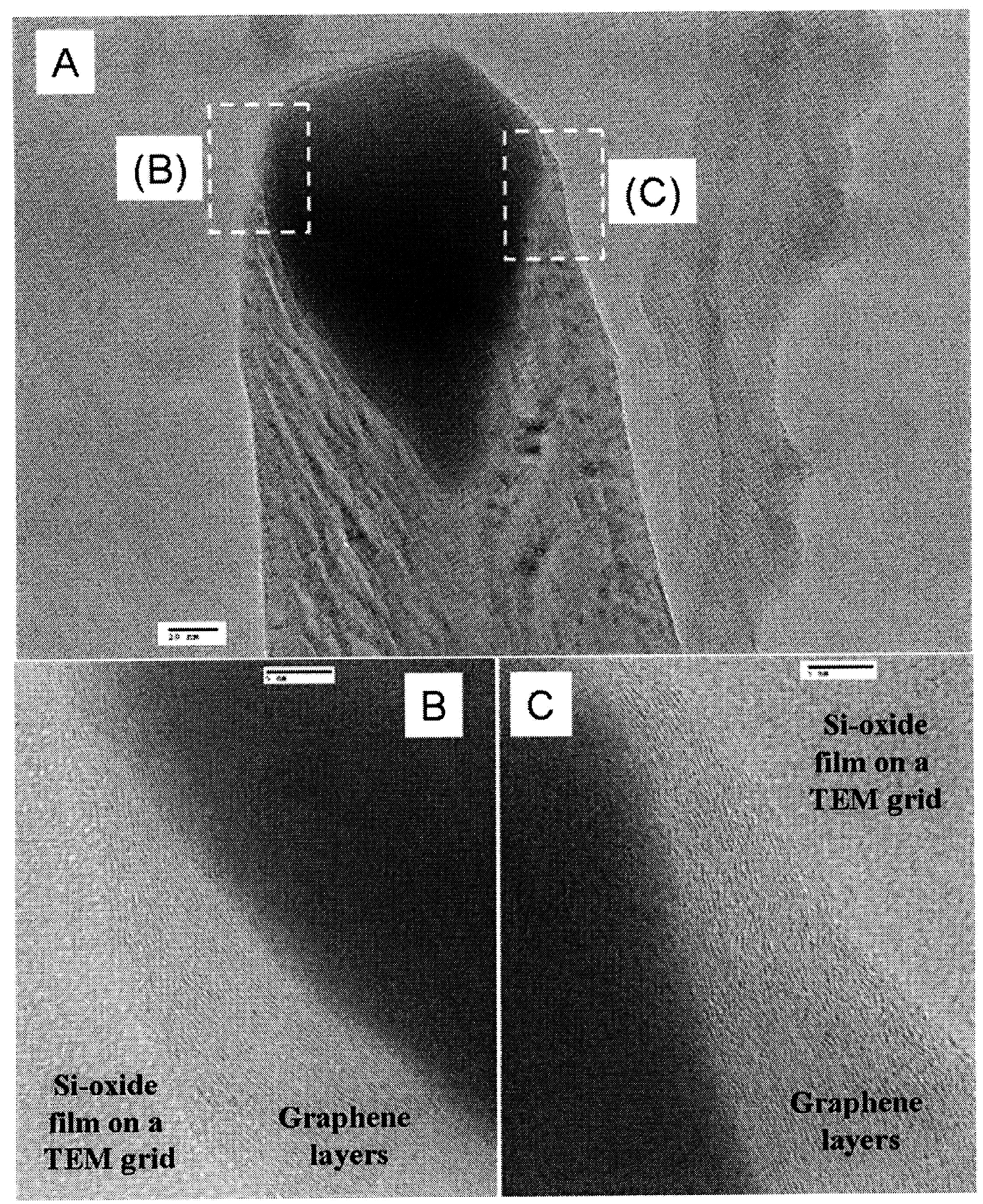

Figure 3.29 (A) HRTEM of the graphene layers near the Ni catalyst. (B, C) Each graphene layer is resolved with HRTEM, and the layers are parallel to the surface of the catalyst.

3.4 Summary

As the first step in transplanting assembly of the individual CNTs, an array of vertically aligned CNTs was grown from an array of Ni catalytic dots at the predefined locations on a Si wafer by direct-writing electron-beam and thin metal lift-off process. The spacing (40 μm) and location (21 by 21 array) of catalytic dots were chosen so that the grown CNTs can be implemented with photolithography process in the subsequent encapsulation step. A home-built PECVD machine has been improved for stable plasma and uniform temperature distributions over the substrate on the cathode to yield straighter CNTs with more uniform cylindrical shape. TEM show that the grown CNTs have stacked cone-shaped internal layers parallel to the outer surface of NI catalytic dots, and they are encapsulated with the external graphene layers.

4 Integration of the individual CNTs into micro-scale carriers

4.1 Introduction: encapsulation procedure

As the second major step in transplanting assembly of the individual CNTs, the individual CNTs are encapsulated into microelectromechanical systems (MEMS) carriers so that each MEMS carrier contains a single CNT. This chapter presents the main issues involved in the encapsulation step, and the design approaches and fabrication results to address the issues.

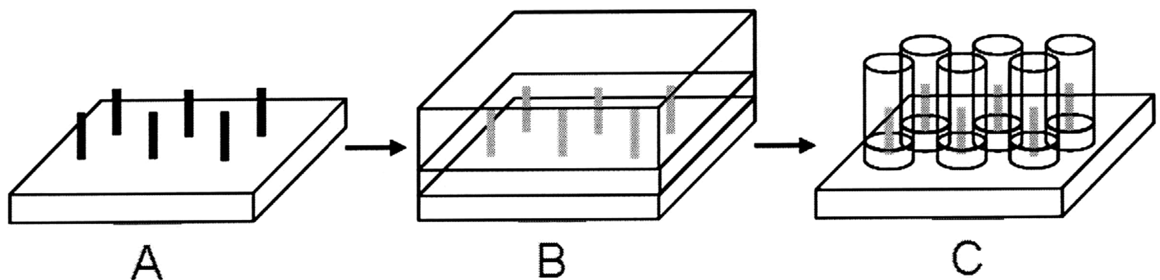

Figure 4.1 Encapsulation procedures: an array of CNTs (A) is embedded in two polymer layers (B), and the layers are patterned using photolithography (C).

This chapter presents the experimental results of encapsulating each grown CNT into the individual polymer blocks. The integrity of CNTs will be compared before and after the encapsulation steps using HRTEM and Raman spectroscopy.

4.2 Experimental results of encapsulation procedure

Table 4.1 Procedures in fabricating a CNT-tipped AFM probe by transplanting a single CNT.

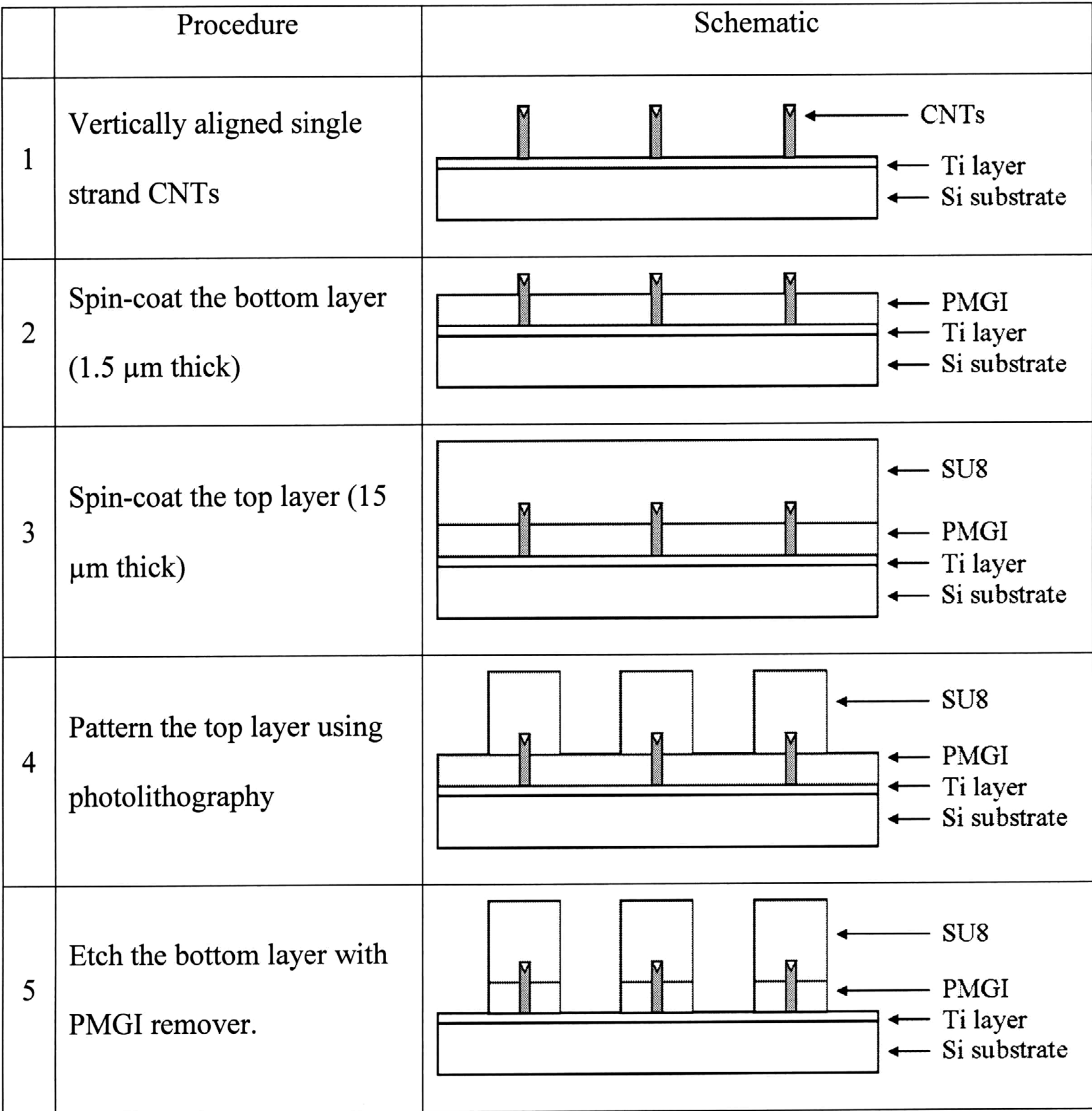

	Procedure	Schematic
1	Vertically aligned single strand CNTs	CNTs; Ti layer; Si substrate
2	Spin-coat the bottom layer (1.5 μm thick)	PMGI; Ti layer; Si substrate
3	Spin-coat the top layer (15 μm thick)	SU8; PMGI; Ti layer; Si substrate
4	Pattern the top layer using photolithography	SU8; PMGI; Ti layer; Si substrate
5	Etch the bottom layer with PMGI remover.	SU8; PMGI; Ti layer; Si substrate

The procedure in encapsulating each CNT into individual blocks is described in Table 4.1.

- **Step 1: Growth of an array of vertically aligned CNTs**

An array of vertically aligned CNTs is grown from the catalytic dots at the predefined locations by PECVD as described in chapter 3. Each CNT is 5-10 μm long, and the spacing between CNTs is 40 μm.

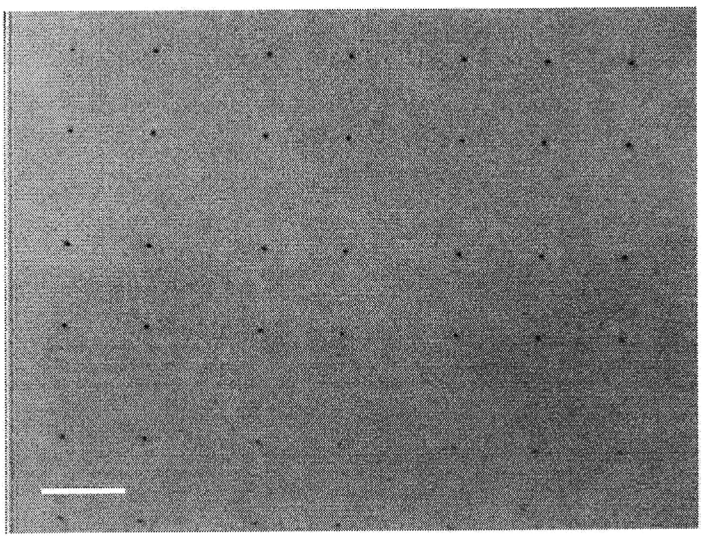

Figure 4.2 An array of CNTs (optical microscopy, top view). An array of small dark dots represents an array of vertical CNTs (scale bar = 40 μm)

Figure 4.2 shows an optical microscope image of an array of CNTs. Although each CNT is seen blurry with optical microscopy, the existence and the location of the individual CNTs can be monitored. Figure 4.3 shows an SEM image of an array of CNTs. The inset represents a high resolution SEM image of a CNT, and this SEM characterization provides the information on the diameter, length, and orientation of the individual CNTs. The cracks present at the Ti layer on the substrate are due to thermal expansion during the heating procedure.

Figure 4.4 shows an optical microscope image of the Si substrate after CNT growth step. There are two different sized marks made of gold or copper on the substrate, and

they will be used to align the mask and the samples for photolithography at the different magnifications.

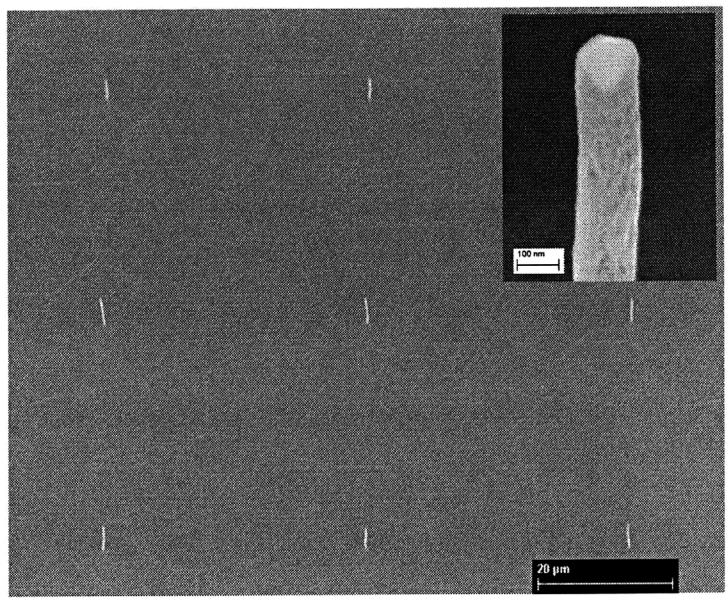

Figure 4.3 An array of CNTs (scanning electron microscopy, tilted by 30°). The inset shows an enlarged view of one single CNT.

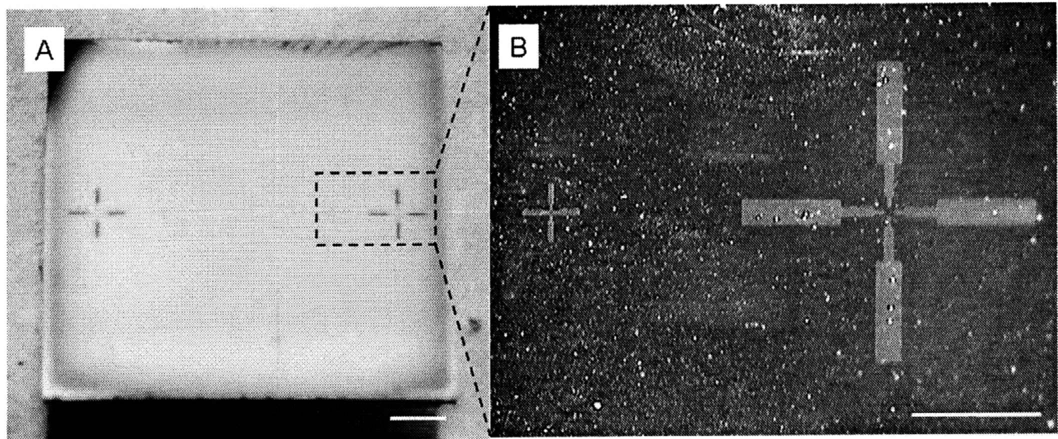

Figure 4.4 (A) An optical microscopy image of the sample after the CNT growth step (scale bar = 2 mm). (B) An enlarged view of mask alignment marks (scale bar = 1 mm).

- **Step 2: Coating of the bottom (PMGI SF 11) layer over the array of CNTs**

5 ml of PMGI SF 11 solution is statically dispensed over the array of CNTs on the substrate. The SU8 spinner is spinning at 3000 rpm for 45 sec to reach the thickness of the bottom layer to 1.5μm. Then the sample is baked on the hot plate at 200 °C for 5 min.

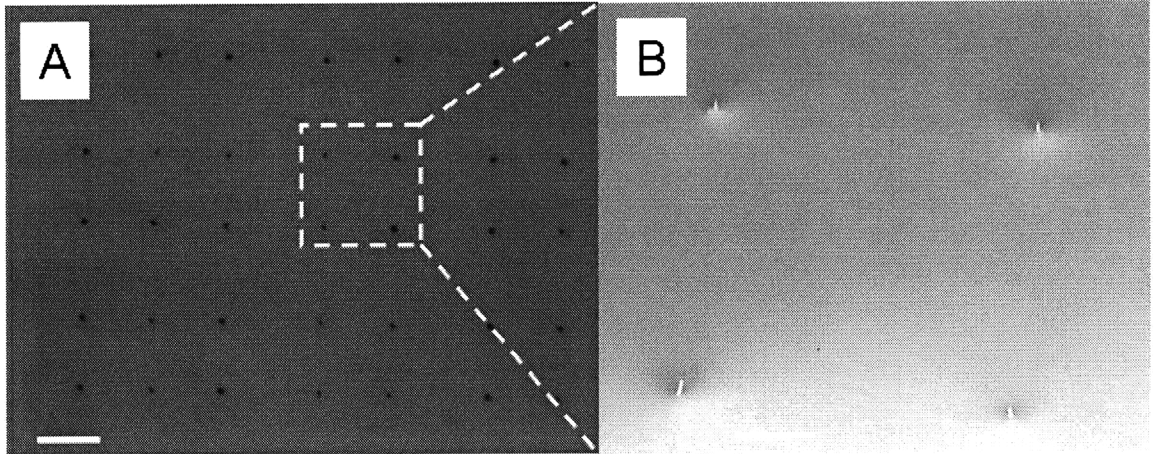

Figure 4.5 An array of CNTs after spin-coating of the bottom (PMGI SF 11) layer; (A) Image by optical microscopy (scale bar = 40 μm). (B) Image by SEM (scale bar = 10 μm).

- **Step 3: Coating of the top (SU8-2015) layer**

After the bottom layer is coated, 10ml of SU8-2015 solution is statically dispensed over the bottom layer and the array of CNTs. The sample is spinning 3000 rpm for 30 sec in order to reach the thickness of 20 μm, and is baked on the hot plate at 95 °C for 4min. Then the sample is cured at the room temperature for 24hours before edge removal procedure. As the whole CNTs are covered with SU8, they are hardly seen using an optical microscope.

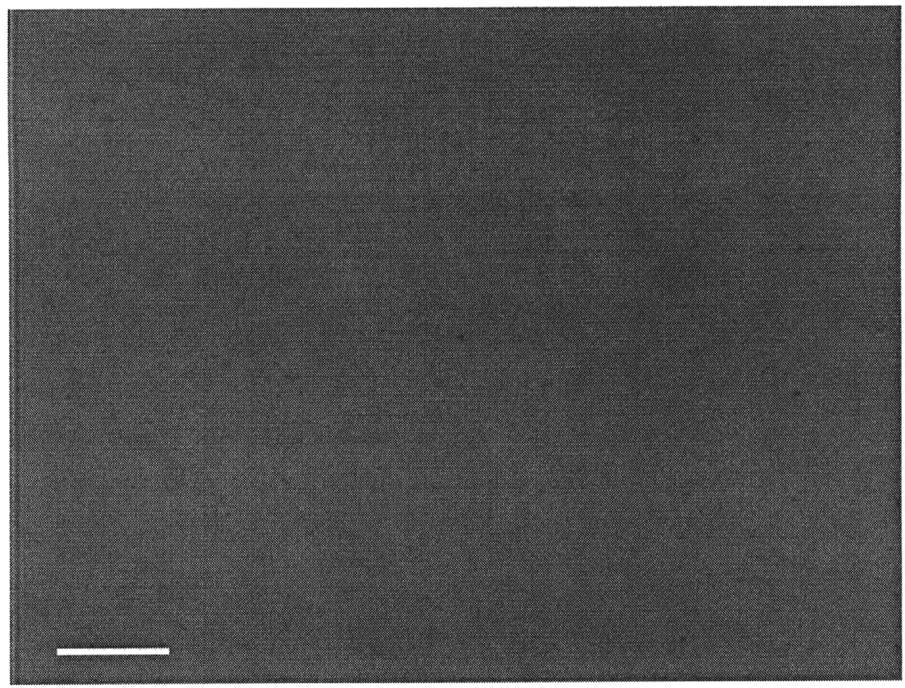

Figure 4.6 An array of CNTs after spin-coating of the top (SU8-2015) layer. An array of CNTs can hardly be seen due to thick top and bottom layers (scale bar = 40 μm).

- **Step 4: Patterning of the top (SU8-2015) layer**

The top, SU8-2015, layer is patterned to form an array of cylinders, and the patterned SU8 pellets are 20 μm in diameter and contain only one CNT inside pellets. Before the exposure step, the side edge of SU8-2015 layer need to be removed to provide a better contact (soft or hard) between the mask and the top layer. Due to the small size of the substrate, 15 by 15 mm, small amount of the edge beads results in poor exposures due to a gap between the SU8 layer and the mask. The cured sample at the room temperature for 24 hours is placed on a flat surface. The edge beads on the side of the sample are removed manually with a developer of SU8-2015 (PM Acetate) on a cotton swab.

After the edge beads are removed, the sample is placed at the room temperature for 30min to ensure that the top SU8 layer is dried fully before the exposure step. Then the sample is mounted on the sample holder of the KSAligner (Karl Suss). The sample is aligned to a Cr mask using alignment marks on both the sample and the Cr mask, and exposed for 180 seconds under a hard contact condition. After exposure step, the sample is hard-baked at 95 °C on the hot plate for 5 min. Once the sample is hard baked, the circular patterns on the SU8 layer are visible as in Figure 4.8. The patterned array of SU8 carriers is formed after development process with PM Acetate for 90 sec followed by rinsing in DI water for 60 sec.

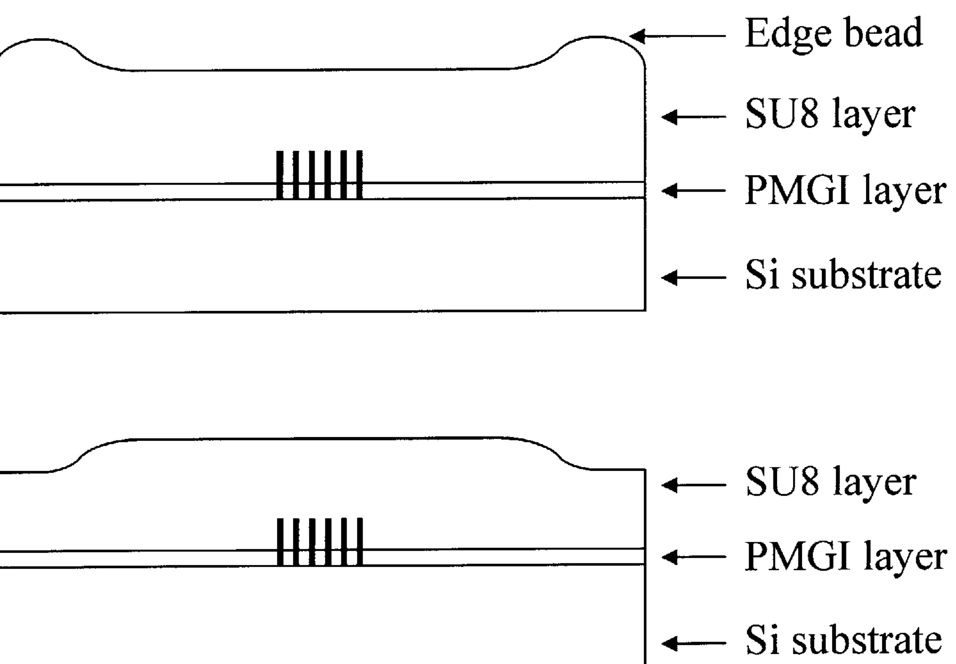

Figure 4.7 A schematic of the edge bead removal procedure. (A) Before the edge bead removal step. (B) After the edge bead removal step.

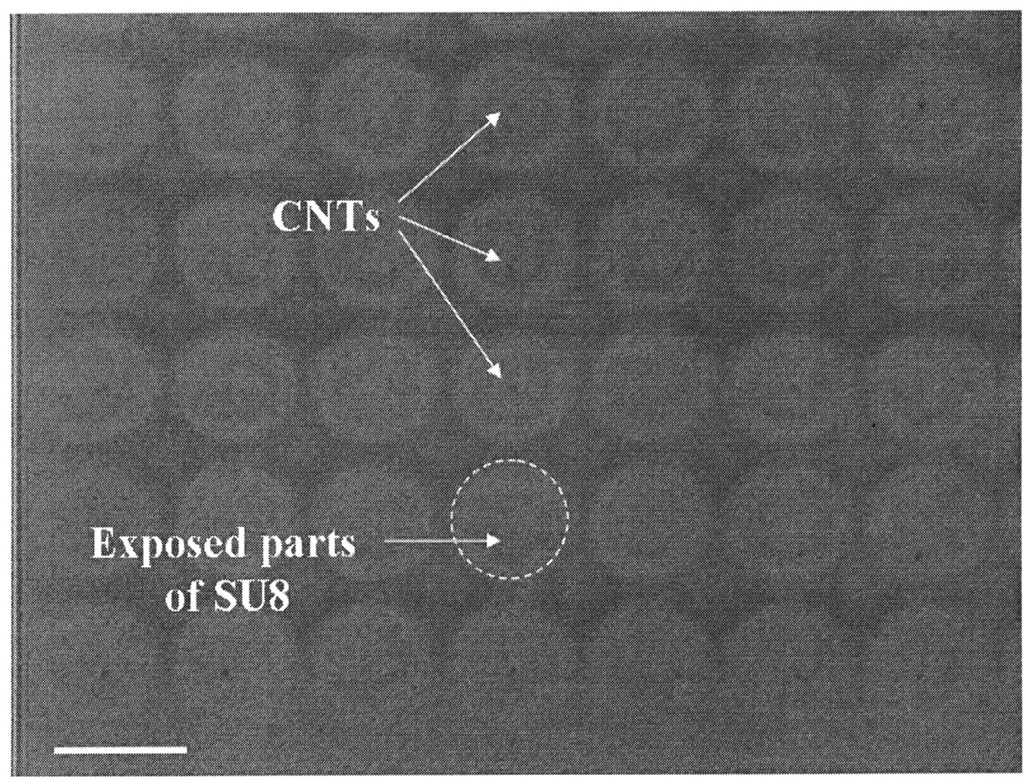

Figure 4.8 An optical microscope image of the top (SU8-2015) layer after the exposure and hard-bake procedure (scale bar = 40 μm).

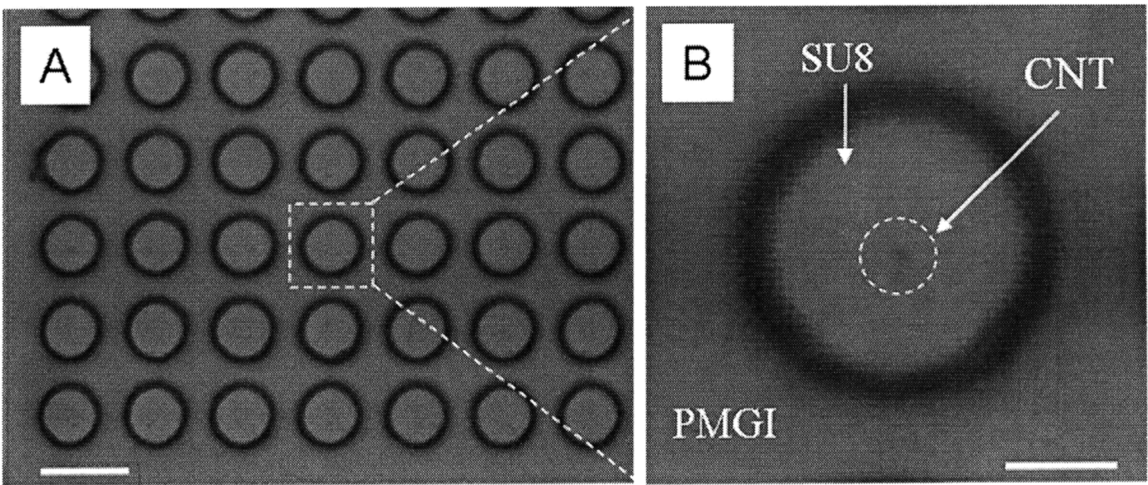

Figure 4.9 (A) An array of SU8 pellets (scale bar = 40 μm). (B) A single CNT is located at the center of the pellet (scale bar = 10 μm).

- **Step 5: Etching of the bottom (PMGI SF 11) layer**

The bottom (PMGI SF 11) layer was etched using PMGI 101 developer (MicroChem, Newton, MA) with the top patterned SU8 pellets as etch masks. The PMGI 101 developer is a tetraethylammonium hydroxide (TEAH)-based positive radiation resist developer , and it exhibits etch selectivity to PMGI over novolac imaging resists such as SU8 [64, 65]. This selectivity enables development of PMGI films independent of an overlying resist layer, and can be used for enhanced undercut in bilayer lift-off processes.

For easier assembly, the bottom (PMGI) layer was etched further until the adhesion between the top (SU8) and the bottom (PMGI) layers are smaller than the adhesion between the top (Su8) and the Si cantilever while the orientation of the SU pellet with the single CNT remains vertical, so the orientation of the CNT can be preserved during the assembly step. The detailed assembly methods will be described in the chapter 5.

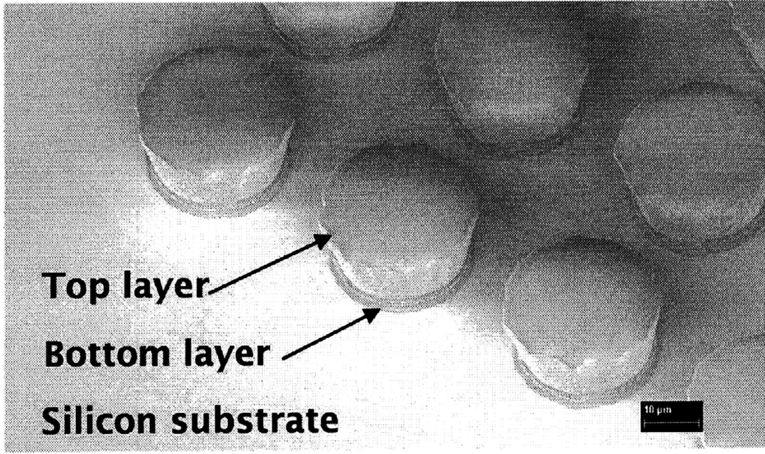

Figure 4.10 An array of MEMS carriers (scanning electron microscopy).

Figure 4.10 shows an array of MEMS carriers on a Si substrate. Each SU8 block carries the single CNT inside. The existence and the location of the single CNT inside MEMS carriers can be monitored using an optical microscope as shown in Figure 4.11.

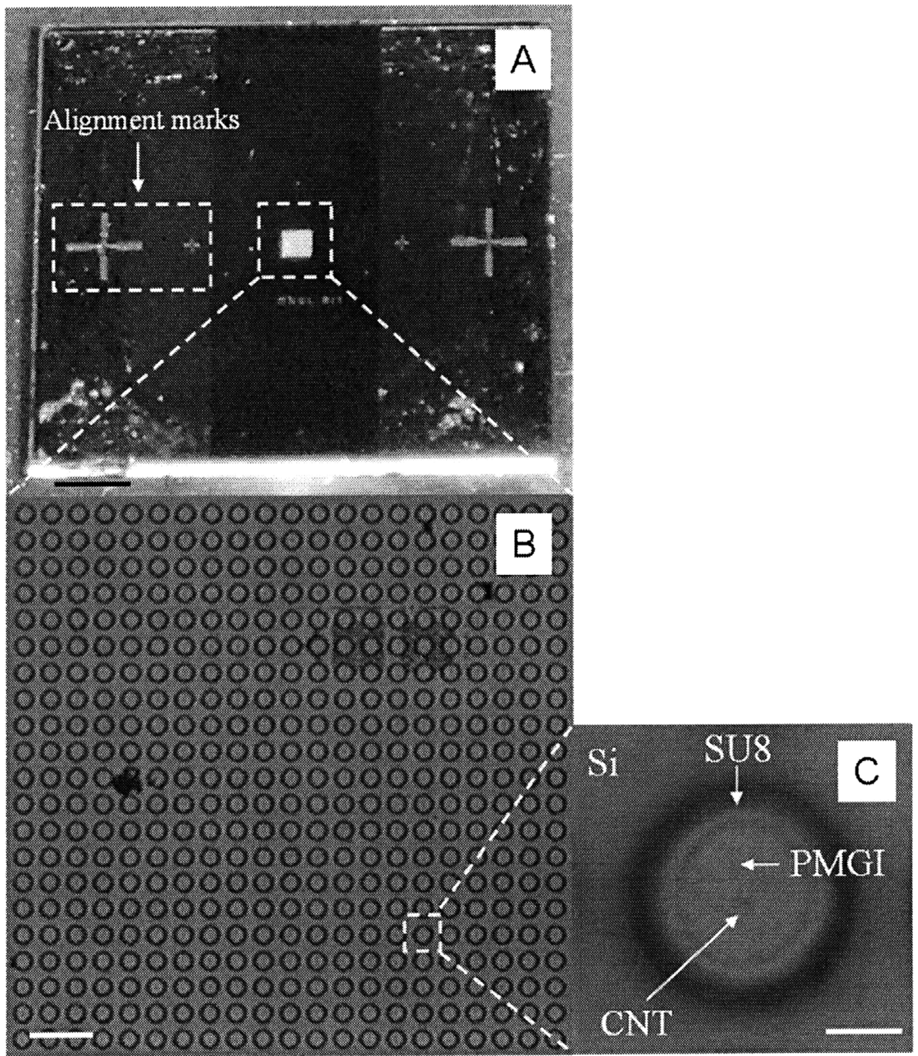

Figure 4.11 (A) An optical microscope image of the sample after encapsulation and bottom layer etching processes (scale bar = 2 mm). (B) An array of MEMS carriers (scale bar = 100 μm). (C) A CNT located at the center of the carrier (scale = 10 μm).

4.2.1 Release of the CNTs from the substrate

Figure 4.17 shows the single CNT with the MEMS carrier. Etching the bottom layer release the CNT with SU8-2015 carrier from the substrate. Part of which is encapsulated in the SU8 block is released from the substrate when the bottom layer is further etched from the previous step. The exposed CNT tip, located at the center of the MEMS carrier, is parallel to the axis of the MEMS carrier, and the CNT tip is about 1.5μm long, which is equivalent to the thickness of bottom layers.

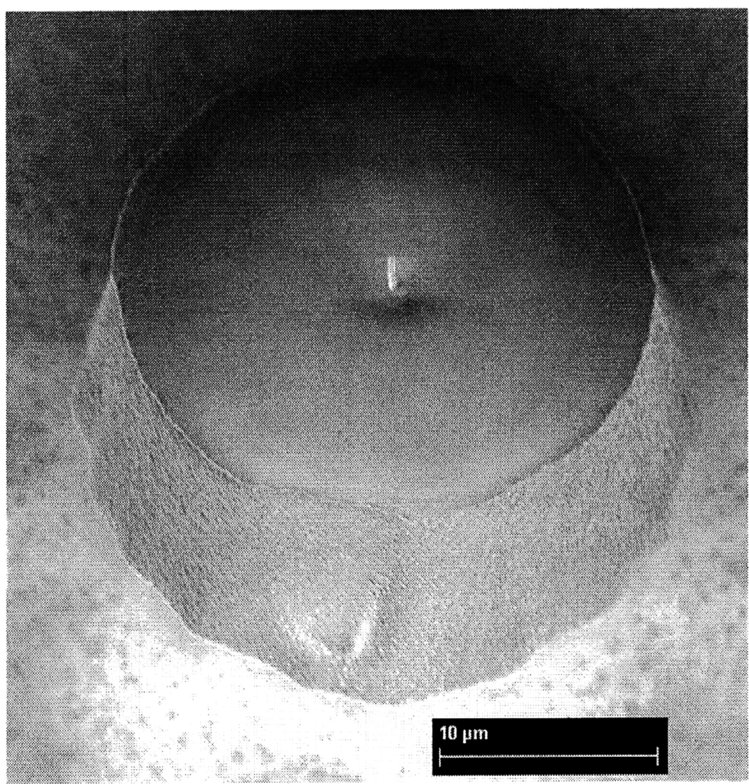

Figure 4.12 A released SU8 block with a single CNT.

4.3 Characterization of the structural integrity of CNTs

Physicochemical interactions of individual CNTs with encapsulating polymers and etchants are investigated to verify whether the pristine properties of CNTs after the growth step can be preserved during the encapsulation step. The encapsulation step involves multiple heating, coating, and etching processes. Additionally, shrinkage of the polymers may influence the external graphene layers resulting in degraded mechanical and chemical properties of CNTs. The integrity of the CNTs is characterized using high resolution TEM and Raman spectroscopy to compare the wall structures and the qualities before and after the encapsulation step.

4.3.1 High resolution transmission electron microscopy

General methods for TEM sample preparations include dispersing multiple CNTs in a solvent such as acetone and isopropyl alcohol, and embedding CNTs into a resin mold followed by slicing with a microtome. These methods may influence the integrity of the CNTs during the sample preparation step, so CNTs are attached to a TEM grid by a direct attach method. An array of CNTs goes through the encapsulation step, and both top and bottom layers are totally removed using removers. A TEM sample grid that consists of a copper grid and thin lacey carbon film is pressed on an array of CNTs. Shearing the sample grid releases the CNTs from the substrate, and Van der Waals force attaches the individual CNTs to the carbon film.

Figure 4.13 shows a TEM image of a single CNT on a TEM sample grid. The CNT consists of the internal graphene layers parallel to the plane of the Ni catalysts, and the outer layers encapsulating the Ni catalysts and the internal graphene layers. Figure 4.14 and Figure 4.15 show HRTEM of the CNT close to the Ni catalyst and its body part respectively. In Figure 4.16, the graphene layers near the Ni catalyst are parallel to the catalyst surface, and their spacing is 0.34 nm. The external graphene layers are compared with those of a CNT before the encapsulating step. The spacing between the graphene layers is 0.34 nm in both CNT samples.

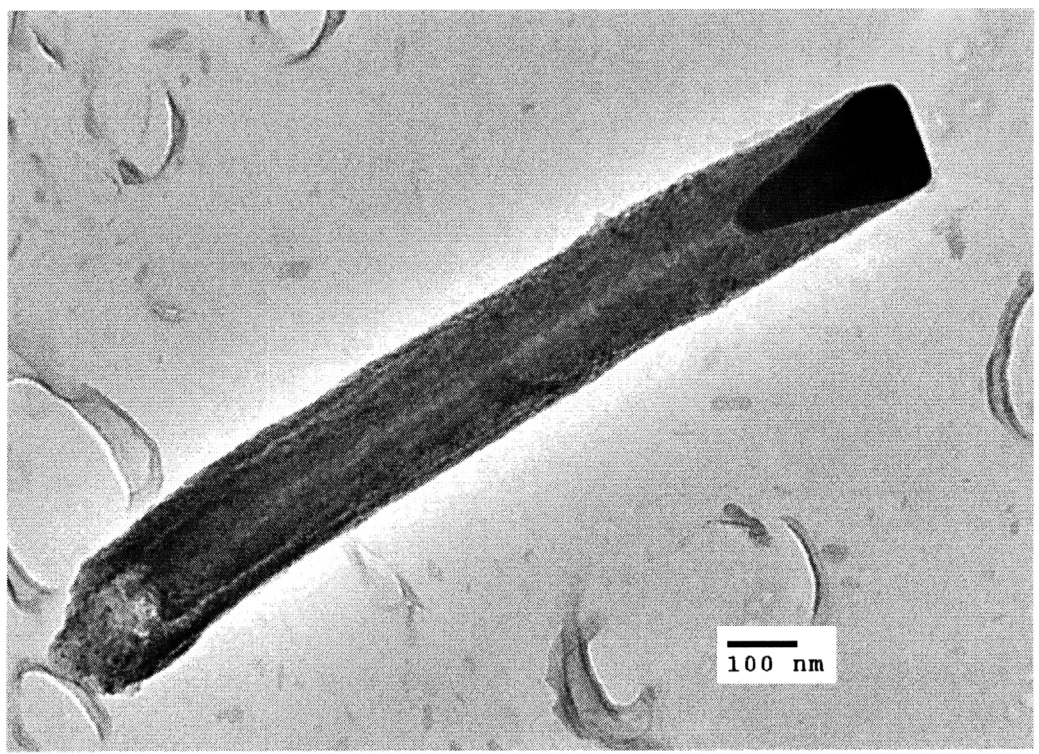

Figure 4.13 TEM of a CNT after encapsulation steps.

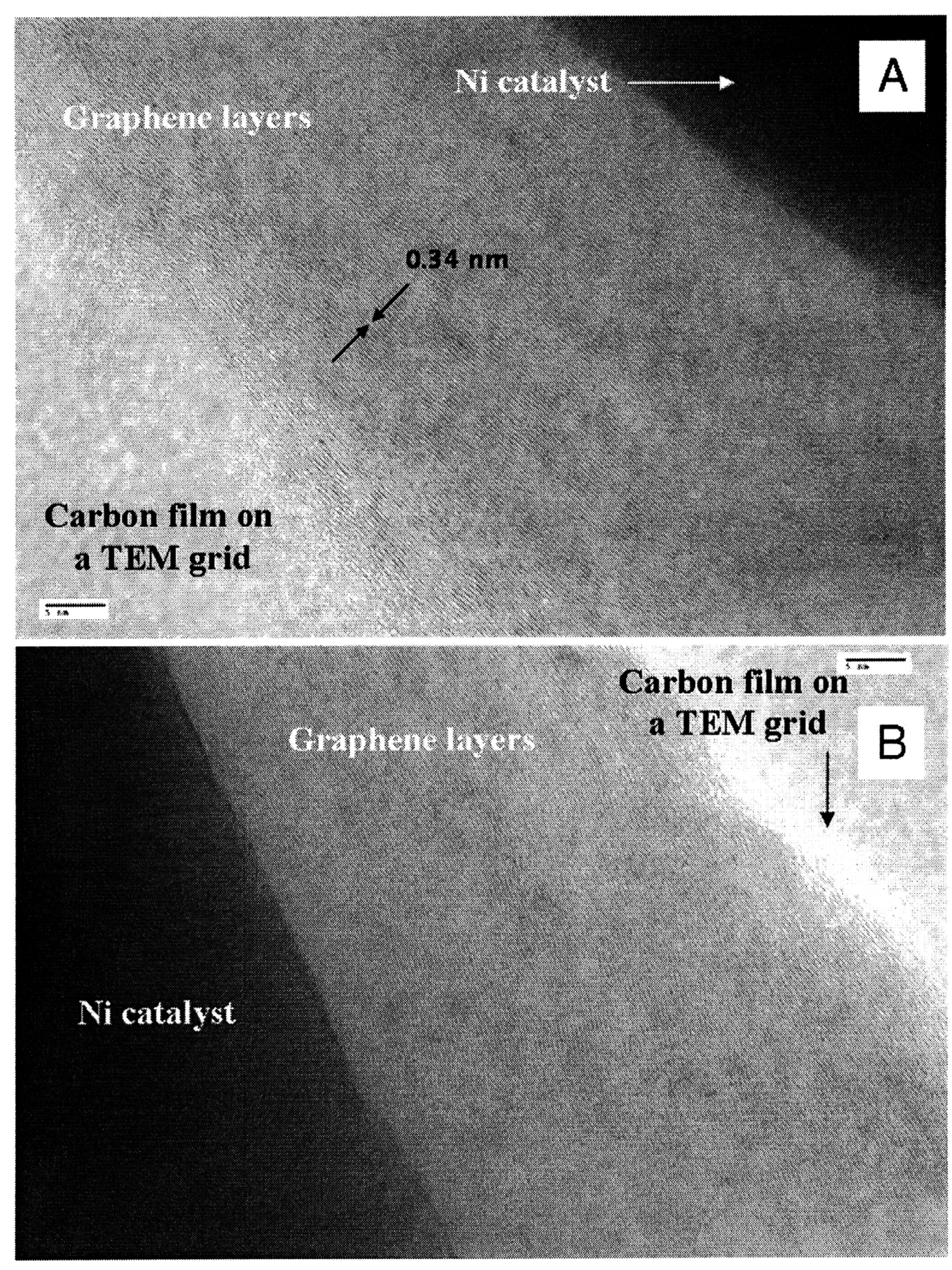

Figure 4.14 HRTEM (JEOL 2011) of a CNT (close to the Ni catalyst). (A) and (B) show the graphene layers near the both sides of a Ni catalyst. In the region close to the catalyst, the graphene layers are parallel to the surface of the Ni catalyst. The external graphene layers are parallel to the CNT axis. The spacing between the graphene layers is 0.34 nm.

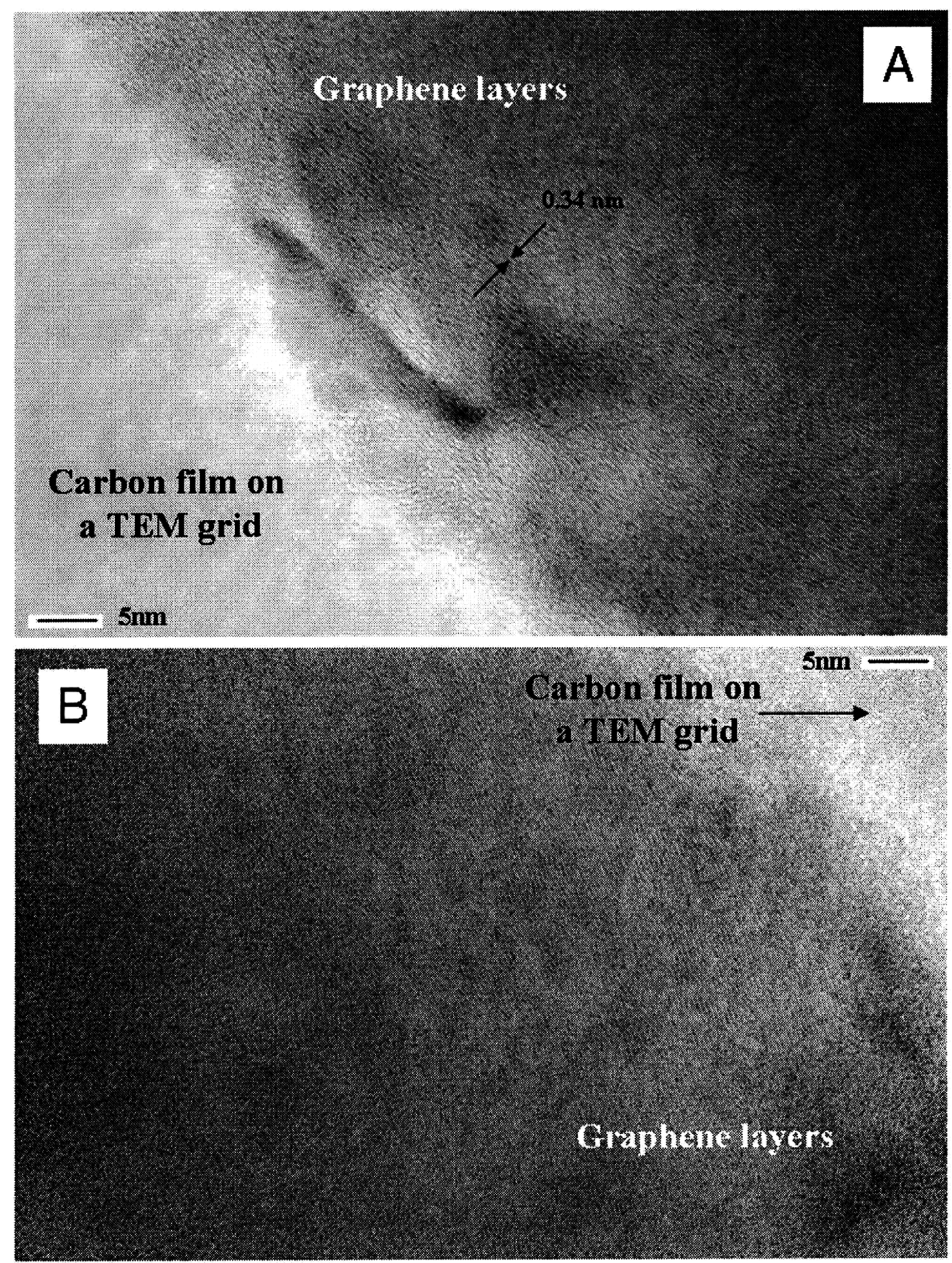

Figure 4.15 HRTEM (JEOL 2011) of a CNT (body). (A) and (B) show the graphene layers on the both sides of a CNT body part. The graphene layers are parallel to the CNT axis with disordered external layers. The spacing between the graphene layers is 0.34 nm.

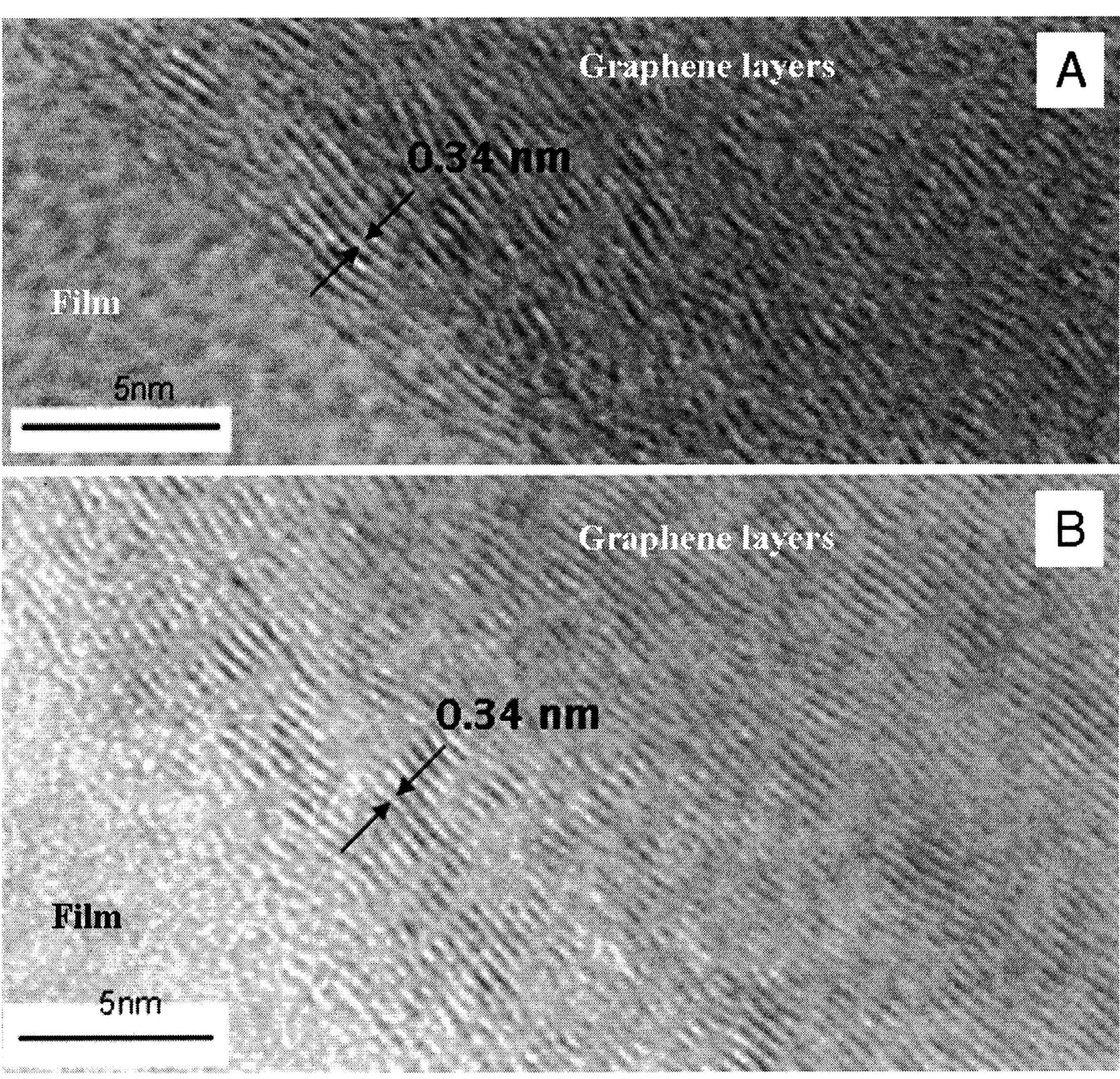

Figure 4.16 Comparison of the graphene layers before and after the encapsulation step using HRTEM (JEOL 2010): Before (A) and after (B) the encapsulation step. It can be seen that there are no noticeable increases of the defects in external graphene layers.

4.3.2 Raman spectroscopy

Raman spectroscopy provides more quantitative comparison of the qualities of CNTs before and after the encapsulation step. The Raman spectrometer, Kaiser Hololab 5000R, was used with a microprobe is used to characterize the CNT samples at the room temperature in the air. Two CNT samples have been prepared: one right after CNT growth process, and the other after growth and encapsulation process. One sample is loaded on the translation stage under optical microscopes. The target CNTs are located inside the circular cursor in the view window, and Raman signals are integrated after the exciting laser is applied to the target CNTs. The frequency of excitation laser is 785 nm, and the acquisition time is set to 40 min for noticeable peaks in the Raman spectra.

In the Raman spectra, it is the locations (the Raman shift) and the shape of the peaks in the Raman spectra that need to be compared. In characterization of MWNTs or carbon nanofibers using Raman spectroscopy, D band (around $1310cm^{-1}$) and G band (around $1600cm^{-1}$) are important: D-band represents the disorder or defect of CNTs, and G-band represent the graphene layers, and the ratio of intensity of the two bands, I_G/I_D, represents the quality of purity of the CNTs.

Figure 4.17 compares Raman spectra of CNTs before and after the encapsulation step. The spectra of CNTs before and after encapsulation show similar two representative peaks (G-band and D-bands) with the same ratio. This implies that the encapsulation step does not involve the degradation in the graphene wall layers due to physicochemical interactions of the individual CNTs with polymers and etchants.

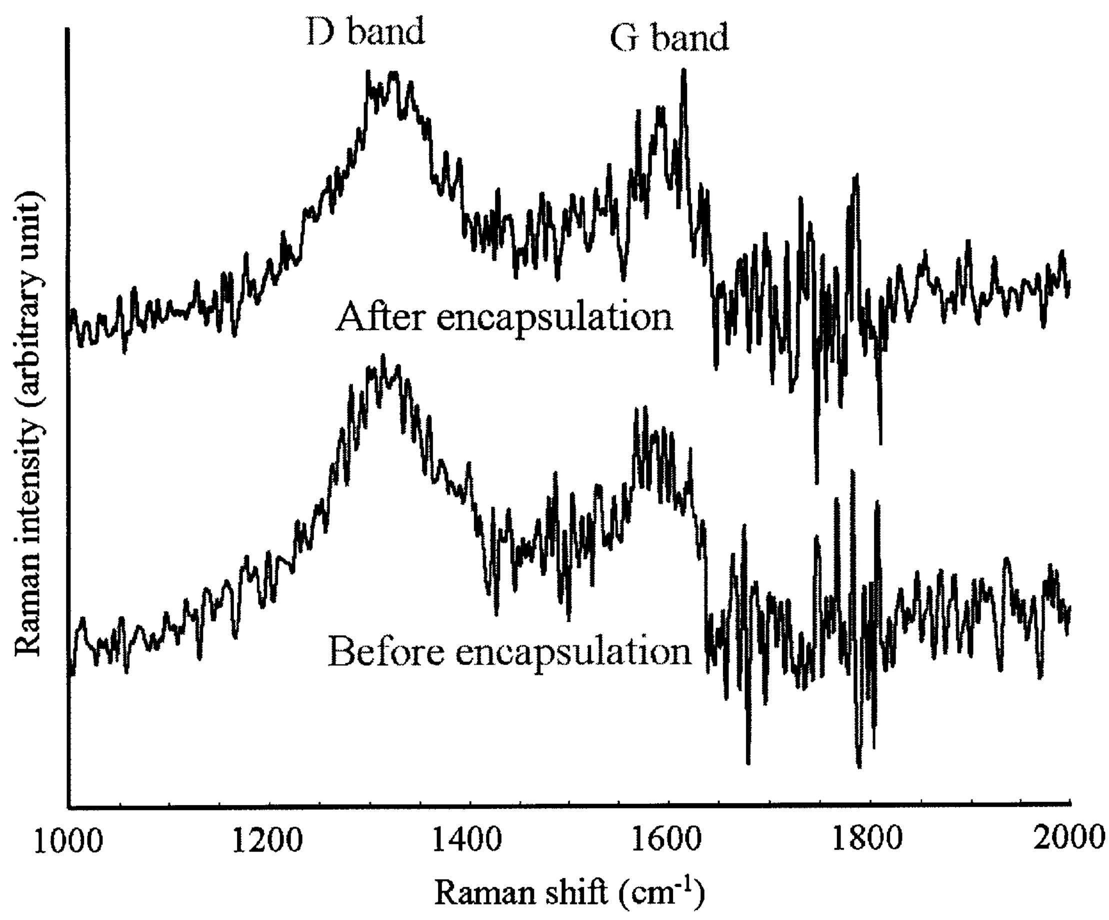

Figure 4.17 Comparison of Raman spectroscopy. Both spectra show the same peaks of D-band and G-band.

4.4 Summary

As the second major step in transplanting assembly of the individual CNTs, each CNT has been encapsulated into the individual MEMS carriers. Dual polymeric layer design provided simple control over the length of CNTs and their easy release from the substrate when the bottom layer is etched away. The length of exposed CNTs is 1.5 μm, which corresponds to the thickness of the bottom layer. The orientation of the CNTS remains unchanged as predicted in chapter 2. HRTEM and Raman spectroscopy confirms the graphene layers of CNTs remain the same through encapsulation processes.

5 Fabrication of CNT probes and their application for scanning probe microscopy (SPM)

5.1 Introduction

The final step in transplanting assembly of the individual CNTs is to transfer the single CNTs encapsulated in the individual MEMS carrier to the target location. For a CNT AFM probe, the target location is the end of an AFM cantilever. This chapter presents experimental results of transferring the individual CNTs with MEMS carriers, its detailed procedures to fabricate CNT AFM probes and the scanning results over various samples.

5.2 Transfer of the individual CNTs

A method for fabricating CNT AFM probes by transplanting the single CNTs should provide a reliable way of maintaining the orientation of the individual CNTs, releasing the CNTs with MEMS carriers from the substrate without losing it, and fixing the CNT carrier on the AFM cantilever securely. One of the ideas to address these issues is to transfer the individual CNTs encapsulated in single MEMS carriers manually with the aid of a small amount of the bottom layer as shown in Figure 5.1.

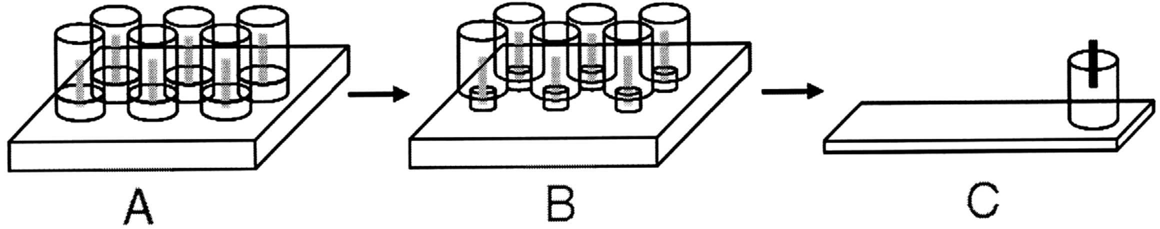

Figure 5.1 Assembly procedure to fabricate CNT probes. (A) An array of MEMS carriers with single CNTs. (B) Further etching of the bottom layer for easy release. (C) A CNT-tipped AFM probe through transferring one block to the end of an AFM cantilever.

Picking and placing the individual nanostructures is the essential step in a deterministic assembly of the nanostructures. The bottom layer is etched further with PMGI 101 remover until a small amount of the bottom layer remains to protect the CNTs from buckling and maintain their orientations. The bonding force between the bottom layer and the substrate will be small enough to break the bonding when the bottom layer is sheared mechanically. A CNT tipped AFM nanoprobe can be readily made by attaching a CNT embedded in a MEMS carrier at the end of a MEMS cantilever. A humid curing adhesive with low viscosity provides a strong bonding between the MEMS carrier and the cantilever. Observing and manipulating a single CNT encapsulated in the MEMS carrier is performed simply using a micro motion stage and an optical microscope. The overall procedures in transplanting assembly of a single CNT to fabricate a CNT-tipped AFM probe are summarized in Table 5.1.

Table 5.1 Procedures in fabricating a CNT-tipped AFM probe by transplanting a single CNT.

	Procedure	Schematic
1	Partial etching of the bottom (PMGI) layer.	PMGI
2	Approach an cantilever to a target CNT.	Adhesive; AFM cantilever
3	Wait until the adhesive is cured.	
4	Shear the bottom layer to break its bonding to the substrate.	
5	Lift off the CNT using the micro motion stage.	
6	Release the CNT tip by etching the bottom layer with PMGI remover.	

The setup for manual assembly of CNTs is shown Figure 5.2. It consists of an optical microscope, a 3-axis motion stage for AFM probes, and a 3-axis motion stage for the CNT samples. The motion stage for AFM probes has a holder on which AFM probes are attached using a carbon tape, and this tape provides a flexible but secure fixation of the probes to the end of the motion stage during assembly procedures. The motion stage for the CNT samples has a magnetic sample holder, and the CNT sample has a steel disc on its back side. This magnetic sample holder allows the rotation of the samples providing easy alignments of the samples.

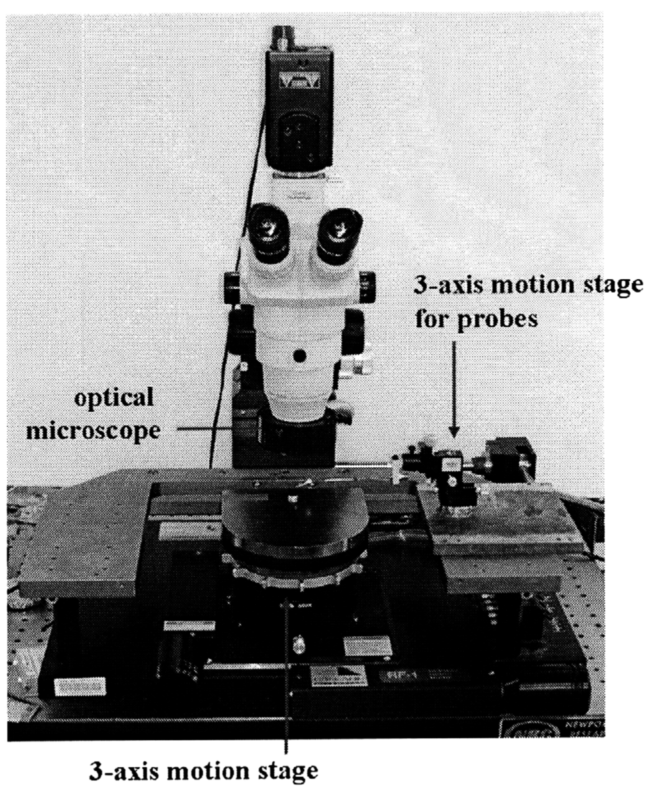

Figure 5.2 A setup for fabricating a CNT-tipped AFM probe.

Before staring the assembly procedure, the sample mounted on the magnetic sample holder is positioned using the motion stage for CNT samples. Then an AFM probe cartridge is mounted on the holder of the manipulator for probes, and approached in the vicinity of the array of the MEMS carriers.

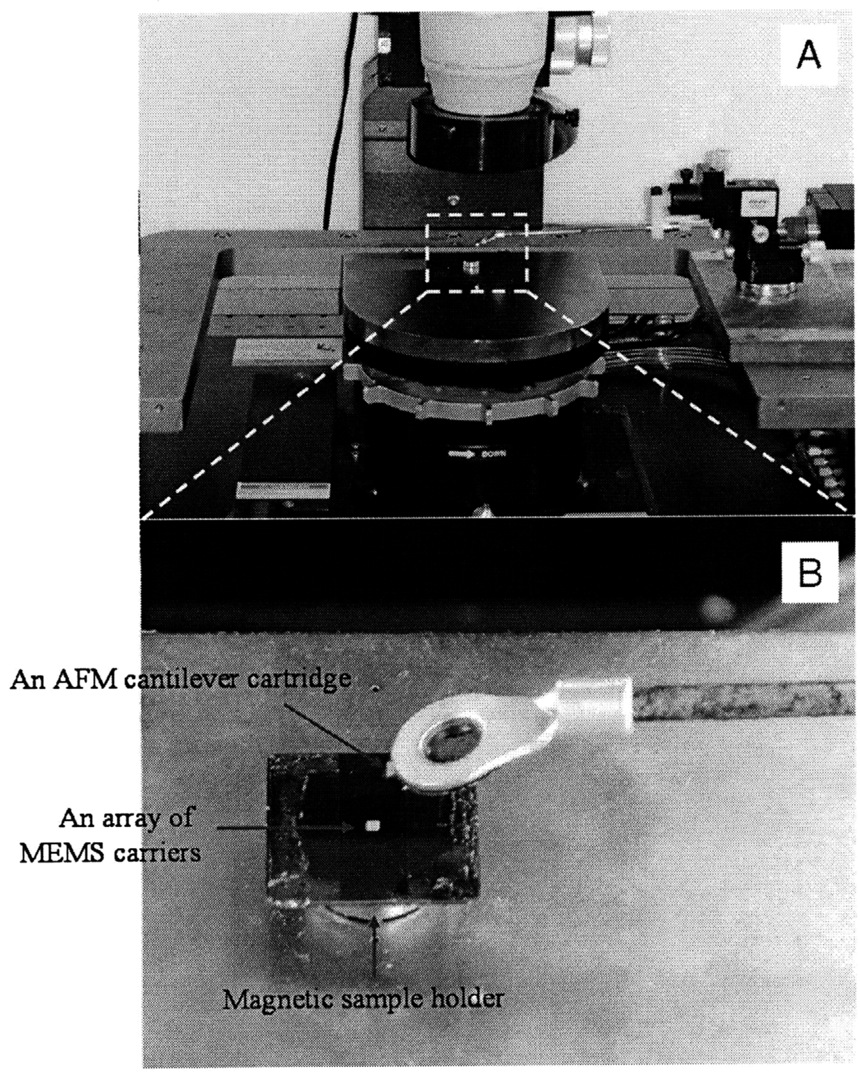

Figure 5.3 An enlarged view of the sample, probes and holders.

- **Step 1: Partial etching of the bottom layer**

Before transferring the CNTs with MEMS carriers, the bottom layer is further etched using PMGI 101 remover until the diameter of the bottom layer reaches less than 7 μm. This enables easy release of CNTs and MEMS carriers while the remaining bottom layer protects the CNT and holds the MEMS carriers to maintain their orientations until they are released.

Figure 5.4 shows an optical microscope image of an array of SU8 MEMS carriers with the partially etched bottom PMGI layer. The cylindrical top SU8 carriers work as a hard mask for wet etching of the bottom layer, so the resultant bottom layer forms an array of thin disks with diameter of 7 μm.

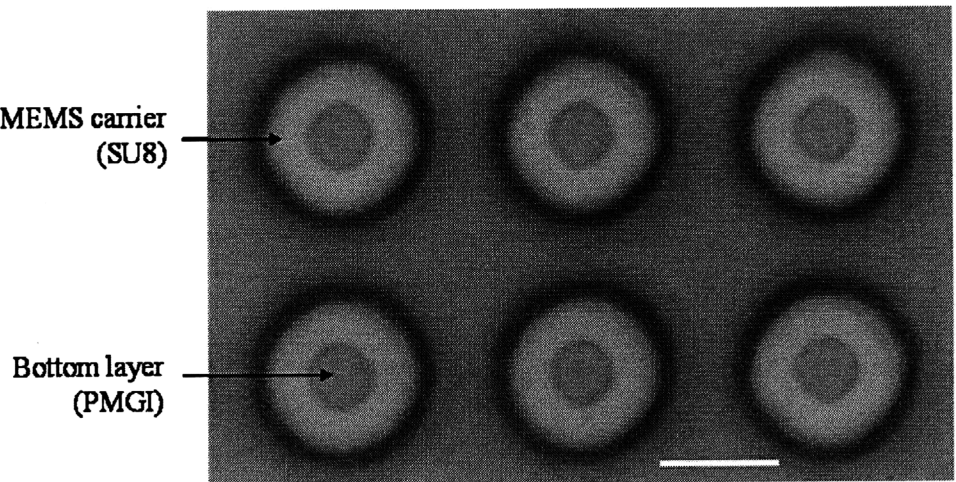

Figure 5.4 An array of MEMS carriers after partial etching of the bottom layer (scale bar = 20 μm).

Figure 5.5 shows optical microscope images of the progress of etching the bottom layer for additional 60 min. The progress of etching procedure is timely controlled by an observation of an optical microscope as shown in Figure 5.5.

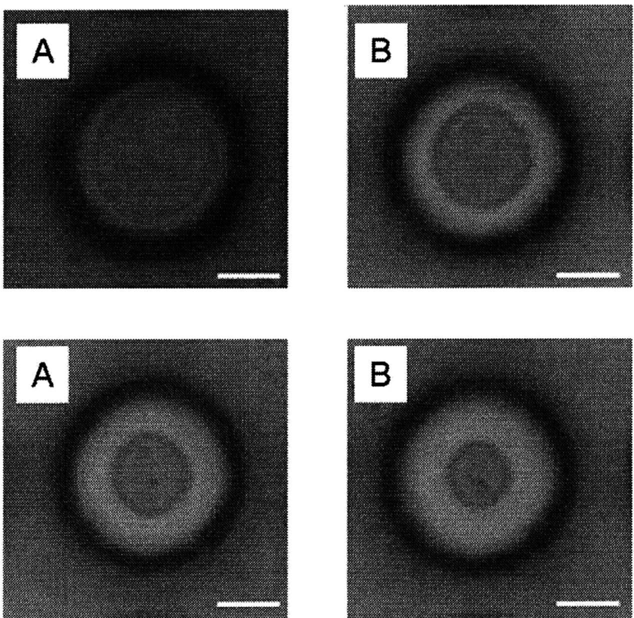

Figure 5.5 Progress of etching procedures of the bottom (PMGI) layer: (A) 0 min. (B) 25 min. (C) 45 min. (D) 60 min.

- **Step 2: Approach a cantilever to a target CNT**

A tipless AFM cantilever (NCS12 of MIKROMASCH, San Jose, California) is mounted on a 3 axis motion stage under a 60X (6X optical and 10X digital) optical microscope. The NCS12 series has 6 tipless Si cantilevers with different lengths on a cartridge, and 3 of them are shown in Figure 5.6. Each cantilever is 2μm thick and 35 μm wide. The shortest cantilever is 90 μm long, and it will be used for tapping mode (spring constant =

14 N/m and resonant frequency = 315 kHz). The longest cantilever is 350 μm long for contact mode (spring constant = 0.3 N/m and resonant frequency = 21 kHz).

The tip which already picked up a small droplet of a humidity curing adhesive (LOCTITE® 408™) is approached to a target block using the micro motion stage while being monitored with the optical microscope as shown in Figure 5.7. The LOCTITE® 408™ is chosen because of its low viscosity (~ 5 cSt) because it enables us to pick up a minimal amount of the adhesive at the end of the cantilever. The adhesive provides both tensile and shearing bonding stress larger than 5 MPa once it is cured.

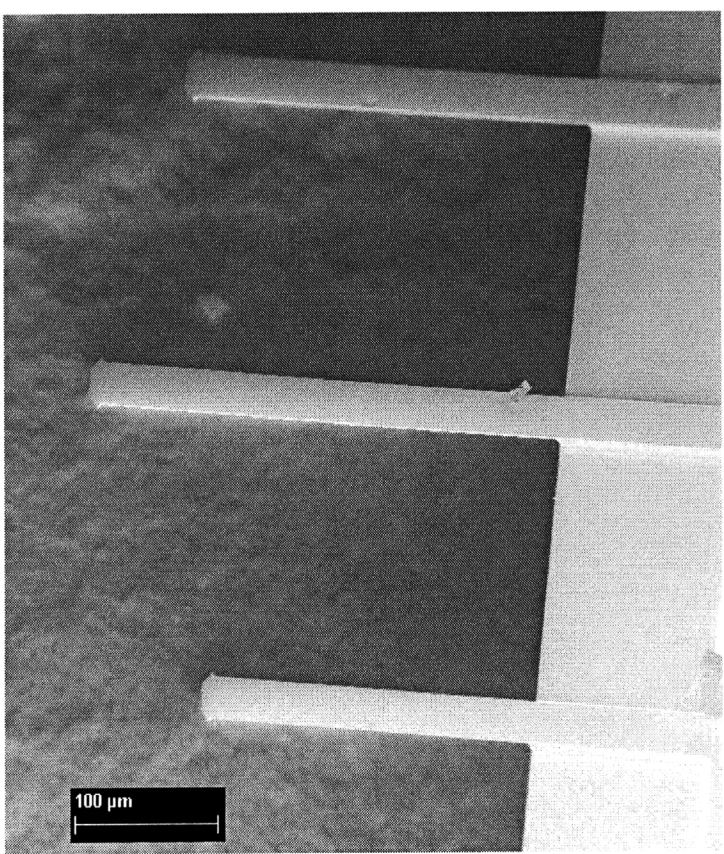

Figure 5.6 3 tipless cantilevers of NCS12.

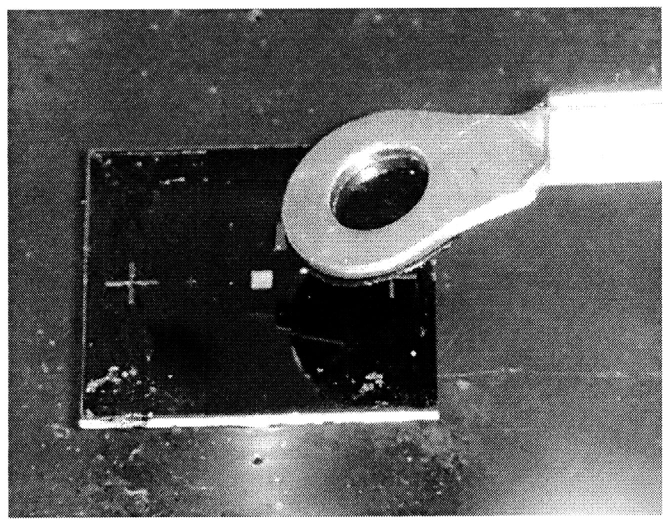

Figure 5.7 A probe approaching to a target CNT encapsulated in MEMS carrier.

- **Step 3: Cure the adhesive**

The adhesive is cured in 5~20 minutes depending on the etching of the bottom (PMGI SF 11) layer. With 120 minute's etching to remain the bottom layer with 7 μm in diameter, 5 minute's curing provides a strong bonding between the MEMS carrier and the Si cantilever.

- **Step 4: Shear the block with a single CNT**

After the adhesive is cured, the bottom PMGI SF 11 layer is sheared mechanically on the substrate using the micro motion stage under an optical microscope. The bonding of the bottom PMGI layer and CNT roots to the substrate has been broken by mechanical shearing, and the individual CNTs with MEMS carriers have been released from the

substrate. The existence of a CNT through the top SU8 layer to the bottom PMGI layer may enforce the bonding between the top and bottom layers when they are sheared.

- **Step 5: Release the block**

The entire block with a single CNT is released from the substrate by being lifted up with the micro motion stage.

- **Step 6: Etch the bottom layer**

After the probe is released from the substrate, the whole probe is put inside of the PMGI 101 developer until the bottom layer is fully removed. Finally, a CNT AFM probe is fabricated with the exposed part of CNT tip which was embedded in the bottom (PMGI SF 11) layer previously. Figures 5.8-5.10 show a few CNT AFM probes fabricated by transplanting assembly of the individual CNTs.

As described in the chapter 2, the previous approaches in fabricating the CNT AFM probes require laborious post-processing: a weeding process to remove any redundant CNT tips, a trimming process to shorten the CNT tip to the desired length, and a welding process to fix the CNT tip to the cantilever more securely. In contrast, the CNT AFM probes fabricated through transplanting assembly of the individual CNTs do not involve those post processes. The single CNT grown from the Ni catalytic dot (the number) is transferred to the end of cantilever (the location). The CNT tip is 1.5 μm long, which is

equivalent to the thickness of the bottom (PMGI SF 11) layer (the length). The CNT tip is parallel to the SU8 block axis (the orientation) with the initial orientation that is defined by the electric fields in plasma during the CNT growth step. In each CNT AFM probe, the CNT tip is anchored to the SU8 MEMS carrier, and the MEMS carrier is bonded strongly to the cantilever. The resultant bonding strength by the adhesive between the SU8 carrier and the silicon cantilever is more than 15 μN. This force is much larger than the adhesion and frictional forces (~10 nN) between CNT tips and samples during AFM scanning.

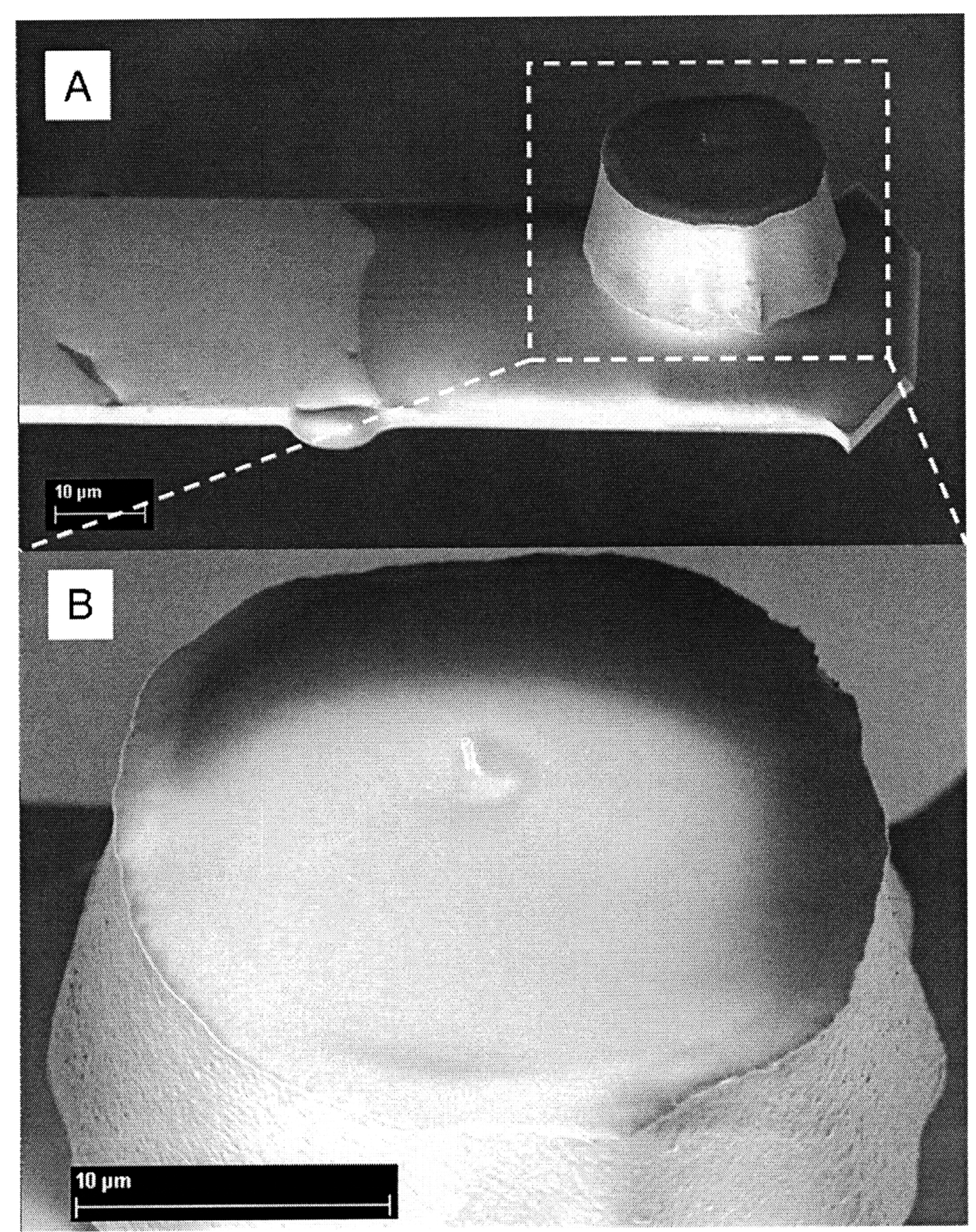

Figure 5.8 A CNT-tipped AFM probe. (A) A CNT-tipped AFM probe is fabricated by transplanting a single CNT encapsulated in a polymer block to the end of an AFM cantilever. (B) An enlarged view of the CNT tip. The CNT tip is located at the center of the carrier, and its length is 1.5 μm.

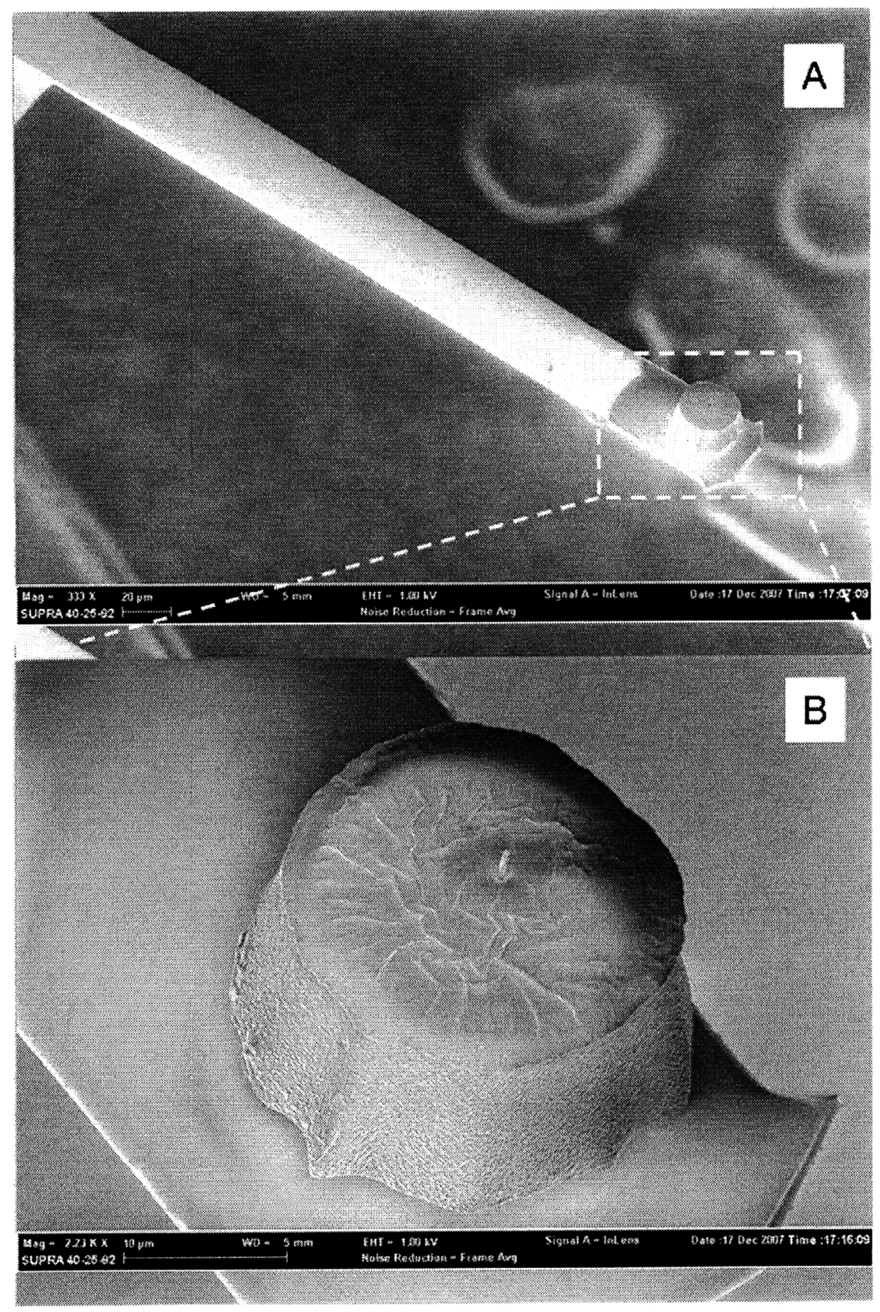

Figure 5.9 Another view of the CNT-tipped AFM probe. (A) A tilted view of the CNT-tipped AFM probe. (B) An enlarged view of the CNT tip.

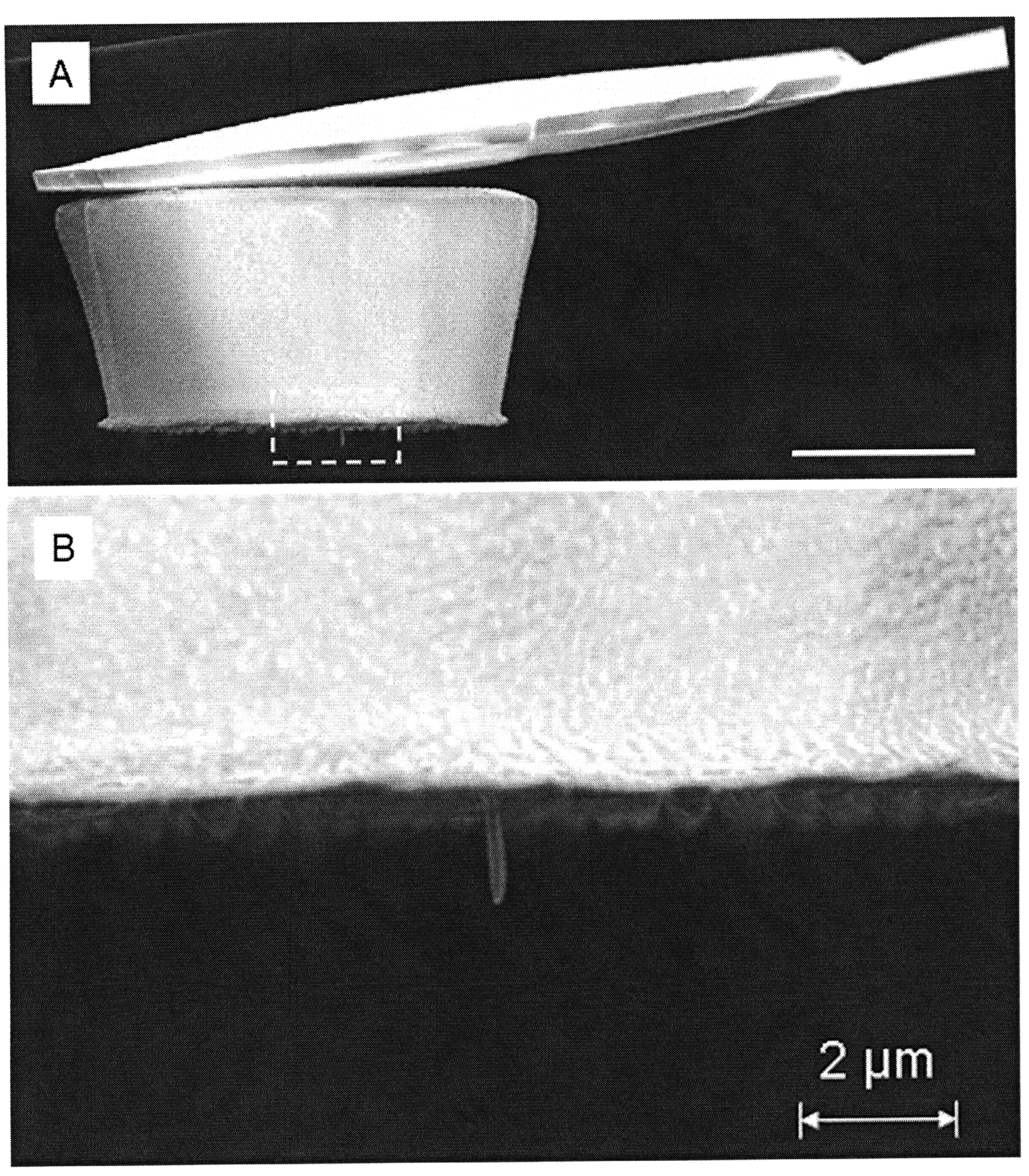

Figure 5.10 (A) A side view of a CNT-tipped AFM probe. (B) An enlarged view of the CNT tip. It is parallel to the block axis and normal to the sample surface.

5.3 Discussion about the assembly results

5.3.1 CNT tips on various cantilevers

Materials of the cantilevers for the CNT AFM probes fabricated by the catalytic growth methods are limited due to high temperatures during the CNT growth step. The transplanting assembly method provides flexibility in choosing the materials of cantilevers, so CN-tipped AFM probes for different operation modes can be fabricated on various AFM cantilevers. Figures 5.11-5.13 show various CNT AFM probes fabricated by transplanting assembly, and their properties are listed in Table 5.2

Table 5.2 Characteristics of the CNT-tipped AFM probes

	Figure 5.11	Figure 5.12	Figure 5.13
AFM mode	Tapping	Contact	Contact
Cantilever material	Si	Si	Si_3N_4 with Au coating
Cantilever length	130 μm	350 μm	196 μm
Spring constant	4.5 N/m	0.3 N/m	0.12 N/m
Resonant frequency	60 kHz	-	-

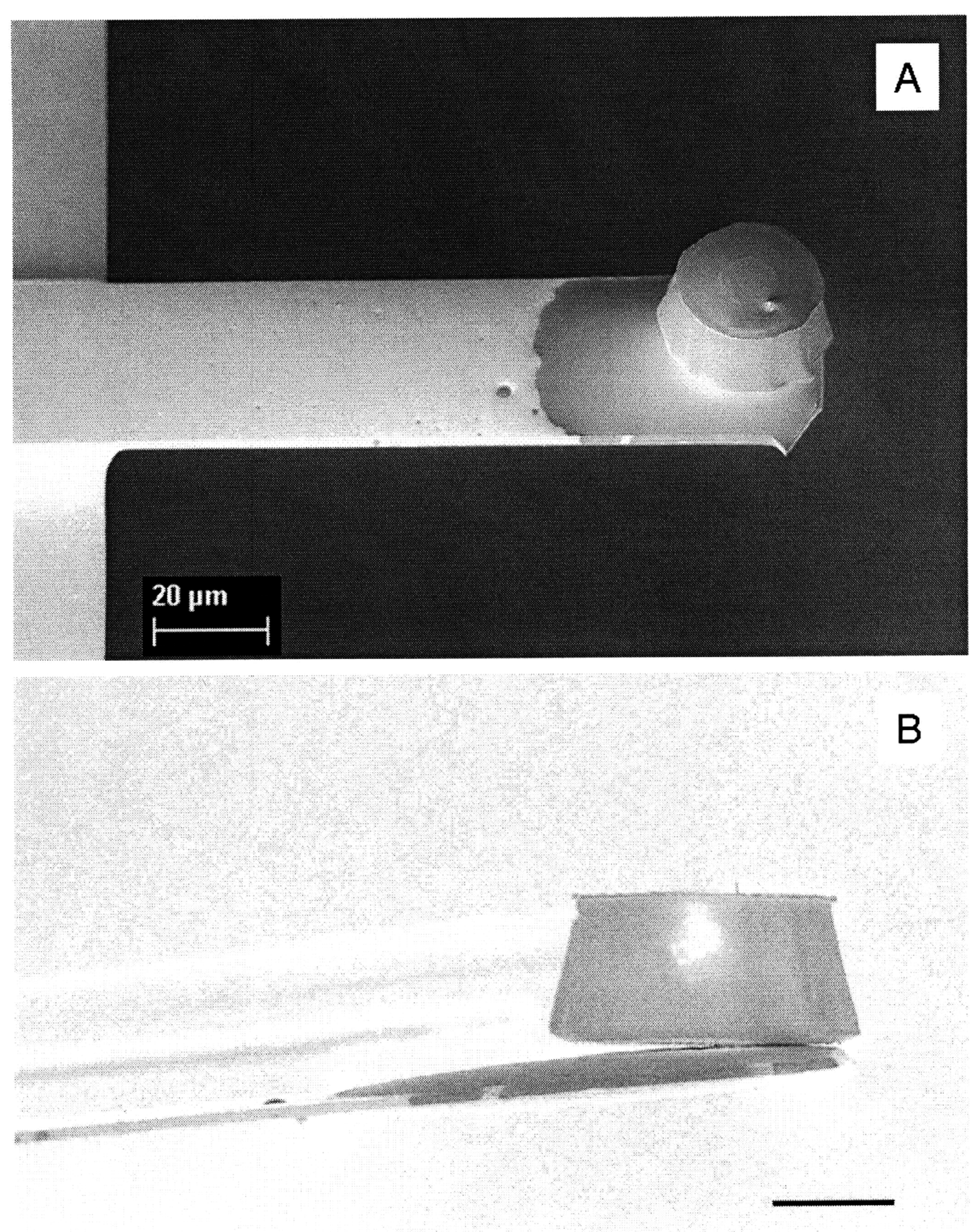

Figure 5.11 A CNT probe for tapping mode: (A) A tilted view (30°). (B) A side view (scale bar = 10 μm)

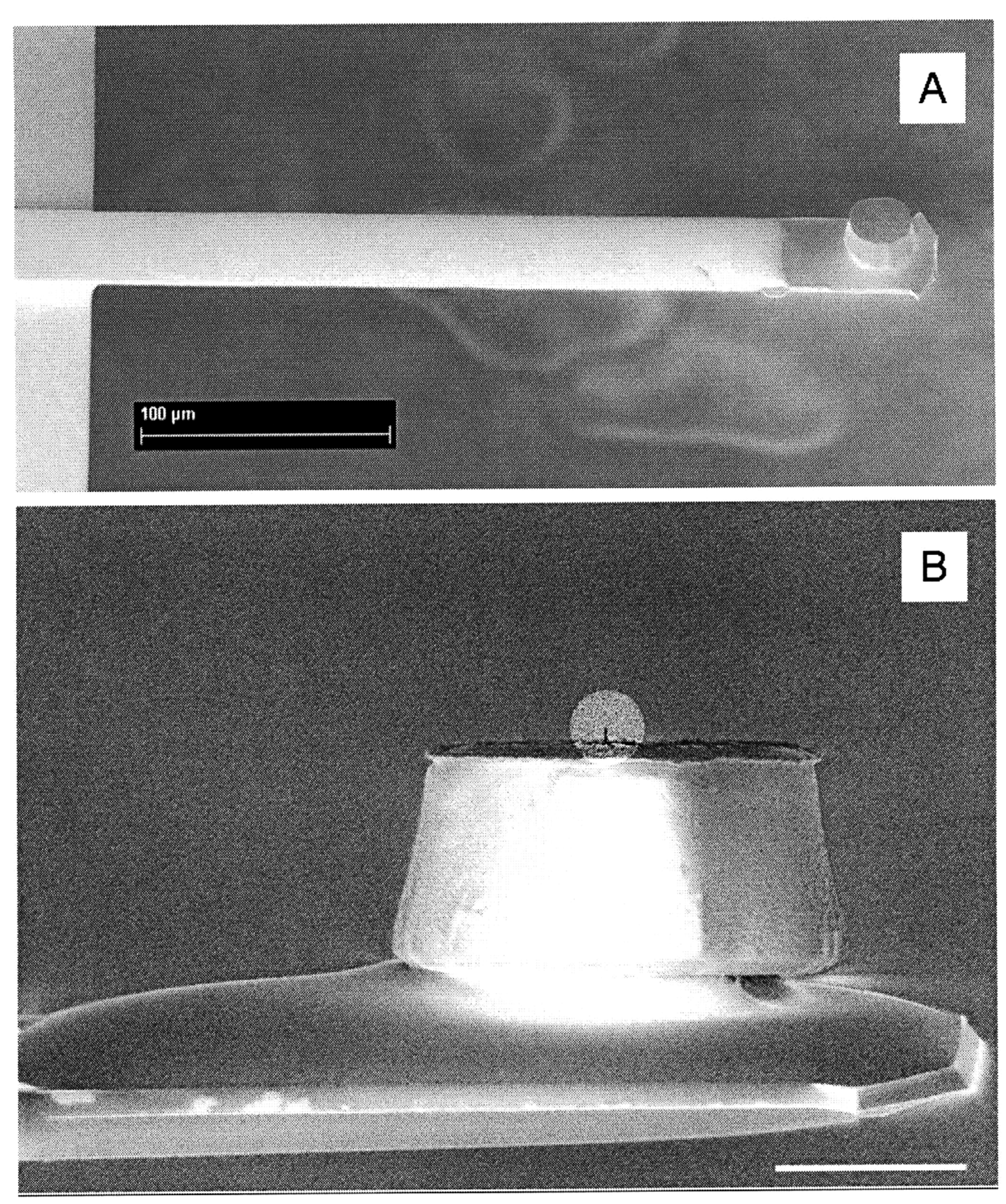

Figure 5.12 A CNT probe for contact mode: (A) A tilted view (30°). (B) A side view (scale bar = 10 μm).

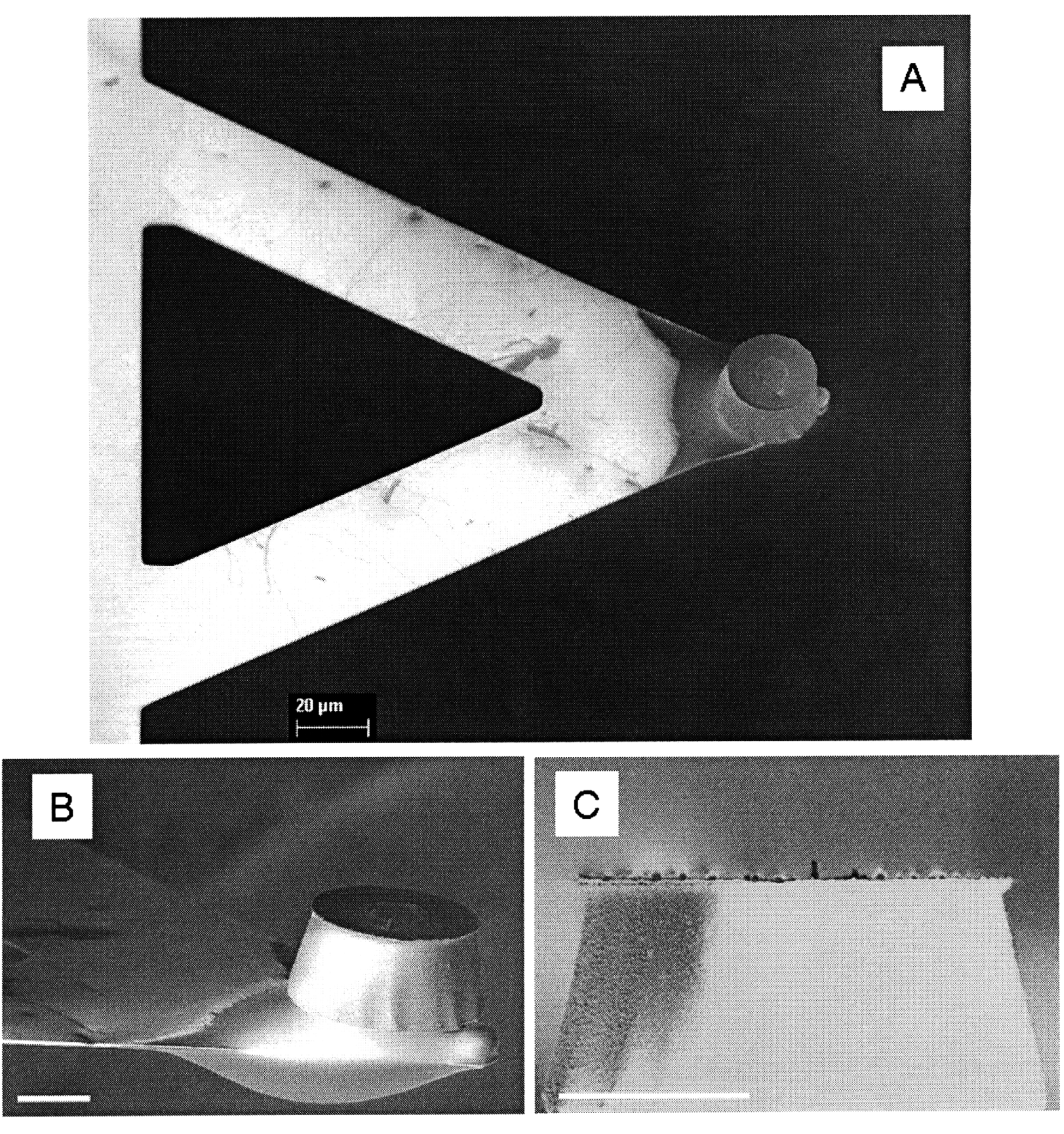

Figure 5.13 A CNT probe for contact mode: (A, B) A tilted view. (C) A side view. (scale bars = 10 µm)

5.3.2 Effective CNT tip shape and radius

Closer observations of the end of CNT tips show that the CNT tips have conical tip ends as shown in Figure 5.14. This means that the effective radius of the CNT tips is the radius of the conical ends rather than that of the CNTs.

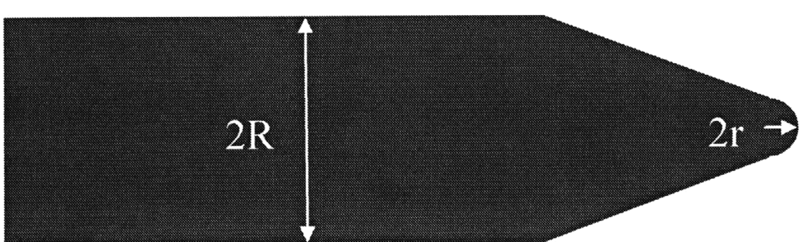

Figure 5.14 The effective radius of the CNT tip, r, vs. the radius of the CNT, R.

During the growth of CNTs with fish-bone wall structures, the successive conical graphene layers are formed parallel to the conical surface of the Ni catalysts. Each graphene layer consists of the covalent bonding of carbon atoms while adjacent layers form the weaker van der Waals bonding. This results in a conical end shape of a CNT tip when it is released from the substrate by shearing forces. This smaller effective radius of CNT tips is beneficial to our application, a probe for AFM, because it provides a better spatial resolution. HRTEM images of CNTs (Figure 5.16 ~ Figure 5.17) show a strong correlations between the shape of Ni catalysts and conical shape of CNT roots.

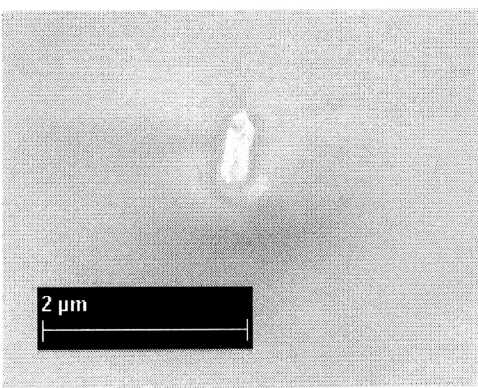

Figure 5.15 A CNT tip of a CNT AFM probe showing a conical end.

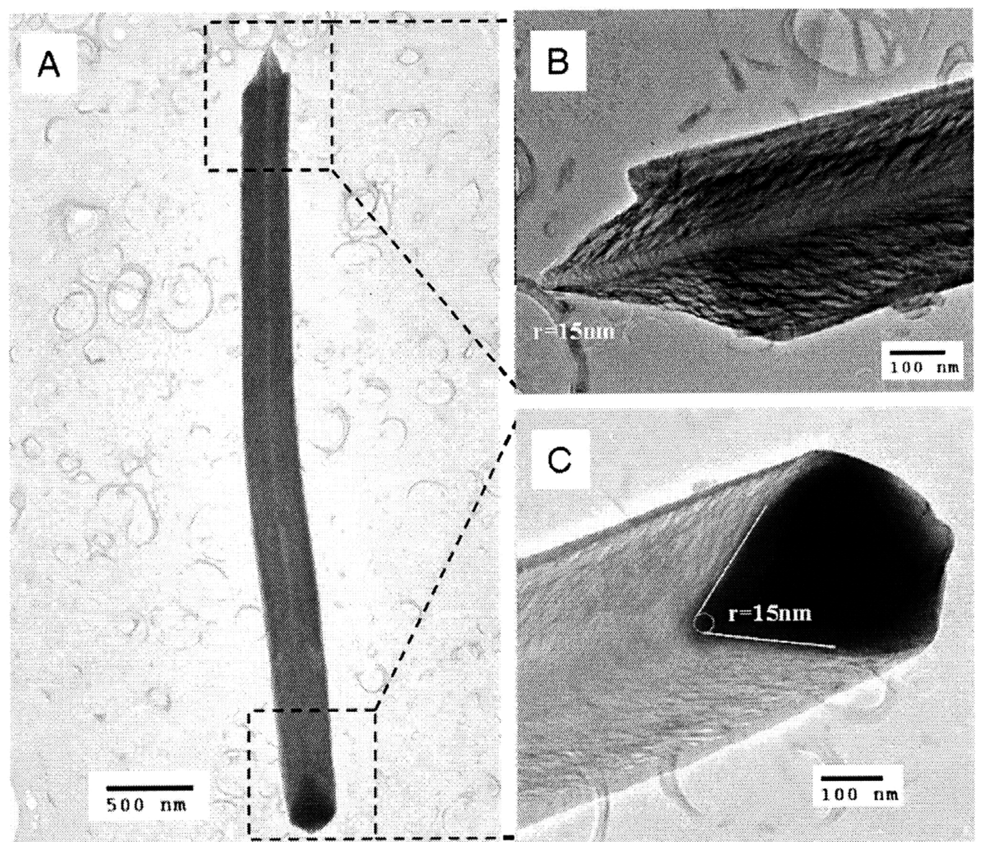

Figure 5.16 A Sharp CNT tip defined by the root shape of the CNT (the effective radius is about 15 nm). (A) TEM of a CNT. (B) The root of the CNT. (C) The part close to the Ni catalyst.

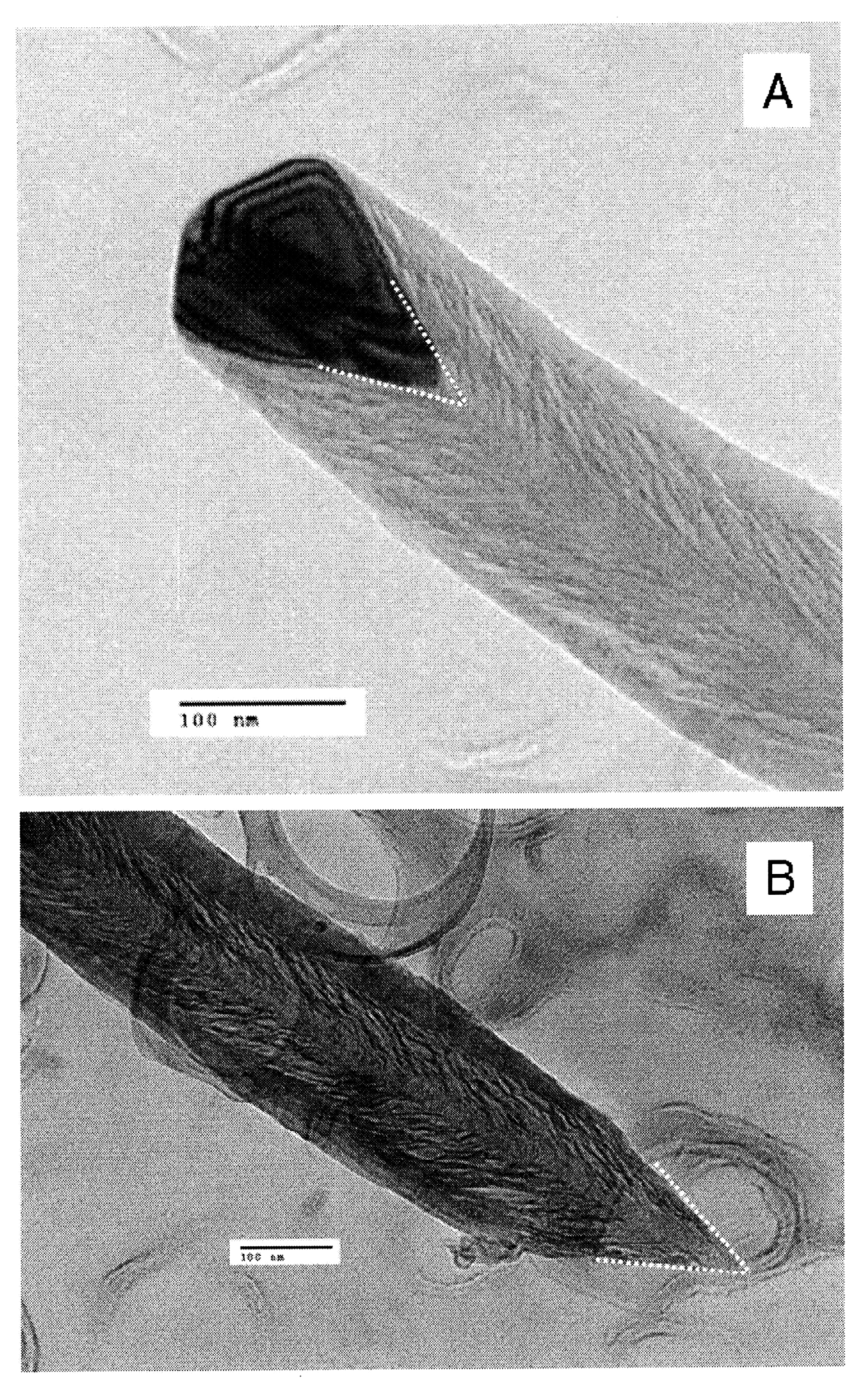

Figure 5.17 HRTEM of a single CNT (the effective radius is about 10 nm): (A) A tip of a CNT. (B) A root of a CNT.

5.4 AFM scanning results with CNT probes over various samples

The performance of a CNT tipped AFM probe fabricated by transplanting assembly is measured and compared with those of standard AFM probes by scanning various samples using a DI3100 AFM machine (Veeco Instrument, Plainview, NY).

5.4.1 Standard grating for AFM calibrations

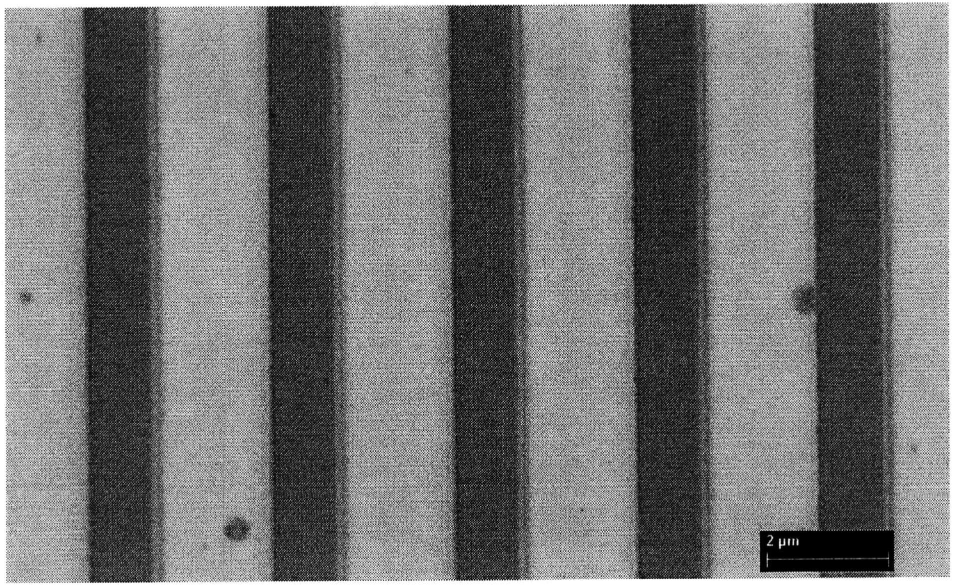

Figure 5.18 SEM image of an AFM standard grating (TGZ02).

TGZ02 (MIKROMASCH, San Jose, CA) is an AFM calibration grating, and it has periodic trenches with 100nm in depth and 3μm in spacing. Figure 5.18 shows an SEM image of the calibration grating, and its trenches are 1.7 μm wide with vertical side walls.

An AFM scanning image (Figure 5.19) with a standard Si AFM probe (RTESP of Veeco Instruments) shows image artifacts due to a pyramid-shaped Si tip. The scanning is performed using tapping mode with a tuned resonant frequency of 260 kHz (the scanning speed is 10 μm/sec). A few bumps (Figure 5.19 (a)) are assumed to be contaminants present on the sample like dark dots in Figure 5.18.

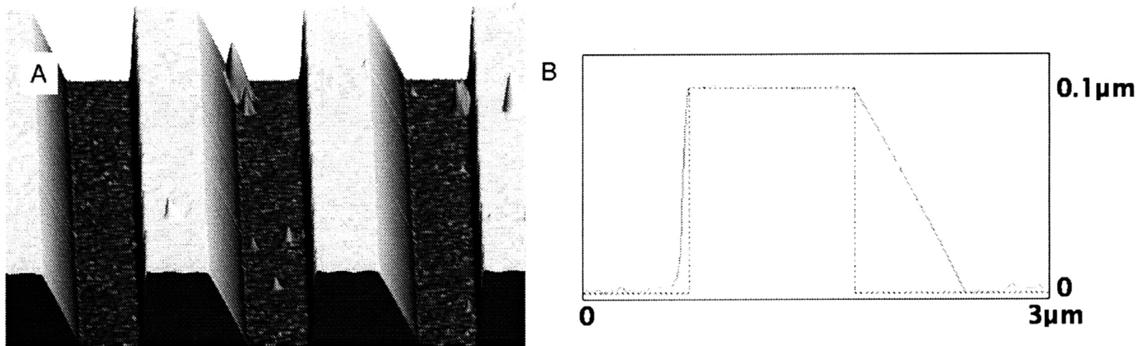

Figure 5.19 AFM scanning results of an calibration grating by a standard Si probe: (A) A standard Si AFM probe. (B) A sectional profile of (A).

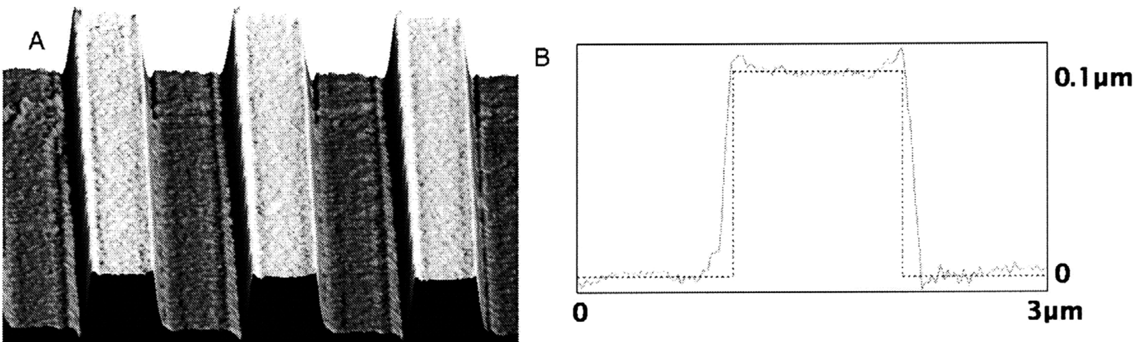

Figure 5.20 AFM scanning results over a standard AFM calibration grating: (A) A CNT tipped AFM probe by transplanting assembly. (B) A sectional profile of (A).

Figure 5.20 (a) and (b) show an AFM scanning result with a CNT AFM probe fabricated by transplanting assembly. The image is obtained using contact mode at the

scanning speed of 5 μm/sec. It is obvious that the CNT tipped AFM probe scan the vertical trenches closer to its original features than the standard Si probe does. The overshot present at both edges (Figure 5.20 (b)) results from non-optimal AFM scanning parameters such as the proportion and integration control gains.

5.4.2 Critical-angle transmission grating

The next sample for scanning experiments is a hard mask in fabricating a critical–angle transmission grating. This mask is patterned by scanning-beam interference lithography, and its main application is to fabricate ultrahigh aspect ratio freestanding gratings for high efficiency x-ray and extreme ultraviolet spectroscopy [66]. The hard mask consists of periodic patterns of photoresist (PR) (PFI-88a7, Sumitomo Corp., Japan), anti-reflection coating (ARC) (XHRiC-11, Brewer Science inc., Rolla, MO), and silicon nitride (SiN) on top of a Si substrate. The period of mask patterns is 580 nm, and each pattern is 680 nm in height and 230 nm in width as shown in Figure 5.21.

A standard tapping mode Si probe can scan the deep mask patterns only to 15nm deep due to a pyramid-shaped tip. In contrast, a CNT AFM probe can scan the mask patterns up to 350 nm. However, the bottom of the trenches (the surface of the Si substrate) is not able to scan, and this may be due to the imperfect orientation of the CNT tip and the considerably large diameter of the CNT tip compared to the width of the deep trenches. CNT tips with smaller diameters can be a solution to address this limitation.

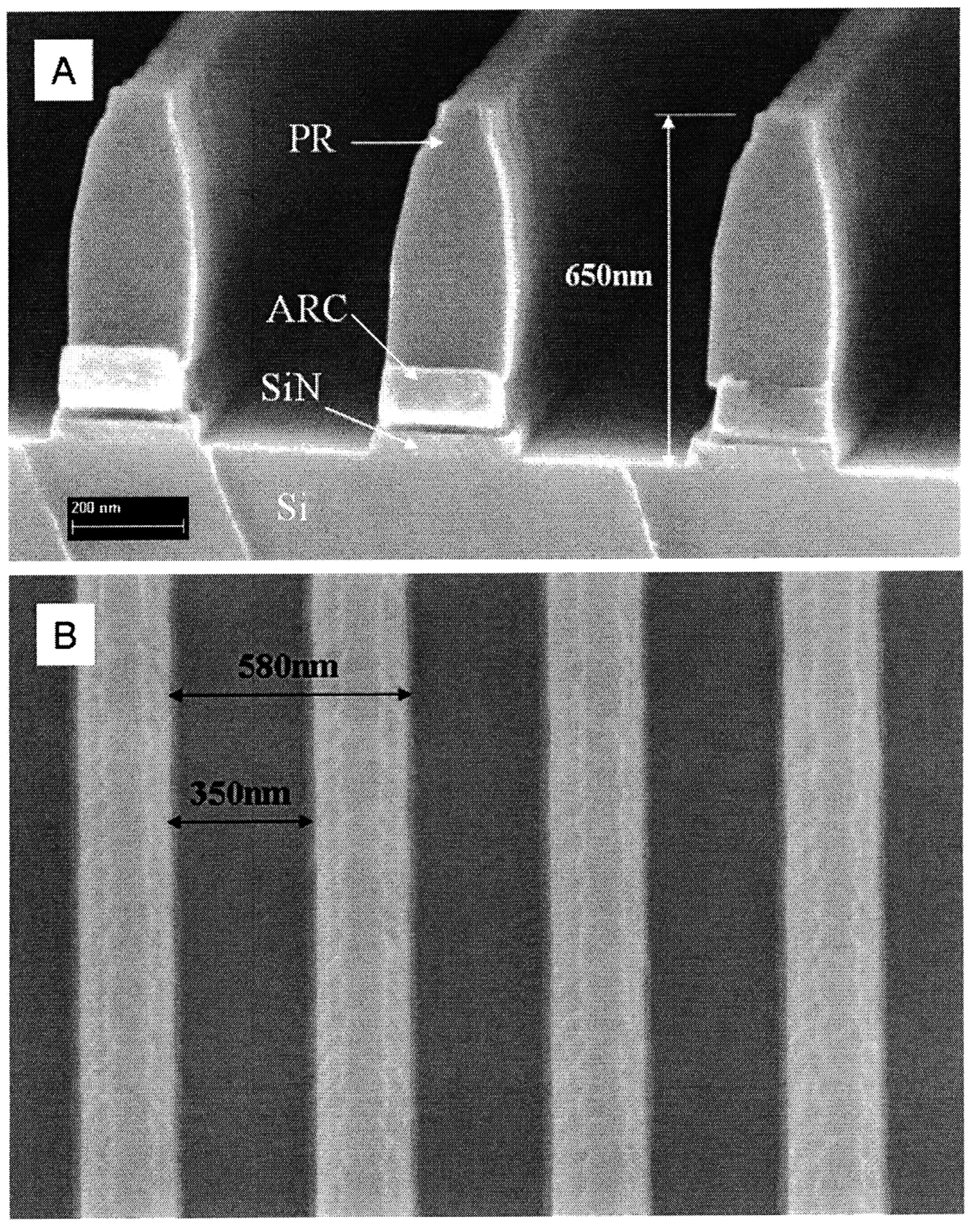

Figure 5.21 A hard mask patterns for critical-angle transmission grating: (A) tilted view. (B) top view.

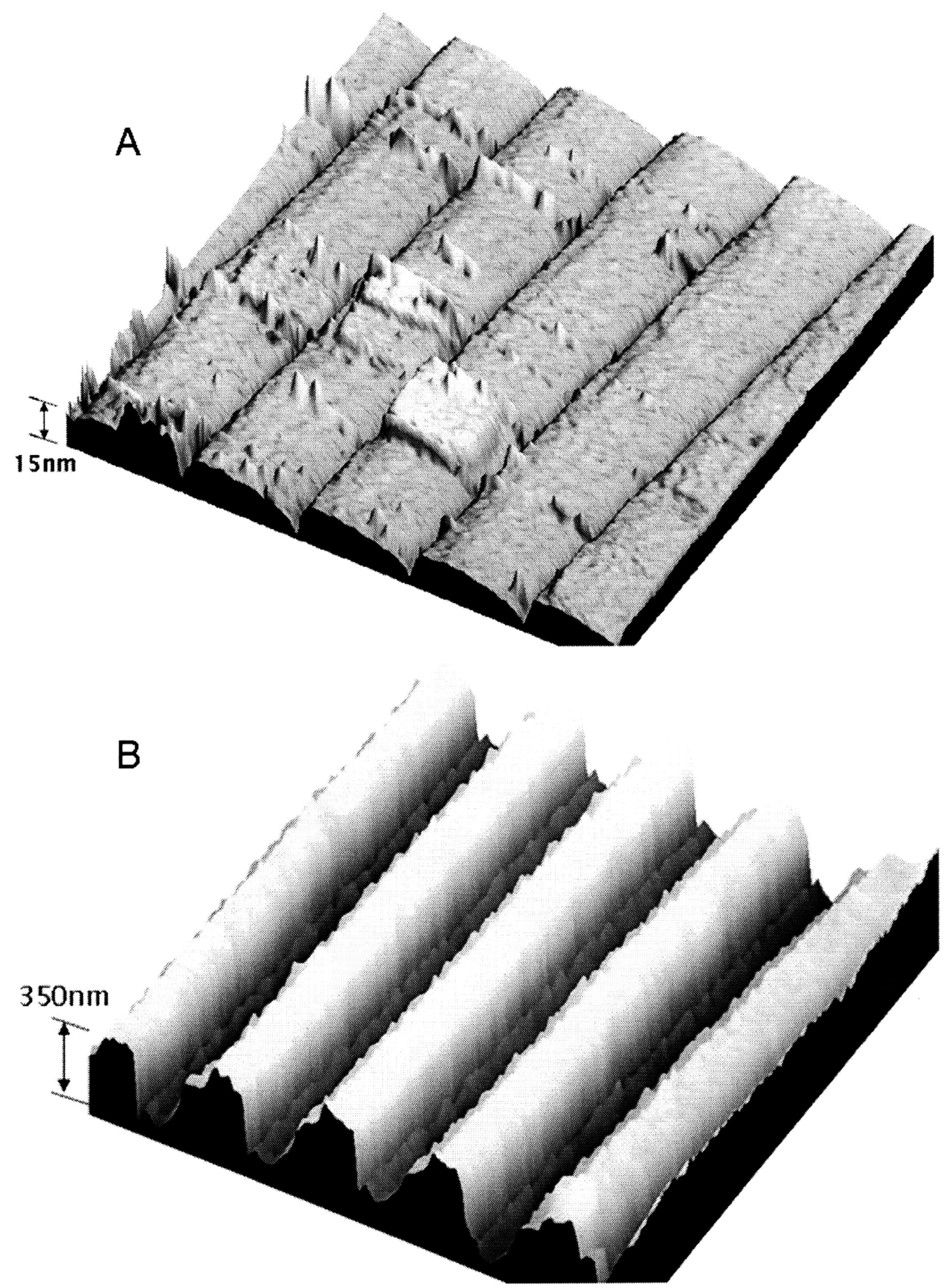

Figure 5.22 Comparison of AFM scanning images of the transmission grating: (A) An AFM image using a Si probe (scanning range: 3 × 3 μm). (B) An AFM image using a CNT probe (scanning range: 3 × 3 μm).

5.4.3 Biological samples

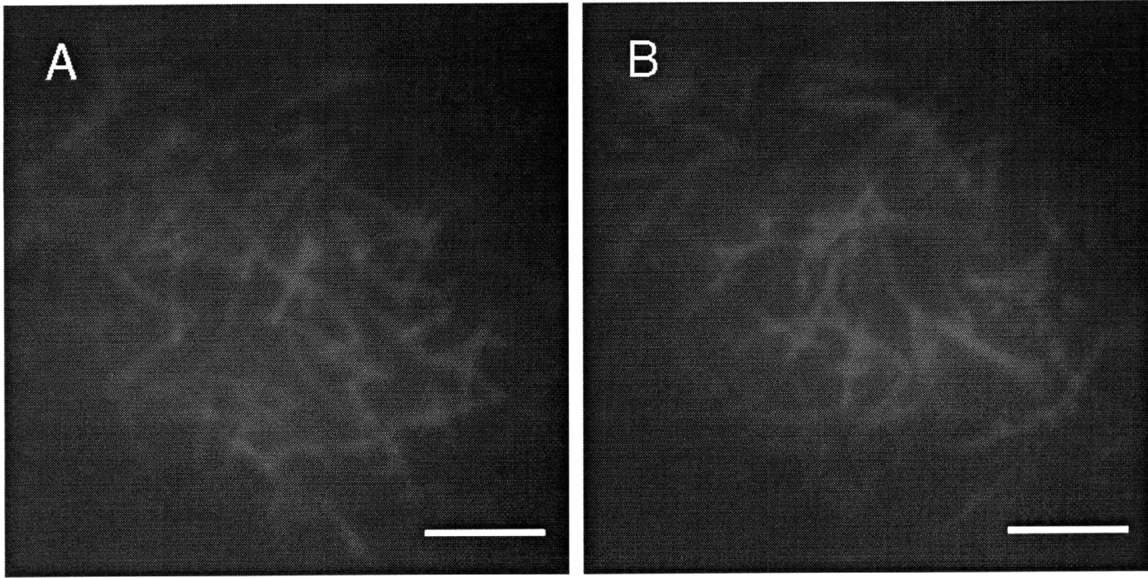

Figure 5.23 Fluorescence microscopy images of filament actions in buffer solution (scale bar = 10 μm).

The scanning capability of the CNT-tipped nanoprobe over biological samples was check with a filament actin (F-actin) sample. 64μl/2.3μM of F-actins was prepared in the 50 ml of a buffer solution (5mM Tris-HCl, 0.5mM ATP, 0.2mM DTT, 100mM KCl, 0.2mM $CaCl_2$, and 2mM $MgCl_2$) and stored at 4 °C before scanning. Fluorescent microscopy (Figure 5.23) show bundles of F-actins in the buffer solution.

10 ml of the solution was dropped on a glass slide, and AFM scanning was performed right after the buffer solution is dried. Figure 5.24 show the contact mode AFM images with the CNT-tipped nanoprobe. It is noted that the sample has large surface roughness which may results from the clustered bundles of actins, remnants from

the buffer solution, and contaminants on the substrate. A mica substrate will have an atomically flat surfaces, it will provide a better sample preparation method.

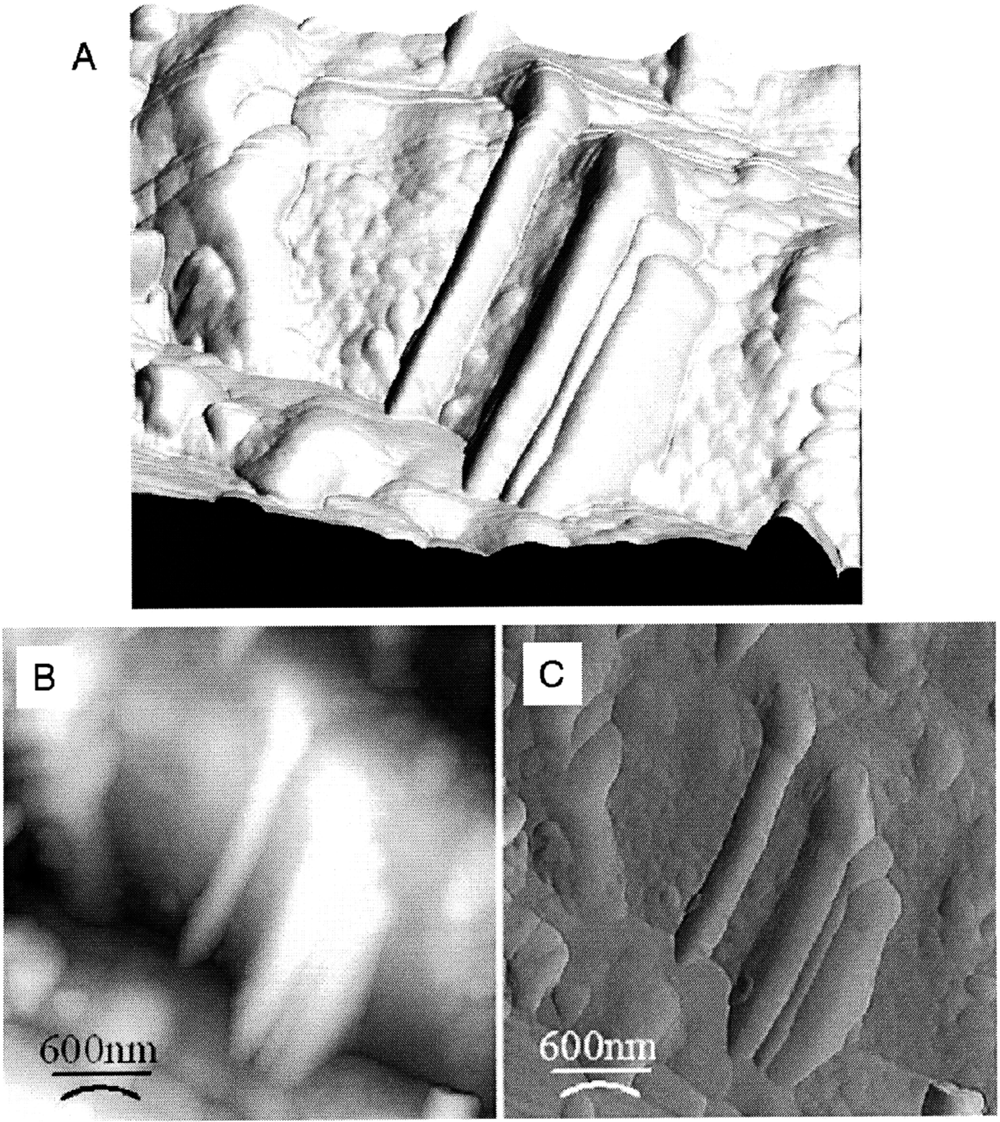

Figure 5.24 AFM scanning results of F-actins: (A) 3D image (scanning range: 3 μm). (B) 2D image (height mode). (C) 2D image (deflection mode).

5.5 Summary

As the final step in transplanting assembly of the individual CNTs, each CNT encapsulated in a single MEMS carrier has been transferred to the end of an AFM cantilever. When the remaining parts of the bottom PMGI layer have been removed by the PMGI remover, the overall assembly forms an AFM probe with a single CNT tip. Transplanting assembly even enabled the manual transfer of the individual CNTs in a reproducible manner. Additionally, transplanting assembly provided the flexibility of assembly so that the CNT-tipped AFM probes on various cantilevers have been achieved. Scanning experiments using the fabricated CNT-tipped AFM probes confirms that the original functionality of the CNT tips, small dimensions with a high aspect ratio, and high toughness, has been achieved on a micro-scale device through deterministic assembly of the individual CNTs.

6 CNT probes for tip enhanced Raman spectroscopy (TERS)

6.1 Introduction

Tip-enhanced Raman spectroscopy (TERS) aims to achieve nanoscale spatial resolution and molecular-scale sensitivity through a highly localized field enhancement by combining scanning probe microscopy (SPM) with enhanced Raman spectroscopy [67]. The geometry (small diameters and high aspect ratio shapes) and properties (high toughness and chemical stability) make the CNT tips a good candidate for the application of TERS. Thin metal coating is one way of functionalization of CNT tips for TERS. However, in order to achieve single molecule detection using TERS, a new design of plasmonic resonator which can be implemented with the CNT-tipped AFM probes.

This chapter presents an application of CNT probes for TERS with a novel design of a conical layered plasmonic resonator. A new design of the plasmonic resonator for TERS is presented with modeling and simulation results, and the fabrication methods are discussed.

6.2 The CNT probe for tip enhance Raman spectroscopy (TERS)

6.2.1 Surface enhanced Raman spectroscopy as a tool for single molecule detection

Raman spectroscopy is a technique to characterize a chemical composition of a material by detecting scattered lights, and it is a kind of vibrational spectroscopy and has a number of advantages such as simple sample preparation and the full accessible spectral range from virtually 0 to more than 4000 wavenumber (cm^{-1}). It is based on the Raman effect that was first observed in 1928 by C.V. Raman and K.S. Krishnan [68], and is essentially inelastic scattering of the light.

The advantages of Raman spectroscopy are that it is independent of the frequency of the incident light, and sample preparations are simple. However, Raman scattering is inherently a weak process in that only one in every 10^6-10^8 photons which scatter is Raman scattered. This main drawback of Raman spectroscopy, the extremely low cross section of the Raman event compared with the much higher probability of other optical processes such as the Rayleigh scatterings, limits wide application of Raman spectroscopy for in situ spectroscopy. With powerful exciting sources and very sensitive detectors, Raman spectroscopy requires a large number of scattering molecules in order to record a Raman spectrum, which is a limiting factor to the single molecule detection.

One way to overcome the obstacle of a low Raman cross section is using Surface-Enhanced Raman Spectroscopy (SERS). This involves enhancement mechanisms that

raise the Raman cross section for adsorbates at metal surfaces by many orders of magnitude. The SERS effect was first reported in 1974 [69], and it was proposed that the intensified spectrum was due to the electrochemical roughening procedure that significantly increased the electrode surface area. In 1977 a Raman scattering signal enhancement factor of 10^8 was reported [70], and this work provided strong evidence demonstrating that the strong Raman signal must be caused by a true enhancement of the Raman scattering efficiency itself.

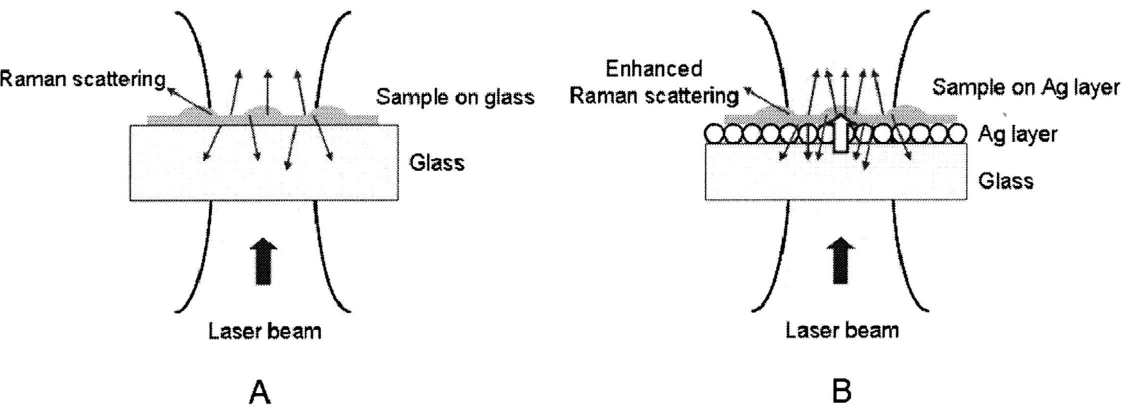

Figure 6.1 Conventional Raman spectroscopy (A) and SERS (B).

There are two different theories of surface enhancement which are currently used. In one, the analyte is adsorbed onto or is held in close proximity to the metal surface, and an interaction occurs between the analyte and the plasmons. This is called electromagnetic enhancement. In the other, the adsorbate chemically bonds to the surface. Excitation is then through transfer of electron from the metal to the molecule and back to the metal again. This is called charge transfer or chemical enhancement. The vast majority of

evidence points to both effects having a part to play although it is generally believed that electromagnetic enhancement may have a greater part to play than charge transfer enhancement.

Since the first observation of SERS, in the literature, enhancement factors of up to a million have been reported, in some cases even up to more than 10^{10}. The improvement of SERS can be categorized into the following research themes: combination of SERS with other Raman methods, and the design of new SERS substrates.

The first single molecule detection (SMD) using surface enhanced Raman spectroscopy (SERS) was reported from two research groups in 1997 independently [71, 72]. In these researches, aggregated silver colloids were used to form “hot-spots” at small gaps between silver particles. Due to the stochastic distribution of those hot-spots, it is very difficult to control SERS enhancement factors even in the same SERS substrate and locate the hot-spots at the desired locations.

Table 6.1 SMD using SERS.

Authors	Kneipp et al. [71]	Nie et al. [72]
Detected molecule	Crystal violet	Rhodamine 6G (R6G)
SERS substrate	Ag colloid (100~150 nm)	Ag colloid (110~120 nm)
Excitation wavelength	830 nm	514.5 nm
SERS cross-section (σ)	$10^{-17} \sim 10^{-16}$ cm^2/molecule	10^{-15} cm^2/molecule
SERS enhancement	10^{14}	$10^{14} \sim 10^{15}$

There have been studies on the plasmonic resonators for surface enhanced Raman spectroscopy (SERS). The electric field enhancement for various configurations of small-sized particles has been studied rigorously by Kelly et al [73]. For isolated particles, the peak values of the electric fields for particle sizes and shapes commonly studied in experiments are on the order of 10^2 or less, which suggests the Raman enhancement factor of 10^8. For dimers of silver particles, the Raman enhancement factors up to 10^{10}~10^{11} are demonstrated. As noted above, the electromagnetic mechanism of SERS predicts enhancements of up to 10^{11} for a dimer of truncated tetrahedron-shaped particles with a 1nm gap. This array consists of 150 silver dimers, and each dimer has two silver spheres of 100nm diameter. The long-range coupling effects in an aggregate or array of widely spaced particles with short-ranged interaction associated with a junction structure enhance the electric fields between the gaps of the central dimer further.

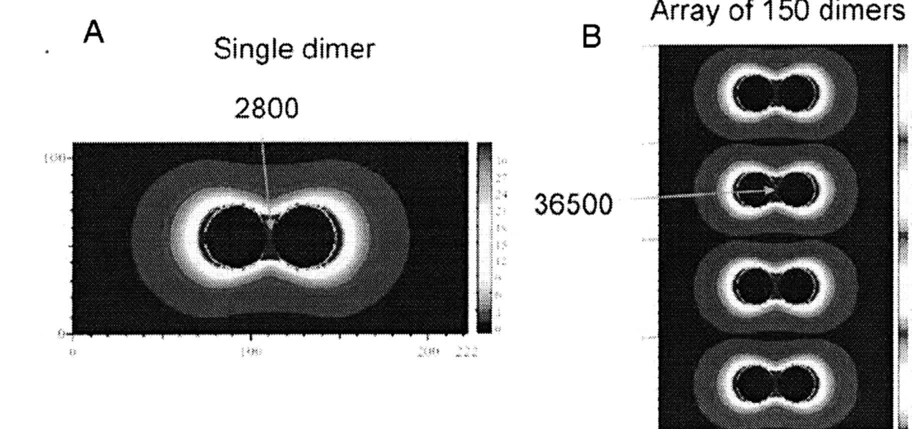

Figure 6.2 Field contours for a single dimer of silver particles and for an array of 150 dimers [73]. (A) Single dimer with 2,800 E.F. (B) Array of 150 dimers with 36,500 E.F.

The combination of local field enhancement associated with plasmon excitation in dimers of metal nanoparticles and long range photonic interactions in a one-dimensional array of particles leads to remarkably high values of E.F. up to 10^{13} when the spheres are replaced with the truncated tetrahedrons [74]. An array of 150 dimers explained above shows the large enhancement factor. However, the main question about it is how to make the hot-spots small enough to detect a single molecule as the diameter of a silver particle is 100 nm while a single molecule sizes a few nanometers.

Li et al. proposed models of a high field enhancement in nanoscale region, one of which is the self-similarity of metal nanoparticles that consists of a linear aggregate of nanospheres with progressively decreasing radii and separation results in the gigantic enhancement of SERS [75, 76]. The simulation results indicate that the design develops a nanofocus in the gap between the minimum-size nanospheres where the local fields are enhanced by a factor of $\sim 10^3$. The simulation results for various configurations are shown in Figure 6.3. However, the fabrication method of the design is questionable as it involves positioning nanospheres of different sizes with nanoscale gaps.

The hot-spots occur on different places based on the relative particle sizes and the gaps between them. The transition of hot-spots with respect to the change in the gaps is shown in Figure 6.4 [77]. With the gap decreasing, the hot-spot moves from the smallest sphere to the junction of the largest and the second largest spheres.

The nanolens system shows the giant field enhancement enough for SMD. However, the questions on the model are how to make the nanospheres with different sizes accurately and how to place them with descending nanoscale gaps precisely. To sum up,

it shows the possibility of designing a nonolens system, but how to realize the system is still questionable.

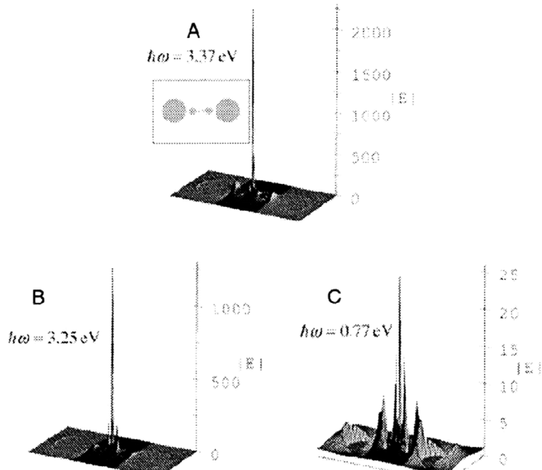

Figure 6.3 Local fields of the linear center-symmetric self-similar chain of six silver nanospheres in the cross section through the equatorial plane of symmetry [75]. The inset in (A) depicts the configuration of the chain of six silver nanospheres.

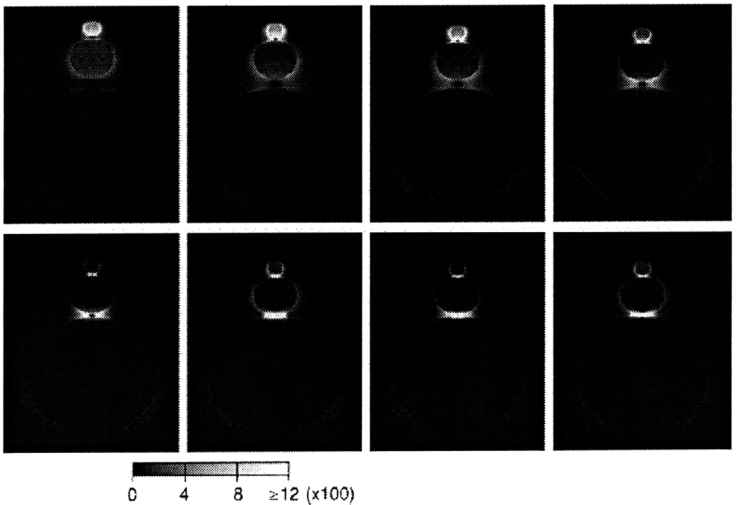

Figure 6.4 Electric field contour in the single nanolens [77].

A design of tunable nano plasmonic resonator (TNPR) is suggested for precise control over the interparticle gaps [78, 79]. TNPR consists of silver and SiO_2 disks stacked vertically rather than being placed horizontally on the substrate, it showed SERS enhancement factors of $(6.1\pm0.3)\times10^{10}$. But, the hot-spot occurs at internal SiO_2 disks, which makes the hot-spot difficult to be located in the vicinity of a target sample as shown in Figure 6.5.

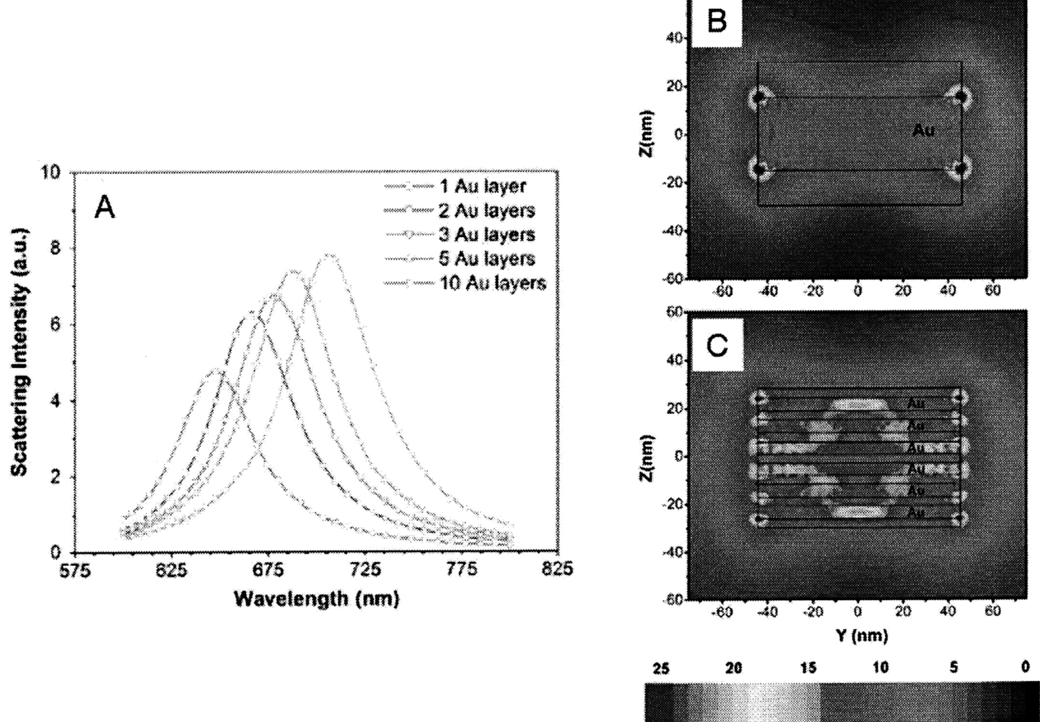

Figure 6.5 TNPR [78]. (A) The effect of the number of layers. (B) One single Au layer design. (C) Six Au layer design.

6.2.2 Tip-enhanced Raman spectroscopy (TERS)

SERS is inherently involved with the metallic SERS substrates which are roughened for the enhancement of Raman signal. However, the heterogeneity of metallic SERS substrates creates variable electromagnetic field enhancement across the surface. It also has been observed that only a very small fraction of adsorbed molecules contribute to SERS. These 'hot spots' limit the utility of the technique and render quantitative measurement unreliable.

As an alternative to the SERS, apertureless scanning near-field optical microscopy can be employed, in which a modified atomic force microscope (AFM) tip or scanning tunneling microscope (STM) tip can be brought into contact with a sample surface. This approach provides highly localized enhancements and offers more uniform enhancement when scanning over the sample. In this approach, the parameters that mostly influence the enhancement factors are the distance of the metal tip from the surface, the tip radius size, the direction of illumination and the exciting laser frequency. Optical quality of the tips is essential, and a tip with a smooth surface and a sharp end, small tip apex, is ideal for the tip-enhanced Raman processes. Ag, Au, and Cu are the materials currently used as metal tips in TERS.

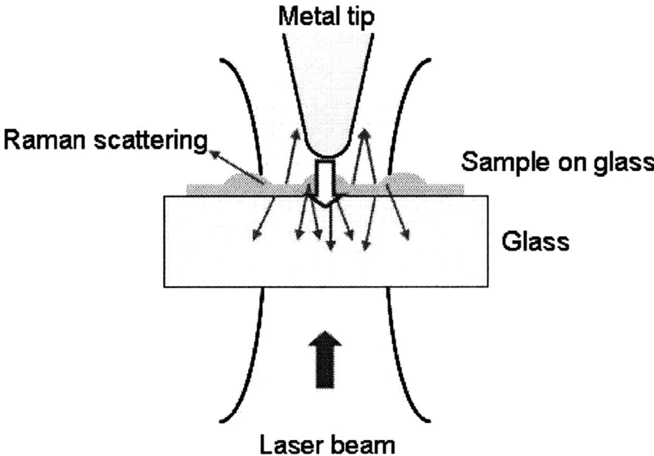

Figure 6.6 A schematic of TERS.

The electromagnetic enhancement described in SERS also account for the enhancement of Raman effect in TERS. However, there is a tip with a spherical end rather than the sphere itself, so we need to consider the effect of the tip in the enhancement. Since there is no closed form solution for the case, we have to rely on numerical simulations to see the effects of the metallic tip in TERS, and there have been several studies about this.

TERS has evolved with the development of scanning near-field optical microscopy. There have been rigorous researches regarding TERS experimentally along with theoretical studies on the fundamental physics underlying TERS. Among the key requirements for realizing an optimal TERS system, the production of suitably shaped tips is a crucial part of any TERS experiment. The tip design determines the location, the magnitude, and the frequency of strong localized enhancement of the electric fields (the hot-spot). Additionally, the design should provide easy engineering schemes at the micro- and nano-meter scales.

There have been a few TERS tip designs developed toward these goals. Using a metalized SPM probe [80] and a SPM tip covered with thin metal layers [81] were the early attempts in realizing TERS. TERS probes were fabricated from an optical fiber with a thin layer of silver islands coated at the tapered tip of the fiber via thermal evaporation [82]. Recently, it was shown that hemispherical gold droplets on top of silicon NWs grown by the vapor-liquid-solid mechanism can produce a significant enhancement of Raman scattering signals [83]. Despite of these attempts, the current TERS tips cannot achieve the high signal enhancement and molecular scale resolutions at the same time which are necessary for scanning molecular scale samples. This chapter presents a new design of plasmonic resonator for TERS that fulfills the requirements of both the high enhancement factor and the easy fabrication scheme, and investigate the characteristics of a new design.

6.3 A conical plasmonic resonator

This section investigates a way of defining and engineering those "hot-spots" in a deterministic manner. This means that the design and fabrication method should provides the predefined information on the size, location and enhancement factor of the hot-spots.

- High Raman enhancement factor: the Raman enhancement factor is defined as the ratio of the Raman intensity with any enhancement mechanism to that in conventional Raman spectroscopy. The high Raman enhancement factor, which results from the large electric field enhancement in part, enables shorter the detecting integration time with the better temporal resolution. The minimum electric field enhancement is 1000 considering the relative intensity (cross section) of Raman spectrum compared to that of infrared spectroscopy.

- The hot-spot at the sample side: the hot-spot should be placed outside the resonator, so the hot-spot can be easily accessible to the target sample. This enables easy manipulation of the hot-spot to the target samples without involving manipulation and adsorption of the samples to the resonators.

- The small sized hot spot: the hot spot should be small enough for scanning and detecting molecular samples. The size of hot-spot will be governed by that of the resonator.

6.3.1 Design of a novel plasmonic resonator

A novel design of a conical plasmonic resonator is shown in Figure 6.7. It consists of multiple thin metal (silver, gold or copper) layers separated by thin dielectric layers in-between. The key design feature is conical metal layers with the decreasing diameter of each layer with a sharp apex at one end. The individual metal layers of the design in Figure 6.7 serve like a metal nanoparticle. The dielectric layers sandwiched by metal layers control the gap between the metal layers, and this provides a deterministic way of controlling the gap at the nanometer scale.

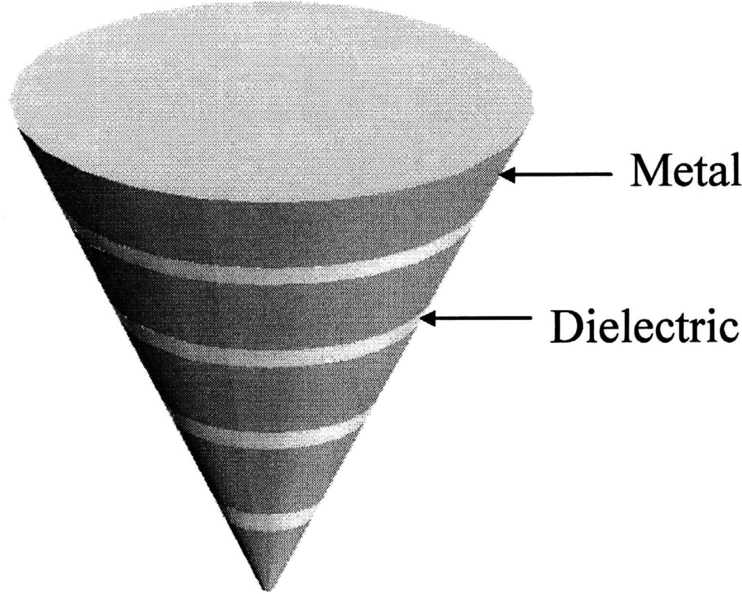

Figure 6.7 A conical plasmonic resonator.

The design is equivalent to an array of separated metal nanoparticles except for the location of the hot-spot. In the conical plasmonic resonator, the hot-spot occurs at the apex of the cone while the hot-spot in the array of metal nanoparticles occur at one gap between the nanoparticles. The location and enhancement mechanism of the hot-spot in the conical plasmonic resonator will be discussed in the later sections.

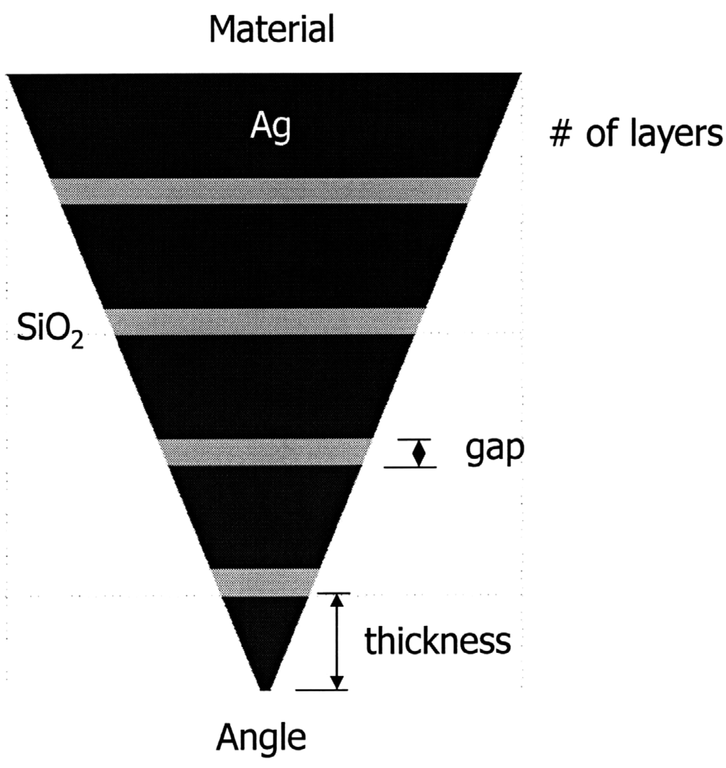

Figure 6.8 Design parameters of a conical plasmonic resonator.

There are several main design parameters in designing the conical plasmonic resonator as shown in Figure 6.8. The parameters include the materials for the metal and dielectric layers, the overall shape of cones (the cone angle and the base diameter), the

number of layers, and thickness of both metal and dielectric layers, and these parameters need to be optimized through parametric simulations because there is no single model or theory that describes the relationship between the location/magnitude of plasmonic resonances and the number/size/shape of multiple nanoparticles.

Silver (Ag) is selected for the metal layer because of its high enhancement in the excitement of visible ranges. Ag has the frequency dependent permittivity, and its value (the measurement data for thin film layer) with respect to the excitation wavelength is plotted in Figure 6.9. Its negative real value provides high enhancement of electric fields. For the dielectric layers, SiO_2 is considered with the relative permittivity 2.25.

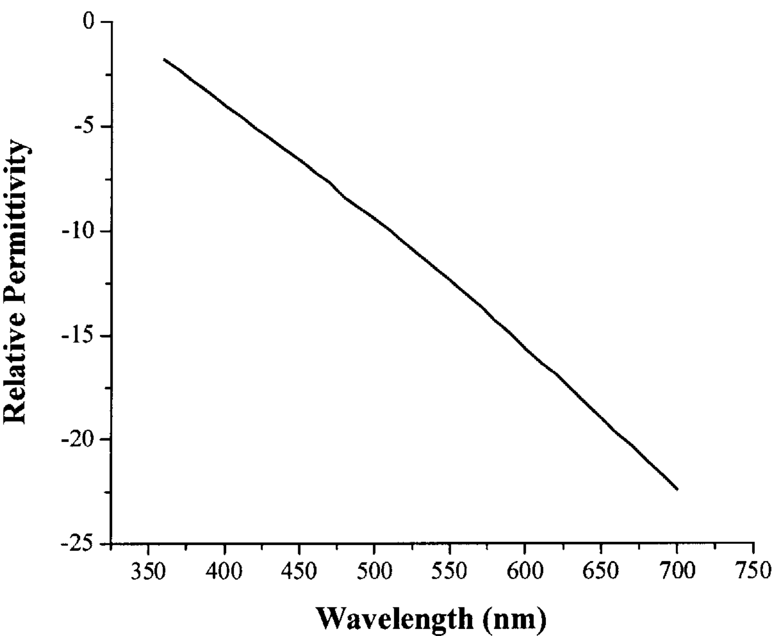

Figure 6.9 Frequency dependent relative permittivity of thin film silver.

The conical shape can locate a "hot-spot" at the apex of the cone, allowing the "hot-spot" to be located directly on the target sample. Compared to other geometries such as spheres and disks, that conical shape also provides for more enhancements because of the confinement of plasmonic resonance modes at the tip as in the lightning-rod.

Stacked Ag layers, separated by thin SiO_2 layers, make the free electrons in Ag layers interact each other, so further enhancement at the tip and the control over resonant frequencies can be achieved. In a system of multi particles (layers), the distances (gaps) between the particles are the critical factor to determine the enhancement and frequency of plasmon resonances. Compare to the lateral positioning of nano-scale particles, the thickness of thin films can be controlled up to Å scale, so we can engineer the array of nanostructures as designed.

Another key features in conical layer configuration is that the thickness of each layer can be designed such that all the layers except for the apex layer can be driven in phase by an incident fields (driving frequency is lower than the those of the plasmonic resonance), resulting in the high driving fields on the apex layer which is in a resonance. Otherwise, all the layers can be in resonances by changing the thickness of each layer.

6.3.2 Finite element analysis and the simulation results

This section focuses on the effects of the number of the layers and the height of the apex layer on the electric field enhancement. Finite element analysis of electromagnetic waves

is carried out using COMSOL Multiphysics® software (COMSOL, Inc., Burlington, MA).

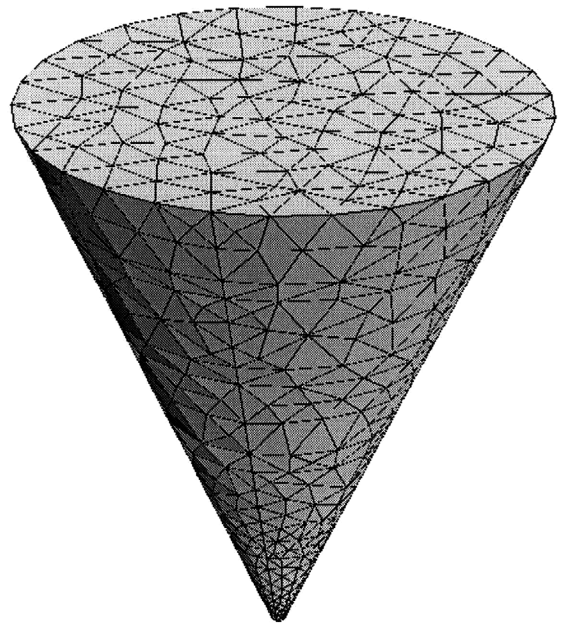

Figure 6.10 FEM mesh modeling of the conical plasmonic resonator.

The meshed model for 5 Ag layers is shown in Figure 6.10. The exciting laser is modeled as the electric field incident from the one boundary. The other boundaries are modeled using matched boundary conditions. It is assumed that the conical plasmonic resonator is surrounded by the air with the vacuum permittivity ($\varepsilon_0 = 8.854\times10^{-12}$ F/m). In each simulation, the wavelength of the incident light is defined with the corresponding permittivity of Ag. The permittivity of SiO_2 is assumed to be 2.25 regardless of the excitation frequency.

In the simulations, the thickness of Ag layers is set to 20 nm, and the gap between the Ag layers determined by the thickness of the SiO_2 layers is 5 nm. The angle of cone is 45 °, and its top diameter (the diameter of the largest layer) is 100 nm. Figure 6.11 shows the result of electromagnetic simulation with an incident filed whose polarization is parallel to the cone axis. The "hot-spot" is located at the apex of cone as predicted.

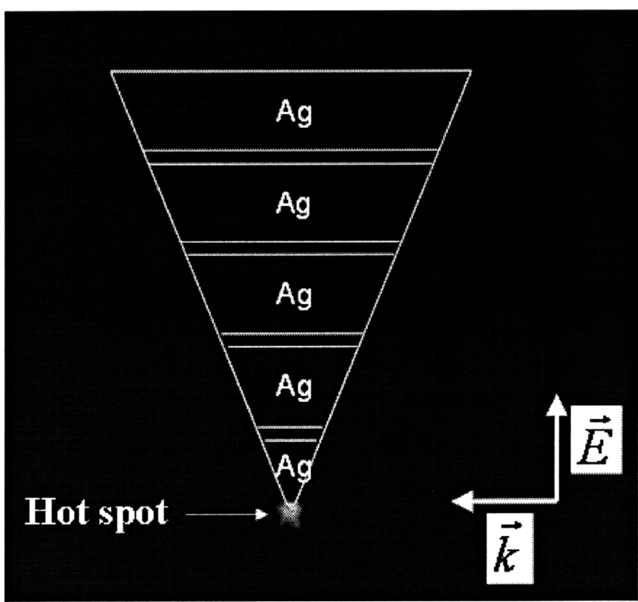

Figure 6.11 The hot-spot of the conical plasmonic resonator.

Figure 6.12 summarize the effect of the size of four single solid Ag cones with different heights (20, 45, 70, and 120 nm). In all cases, the four cones show a resonance (whether primary or secondary) at the 400nm excitation. The three short cones (20, 45 and 75 nm long) have the primary resonance at the 400 nm excitation with the enhancement factors proportional to the height. The 120 nm-long cone has the primary resonance with the enhancement factor larger than 4000 at the 440 nm excitation as well

as a secondary resonance at the 400nm excitation. The increased free surface electrons with the increasing the height result in the increased enhancement factor.

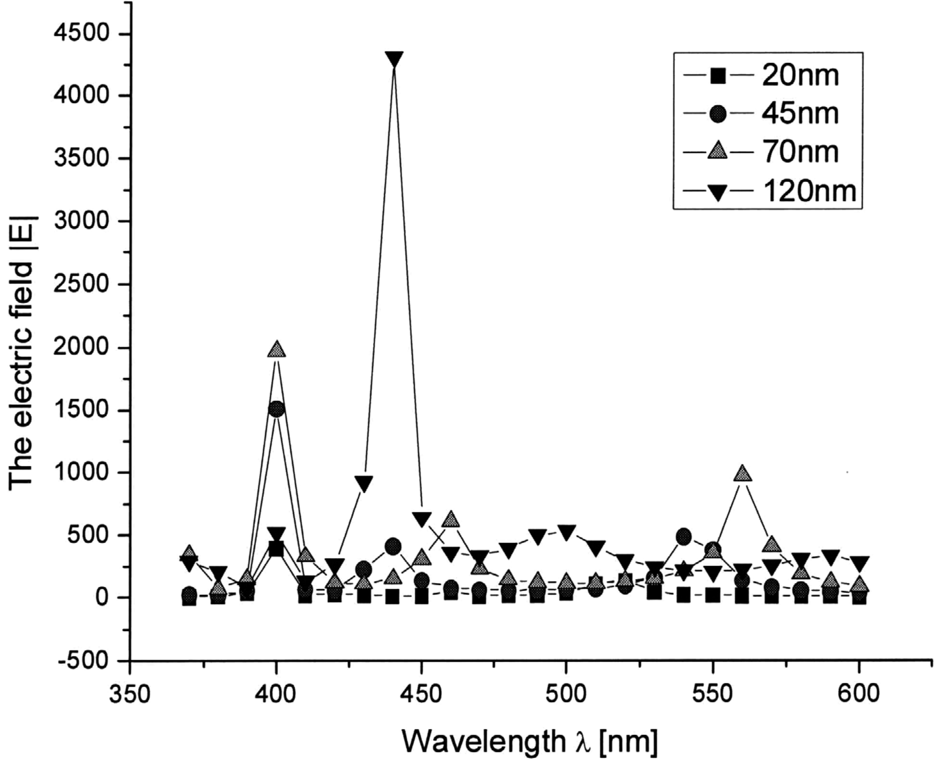

Figure 6.12 The electric field enhancement factor vs. the height of the cone.

The size dependency of the resonant frequency can be explained using a spherical nanoparticle model under the electrostatic assumption. For particles smaller than the mean-free-path of the materials (~70 nm in case of silver), the resonance frequencies do not change much. By Lorentz force law, the force acting on a unit charge (or electron) due to a point charge q is

$$F_C = \frac{1}{4\pi\varepsilon_0}\frac{q}{r^2}. \qquad (6.1)$$

In the surface plasmon resonance, the charges are placed closer (smaller r) for smaller particles resulting in the increase in the force, but smaller surface area gives the smaller number of charges. Therefore, the size effect in the total electrostatic force cancels out giving no shifts in the resonance frequencies.

For larger particles than the mean-free-path of the materials, the resonance peaks shift to the larger wavelengths (red-shifts) and get broadened with the increasing size of the particles. As the size increases, the electrons in the particles shift further due to the exciting fields. This means the increase in the distance of the dipole moments, resulting in decreased restoring forces and the decreased resonance frequencies (the increased wavelengths).

Figure 6.13 summarizes the effect of the number of Ag layers on the EF at the hot-spot as well as that of a single solid Ag cone (120 nm long). The 3 and 5 layered designs show the primary resonance peaks at the 400 nm excitation which is the primary resonance frequency of the single Ag layer. The peak magnitudes of |E| depend on the number of layers, and the resonator with 3 Ag layers show g larger than 11,000. The approximate Raman enhancement factor G is larger than 10^{16} from this electric field enhancement. The fact that increasing the number of Ag layers does not result in the increase in EF suggests that the further investigation to optimize the design parameters be pursued.

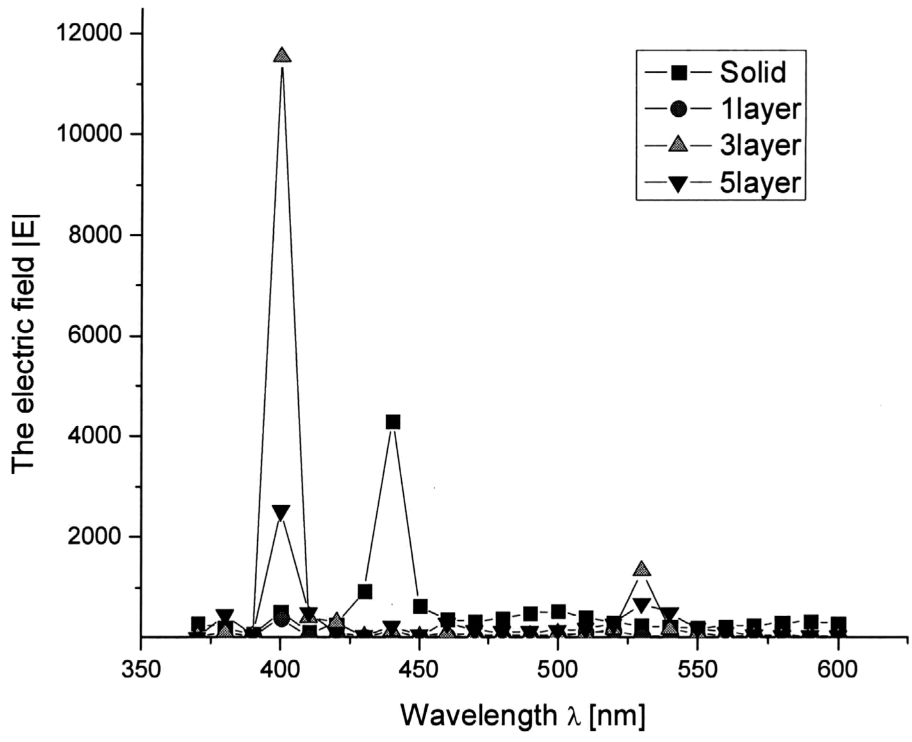

Figure 6.13 The electric field enhancement factor vs. the number of Ag layers.

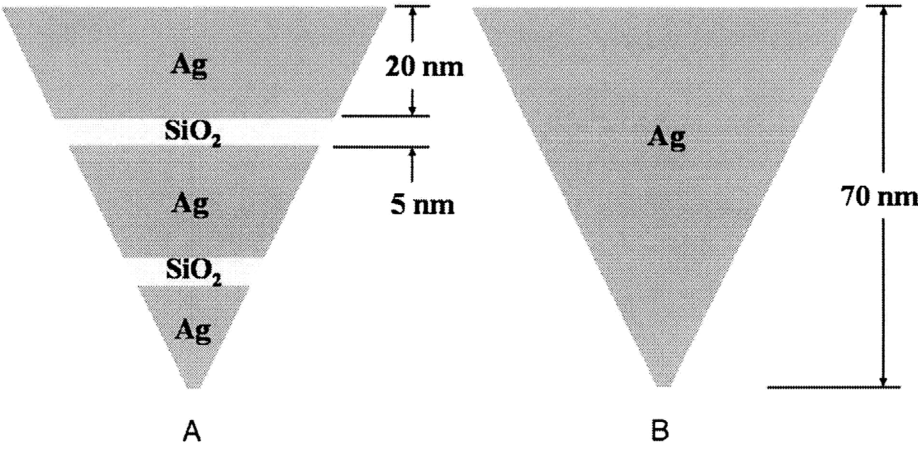

Figure 6.14 The conical plasmonic resonators: (A) A resonator with 3 Ag layers. (B) A solid single Ag resonator.

The results of two designs of the resonator, a conical resonator with 3 Ag layers and a single solid Ag resonator as shown in Figure 6.14, were compared in order to discuss the coupling of the plasmonic resonance between nanoparticles. In both cases, the overall height of the resonators is 70nm, and the resonance frequency is 400nm. More importantly, the hot-spots always occur at the apex of the cone at both cases. However, the resonator with 3 Ag layer exhibit much higher g of 11,550 than that of solid single Ag resonator (g = 1,975). The field enhancement factor $g > 10^4$ can provide the Raman enhancement factor $G > 10^{16}$. This enhancement is high enough for single molecule detection with the hot-spot at the apex of the tip. The huge Raman EF may result from the strong interaction of electrons on the boundary of each layer separated by the small gap (5nm).

Compared to other geometries such as spheres or disks, the conical shape also provides for more enhancements because of the confinement of plasmonic resonance modes at the tip as in the lightning-rod. Stacked Ag or Au layers, separated by thin SiO_2 layers, make the metal layers interact each other, so further enhancement at the tip and control over resonance frequencies can be achieved. In a system of multi particles (layers), the distances (gaps) between the particles are the critical factor to determine the enhancement and frequency of plasmon resonances.

In order to explain our hypothesis in detail, we discuss the shape dependence of the resonant frequency in the case of ellipsoid [84]. If the incident electric field is parallel to a principal axis of a small, homogeneous ellipsoid of volume V, then its induced dipole

moment is (under the electrostatic assumption in which the size of the ellipsoid is less than a quarter of the wavelength) [84]

$$\vec{p} = V \frac{\varepsilon - \varepsilon_0}{\varepsilon_0 + L(\varepsilon - \varepsilon_0)} \vec{E} . \tag{6.2}$$

Here ε and ε_0 denote the permittivity of the Ag and the medium (the air), respectively. L is the geometrical factor ranging from 0 to 1. The real part of the permittivity of Ag is – 4 at the incident fields with λ = 400nm, which corresponds to an ellipsoid with L = 0.2. The upper Ag layers should have its resonance frequencies higher than that of the cone apex layer, so the surface plasmon in the upper layers is an in-phase excitation to the plasmon resonance of the cone apex layer [75~77].

The design of the conical plasmonic resonators requires further optimization by considering the effects of the additional design parameters. Additional factors such as the effects of the sample (dielectric material) and substrates can be included. The fabrication of the conical plasmonic resonators with experimental verifications is in progress, and this will enables better understandings on the fundamental of the interactions of the incident light with an object at the nanometer scale.

6.3.3 Discussion on fabrication and assembly of the plasmonic resonator

In realizing the conical plasmonic resonator, there are two main issues in realizing the resonator at the tip of nanoprobe: 1) how to fabricate the conical layered plasmonic resonator at the nano-scale, and 2) how to assemble it at the tip of nanoprobe.

A conical shape of the plasmonic resonator provides the maximum enhancement, but it is very challenging to realize using the existing fabrication techniques. An alternative is a 2-dimensional resonator design, a wedge shaped plasmonic resonator. This wedge shaped plasmonic resonator may have a hot spot in a line form while the conical plasmonic resonator has a point hot spot at its apex. If we can make a thin wedge with about 50nm thickness, then the line hot spot can be localized more. A microtome can be used to slide V-shaped layers with a thin thickness. Additionally, a way of assembling the resonators at the tip of CNT AFM probes should be investigated in the future.

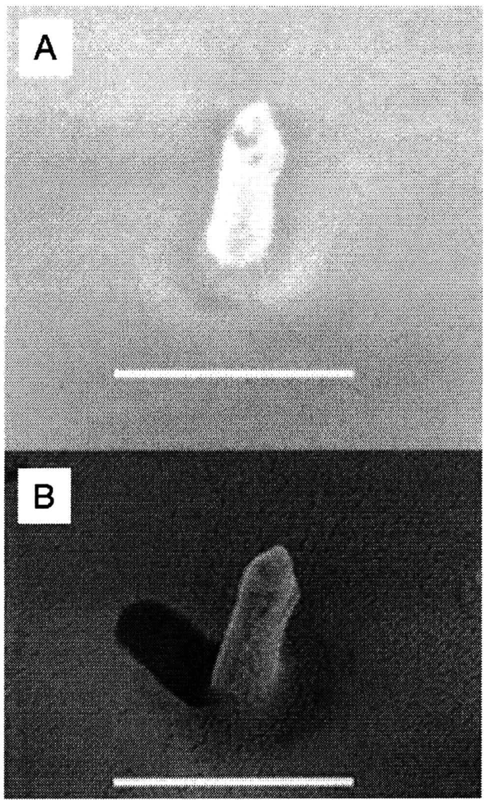

Figure 6.15 A CNT probe for TERS with gold coating: (A) Before gold deposition. (B) After 10nm gold layer deposition.

An immediate application of CNT AFM probes to TERS can be possible by coating the CNT tip with thin metal layer. Figure 6.15 show a CNT tip with 10nm thick gold coating. The directional deposition of thin gold layer by evaporation can enable a small amount of gold particles at the tip apex.

6.4 Summary

TERS can be one of the potential applications of the CNT-tipped AFM probes utilizing high aspect ratio CNT tips that locate a plasmonic resonator close to a target sample. The limitation of SERS, stochastic distributions of "hot-spots" in terms of the location and magnitude, can be overcome with a plasmonic resonator consisting of a stack of multiple Ag layers with a conical overall shape. In the conical plasmonic resonator, the gap between Ag layers can be controlled in-between dielectric layers, and the hot-spot occurs at the apex of the conical resonator because of the confined local fields when it is excited parallel to the axis of conical resonators. The simulation results show possibility of high Raman intensity enhancement up to 10^{14} that is applicable to SMD. The fabrication and experimental verification remains as future work.

7 Conclusion

7.1 Summary and major contributions

This thesis has demonstrated a deterministic assembly of individual carbon nanotubes by transplanting one CNT strand to a MEMS cantilever. This thesis has also provided a robust technique for realizing practical products with CNTs by transforming individual CNTs assemblable, which even enabled manual assembly in a deterministic way.

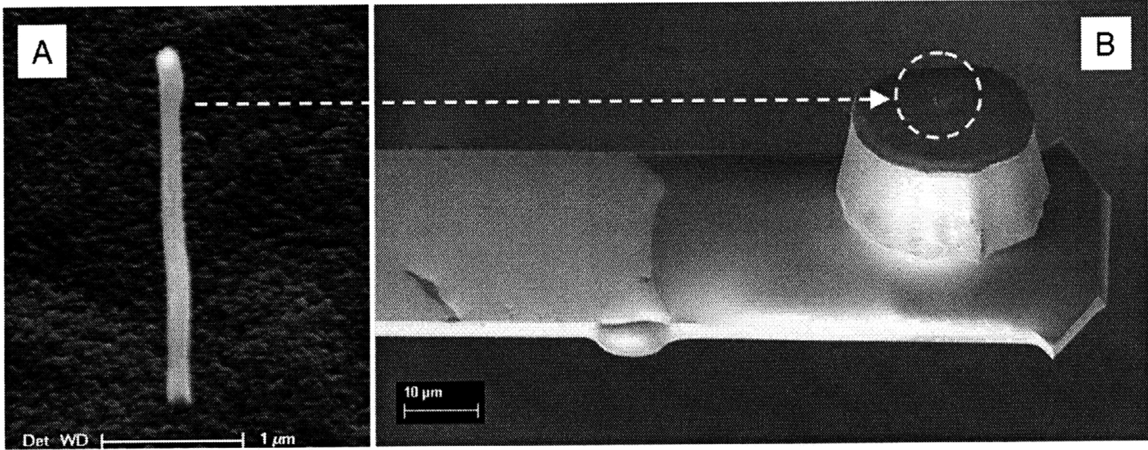

Figure 7.1 Transplanting assembly of the individual CNTS: (A) The single CNT. (B) A CNT-tipped AFM probe with a single CNT tip.

The key idea of the transplanting assembly was to grow individual CNT strands on a separate substrate, to encapsulate each CNT into a polymer carrier block and to transplant it to the target location. The individual CNTs were grown using nanofabrication process while each CNT was transplanted via microfabrication technique, and each step was

carried out at its optimal process conditions. This new assembly method enabled the development of CNT-tipped AFM probes in a predictable and repeatable manner. The major research topics discussed in this thesis were: (1) the methods to grow vertically aligned single strand CNTs at predefined locations, (2) the encapsulation strategy to preserve/control the orientation/exposed length of an individual CNT during transplanting, and (3) the assembly scheme to locate/release an individual CNT at the target location.

An array of CNTs was grown from the Ni nano-dots, which were defined on Si substrates using electron-beam lithography followed by metal deposition and lift-off processes. Each CNT strand was embedded into a MEMS scale polymer block which serves as a CNT carrier. A double polymeric layer encapsulation design was implemented: the top SU-8 forms the body of the carrier while the bottom PMGI layer holds the body until the release of the carrier from the substrate and then is going to be removed to expose the CNT tip with a predefined length. A model using fluid and solid mechanics was developed to predict interactions of individual CNTs with liquid polymers.

Manual assembly of a polymer block to the end of a tipless AFM cantilever formed a CNT-tipped AFM probe. No laborious weeding, trimming and welding process was required, and the transplanting assembly technique enabled reliable assembly of CNT tips on various AFM cantilevers. The scanning results over a calibration grating and a biological sample confirmed the CNT AFM probe's much improved scanning performance and potential for soft biological samples. As an extended application of the

CNT AFM probes, a new design of plasmonic resonator for TERS was suggested and analyzed.

The major contributions of this thesis are threefold. First, design and fabrication schemes to achieve transplanting assembly of the individual nanostructures were proposed. Double polymeric layer design enabled us to control the length of CNTs deterministically and to release the CNTs easily from the substrate. SU8-2015 was used for the MEMS carrier layer and PMGI SF 11 for the bottom layer. Well-established process parameters for SU8 provided reliable fabrication results with various achievable thicknesses ranging from 1 to 1,000 μm, which will enable versatile MEMS carriers aimed at the target applications. This thesis also opened up a new application of PMGI organic solutions for integrating the nanostructures into MEMS. Its flexible range of the thickness (about 10 nm to a few μm) in combination with process compatibility to novolac-based epoxy provides easy implementation to a variety of applications for microfabrication.

Second, fabrication of a micro-scale device with nanostructure functionality has been achieved through realizing the CNT-tipped AFM probes by transplanting assembly. The superior properties of CNTs, such as small size, high aspect ratio, and high toughness and wear resistance, makes them an ideal candidate for a tip of AFM probes. The scanning experiment over various samples (AFM standard gratings, critical-angle transmission gratings, and soft biological samples) demonstrated the usability of the fabricated CNT-tipped AFM probes through transplanting assembly. In addition to that, transplanting assembly concept provided a mechanical assembly method to achieve the CNT-tipped

AFM probes in a predictable and repeatable manner, so we could expect the quality of CNT tips upon assembly of the single CNT tips to MEMS cantilevers.

Finally, physicochemical interactions of the individual CNTs with polymers and chemicals have been investigate both analytically and experimentally. A model has been developed to predict the effects of fluidic sharing forces during the spin-coating step on the alignment of the individual CNTs. A negligible change in the CNT alignment compared to the diameters of CNTs was achieved by careful considerations of process parameters and material selections, and the estimated results matched with the experimental verifications. The amount of the degraded graphene wall structures caused by the interactions with polymers and etching chemicals has been monitored qualitatively and quantitatively. HRTEM showed the preservation of the graphene wall layers through transplanting assembly procedures, and the characterization by Raman spectroscopy confirmed the observation quantitatively.

The transplanting assembly method can open up the opportunity of creating CNT-based devices that could not otherwise be reliably made, and enabling the massive parallel assembly of nanostructures in a deterministic manner with high productivity.

7.2 Discussions and future work

The concept and method of transplanting assembly provides a framework for deterministic assembly of the individual nanostructures. This technique can be developed further in several ways, and the following sections will discuss the future work with possible solutions in the three main categories.

7.2.1 CNT growth

The growth mechanism of CNTs still remains as the key questions of CNT researches. In the application of CNTs for SPM, CNTs with smaller diameters are preferable. We recently achieved the small sized (down to 50 nm in diameter) catalytic dots by optimizing the process parameters in electron beam lithography. Process optimization in growing vertically aligned CNTs from the various sized catalytic dots by PECVD will provide better understanding of the growth mechanism of the freestanding individual CNTs.

Our recent attempts to grow the CNTs on various sized catalytic dots showed the transition of the internal graphene layers from stacked-cone structures to bamboo-like structures as the size of Ni catalyst shrinks, which implied a possibility of growing CNTs with cylindrical graphene layers by DC-PECVD using Ni catalysts. The CNT growth experiment on small catalysts as mentioned in the above, along with different catalytic materials such as cobalt and iron, will help us understand how the CNTs grow.

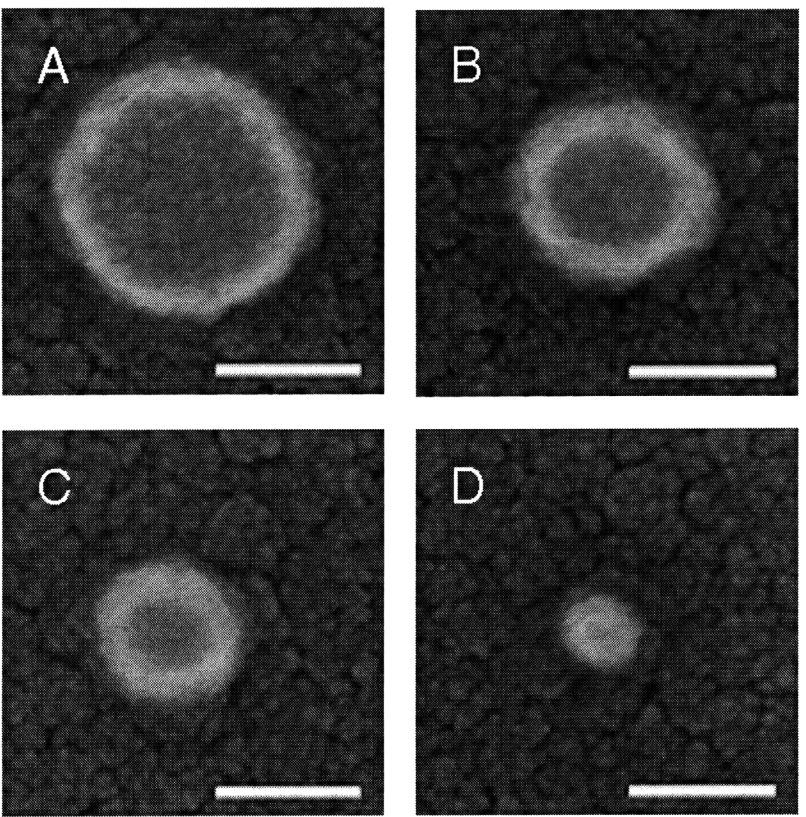

Figure 7.2 SEM images of Ni catalysts with various diameters: (A) diameter = 175 nm. (B) 117 nm. (C) 87 nm. (D) 50 nm. (scale bars = 100 nm).

7.2.2 Encapsulation of the individual CNTs

This thesis has demonstrated transplanting assembly of the individual CNTs by implementing double polymer layer design through photolithography. These design and fabrication schemes can be expanded according to the requirements of the potential applications. In the applications where the MEMS blocks need to be removed after transplanting assembly, easy removable polymer, for example, AZ 5214 E, can be used

instead of SU8 as it can be etched easily using acetone after it is patterned. AZ 5214 E has nominal thickness of 1~2 μm and is also known to be compatible with PMGI for multiple layer processing, and it will be an ideal candidate for non-structural applications.

Thin metal layer with pre-patterned AZ 5214 E layer can replace the SU8 layers when electrical connections are required for CNTs. Additionally, the thickness of the metal layer can be controlled precisely up to nanometer scales, so this deposition process can be implemented for the applications where the precise CNT length control at the nanometer resolution is needed.

7.2.3 Transfer of the individual CNTs

The method of transplanting assembly of the individual CNTs presented in this thesis is manual transfer of each CNT with a single MEMS carrier. The adhesive curing procedure takes 20~25 min while the transfer procedure takes only 2~3 min for the cantilever approach and the CNT release steps. This implies that more rapid assembly can be achieved by use of a quick curing adhesive with low-viscosity (1~10 cSt). Alternatively, simultaneous transfer of the single CNTs is possible by mounting multiple cantilevers and addressing the individual CNTs and MEMS carriers at the matching locations.

A large scale assembly of the individual CNTs can be readily possible through parallel transplanting assembly with the aid of micro-scale assembly techniques. One example is the fluidic assembly technique based on patterned shapes of hydrophobic SAMs and capillary forces to self-assemble microfabricated silicon blocks onto silicon

and quartz substrates demonstrated by Srinivasan et al. [85] as shown in Figure 7.3. Patterns are defined on the substrate to indicate the locations of the individual MEMS carriers encapsulating the single CNTs. When the direction of assembly also needs to be defined, combination of both hydrophobic and hydrophilic treatment on the top and bottom surface of the carriers provides control over the direction. Etching of the Si substrate in combination with the gravitational force can be another type of driving forces to utilize in assembling the individual CNTs [86]. These parallel assembly schemes can be implemented in fabricating an array of CNTs for field emission applications.

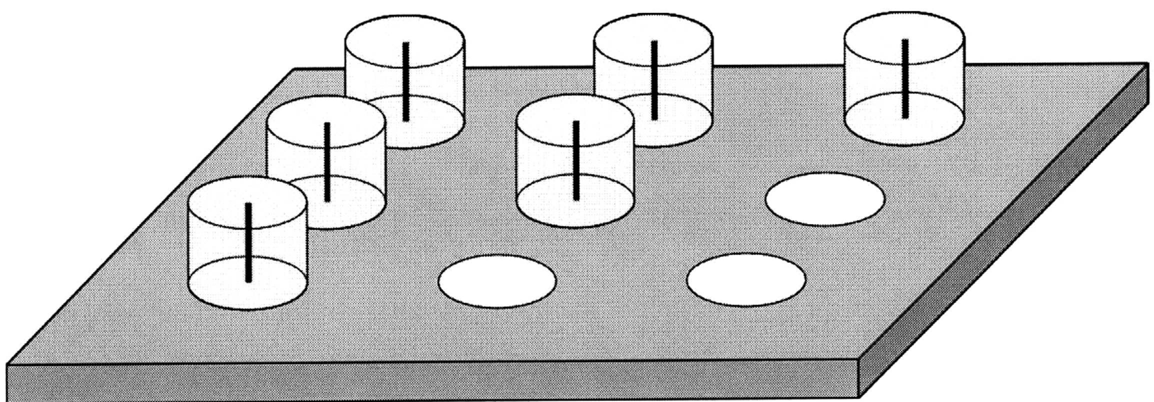

Figure 7.3 Large-scale transplanting assembly of the individual CNTs using patterns defined on the substrate.

Bibliography

1. S. G. Kim, "Multi-scale assembly: design, processes and complexity," Nanomanufacturing, Ed. S. Chen, eds., American Scientific Publishers, Stevenson Ranch, California, in press.
2. T. A. E. Aguizy, "Large-scale fabrication and assembly of carbon nanotubes via nanopelleting," M.S. Thesis, Massachusetts Institute of Technology (2004).
3. T. A. El-Aguizy, J. Jeong, Y. Jeon, W.Z. Li, Z. F. Ren, and S.-G. Kim, "Transplanting carbon nanotubes," Appl. Phys. Lett. 85, 5995-5997 (2004).
4. S. Iijima, "Helical microtubules of graphitic carbon," Nature 354, 56-58 (1991).
5. N.R. Franklin, Q. Wang, T. W. Tombler, A. Javey, M. Shim, and H. Dai, "Integration of suspended carbon nanotube arrays into electronic devices and electromechanical systems," Appl. Phys. Lett., Vol. 81, 913-915 (2002).
6. J. Chung, K. Lee, J. Lee, and R. S. Ruoff, "Toward large-scale integration of carbon nanotubes," Langmuir 20, 3011-3017 (2004).
7. J. C. Huie, "Guided molecular self-assembly: a review of recent efforts," Smart Mater. Struct. 12, 264-271 (2003).
8. Y. Kim, N. Minami, W. Zhu, S. Kazaoui, R. Azumi and M. Matsumoto, "Langmuir-Blodgett films of single-wall carbon nanotubes: layer-by-layer deposition and in-plane orientation of tubes," Jpn. J. Appl. Phys. 42, 7629-7634 (2003).
9. Y. Huang, X. Duan, Q. Wei and C.M. Lieber, "Directed assembly of one-dimensional nanostructures into functional networks," Science 291, 630-633 (2001).
10. S. Jin, D. Whang, M. C. McAlpine, R. S. Friedman, Y. Wu, and C. M. Lieber, "Scalable interconnection and integration of nanowire devices without registration," Nano Lett. 4, 915-919 (2004).
11. J. Gao, A. Yu, M. E. Itkis, E. Bekyarova, B. Zhao, S. Niyogi and R. C. Haddon, "Large-scale fabrication of aligned single-walled carbon nanotube array and

hierarchical single-walled carbon nanotube assembly," J. Am. Chem. Soc. 126, 16698 (2004).

12. S. Jung and C. Livermore, "Achieving selective assembly with template topography and ultrasonically induced fluidic forces," Nano Lett. 5, 2188-2194 (2005).
13. F. Eid, S. Jung, and C. Livermore, "Templated assembly by selective removal: simultaneous, selective assembly and model verification," Nanotechnology 19, 285602 (2008).
14. K. Keren, R. S. Berman, E. Buchstab, U. Sivan and E. Braun, "DNA-templated carbon nanotube field-effect transistor," Science 302, 1380-1382 (2003).
15. P. A. Smith, C. D. Nordquist, T. N. Jackson, T. S. Mayer, B. R. Martin, J. Mbindyo and T. E. Mallouk, "Electricfield assisted assembly and alignment of metallic nanowires," Appl. Phys. Lett. 77, 1399-1401 (2000).
16. H.A. Pohl, Dielectrophoresis, Cambridge University Press, Cambridge (1978).
17. M. R. Diehl, S. N. Yaliraki, R. A. Beckman, M. Barahona and J. R. Heath, "Self-assembled, deterministic carbon nanotube wiring networks," Angew. Chem. Int. Ed. 41, 353-356 (2002).
18. R. H. M. Chan, C. K. M. Fung and W. J. Li, "Rapid assembly of carbon nanotubes for nanosensing by dielectrophoretic force," Nanotechnology 15, S672-S677 (2004).
19. X. Duan, Y. Huang, Y. Cui, J. Wang and C. M. Lieber, "Indium phosphide nanowires as building blocks for nanoscale electronic and optoelectronic devices," Nature 409, 66-69 (2001).
20. S. J. Kang, C. Kocabas, T. Ozel, M. Shim, N. Pimparkar, M. A. Alam, S. V. Rotkin and J. A. Rogers, "High-performance electronics using dense, perfectly aligned arrays of single-walled carbon nanotubes," Nature Nanotechnology 2, 230-236 (2007).
21. Y. C. Chang, C. S. Chang, D. C. Wang, M. H. Lee, T. F. Wang, M. Y. Wu, T. Y. Fu, and T. T. Tsong, "Nanoscale imaging of biomolecules by controlled carbon nanotube probes," Jpn. J. Appl. Phys. 43, 4517-4520 (2004).

22. L. Guo, J. Liang, S. Dong, Z. Xu, and Q. Zhao, "Property of carbon nanotube tip for surface topography characterization," Appl. Surf. Sci. 228, 53-56 (2004)
23. H. Dai, J. H. Hafner, A. G. Rinzler, D. T. Colbert, and R. E. Smalley, "Nanotubes as nanoprobes in scanning probe microscopy," Nature 384, 147-150 (1996).
24. C. V. Nguyen, R. M. D. Stevens, J. Barber, J. Han, and M. Meyyappan, "Carbon nanotube scanning probe for profiling of deep-ultraviolet and 193 nm photoresist patterns," Appl. Phys. Lett. 81, 901-903 (2002).
25. C. V. Nguyen, K. Chao, R. M. D. Stevens, L. Delzeit, A. Cassell, J. Han, and M. Meyyappan, "Carbon nanotube tip probes: stability and lateral resolution in scanning probe microscopy and application to surface science in semiconductors," Nanotechnology 12, 363-367 (2001).
26. L. Larsen, K. Moloni, F. Flack, M. A. Eriksson. M. G. Lagally, and C. T. Black, "Comparison of wear characteristics of etched-silicon and carbon nanotube atomic-force microscopy probes," Appl. Phys. Lett. 80, 1996-1998 (2002).
27. S. Akita, H. Nishijima, Y. Nakayama, F. Tokumasu, and K. Takeyasu, "Carbon nanotube tips for a scanning probe microscope: their fabrication and properties," J. Phys. D.: Appl. Phys. 32, 1044-1048 (1999).
28. H. Nishijima, S. Kamo, S. Akita, Y. Nakayama, K. I. Hohmura, S. H. Yoshimura, and K. Takeyasu, "Carbon-nanotube tips for scanning probe microscopy: Preparation by a controlled process and observation of deoxyribonucleic acid," Appl. Phys. Lett. 74, 661-664 (1999).
29. J. H. Hafner, C. L. Cheung, T. H. Oosterkamp and C. M. Lieber, "High-yield assembly of individual single-walled carbon nanotube tips for scanning probe microscopies," J. Phys. Chem. B 105, 743-746 (2001).
30. K Carlson, K. N. Anderson, V. Eichhorn, D. H. Petersen, K. Mølhave, I. Y. Y. Bu, K. B. K. Teo, W. I. Milne, S. Fatikow, and P. Bøggild, "A carbon naonfibre scanning probe assembled using an electrothermal microgripper," Nanotechnology 18, 345501 (2007).

31. R. M. D. Stevens, N. A. Frederick, B. L. Smith, D.E. Morse, G.D. Stucky, and P. K. Hansma, "Carbon nanotubes as probes for atomic force microscopy," Nanotechnology 11, 1-5 (2000).
32. D. Stevens, C. Nguyen, A. Cassell, L. Delzeit, M. Meyyappan, and J. Han, "Improved fabrication approach for carbon nanotube probe devices," Appl. Phys. Lett. 77, 3453-3455 (2000).
33. A. Hall, W.G. Matthews, R. Superfine, M.R. Falvo, and S. Washburn, "Simple and efficient method for carbon nanotube attachment to scanning probes and other substrates," Appl. Phys. Lett. 82, 2506-2508 (2003).
34. J. Tang, G. Yang, Q. Zhang, A. Parhat, B. Maynor, J. Liu, L. Qin, and O. Zhou, "Rapid and reproducible fabrication of carbon nanotube AFM probes by dielectrophoresis," Nano Lett. 5, 11-14 (2005).
35. J. H. Hafner, C. L. Cheung, and C. M. Lieber, "Growth of nanotubes for probe microscopy tips," Nature 398, 761-762 (1999).
36. J. H. Hafner, C. L. Cheung, and C. M. Lieber, "Direct growth of single-walled carbon nanotube scanning probe microscopy tips," J. Am. Chem. Soc. 121, 9750-9751 (1999).
37. E. Yenilmez, Q. Wang, R.J. Chen, D. Wang, and H. Dai, "Wafer scale production of carbon nanotube scanning probe tips for atomic force microscopy," App. Phys. Lett. 80, 2225-2227 (2002).
38. Q. Ye, A. M. Cassell, H. Liu, K. Chao, J. Han, and M. Meyyappan, "Large-scale fabrication of carbon nanotube probe tips for atomic force microscopy critical dimension imaging applications," Nano Lett. 4, 1301-1308 (2004).
39. D. J. Burns and K. Youcef-Toumi, "Shortening carbon nanotube-tipped AFM probes," International Journal of Nanomanufacturing 1, 799-809 (2007).
40. L. A. Wade, I. R. Shapiro, Z. Ma, S. R. Quake, and C. P. Collier, "Correlating AFM probe morphology to image resolution for single-wall carbon nanotube tips", Nano Lett. 4, 725-731 (2004).

41. E. S. Snow, P. M. Campbell, and J. P. Novak, "Single-wall carbon nanotube atomic force microscope probes," Appl. Phys. Lett. 80, (2002).
42. E. S. Snow, P. M. Campbell, and J. P. Novak, "Atomic force microscopy using single-wall C nanotube probes," J. Vac. Sci. Technol. B 20(3), 822-827 (2002).
43. S. D. Solares, Y. Matsuda, and W. A. Goddard III, "Influence of the carbon nanotube probe tilt angle on the effective probe stiffness and image quality in tapping-mode atomic force microscopy," J. Phys. Chem. B 109, 16658-16664 (2005).
44. M. C. Strus, A. Raman, C.-S. Han, and C. V. Nguyen, "Imaging artefacts in atomic force microscopy with carbon nanotube tips," Nanotechnolgy 16, 2482-1492 (2005).
45. K. Moloni, A. Lal, and M. Lagally, "Sharpened carbon nanotube probes," Proceedings of SPIE 4098, 76-83 (2000).
46. K. Moloni, "Method for sharpening nanotube bundles," U. S. Patent 6452171 (2002).
47. J. Martinez, T. D. Yuzvinsky, A. M. Fennimore, A. Zettle, R. Garcia, and C. Bustamante, "Length control and sharpening of atomic force microscope carbon nanotube tips assisted by an electron beam," Nanotechnology 16, 2493-2496 (2005).
48. C. P. Collier, M. Ziyang, S. R. Quake, I. R. Shapiro, and L. Wade, "Method for manufacturing single wall carbon nanotube tips," U. S. Patent 7211795 (2007).
49. Y. C. Chang, D. C. Wang, C. S. Chang, and T. T. Tsong, "Easy method to adjust the carbon nanotube probe of an atomic force microscope," Appl. Phys. Lett. 82, 3541-3543 (2003).
50. Z. Deng, E. Yenilmez, A. Reilein, J. Leu, H. Dai, and K. A. Moler, "Nanotube manipulation with focused ion beam," Appl. Phys. Lett. 88, 023119 (2006).
51. Nanoscience Instruments, Inc. (http://www.nanoscience.com).
52. R. F. Probstein, Physicochemical Hydrodynamics, John Wiley & Sons, Inc., Hoboken, New Jersey (2003).
53. F. M. White, Fluid Mechanics, McGraw-Hill, Singapore (1988).

54. M. Dresselhaus, G. Dresselhaus, P. Avouris, Eds., Carbon nanotubes: synthesis, sructure properties and applications, Springer-Verlag, Berlin (2001).
55. T. W. Ebbesen, P. M. Ajayan, "Large-scale synthesis of carbon nanotubes," Nature 358, 220–222 (1992).
56. C. Journet, W. K. Maser, P. Bernier, A. Loiseau, M. Lamy De La Chapelle, S. Lefrant, P. Deniard, R. Lee, J. E. Fischer, "Large-scale production of single-walled carbon nanotubes by the electric-arc technique", Nature 388, 756-758 (1997).
57. T. Guo, P. Nikolaev, A. Thess, D.T. Colbert, R.E. Smalley, "Catalytic growth of single-walled nanotubes by laser vaporization", Chem. Phys. Lett. 243, 49-54 (1995).
58. V. Ivanov, J. B. Nagy, Ph. Lambin, A. Lucas, X. B. Zhang, X. F. Zhang, D. Bernaerts, G. Van Tendeloo, S. Amelinckx, J. Van Landuyt, "The study of carbon nanotubules produced by catalytic method," Chem. Phys. Lett. 223, 329-335 (1994).
59. D. S. Bethune, C. H. Kiang, M. S. deVries, G. Gorman, R. Savoy, J. Vazquez, R. Beyers, "Cobalt-catalysed growth of carbon nanotubes with single-atomic-layer walls," Nature 363, 605-607 (1993).
60. A. Thess, R. Lee, P. Nikolaev, H. Dai, P. Petit, J. Robert, C. Xu, Y. H. Lee, S. G. Kim, A. G. Rinzler, D. T. Colbert, G. E. Scuseria, D. Tomanek, J. E. Fischer, R. E. Smalley, "Crystalline ropes of metallic carbon nanotubes," Science 273, 483-487 (1996).
61. A. J. Hart and A. H. Slocum, "Force output, control of film structure, and microscale shape transfer by carbon nanotube growth under mechanical pressure," Nano Lett. 6, 1254-1260 (2006).
62. Z. F. Ren, Z. P. Huang, J. W. Xu, J. H. Wang, P. Bush, M. P. Siegal, and P. N. Provencio, "Synthesis of large arrays of well-aligned carbon nanotubes on glass," Science 282, 1105-1107 (1998).
63. Z. F. Ren, Z. P. Huang, D. Z. Wang, J. G. Wen, J. W. Xu, J. H. Wang, L. E. Calvet, J. Chen, J. F. Klemic, M. A. Reed, "Growth of a single freestanding multiwall carbon nanotube on each nanonickel dot", Appl. Phys. Lett. 75, 1086-1088 (1999).

64. MicroChem Corp. (http://www.microchem.com).
65. I. G. Foulds, R.W. Johnstone, S.-H. Tsang, M. Pallapa, A. M. Parameswaran, "Exposure and development of thick polydimethylglutarimide films for MEMS applications using 254-nm irradiation," J. Micro/Nanlith. MEMS MOEMS 7, 023003 (2008).
66. M. Ahn, R. K. Heilmann, and M. L. Schattenburg, "Fabrication of ultrahigh aspect ratio freestanding gratings on silicon-insulator wafers," J. Vac. Sci. Technol. B 25, 2593-2597 (2007).
67. D. Richards, R.G. Milner, F, Huang, and F. Festy, "Tip-enhanced Raman microscopy: practicalities and limitations," J. Raman Spectrosc.34, 663-667 (2003).
68. C. V. Raman and K.S. Krishnan, "A new type of secondary radiation," Nature 121, 501-502 (1928).
69. M. Fleischmann, P. J. Hendra, and A. J. McQuillan, "Raman spectra of pyridine adsorbed at a silver electrode," Chem. Phys. Lett. 26, 163-166 (1974).
70. D. Jeanmaire and R. P. van Dyne, "Surface Raman spectroelectrochemstry Part I. Heterocyclic, aromatic, and aliphatic amines adsorbed on the anodized silver electrode," J. Electroanalyt, Chem. 84, 1-20 (1977).
71. K. Kneipp, Y. Wang, H. Kneipp, L. T. Perelman, I. Itzkan, R. R. Dasari, and M. S. Feld, "Single molecule detection using surface-enhanced Raman scattering (SERS)," Phys. Rev. Lett. 78, 1667-1670 (1997).
72. S. Nie and S. R. Emory, "Probing single molecule and single nanoparticles by surface-enhanced Raman scattering," Science 275, 1102-1106 (1997).
73. K. L. Kelly, E. Coronado, L. L. Zhao, and G. C. Schatz, "The optical properties of metal nanoparticles: The influence of size, shape, and dielectric environment," J. Phys. Chem. B 107, 668-677 (2003).
74. S. Zou and G. C. Schatz, "Silver nanoparticle array structures that produce giant enhancements in electromagnetic fields," Chem. Phys. Lett. 403, 62-67 (2005).
75. K. Li, M. I. Stockman, and D. J. Bergman, "Self-similar chain of metal nanospheres as an efficient nanolens," Phys. Rev. Lett. 91, 227402 (2003).

76. K. Li, X. Li, M. I. Stockman, and D. J. Bergman, "Surface plasmon amplification by stimulated emission in nanolenses," Phys. Rev. B 71, 115409 (2005).
77. S. E. Sburlan, L. A. Blanco, and M. Nieto-Vesperinas, "Plasmon excitation in sets of nanoscale cylinders and spheres," Phys. Rev. B 73, 035403 (2006).
78. K. H. Su, Q. H. Wei, and X. Zhang, 'Tunable and augmented plasmon resonances of Au/SiO_2/Au nanodisks," Appl. Phys. Lett. 88, 063118 (2006).
79. K. H. Su, S. Durant, J. M. Steele, Y. Xiong, C. Sun, and X. Zhang, "Raman enhancement factor of a single tunable nanoplasmonic resonator," J. Phys. Chem. B 110, 3964-3968 (2006).
80. A. Hartschuh, N. Anderson, and L. Novotny, "Near-field Raman spectroscopy using a sharp metal tip," J. Microscopy 210, 234-240 (2003).
81. B. Ren, G. Picarde, and B. Pettinger, "Preparation of gold tips suitable for tip-enhanced Raman spectroscopy and light emission by electrochemical etching," Rev. Sci. Instrum. 75, 837-841 (2004).
82. D. L. Stokes, Z. Chi, and T. Vo-Dinh, "Surface-enhanced-Raman-scattering-inducing nanoprobe for spectrochemical analysis," Appl. Spectroscopy 58, 292-298 (2004).
83. M. Becker, V. Sivakov, G. Andra, R. Geiger, J. Schreiber, S. Hoffmann, J. Michler, A. P. Milenin, P. Werner, and S. H. Christiansen, "The SERS and TERS effects obtained by gold droplets on top of Si Nanowires," Nano Lett. 7, 75-80 (2007).
84. C. F. Bohren and D. R. Huffman, Absorption and scattering of light by small particles, Wiley-VCH, Berlin (2004).
85. U. Srinivasan, D. Liepmann, and R. T. Howe, "Microstructure to substrate self-assembly using capillary forces," J. Microelectromech. Syst. 10, 17-24 (2001).
86. J. S. Smith, "Fluidic self-assembly of active antenna," U. S. Patent 6611237 (2003).

Appendix

1. Spin-coating of photoresists

1.1 SU8 and Polymethylglutarimide (PMGI)

Headway Research Inc., Model CB15 (SU8 spinner) is used for spinning MicroChem's SU8 2000 series negative epoxy resists and PMGI series.

1) Set the SU8spinner on the two stage "speed 1&2" setting; speed 1 at 500 rpm for 10 seconds and speed 2 for 40 seconds at the recipe specific speed (3000 rpm for both SU8-2015 and PMGI SF 11). Put a wafer on the appropriately sized chuck and make sure it is well centered.

In general, the wafer MUST be bigger than the chuck in all directions, or resist will be sucked into the spinner by the wafer vacuum. When a small piece of a wafer is used, covering the chuck with the blue tape is a better way than using a smaller chuck.

2) Statically dispense resist onto clean, dehydrated wafers, and press the "STRAT" button.

3) Use a swab with a squirt of acetone on it to "edge bead" clean the wafer, or wet resist will be deposited upon the chucks of downstream equipment such as the hot plates and aligner.

4) Put the wafer on the 95 °C hotplate without cooling or stopping for the 5 minute soft-bake. At the end of the soft-bake, after cooling, make sure that the surface is hardened.

5) Exposure: see the later parts for descriptions on the mask aligners.

6) Post Exposure Bake (PEB): Put the wafer on the 95 °C hot plates for 5min.

7) Develop: For SU8-2015, develop in PM Acetate, PGMEA, or SU8 developer, in a Pyrex bowl. For PMGI SF 11, develop in PMGI 101 developer. If fully developed, rinse developer (displacing the solvent) off of the wafer with 2-propanol (IPA). If a milky white color is apparent, it is from partially dissolved SU8-2015; the wafer may need more developing. Dry the IPA with the N2 gun and inspect.

1.2 Polymethly methacrylate (PMMA)

Cee 100 (PMMA spinner) and the associated hotplate are primarily used for the PMMA photoresist coating of samples that will use the SEBL facility of MIT. PMMA spinner uses a manual dispense operation with supplied pipettes.

1) Press PROG key [display reads: PROG MODE/ PROG #]. Press a program number, then ENTER. Continue to press ENTER as the values for VEL, RAMP RATE and TIME display for each step of the program. The parameters for electron-beam lithography to generate patterns for catalytic dots are stored in the program 5.

2) Prepare for spin-coating by readying PMMA solutions and a plastic pipette, and performing any pre-bake the wafers require. Change the chuck if necessary with the hex wrench provided. Choose the program by pressing RUN-followed by PROG 5 - ENTER.

3) Load a wafer onto the spin chuck, close the lid and press START. Do not dispense a photoresist yet, the system will perform a three second wafer centering test and check chuck vacuum. At the end of this test the display will read [0 to RETEST / START].

4) If there are no errors, open the lid and secure it. Dispense PMMA solutions. Close the lid and press START. The process will sequence automatically and display the rpm and time remaining. When complete an alarm will sound and the display will prompt you to unload the wafer. Move the wafer to the bake hotplate, and bake it for 15 min.

2. Exposing photoresists

2.1 MA-4 (KSAligner2)

The Karl Suss aligner is a precision mask alignment and exposure system, incorporating conventional as well as IR (back-to-front) alignment capabilities. The optical system employs a splitfield revolving microscope with 3.5x, 10x, and 25x objectives, and 10x binocular eyepieces. Three viewing modes (splitfield, full left-hand image, and full right-hand image) are possible. The exposure system uses a 350 W high pressure mercury lamp (the wavelength: 320 nm, the power density: 6 mW/cm^2). Wafer stage movement is controlled by x, y and theta aligning verniers.

1) Turn power on by pressing red POWER switch; red button will light up. Press load switch, as directed by LCD. Shuttle will move under microscope. Press ALIGN.

2) Set the parameters.

- Exposure time
- Contact mode

3) Load mask to a mask holder, and toggle vacuum ON to the mask-holder.

4) Align the microscope to the mask, and find the alignment marks on the mask.

5) Slide TRANSPORT SLIDE chuck assembly from underneath the mask, and place the wafer on the chuck with the wafer resting against the pins.

6) Slide TRANSPORT SLIDE in until it locks. Vacuum to chuck will automatically activate as TRANSPORT SLIDE is brought under the mask. Make sure SEPARATION LEVER is at zero.

7) Have the wafer contact to the mask by using the CONTACT LEVER located on the left hand side of WAFER SHUTTLE. Separate wafer from the mask by pulling SEPARATION LEVER toward the front of WAFER SHUTTLE. Separation can be adjusted from 0 to 90 um. Then, align mask pattern to wafer. If you are working on a piece of the wafer less than the gap between two optical microscopes, only one optical microscope can be used for aligning the masks, which may reduce the alignment accuracy up to a few micrometers. Locating the sample at the center of the chuck, and designing the mask accordingly may improve the alignment accuracy by enabling easy manipulation of the wafer.

8) Press LOAD to bring WAFER SHUTTLE under UV lamp, and press EXPOSE to expose wafer.

2.2 Electronic Visions Model EV620 Mask Aligner (EV1)

The EV1 is a precision mask alignment and exposure system, incorporating conventional as well as back-to-front alignment capabilities. The exposure system uses a 350-watt high pressure mercury lamp (the wavelengths: 365-405 nm, power density: 10mW/cm^2/sec).

1) After the initialization is complete, open a recipe window such as the one pictured here. At this point the process parameters need to be set in the recipe window.

- Mask size
- Exposure time
- Contact mode
- Process mode
- Exposure mode
- Separation distance

2) After the process parameters are set, click on "Run", and follow screen prompts.

3) Alternate masks and chucks are kept in slotted holders by the machine. Leave the tooling used in place at the end of a run.

4) Wafer stage movement, for alignment of the wafer to the mask, is controlled by mechanical micrometers, in x, y and theta, and is done after the mask has been loaded, and aligned.

3. Growing the vertically aligned CNTs

3.1 Loading samples

1) Vent the plasma chamber with nitrogen (N_2) until the pressure reaches to the atmospheric pressure using the N_2-purging valve. When the filling process is finished, the chamber will over pressurize, and N_2 will start blowing out of the chamber base. Close N2-venting valve when finished.

2) Push the "Hoist" button once to open the plasma chamber. Wait until the mechanical system is fully opened before proceeding.

3) Load your samples on the wafer chuck. Center the active area of your substrate with respect to the wafer chuck center. The CNT chuck holds both pieces and complete wafers. Adjust the gap between the sample and the anode to 0.5-inch.

4) Push the "Hoist" button to close the plasma chamber. Make sure that the o-ring of the plasma chamber hull has a clean surface to seal against.

3.2 Making vacuum before deposition

1) Open the Gate Valve and pump down to 3 Torr.

2) Once the pressure in the plasma chamber is below 3 Torr, activate the turbo molecular pump by pushing the "Start" button on the turbo controller panel. Wait approximately for 1.5 hours until the plasma chamber pressure goes down to 1×10^{-6} Torr.

3.3 Heating the substrate

1) Start the flow of cooling water by opening the two yellow valves for water placed on the wall behind the CNT machine.

2) Turn ON the power of the heater controller located at the bottom of the control panel.

3) Set the temperature of the zone 1 controller by holding the up button (▲). The temperature for CNT growth falls in the 580 °C range.

4) Open the Turbo N_2 purge (this prevents corrosives from going into the turbo bearings, and is different from the chamber N_2 purge/vent).

3.4 Preparing gas flows and chamber run pressure

1) Make the reacting gases available to the plasma chamber. To do this, turn the three yellow valves and the tank valve of the gas tank cabinet that supplies ammonia. Also, turn the two yellow valves and the tank valve of the gas cabinet that supplies acetylene. Flip over the "closed" labels on both gas cabinets to re-label them as "open".

2) Turn on the MFC controller power switch.

3) Set the flow rates of acetylene (C_2H_2: channel 1) and ammonia (NH_3: channel 2). There is an On/Off switch for each gas, as well as for two unused MFC channels, and there is a dial to view the flow rate of one of these at a time. The flow rate can be adjusted by turning the set point screw and watching the change in actual flow if the dial is set to the correct channel.

3a) Select display channel 2 without turning on the switch for Channel 2 (the ammonia should not be flowing). Set the flow rate value of ammonia by pushing up the

set point switch of channel 2 and, at the same time, turning the potentiometer on the right of the set point 2 with a screwdriver. A recommended starting value is 160 sccm.

3b) Select display channel 1 without turning on the switch for channel 1 (the acetylene should not be flowing). Set the flow rate value of acetylene by pushing up the set point switch of channel 1 and, at the same time, turning the potentiometer on the right of the set point with a screwdriver. The recommended starting value is 45 sccm.

4) Turn on the channel 2 switch to start the flow of ammonia. Set chamber pressure by partially closing the gate valve while inlet gas is flowing. Adjust to about 8 Torr. Wait until the temperature stabilizes at the target temperature. Ammonia etches the CNT seed, and we know that in this machine a 15 nm thick Nickel seed disappears after about 30 minutes of ammonia flow without the presence of acetylene. For films 15 nm Ni films, do not flow the ammonia without flowing acetylene for more than about 15 minutes.

5) Quickly turn on Acetylene, channel 1, which should be at the correct flow rate already, and adjust the gate valve to reach 8 Torr. The temperature should not substantially change, as the acetylene flow rate is smaller than the ammonia flow rate.

3.5 Deposition

1) Turn the dc plasma supply ON. The output should be in OFF, the current should be in ON. Current and voltage indicators should be in 0.0

2) Turn on the output switch. Then, gradually rotate the Power level knob clockwise, observing the input voltage (current or power) increase, until plasma ignites, which usually occurs at about 500 V. As a reference, the plasma should be purple.

3) Start the deposition timer.

4) After process time is over, turn off the plasma power by rotating the Power level knob counter-clockwise, until no voltage is biased to the plasma. Then, turn off the output, and turn off the Plasma power.

5) Turn off the MFCs by setting OFF Channel 1 and Channel 2. Turn off the Main MFC switch.

6) Set the zone 1 (and zone 2 if used) the heater value to 15 °C. Turn off the Heater Controller main switch, to allow the heater to cool down slowly so its ceramic elements don't break.

3.6 Sample unloading

1) Close the three yellow valves and the tank valve of the ammonia, and the two yellow valves and the tank valve of the acetylene, and flip over the "open" labels on both gas cabinets to re-label them as "closed".

2) Open fully the gate valve for 30 minutes.

3) After 30 min, turn off the turbo by pushing the start button on the turbo panel, and turn off the turbo N_2 purge.

4) Fully close gate valve.

5) Open the N_2 vent, until the chamber is over pressurized and starts venting excess N_2.

6) Push the Hoist button to open the plasma chamber, and turn off N_2 vent. Wait until the mechanical system fully lifts the plasma chamber hull.

7) Remove your samples from the wafer chuck with dedicated tweezers and store in compatible locations.